

Advances in Functionalized Materials Research

Guest Editors: Daniela Predoi, Mikael Motelica-Heino,
and Philippe Le Coustumer





Advances in Functionalized Materials Research

Journal of Nanomaterials

Advances in Functionalized Materials Research

Guest Editors: Daniela Predoi, Mikael Motelica-Heino,
and Philippe Le Coustumer



Copyright © 2015 Hindawi Publishing Corporation. All rights reserved.

This is a special issue published in "Journal of Nanomaterials." All articles are open access articles distributed under the Creative Commons Attribution License, which permits unrestricted use, distribution, and reproduction in any medium, provided the original work is properly cited.

Editorial Board

Katerina Aifantis, Greece
Nageh K. Allam, USA
Margarida Amaral, Portugal
Xuedong Bai, China
Enrico Bergamaschi, Italy
Theodorian Borca-Tasciuc, USA
C. Jeffrey Brinker, USA
Christian Brosseau, France
Xuebo Cao, China
Sang-Hee Cho, Republic of Korea
Shafiq Chowdhury, USA
Cui Chunxiang, China
Miguel A. Correa-Duarte, Spain
Shadi A. Dayeh, USA
Ali Eftekhari, USA
Claude Estournes, France
Alan Fuchs, USA
Lian Gao, China
Russell E. Gorga, USA
Hongchen Chen Gu, China
Mustafa O. Guler, Turkey
John Zhanhu Guo, USA
Smrati Gupta, Germany
Michael Harris, USA
Zhongkui Hong, USA
Michael Z. Hu, USA
David Hui, USA
Y.-K. Jeong, Republic of Korea
Sheng-Rui Jian, Taiwan
Wanqin Jin, China
Rakesh K. Joshi, India
Zhenhui Kang, China

Fathallah Karimzadeh, Iran
Do Kyung Kim, Republic of Korea
Kin Tak Lau, Australia
Burtrand Lee, USA
Benxia Li, China
Jun Li, Singapore
Shijun Liao, China
Gong Ru Lin, Taiwan
J.-Y. Liu, USA
Jun Liu, USA
Tianxi Liu, China
Songwei Lu, USA
Daniel Lu, China
Jue Lu, USA
Ed Ma, USA
Gaurav Mago, USA
Sanjay R. Mathur, Germany
Nobuhiro Matsushita, Japan
A. McCormick, USA
Vikas Mittal, UAE
Weihai Ni, Germany
Sherine Obare, USA
Edward Andrew Payzant, USA
Kui-Qing Peng, China
Anukorn Phuruangrat, Thailand
Ugur Serincan, Turkey
Huaiyu Shao, Japan
Donglu Shi, USA
Suprakas Sinha Ray, South Africa
Vladimir Sivakov, Germany
Marinella Striccoli, Italy
Bohua Sun, South Africa

Saikat Talapatra, USA
Nairong Tao, China
Titipun Thongtem, Thailand
Somchai Thongtem, Thailand
Valeri P. Tolstoy, Russia
Tsung-Yen Tsai, Taiwan
Takuya Tsuzuki, Australia
Raquel Verdejo, Spain
Mat U. Wahit, Malaysia
Shiren Wang, USA
Yong Wang, USA
Cheng Wang, China
Zhenbo Wang, China
Jinquan Wei, China
Ching Ping Wong, USA
Xingcai Wu, China
Guodong Xia, Hong Kong
Zhi Li Xiao, USA
Ping Xiao, UK
Shuangxi Xing, China
Yangchuan Xing, USA
N. Xu, China
Doron Yadlovker, Israel
Ying-Kui Yang, China
Khaled Youssef, USA
Kui Yu, Canada
Haibo Zeng, China
Tianyou Zhai, Japan
Renyun Zhang, Sweden
Yanbao Zhao, China
Lianxi Zheng, Singapore
Chunyi Zhi, Japan

Contents

Advances in Functionalized Materials Research, Daniela Predoi, Mikael Motelica-Heino, and Philippe Le Coustumer
Volume 2015, Article ID 412690, 2 pages

Clarification of the Magnetocapacitance Mechanism for Fe₃O₄-PDMS Nanocomposites, Chen Guobin, Yang Hui, Zhang Xiaoming, Liu Jun, and Tang Jun
Volume 2015, Article ID 982174, 6 pages

Characterization of the Oxides Present in a Polydimethylsiloxane Layer Obtained by Polymerisation of Its Liquid Precursor in Corona Discharge, A. Groza and A. Surmeian
Volume 2015, Article ID 204296, 8 pages

Multifunctional DNA Nanomaterials for Biomedical Applications, Dick Yan Tam and Pik Kwan Lo
Volume 2015, Article ID 765492, 21 pages

Advances in Multiferroic Nanomaterials Assembled with Clusters, Shifeng Zhao
Volume 2015, Article ID 101528, 12 pages

Hydrothermal Synthesis of Bi₂MoO₆ Visible-Light-Driven Photocatalyst, Anukorn Phuruangrat, Sunisa Putdum, Phattranit Dumrongrojthanath, Somchai Thongtem, and Titipun Thongtem
Volume 2015, Article ID 135735, 6 pages

Rare Earth Doped Apatite Nanomaterials for Biological Application, Thalagalage Shalika Harshani Perera, Yingchao Han, Xiaofei Lu, Xinyu Wang, Honglian Dai, and Shipu Li
Volume 2015, Article ID 705390, 6 pages

Generation of Porous Alumina Layers in a Polydimethylsiloxane/Hydrogen Peroxide Medium on Aluminum Substrate in Corona Discharges, A. Groza, A. Surmeian, C. Diplasu, C. Luculescu, C. Negriila, and M. Ganciu
Volume 2014, Article ID 578720, 6 pages

Tetraethyl Orthosilicate Coated Hydroxyapatite Powders for Lead Ions Removal from Aqueous Solutions, Rodica V. Ghita, Simona Liliana Iconaru, Cristina Liana Popa, Adrian Costescu, Philippe Le Coustumer, Mikael Motelica-Heino, and Carmen Steluta Ciobanu
Volume 2014, Article ID 176426, 7 pages

Preparation of Mesoporous SBA-16 Silica-Supported Biscinchona Alkaloid Ligand for the Asymmetric Dihydroxylation of Olefins, Shaheen M. Sarkar, Md. Eaqub Ali, Md. Lutfor Rahman, and Mashitah Mohd Yusoff
Volume 2014, Article ID 123680, 5 pages

Improved Ferroelectric and Leakage Properties of Ce Doped in BiFeO₃ Thin Films, Alima Bai, Shifeng Zhao, and Jieyu Chen
Volume 2014, Article ID 509408, 7 pages

Editorial

Advances in Functionalized Materials Research

Daniela Predoi,¹ Mikael Motelica-Heino,² and Philippe Le Coustumer³

¹National Institute of Materials Physics, P.O. Box MG 07, Bucharest, 077125 Magurele, Romania

²ISTO, UMR 7327 CNRS, Université d'Orléans, 1A rue de la Férollerie, 45071 Orléans Cedex 2, France

³EA 4592 Géoressources & Environnement, ENSEGID, Université Bordeaux, 1 allée F. Daguin, 33607 Pessac Cedex, France

Correspondence should be addressed to Daniela Predoi; dpredoi@gmail.com

Received 11 December 2014; Accepted 11 December 2014

Copyright © 2015 Daniela Predoi et al. This is an open access article distributed under the Creative Commons Attribution License, which permits unrestricted use, distribution, and reproduction in any medium, provided the original work is properly cited.

During the last couple of decades an intensive attention has been given by the scientific communities to the development of a variety of nanomaterials such as inorganic, organic, polymeric, biological, and polymer composites for various applications from biomedical to environmental. Of these, the inorganic ones have been the most investigated as their properties can be changed through functionalization. They can also be made multifunctional with the ability to incorporate broad categories of functions relevant for biomedicine and environment.

This special issue is focused on current and expected advances in the area of functionalized nanomaterials. Due to the interdisciplinary nature of the topic, researchers from the scientific community were invited to contribute with a broad range of original research articles as well as review articles on the following topics: design and synthesis of functionalized nanomaterials, structural and morphological characterization of newly functionalized compounds, advanced functionalized materials for biomedical and environmental applications, and functionalized nanomaterials with magnetic properties.

R. V. Ghita et al. reported the synthesis of a new porous nanocomposite material based on tetraethyl orthosilicate (TEOS) coated hydroxyapatite. In their study, the authors have investigated the ability of these new materials to remove Pb^{2+} ions from aqueous solutions with different concentration and pH values. Their study showed that the HAP/Th nanopowders are promising materials for lead ions removal from aqueous solutions with different pH values, being able to be used in the future for depollution of wastewaters.

In his work, S. Zhao presents a review which highlights that the multiferroic properties of heterostructured multiferroic films assembled with clusters prepared by low energy cluster beam deposition can be controlled or improved by tuning the size of the clusters. In his review, he revealed that thin-film heterostructure is not destroyed due to low temperature and energy during LECBD progress, rendering the LECBD technique ideal to prepare multiferroic nanostructure for applications on NEMS devices.

A. Groza and A. Surmeian evidenced the type of the silicon oxide structures in the PDMS layer deposited on different supports in corona discharges using studies performed by reflection-absorption IR spectroscopy coupled with peak fitting. Their study revealed that at high currents (40 μA) the distribution of silicon oxide structures in the PDMS layer deposited on aluminium is influenced by the anodization of the Al substrate.

S. M. Sarkar et al. presented successfully synthesized air and moisture stable SBA-16-supported bis-cinchona alkaloid chiral ligand and demonstrated that SBA-16 silica is an excellent support material for the heterogeneous chiral ligands.

S. Putdum et al. reported the synthesis of bismuth molybdate (Bi_2MoO_6) nanoplates using the hydrothermal reaction of bismuth nitrate and sodium molybdate. In their work, the authors have also investigated the effect of the reaction temperature and time of photocatalytic nanoplates on phase, morphology, and photocatalytic properties. Their study revealed that Bi_2MoO_6 nanoplates synthesized at 180°C for 5 h exhibit the highest photocatalytic efficiency (over 96%) within 100 min of visible light irradiation.

A. Groza et al. reported for the first time the formation of a porous anodic Al oxide layer in negative corona discharge in the presence of the PDMS/H₂O₂ lying on the surface of the Al substrate. They revealed that the process was favored by the enhanced infusion of H₂O and OH radicals, respectively, by the negative ions of oxygen and neutral species (O₃) produced in negative corona discharge in air at atmospheric pressure.

A. Bai et al. presented the preparation of pure and Ce doped BiFeO₃ thin films by solution-gelation process and also the investigation of their phase structures and ferroelectric and leakage properties. They have attributed the enhanced ferroelectric properties to the structural transformation due to the Ce doping. Their work provides an available way of enhancing ferroelectric properties and possible multifunctional applications for BiFeO₃ based thin films.

C. Guobin et al. reported that they obtain Fe₃O₄-PDMS nanocomposites. Their study has shown that the magnetic properties of the nanocomposites depend on the magnetic properties of nanoparticles and that the variation of magnetocapacitance depends on the elastic module and the viscosity of PDMS. By comparing the calculated value with the experimental value, they have demonstrated that the model can well explain the magnetocapacitance effect in Fe₃O₄-PDMS nanocomposites.

In their work, T. S. H. Perera et al. summarized some recent progress on the synthesis, properties, and application of lanthanide doped Anps. They highlight the many synthesis methods reported by now in the literature and identified the in situ precipitation method as the most effective method. The review is focused on the new generation of fluorophores called rare earth doped apatite nanoparticles (REAnps) and their ability to emit near infrared radiations which have low absorptivity by tissue chromophores and are suitable for biological system imaging and also discusses the opportunity for future studies on the effective biological applications of REAnps.

In their work, D. Y. Tam and P. K. Lo make a review of the cutting edge research in the DNA nanotechnology field. The review focuses on the important role of DNA in nanotechnology and summarizes recent progress of drug delivery systems based on multidimensional DNA nanostructures and the understanding of cellular uptake mechanism such as their intracellular pathway and pharmacokinetics.

Acknowledgments

The editors would like to thank the authors who have submitted a manuscript to this special issue. The lead editor thanks all the editors for their time spent in reviewing and assigning reviews for the submitted manuscripts.

*Daniela Predoi
Mikael Motelica-Heino
Philippe Le Coustumer*

Research Article

Clarification of the Magnetocapacitance Mechanism for Fe₃O₄-PDMS Nanocomposites

Chen Guobin,¹ Yang Hui,² Zhang Xiaoming,¹ Liu Jun,³ and Tang Jun³

¹Key Laboratory of Instrumentation Science & Dynamic Measurement, Ministry of Education, North University of China, Taiyuan, Shanxi 030051, China

²Department of Mechatronic Engineering, Zeda Vocational & Technical College, Suqian, Jiangsu 223800, China

³Science and Technology on Electronic Test & Measurement Laboratory, North University of China, Taiyuan, Shanxi 030051, China

Correspondence should be addressed to Zhang Xiaoming; dace@nuc.edu.cn

Received 30 June 2014; Accepted 1 September 2014

Academic Editor: Mikael Motelica-Heino

Copyright © 2015 Chen Guobin et al. This is an open access article distributed under the Creative Commons Attribution License, which permits unrestricted use, distribution, and reproduction in any medium, provided the original work is properly cited.

We mainly focused on the magnetocapacitance effect of Fe₃O₄-PDMS nanocomposites. We also proposed the preparation method and measured microstructures, magnetic properties, and magnetocapacitance value of the nanocomposites. The magnetocapacitance measurement results show that the nanocomposites have magnetocapacitance property, the magnetocapacitance with magnetic field depends on the magnetic property, and the value at the same magnetic field is increasing with the volume fraction of Fe₃O₄ nanoparticles. The magnetocapacitance model is proposed to explain this phenomenon by analyzing the magnetic interaction between particles and the viscoelasticity of PDMS. We also calculated the theoretical capacitance value of all samples using the magnetization of nanoparticles and mechanical parameters of PDMS. From the theoretical values, it is concluded that the model we proposed can well explain the magnetocapacitance effect of Fe₃O₄-PDMS nanocomposites.

1. Introduction

Materials with magnetocapacitance effect are promising for advanced applications in magnetic field sensors, data storage, and microwave communication devices [1–3]. Currently, main attention has been paid to the magnetocapacitance composites with magnetoelectric coupling, which consist of piezoelectric phase and piezomagnetic or magnetostrictive phase, such as CFMO-PBT, CFO-KNN, and Terfenol-D-PZT [4–9]. Recently, magnetocapacitance nanocomposites without magnetoelectric coupling composed of magnetic nanoparticles and polymer have also been reported [10, 11]. However, most of the studies on the composite have focused on the magnetocapacitance effect at radio frequencies [12] and the variation of magnetocapacitance with magnetic field at lower frequency electric field and the mechanism of magnetocapacitance effect are rarely discussed. Further, this magnetocapacitance effect is very significant for designing magnetic field sensors and actuators with novel mechanism.

Fe₃O₄ nanoparticles have wide applications because of their good electrical and magnetic characteristics, such as drug delivery and magnetic resonance imaging (MRI) [13, 14]. There are also plenty of studies on synthesis and properties of the particles in recent papers [15–17]. Polydimethylsiloxane (PDMS) is mainly used in microfluidic devices due to its biocompatibility and easy fabrication [18, 19]. Recently, researchers also have reported conducting property of the composites with PDMS and silver or carbon nanoparticles [20–22].

In this study, we investigated the magnetocapacitance effect of Fe₃O₄ nanoparticles-PDMS composite at lower frequency (200 kHz). Firstly, the composite preparation method is introduced, and samples with different volume fraction of nanoparticles are prepared. Then, the variation of the composite magnetocapacitance dependence of magnetic field is studied. Finally, the model of composite magnetocapacitance effect is also analyzed.

TABLE 1: Experimental compositions and volume fractions of nanoparticles.

Sample number	Fe ₃ O ₄ particle size (nm)	Particle content (vol%)
1	200	20
2	200	17
3	200	13
4	200	9
5	200	5
6 (Pure PDMS)	—	—

2. Experimental Section

In this experiment, Fe₃O₄ particles (200 nm, 99%) were used (Beijing DK Nanotechnology, china). Sylgard 184 Silicone from (Dow Corning, MI, USA) was chosen as PDMS polymer matrix. All materials were used as received.

The preparation procedure of Fe₃O₄-PDMS nanocomposite was as follows. First, Fe₃O₄ particles were weighted and mixed with alcohol, and then the suspension was sonicated for about 10 min. Amount of PDMS was added to the suspension. After a stirring of about 15 min, the mixture was dried at 100°C for 1 h in a vacuum for evaporating all alcohol. The curing agent was added with the ratio of 10 : 1 of PDMS to curing agent and stirred for 10 min. The prepolymer mixture was dropped into a square module with a size of 15 mm × 15 mm × 1.5 mm, degassed at ambient temperature under vacuum for 30 min to remove any air bubbles, and then cured for 2 h at 90°C in air atmosphere. After curing, the nanocomposite film was peeled off from the module. The detail experimental compositions are shown in Table 1.

Microstructures of the prepared samples were examined by scanning electron microscope (SEM, Quanta 250 FEG). Magnetic properties of particles and nanocomposites were investigated using superconducting quantum interference device (SQUID, MPMS-XL-7) magnetometry. Elastic modulus of PDMS was measured by dynamic thermomechanical analysis (DMA, SDTA861e) at ambient temperature. In order to determine the magnetocapacitance properties of the nanocomposite, the film samples were fabricated to be parallel plate capacitor with copper electrode and shielding shell. The magnetic field dependence of the capacitance was measured in the magnetic field range of -10 Gs to 10 Gs at the frequency of 200 kHz using an Agilent high-precision LCR meter (HP4284A). The magnetic field was applied by electromagnet (EMP3, East Changing Technologies). The scheme of the experimental setup is depicted in Figure 1.

3. Results and Discussion

3.1. The Characterizations of Fe₃O₄ Particles and Fe₃O₄-PDMS Nanocomposites. The SEM micrographs of sample number 1 are shown in Figure 2. The particles are equally distributed in the composite materials with the average size of 200 nm. Figure 3 shows magnetization at the room temperature as a

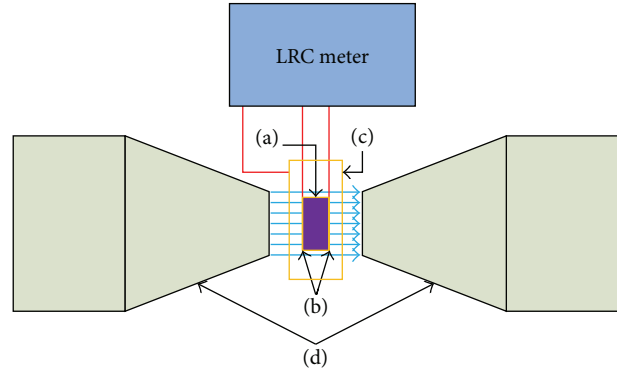


FIGURE 1: The scheme of the experimental setup: (a) nanocomposite; (b) Cu electrode; (c) Cu shielding shell; (d) electromagnet.

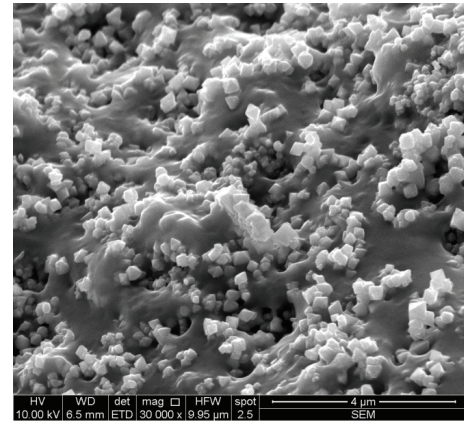


FIGURE 2: Scanning electron microscope (SEM) photographs of sample number 1.

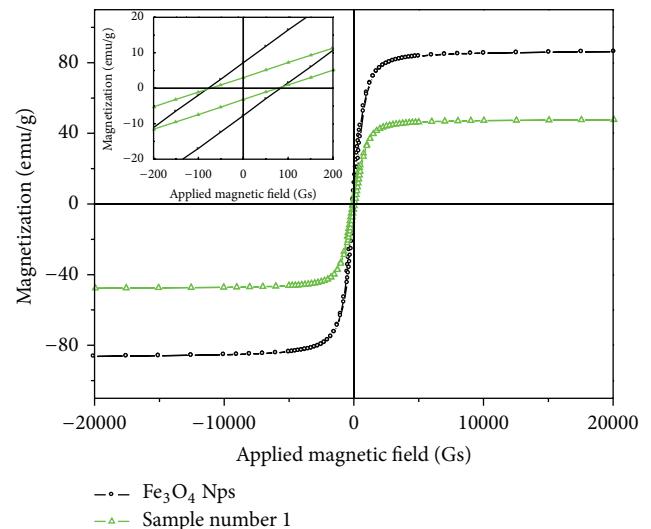


FIGURE 3: Variation of magnetization with applied magnetic field for 200 nm Fe₃O₄ nanoparticles (Nps) and sample number 1 at ambient temperature.

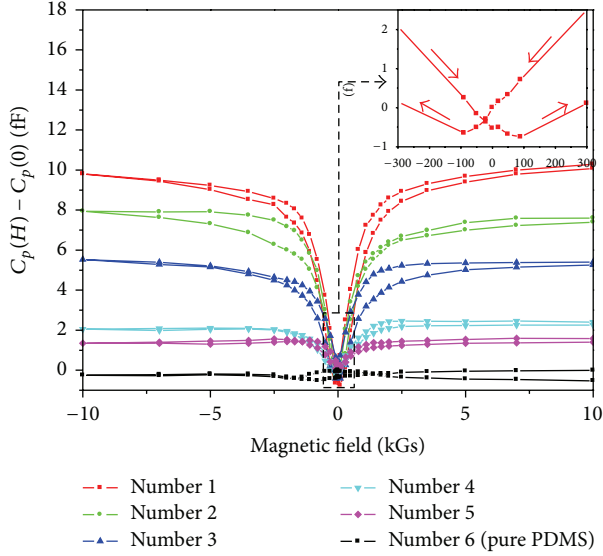


FIGURE 4: Variation of magnetocapacitance with applied magnetic field for all samples. Inset: an amplification of the curve for sample number 1.

function of applied magnetic field for 200 nm Fe_3O_4 nanoparticles and sample number 1. There is hysteresis present for Nps and nanocomposites with the same coercivity of 90 Oe, which is consistent with ferrimagnetic behavior. When the magnetic field exceeds 2 kGs, their magnetization would be saturated. However, the magnetic permeability and the saturation magnetization of the nanocomposites are smaller than that of the particles, because there is nonmagnetic material in the nanocomposites. Therefore, we can conclude that the magnetic properties of magnetocapacitance nanocomposites depend on the magnetic properties of magnetic nanoparticles in the nanocomposites.

3.2. Magnetocapacitance Properties of the Fe_3O_4 -PDMS Nanocomposites. For analyzing the magnetocapacitance effect of nanocomposite, we have measured the magnetic field dependences of the capacitance of all samples at the frequency of 200 kHz. During the measurements, the magnetic field and the electric field are parallel. At one measurement, the magnetic field starts at 10 kGs and gradually decreases to -10 kGs (defined as decreasing cycle) and then gradually increases to 10 kGs back (defined as increasing cycle).

Figure 4 shows the variation of difference capacitance with applied magnetic field. The magnetocapacitance (MC) effect is defined as $[C_p(H) - C_p(0)]$, where $C_p(H)$ and $C_p(0)$ are the capacitance at magnetic field H and zero field. Here, magnetocapacitance was found to increase with increasing the magnetic field for all samples, which illustrates that Fe_3O_4 -PDMS nanocomposites have magnetocapacitance property. The sample with higher volume fraction of nanoparticles has bigger magnetocapacitance, and the magnetocapacitance effect was not observed in the sample of pure PDMS. When the magnetic field exceeds 2 kGs, the magnetocapacitance of all samples would be saturated. It can be seen from the inset of Figure 4 that the magnetocapacitance

of the composite did not reach the minimum at zero field, but the magnetocapacitance minimum is at -90 Gs when the magnetic field decreases from 10 kGs to -10 kGs and is also at 90 Gs when the magnetic field increases from -10 kGs to 10 kGs. It can be seen that the magnetocapacitance effect for nanocomposite with magnetic field is similar to that for nanoparticles.

3.3. The Magnetocapacitance Effect Mechanism of Fe_3O_4 -PDMS Nanocomposite. The capacitance dependence of the magnetic field is mainly induced by the magnetostriction effect of Fe_3O_4 -PDMS nanocomposite. We assumed that the particles are completely equally distributed in the composites. When the magnetic field is applied to the composites, the arrangement of particles and the attraction between particles are directed along magnetic field vector. Because of the similarity between the magnetic nanoparticles and the magnetic dipole, the strength of the magnetic attraction force is given by

$$F = -\frac{3\mu_0 m^2}{2\pi r^4}, \quad m = \frac{4}{3}\pi a^3 B. \quad (1)$$

Here, r is the distance between the two particles dipole, a is the radius of the particle, B is the magnetic induction of the particle, and μ_0 is the permeability of vacuum.

Due to the viscoelasticity of PDMS which is the matrix of the nanocomposite, the motion of particles in the composites induced by applied magnetic field depends on elastic force, viscous force of PDMS, and the attraction force between two adjacent particles. The viscoelasticity of PDMS can be depicted as Kelvin model which contains parallel spring and damper. The particles are supposed as spherical. According to Stokes Law, the motion of dipoles with magnetic field can be described as follows:

$$m_p \frac{d^2 r}{dt^2} + 6\pi\eta a \frac{dr}{dt} + \pi a^2 E \frac{r - \delta}{\delta} = -\frac{8\pi\mu_0 a^6 B^2}{3r^4}, \quad (2)$$

in which m_p , η , E , δ , and r are the mass of one particle, the viscosity of PDMS, the elasticity modulus of PDMS, the mean mutual distance between the two adjacent particles at zero field, and the distance between the two neighboring particles with applying magnetic field in the direction of magnetic field, respectively.

If the particles are completely equally distributed in the composites, the mean mutual distance between the two adjacent particles at zero field is given by

$$\delta = \sqrt[3]{\frac{Lld_0}{n}} = \sqrt[3]{\frac{4\pi}{3\Phi}} a, \quad n = \frac{Lld_0\Phi}{(4/3)\pi a^3}, \quad (3)$$

in which L is the length of the sample, l is the width of the sample, d_0 is the thickness of the sample at zero field, Φ is the volume fraction of the nanoparticles, and n is the number of particles in the sample.

The distance r can be defined as

$$r = \delta + \Delta, \quad (4)$$

in which Δ is the distance variation between particles induced by applied magnetic field.

Therefore, (2) can be rewritten as follows by substituting (4) for r in (2):

$$m_p \frac{d^2 \Delta}{dt^2} + 6\pi\eta a \frac{d\Delta}{dt} + \pi a^2 E \frac{\Delta}{\delta} = -\frac{8\pi\mu_0 a^6 B^2}{3(\delta + \Delta)^4}. \quad (5)$$

It is known that $m_p \approx 2.09 \times 10^{-17}$ kg and the first term of (5) becomes negligible with respect to the others. For simplifying (5), we use Taylor expansion method to rewrite the right part of the equation. The variation distance Δ is small enough to make the higher order Taylor expansion terms be also negligible. Accordingly, (5) becomes

$$6\pi\eta a \frac{d\Delta}{dt} + \pi a^2 E \frac{\Delta}{\delta} \approx -\frac{8\pi\mu_0 a^6 B^2}{3} \left(\frac{1}{\delta^4} - \frac{4}{\delta^5} \Delta \right). \quad (6)$$

If a stable compressive stress is applied, the variation of the strain with time for PDMS has the creep property and Δ is given by

$$\Delta = 0 \quad (t = 0; B \neq 0). \quad (7)$$

Using the initial condition (7), the solution of (6) becomes

$$\Delta = \frac{8\mu_0 a^4 B^2 \delta}{32\mu_0 a^4 B^2 - 3E\delta^4} \left(1 - e^{((32\mu_0 a^5 B^2 - 3aE\delta^4)/18\eta\delta^5)t} \right). \quad (8)$$

The number of each chained particle directed along the magnetic field on the sample thickness can be calculated by

$$n_d = \frac{d_0}{\delta}. \quad (9)$$

When $t \neq 0$, $B \neq 0$, the thickness of the sample d can be approximated as

$$d = (n_d - 1)(\delta + \Delta) \cong d_0 \left(1 + \frac{\Delta}{\delta} \right) \quad \text{for } n_d \gg 1. \quad (10)$$

On the other hand, the capacitance of the sample is

$$C = \varepsilon_0 \varepsilon_r \frac{Ll}{d} = \varepsilon_0 \varepsilon_r \frac{Ll}{d_0} \left(\frac{\delta}{\delta + \Delta} \right), \quad (11)$$

where ε_0 is the dielectrical permittivity of the vacuum and ε_r is the relative permittivity of sample.

When the magnetization of the particles is zero, the capacity of the sample is

$$C_0 = \varepsilon_0 \varepsilon_r \frac{Ll}{d_0}. \quad (12)$$

Equation (13) describing the variation of the capacitance of the sample with the magnetization of particles and time

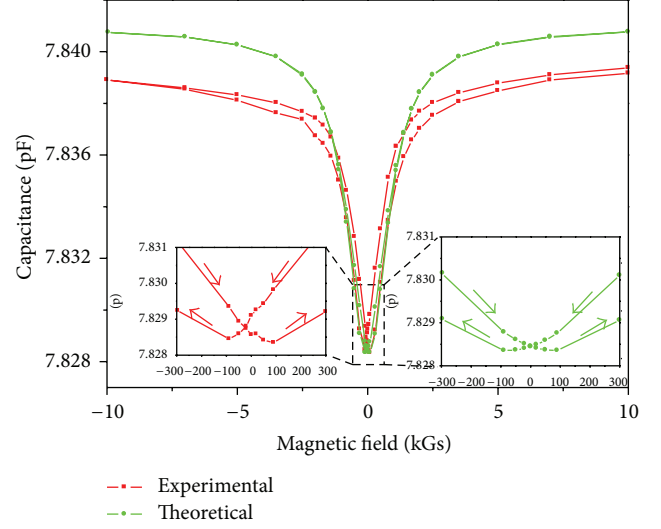


FIGURE 5: Variation of experimental and theoretical capacitance with magnetic field for sample number 1. Left inset: an amplification of experimental data. Right inset: an amplification of theoretical data.

of magnetic field can be obtained by substituting (8) and (11) into (12), as follows:

$$\begin{aligned} C &= C_0 \left(\frac{\delta}{\delta + \Delta} \right) \\ &= C_0 \left(\left(32\mu_0 B^2 - 3E \left(\frac{4\pi}{3\Phi} \right)^{4/3} \right) \right. \\ &\quad \times \left(40\mu_0 B^2 - 3E \left(\frac{4\pi}{3\Phi} \right)^{4/3} \right. \\ &\quad \left. \left. - 8\mu_0 B^2 e^{((32\mu_0 B^2 - 3E(4\pi/3\Phi)^{4/3})/18\eta(4\pi/3\Phi)^{5/3})t} \right)^{-1} \right). \end{aligned} \quad (13)$$

Therefore, we can conclude from (13) that the magneto-capacitance variation of nanocomposites with magnetic field depends on the elastic module and the viscosity of PDMS; it also depends on the magnetic property and the volume fraction of nanoparticles.

We can know that elastic modulus of PDMS is 6.72 Mpa and viscosity is 5.09×10^3 Pa·s by using DMA. We can also obtain the magnetic induction B of nanoparticles at different magnetic field from the hysteresis loop of nanoparticles in Figure 3. Accordingly, we can calculate the capacitance of the samples with different volume fraction of nanoparticles at $t = 10$ s by using (13). Figure 5 shows the variation of experimental and calculated capacitance value with magnetic field for sample number 1. Figure 6 shows the variation of calculated magnetocapacitance with applied magnetic field for samples with various volume fractions. It is clear from these figures that the variation of experimental and calculated capacitance value with magnetic field has the same characteristic and the deviation between the experimental

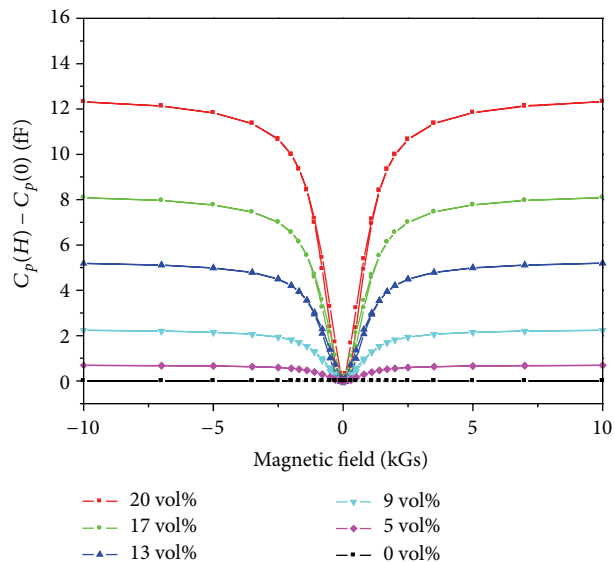


FIGURE 6: Variation of calculated magnetocapacitance with applied magnetic field for samples with various volume fraction.

and calculated capacitance value is smaller, which is caused by the unknown measurement errors. In conclusion, the proposed model can describe the magnetocapacitance effect of Fe_3O_4 -PDMS nanocomposites well.

4. Conclusions

In this paper, Fe_3O_4 -PDMS nanocomposites are prepared. The morphology characteristics, magnetic property, and magnetocapacitance effect are investigated. By analyzing the viscoelasticity of PDMS and the magnetic interaction between particles, the magnetocapacitance model of nanocomposites is also proposed. The particles are equally distributed in the composite materials with the average size of 200 nm. The magnetic properties of nanocomposites depend on the magnetic properties of nanoparticles. The magnetocapacitance effects of nanocomposites are observed. The velocity, hysteresis, and saturation value of the variation of the magnetocapacitance with applied magnetic field depend on the magnetic property and the volume fraction of Fe_3O_4 nanoparticles. The magnetocapacitance model shows that the variation of magnetocapacitance also depends on the elastic module and the viscosity of PDMS. By comparing the calculated value with experimental value, we demonstrate that the model can well explain the magnetocapacitance effect in Fe_3O_4 -PDMS nanocomposites.

Conflict of Interests

The authors declare that there is no conflict of interests regarding the publication of this paper.

Acknowledgment

This work was financially supported by the National Natural Science Foundation of China (Grant no. 51375463).

References

- [1] T. Siegrist and T. A. Vanderah, "Combining magnets and dielectrics: crystal chemistry in the $\text{BaO-Fe}_2\text{O}_3\text{-TiO}_2$ system," *European Journal of Inorganic Chemistry*, vol. 2003, no. 8, pp. 1483–1501, 2003.
- [2] W. Eerenstein, N. D. Mathur, and J. F. Scott, "Multiferroic and magnetoelectric materials," *Nature*, vol. 442, no. 7104, pp. 759–765, 2006.
- [3] C.-W. Nan, M. I. Bichurin, S. Dong, D. Viehland, and G. Srinivasan, "Multiferroic magnetoelectric composites: historical perspective, status, and future directions," *Journal of Applied Physics*, vol. 103, no. 3, Article ID 031101, 2008.
- [4] S. Dong, J. Zhai, J. Li, and D. Viehland, "Enhanced magnetoelectric effect in three-phase $\text{MnZnFe}_2\text{O}_4/\text{Tb}_{1-x}\text{Dy}_x\text{Fe}_{2-y}/\text{Pb}(\text{Zr,Ti})\text{O}_3$ composites," *Journal of Applied Physics*, vol. 100, no. 12, Article ID 124108, 2006.
- [5] S. He, G. Liu, J. Xu et al., "Magnetodielectric effect in lead-free multiferroic $\text{CoFe}_2\text{O}_4/\text{K}_{0.5}\text{Na}_{0.5}\text{NbO}_3$ bilayers," *Materials Letters*, vol. 89, pp. 159–162, 2012.
- [6] S. M. Salunkhe, S. R. Jigajeni, M. M. Sutar, A. N. Tarale, and P. B. Joshi, "Magnetoelectric and magnetodielectric effect in CFMO-PBT nanocomposites," *Journal of Physics and Chemistry of Solids*, vol. 74, no. 3, pp. 388–394, 2013.
- [7] C. Thirnal, C. Nayek, P. Murugavel, and V. Subramanian, "Magnetic, dielectric and magnetodielectric properties of PVDF- $\text{La}_{0.7}\text{Sr}_{0.3}\text{MnO}_3$ polymer nanocomposite film," *AIP Advances*, vol. 3, no. 11, Article ID 112109, 2013.
- [8] T. Cheng, L. F. Xu, P. B. Qi, C. P. Yang, R. L. Wang, and H. B. Xiao, "Tunable dielectric behaviors of magnetic field of $\text{PZT}_5/\text{NiFe}_2\text{O}_4$ ceramic particle magnetoelectric composites at room temperature," *Journal of Alloys and Compounds*, vol. 602, pp. 269–274, 2014.
- [9] S. M. Salunkhe, S. R. Jigajeni, A. N. Tarale, M. M. Sutar, and P. B. Joshi, "Investigations on magnetoelectric and magnetodielectric properties of CMFO-PBT composites," *Journal of Electronic Materials*, vol. 42, no. 6, pp. 1122–1132, 2013.
- [10] T.-I. Yang, R. N. C. Brown, L. C. Kempel, and P. Kofinas, "Magneto-dielectric properties of polymer- Fe_3O_4 nanocomposites," *Journal of Magnetism and Magnetic Materials*, vol. 320, no. 21, pp. 2714–2720, 2008.
- [11] W. Yang, S. Yu, R. Sun, and R. Du, "A compact low-pass filter based on the $\text{Fe}_3\text{O}_4@\text{SiO}_2$ -CCTO-epoxy composite film," *Integrated Ferroelectrics*, vol. 142, no. 1, pp. 61–72, 2013.
- [12] T.-I. Yang, R. N. C. Brown, L. C. Kempel, and P. Kofinas, "Surfactant-modified nickel zinc iron oxide/polymer nanocomposites for radio frequency applications," *Journal of Nanoparticle Research*, vol. 12, no. 8, pp. 2967–2978, 2010.
- [13] Y. Tian, B. Yu, X. Li, and K. Li, "Facile solvothermal synthesis of monodisperse Fe_3O_4 nanocrystals with precise size control of one nanometre as potential MRI contrast agents," *Journal of Materials Chemistry*, vol. 21, no. 8, pp. 2476–2481, 2011.
- [14] X. Yang, X. Zhang, Y. Ma, Y. Huang, Y. Wang, and Y. Chen, "Superparamagnetic graphene oxide- Fe_3O_4 nanoparticles hybrid for controlled targeted drug carriers," *Journal of Materials Chemistry*, vol. 19, no. 18, pp. 2710–2714, 2009.

- [15] M.-T. Chang, L.-J. Chou, C.-H. Hsieh et al., "Magnetic and electrical characterizations of half-metallic Fe_3O_4 nanowires," *Advanced Materials*, vol. 19, no. 17, pp. 2290–2294, 2007.
- [16] J. Sun, S. Zhou, P. Hou et al., "Synthesis and characterization of biocompatible Fe_3O_4 nanoparticles," *Journal of Biomedical Materials Research A*, vol. 80, no. 2, pp. 333–341, 2007.
- [17] D. Caruntu, G. Caruntu, Y. Chen, C. J. O'Connor, G. Goloverda, and V. L. Kolesnichenko, "Synthesis of variable-sized nanocrystals of Fe_3O_4 with high surface reactivity," *Chemistry of Materials*, vol. 16, no. 25, pp. 5527–5534, 2004.
- [18] T. Fujii, "PDMS-based microfluidic devices for biomedical applications," *Microelectronic Engineering*, vol. 61-62, pp. 907–914, 2002.
- [19] B. H. Jo, L. M. van Lerberghe, K. M. Motsegood, and D. J. Beebe, "Three-dimensional micro-channel fabrication in polydimethylsiloxane (PDMS) elastomer," *Journal of Microelectromechanical Systems*, vol. 9, no. 1, pp. 76–81, 2000.
- [20] X. Z. Niu, S. L. Peng, L. Y. Liu, W. Wen, and P. Sheng, "Characterizing and patterning of PDMS-based conducting composites," *Advanced Materials*, vol. 19, no. 18, pp. 2682–2686, 2007.
- [21] L. Liu, S. Peng, X. Niu, and W. Wen, "Microheaters fabricated from a conducting composite," *Applied Physics Letters*, vol. 89, no. 22, Article ID 223521, 2006.
- [22] S. M. Mehdi, K. H. Cho, and K. H. Choi, "Stretchability and resistive behavior of silver (Ag) nanoparticle films on polydimethylsiloxane (PDMS) with random micro ridges," *Journal of Materials Science: Materials in Electronics*, vol. 25, no. 8, pp. 3375–3382, 2014.

Research Article

Characterization of the Oxides Present in a Polydimethylsiloxane Layer Obtained by Polymerisation of Its Liquid Precursor in Corona Discharge

A. Groza and A. Surmeian

National Institute of Lasers, Plasma and Radiation Physics, Bucharest, 077125 Măgurele, Romania

Correspondence should be addressed to A. Groza; andreea@infim.ro

Received 20 August 2014; Accepted 28 September 2014

Academic Editor: Daniela Predoi

Copyright © 2015 A. Groza and A. Surmeian. This is an open access article distributed under the Creative Commons Attribution License, which permits unrestricted use, distribution, and reproduction in any medium, provided the original work is properly cited.

By combining the reflection-absorption infrared spectral studies with the peak fitting analysis we determined the type of the silicon oxides present in polydimethylsiloxane layers obtained on germanium and aluminium substrates in corona discharges. We have also evidenced that the dependence of silicon oxides density on the corona discharge current intensity is related to the existence of a concurrent anodizing process occurring at the polymer/Al substrate interface. The morphology of the Al substrate surface investigated by scanning electron microscopy proved that the anodizing process occurs.

1. Introduction

Polydimethylsiloxanes (PDMS) are widely used as protective corrosion media or in medical applications. The strength of the Si–O bonds gives them a remarkable thermal stability, most oxidizing agents not being able to attack their structure. They are elastic, transparent, and compatible with human tissue and are biologically inert [1].

The PDMS layers are known for their hydrophobic character, although for biomedical applications regarding cell adhesion [2] or antibacterial activity [3] it is important that PDMS layers have a hydrophilic character. By oxygen plasma, water vapor plasma, or ultraviolet-ozone (UV-ozone) treatments their surfaces can be functionalized [4] becoming more SiO₂ like surfaces with more –OH groups [2–5]. Recently [6], it was shown that SiO₂ layers, which have an excellent compatibility with the living tissues, can be used as interlayers for improving the delamination of hydroxyapatite (HAP) [7] coatings.

In our previous papers we presented a method of generation of PDMS layers on different substrates in corona discharges starting from different liquid precursors [8–10]. In [11] we showed by Fourier transformer infrared spectroscopy,

glow discharge optical emission spectroscopy, and scanning electron microscopy that function of the liquid precursor end group and substrate material, in the polymer bulk, mainly on the polymer surface, on some SiO₂ like structures can be generated.

In the present work, by peak fitting analysis of the reflection-absorption infrared (IR) spectra of the PDMS layers we have investigated the type of silicon oxides formed in the polymeric layer function of corona discharge current intensity and substrate material. Also, by scanning electron microscopy (SEM) we have analyzed the morphology of the substrate surface after the complete removal of the polymer layer.

We showed that the reflection-absorption IR spectral analysis could be used for the investigation of thin films deposited on different substrates, highlighting the processes occurring at thin film/substrate interface. The understanding of these interfacial processes can be useful in the studies of the different mechanical properties of thin polymeric layers, like adherence. For example, the interlinked bonds performed by the Si–OH groups can improve the adherence of thin layers to substrate surfaces avoiding the polymer delamination.

2. Materials and Methods

In this paper, using a SPI100 IR Perkin Elmer spectrometer (with a resolution of 4 cm^{-1}) and a SPECTRUM acquisition software version 6.4.1, we investigated by reflection-absorption and transmission IR spectroscopy the PDMS layers deposited in corona discharges on germanium and aluminium mirror like surfaces.

The PDMS layers have been obtained in negative corona discharges in a point (cathode) to plane (anode) electrode configuration (10 mm interelectrode gap) in air at atmospheric pressure for different values of current intensity ($10\ \mu\text{A}$ and $40\ \mu\text{A}$), starting from liquid precursors of hydroxyl terminated polydimethylsiloxane. These experimental conditions are proper for operating of the negative corona discharge in a Trichel pulse regime known for its uniformity of the current density distribution on the anode surface. Also, in this regime, the pulsating nature of the current assures uniform and periodically charged species (O_2^- , O_3^- , O_4^- , CO_2^- , and CO_3^-) transport between electrodes [11].

The procedure of PDMS thin film generation was as follows: a drop of hydroxyl terminated PDMS lying on the plane electrode is uniformly stretched in a liquid film under the injection of the negative ions produced in corona discharge. The electrohydrodynamic instabilities induced in the liquid film determine the formation of some stationary convective structures of Bernard cell type [8]. Consequently, after 2 hours of corona charge injection on the free surface of the liquid film, a solid PDMS layer, in our case with an average thickness of few hundred of nanometers [11], is generated.

It is well known that specular techniques provide reflectance measurement for reflective materials and reflection-absorption measurement for thin films deposited on reflective surfaces. In reflection-absorption measurements, a part of the radiation is reflected on the upper interface and contributes towards the spectrum via specular reflection. Another part of the radiation penetrates the surface film and is reflected by the reflective surface and, thus, the light passes through the surface layer twice, leading to an increase in intensity of the reflectance spectrum as compared to the normal transmission. The path length of the light through the sample depends on the angle of incidence [12].

In order to get information about the molecules bonds arrangement in the polymer layer and as close as possible to its surface, we recorded the reflection-absorption IR spectra of the PDMS layers deposited on germanium and aluminium mirror like surfaces using a variable angle specular reflectance accessory positioned inside the IR spectrometer. This accessory allows the variation of the angle of incidence of the light on the sample. The path length of the light and consequently the penetration depth of the light into the layer can be changed by varying the angle of incidence light on the sample. The reflection-absorption measurements were performed by varying the angle of reflection in the range of 30° – 60° [13].

The acquired reflection-absorption and transmission IR spectra were transformed into absorption spectra according to the formulas $A = \log(1/R)$ and $A = \log(1/T)$, respectively, using the SPECTRUM software.

In order to better reveal the structure of the obtained absorption spectra of the PDMS layers we proceed with the peak fitting analysis performed using the MagicPlotPro software specialized for these kinds of investigations in accordance with the National Institute of Standard and Technology (NIST) [22]. The procedure consists in a baseline correction of experimental IR spectrum followed by the calculation of the second order derivative for peak wavenumbers identification.

For each identified peak we used a Lorentz type profile curve as fitted curve. In the peak fitting analysis process, a sum of all the Lorentz fitted curves is generated by multiple iteration of the nonlinear least squares data fitting algorithm of the software. If the sum of all the fitted curves is set correctly the algorithm gives a valid and convergent solution. The theoretical curve, obtained as a result of peak fitting analysis versus experimental IR curve, will be presented and analysed in our further discussions.

3. Results and Discussions

Our previous papers have shown that, during the polymerization process of hydroxyl terminated polydimethylsiloxane liquid precursors in corona discharges, some SiO_2 like structures are generated. The morphology of these layers deposited on different substrates and their elemental depth profiles [11] showed that the SiO_2 structures are formed in the polymer bulk, mainly on the polymer surface.

In this work, the silicon oxides type in the polymeric layer was revealed by the peak fitting analysis of their reflection-absorption IR spectra. Also, the influence of the anodization process of the substrate on the IR reflection-absorption spectra of the PDMS layers will be analyzed.

3.1. FT-IR Analysis of Polymers Generated on Germanium Substrates. The IR spectra of the PDMS layer generated on a Ge substrate in corona discharge for an intensity of the current of $10\ \mu\text{A}$ are presented in Figure 1. Although there are some differences, both reflection-absorption, Figure 1(a), and transmission, Figure 1(b), spectra indicate the same IR bands specific to PDMS layers: 860 and 792 cm^{-1} peaks attributed to Si-CH_3 rocking and Si-C stretching vibrations; 1400 and 1254 cm^{-1} peaks assigned to symmetrical and asymmetrical deformation of CH_3 bonds in Si-CH_3 groups; 1080 and 1015 cm^{-1} peaks belonging to Si-O-Si stretching vibrations [15].

Knowing germanium as a transparent material to the IR light, we record the transmission IR spectrum of the PDMS layer as a marker for a proper identification of the absorption bands from 870 , 570 , and 750 cm^{-1} belonging to Ge-O-Ge and Ge-OH vibrational groups [10, 20]. The decrease of the intensity of these absorption bands in the reflection-absorption IR spectrum, Figure 1(a), is accompanied by the increases of the Si-O-Ge IR band from 660 cm^{-1} [10] and the evidence of the Si-OH IR band from $\sim 960\text{ cm}^{-1}$ [18]. As the elemental depth profile of a PDMS layers deposited on a Ge substrate previously showed the presence of a germanium oxide at the polymer/substrate interface [10], we suppose

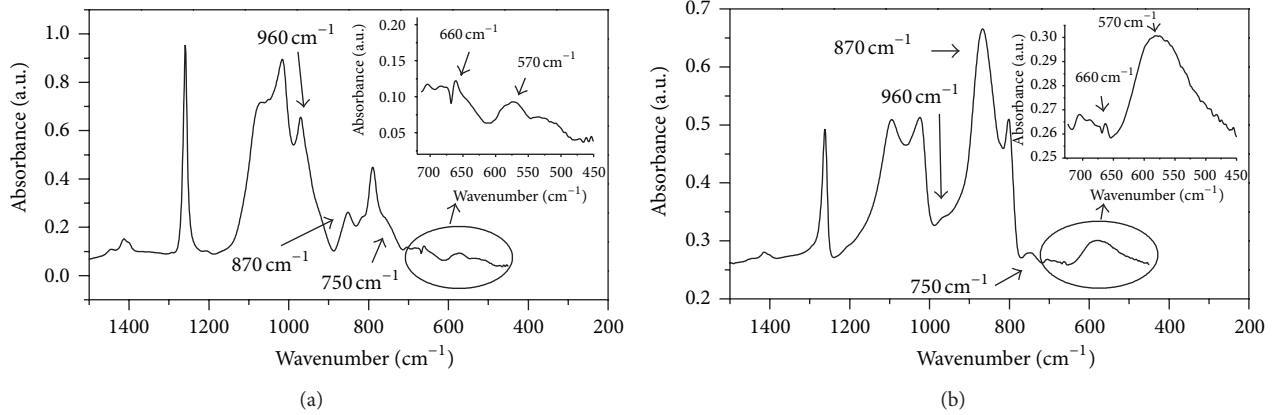


FIGURE 1: IR spectrum of the PDMS layer obtained by (a) reflection-absorption spectroscopy for a reflection angle of 30° and (b) transmission spectroscopy.

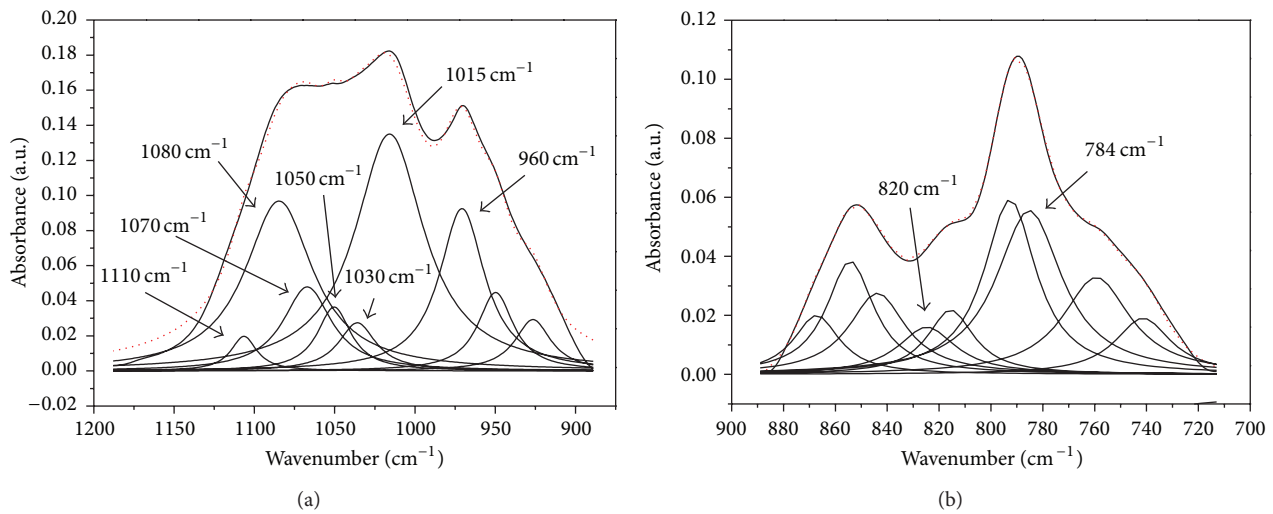


FIGURE 2: Deconvoluted reflection-absorption IR spectra (30° reflection angle) of PDMS layers deposited on Ge substrate in the spectral regions: (a) $1200\text{--}900\text{ cm}^{-1}$ and (b) $900\text{--}700\text{ cm}^{-1}$. The experimental curve is plotted in black and the theoretical fitted curve is in red dotted line.

that the IR spectrum obtained for 30° reflection angle can give information about the processes that take place at polymer/substrate interface.

Besides the evidence of the Si–O–Ge interlinked bonds between the polymer layer and the germanium substrate, the strong absorption band of the Si–OH groups present in the reflection-absorption IR spectrum, Figure 1(a), indicates the possibility of the development of some additional processes in the polymer layer, other than the polymerization one.

Therefore, we performed a peak fitting analysis for certain spectral regions of the reflection-absorption IR spectrum from Figure 1(a). This analysis reveals the formation of a SiO_2 network with some specific $\text{SiO}_{0.5}$, $\text{SiO}_{1.5}$, and SiO_4 structures in the polymer layer, as is shown in Figure 2 and Table 1.

3.2. FT-IR Analysis of Polymers Generated on Aluminum Substrates. The PDMS layers deposited on Al substrates in negative corona discharges for $10\ \mu\text{A}$ and $40\ \mu\text{A}$ values of

the discharge current are investigated by reflection-absorption spectroscopy. The peak fitting analysis of the IR spectra obtained for different reflection angles of the light from the sample allowed us to evidence the silicon oxides type: at polymer/Al substrate interface, into the polymer bulk, and as close as possible to its surface, as function of corona discharge current intensity.

In Figure 3 and Table 1 the results of the peak fitting analysis of the IR spectra of the PDMS layer deposited on Al substrate for a value of the corona discharge current of $10\ \mu\text{A}$ are presented. It can be seen that in the spectra of PDMS layers deposited on Al and Ge substrates are identified as the same types of silicon oxides.

Looking carefully at the evolution of the IR bands specific to silicon oxides developed in the PDMS layer function of the reflection angle, Table 1, we can find out the distribution of these structures in the PDMS layer. There are no major increases in the intensities of the IR bands characteristic to

TABLE 1: Identification and characterization of IR bands evidenced in the IR reflection-absorption spectra of the PDMS layers generated on Ge, respectively, Al substrate.

Wavenumber cm ⁻¹	IR bands	Oxide type	Absorbance [a.u.]					
			Ge		Al		Al	
			r = 30°	r = 30°	r = 40°	r = 50°	r = 60°	
1110	Si-O asymmetrical stretching vibration [14]	SiO ₄ tetrahedra structures [14]	0.019	0.14	0.55	0.65	0.69	
1080	Si-O-Si stretching vibration of the siloxane groups [15]		0.096	0.27	0.27	0.37	0.39	
1070	Si-O network stretching vibration [16]	SiO ₂ network	0.048	0.14	0.16	0.17	0.17	
1050	Si-O vibrational group [17]	SiO _{1.5} structures [17]	0.038	0.18	0.26	0.30	0.34	
1030	Si-O vibrational group [17]	SiO _{0.5} structures [17]	0.023	0.22	0.26	0.28	0.29	
1015	Si-O-Si stretching vibrations of the siloxane groups [15]		0.13	0.31	0.37	0.33	0.34	
960	Si-OH vibrational group [18]		0.09	—	—	—	—	
950	Si-OH vibrational group [18]		0.04	—	—	—	—	
920	Si-OH vibrational group [18]		0.027	—	—	—	—	
912	Al-OH vibrational group [19]		—	0.02	0.02	0.026	0.035	
900	Al-O vibrational group [19]	Al ₂ O ₃ [17]	—	0.033	0.026	0.06	0.06	
875	Si-OH vibrational group [18]		—	0.040	0.054	0.1	0.11	
870	Ge-O-Ge vibrational group [10, 20]	GeO ₂	0.017	—	—	—	—	
860	Si-CH ₃ rocking vibration [14, 16]		0.037	0.067	0.084	0.11	0.11	
852	Si-O asymmetric stretching vibration [14]	SiO ₄ tetrahedra structures [14]	0.026	—	—	—	—	
840	Si-O asymmetric stretching vibration [14]	SiO ₄ tetrahedra structures [14]	0.026	—	—	0.05	0.06	
820	Si-O-Si bending vibration [21]	SiO ₂	0.015	0.15	0.38	0.51	0.52	
815	Si-OH vibrational group [18]		0.021	0.13	0.23	0.31	0.33	
792	Si-C stretching vibration [15]		0.059	0.40	0.30	0.28	0.28	
784	Si-O symmetrical stretching vibration [14]	SiO ₄ tetrahedra structures [14]	0.055	0.18	0.18	0.19	0.19	
750	Ge-OH vibrational group [10, 20]		0.033	—	—	—	—	
740	Si-O/Si-CH ₃ vibrational groups [14, 16]		0.019	—	—	—	—	
660	Si-O-Ge vibrational group [10]		—	—	—	—	—	
570	Ge-O-Ge vibrational group [10, 20]	GeO ₂	—	—	—	—	—	

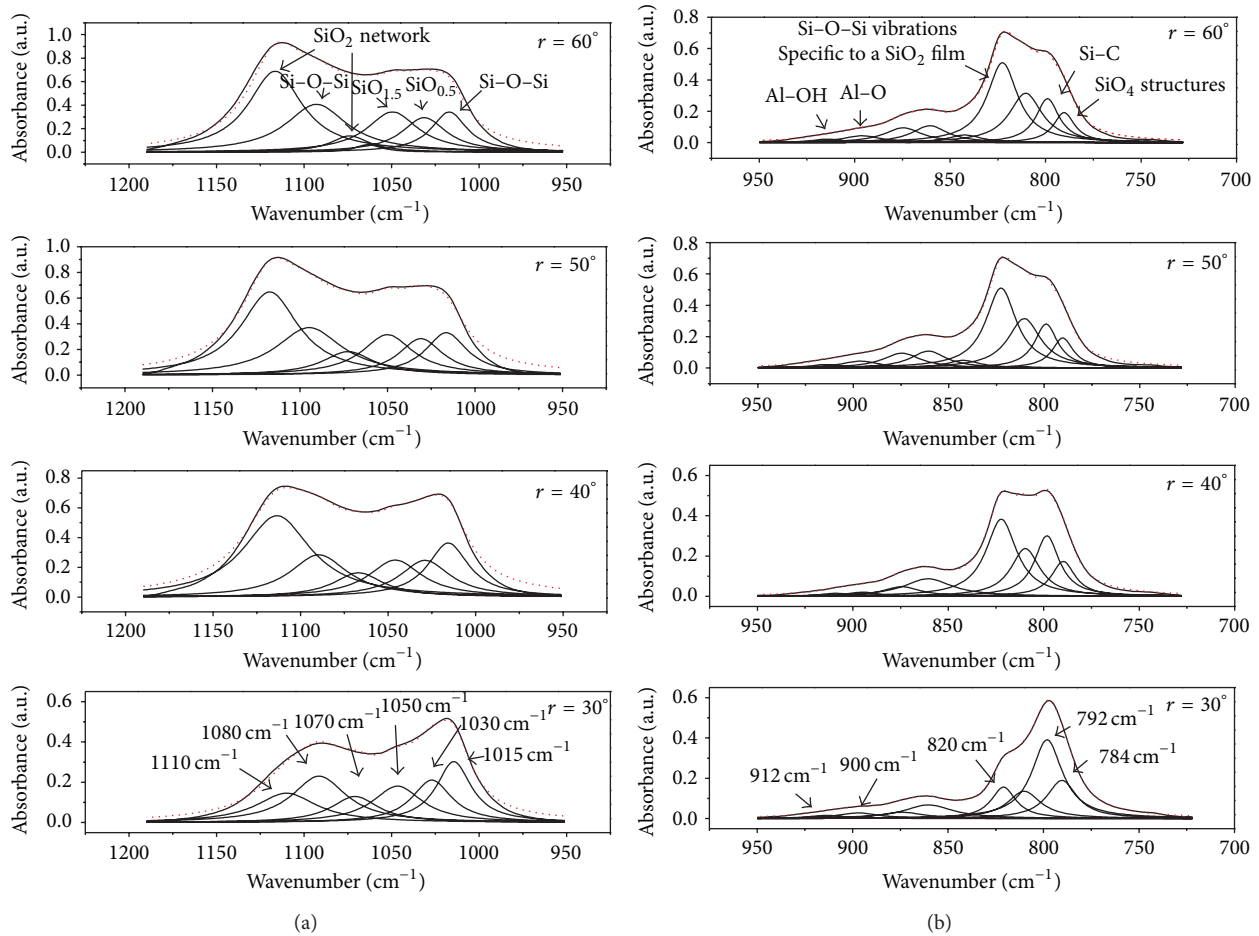


FIGURE 3: The dependence of the deconvoluted IR reflection-absorption spectra of PDMS layers deposited on Al substrate on the reflection angle in (a) 1200–900 cm^{-1} and (b) 900–700 cm^{-1} spectral regions.

siloxane groups (1080 and 1015 cm^{-1}), $\text{SiO}_{0.5}$, $\text{SiO}_{1.5}$ suboxides (1050 and 1030 cm^{-1}), and SiO_4 (784 cm^{-1}) structures. This fact indicates that the polymerization process of PDMS liquid film and that of the silicon oxides generation in corona discharge are produced homogeneously.

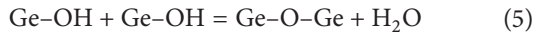
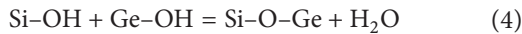
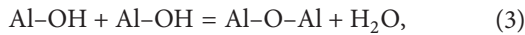
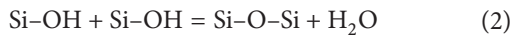
The intensities of the 1110 and 820 cm^{-1} (specific to stoichiometric SiO_2 layers [21]) IR bands increase gradually with the reflection angle mainly due to the higher density of SiO_4 structures formed at polymer surface as the scanning electron microscopy measurements previously showed [11]. In [16], the Si–O vibrations manifested at 1110 cm^{-1} and 1070 cm^{-1} were attributed to a cage like Si–O stretching mode and, respectively, to a Si–O network stretching mode that appears in a SiO_2 network. As the IR bands from 1070 cm^{-1} and 784 cm^{-1} do not present a gradual increase with the reflection angle, it means that at the proximity of the surface a cage like network of SiO_4 structures formation is favored. The results presented in Figure 3(b) and Table 1 also indicate that the intensity of the Si–OH IR band at 875 cm^{-1} increases as we increase incrementally the reflection angle from 30° to 60°. In some previous papers [18] it was shown that the formation of the OH groups on the surface of PDMS layers increases

the bioactivity properties of these materials, making them more proper for biological applications.

The distribution of the Si–O based network in the polymer can be explained if we consider the negatively charged particles deposition at the free surface of the liquid precursor during the polymerization process of the hydroxyl terminated PDMS in corona discharge. The negative ions of oxygen O_2^- , O_3^- , O_4^- , CO_2^- , and CO_3^- and water vapors from the atmosphere [23] are then continuously and uniformly injected into the liquid precursor generating a convective movement of the liquid. In this way, they propagate through the liquid until reaching the substrate. As a result of these processes, the charged particles attack like solvents the chemical structure of the precursor initiating a polymerization process. As the polymerization process advances and the convective movement of the liquid is diminished, the charge particle deposition from the free surface of the material favors the SiO_4 structures formation mainly at the polymer surface [11].

The presence of the polymers deposited on both Ge and Al substrates of the Si–OH, Ge–OH, Al–OH, Si–O–Si, Ge–O–Ge, Al–O–Al, and Si–O–Ge groups in the IR spectra may be considered as a result of the following reactions occurring

in the polymer, respectively [10, 11, 24]:



Although the PDMS layers are produced in the same experimental conditions on both Ge and Al substrates ($10 \mu\text{A}$ current intensity of the corona discharge), there are no Si-O-Al vibrational bands identified in the IR spectrum from Figure 3.

During the polymerization process of the hydroxyl terminated PDMS liquid precursor in negative corona discharge some water molecules are generated. They can be decomposed under the influence of corona electric fields and associated charge injection, generating OH radicals. Thus, the negative ions of oxygen produced in corona discharge and the OH radicals present in the material bulk can oxidize the substrate surface generating oxides by a process similar to anodization [25]. In a classical electrochemical anodization process, these species are responsible for the oxidation of the material interface and the generation of oxides.

The IR spectra of a PDMS layer deposited on Al substrate in a negative corona discharge for a discharge current of $40 \mu\text{A}$ are presented in Figure 4. As we increase the reflection angle from 30° to 60° the IR spectra look alike. Although in Figure 4 there are no visible IR bands attributed to Si-O bonds, other than those specific to siloxane groups, the peak fitting analysis allowed the identification of the IR bands characteristic to the SiO_2 network. The distribution of these IR bands (for all the reflection angles) is similar to that one presented in Figure 3 in the case of the PDMS layer deconvoluted spectra from 30° reflection angle. This fact could indicate that some concurrent processes that inhibit the major development of the SiO_2 network on the polymer layer surface have occurred during the polymerization of the PDMS.

The IR band from 642 cm^{-1} , previously assigned to Si-O-Al bonds formation [11, 26], appears in the spectra in Figure 4, having almost the same intensity for all the reflection angles. This band was not observed in the IR spectrum of the PDMS layer generated on Al substrate for a value of the corona discharge current of $10 \mu\text{A}$. It indicates that, at higher values of the corona discharge currents ($40 \mu\text{A}$), Si-OH bonds are rather involved in the generation of Si-O-Al bonds than in the formation of the silicon oxides.

The dependence of the Si-O-Al IR band intensity on the corona discharge current values observed for a reflection angle of 30° was previously associated with an anodization process of the Al substrate at polymer/substrate interface. The aluminum oxide layer formed at polymer/substrate interface was evidenced by the elemental depth profile of the PDMS layer deposited on an Al substrate for $10 \mu\text{A}$ corona discharge current intensity [11].

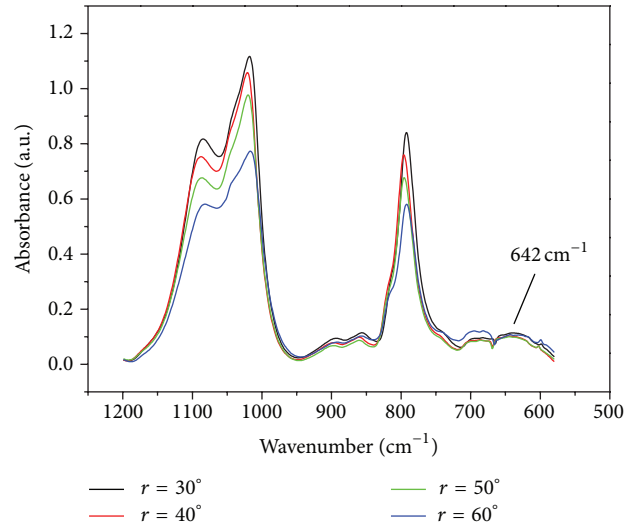


FIGURE 4: IR reflection-absorption spectra of the PDMS layer deposited on Al substrate (at $40 \mu\text{A}$ discharge current) for different reflection angles.

Therefore, we suppose that the similar values of the Si-O-Al IR band intensities obtained when the reflection angle was gradually increased up to 60° (for $40 \mu\text{A}$ corona discharge current), Figure 4, could indicate an advanced anodization of the substrate with the formation of some columnar structures [24]. Thus, as the polymer is formed, it follows perfectly the complex surface of the anodized Al interface and the Si-O-Al bonds are uniformly distributed inside the polymer bulk.

The presence of the Si-O-Al bonds in the IR spectrum, Figure 4, indicates that the Si-OH + Al-OH = Si-O-Al + H_2O reaction is also possible to occur in the PDMS layer.

3.3. Scanning Electron Microscopy (SEM) Investigation of the Al Substrate Surfaces. The surface morphology of the substrate, after the complete removal of the polymers obtained at two different corona discharge current intensities, was examined using the scanning electron microscopy (SEM). Images were acquired with a FEI Inspect S scanning electron microscope in both high-vacuum and low-vacuum modes.

In Figure 5(a) it can be seen that, for $10 \mu\text{A}$ intensity of the corona discharge current, the anodized Al surface is rugged with no defined pore structures. On the contrary, when the corona discharge current is increased up to $40 \mu\text{A}$, Figure 5(b), the distribution and shape of the pores are changed. Their structure is ordered indicating some columns formation into the material bulk.

These SEM results are in good agreement with the IR spectral analysis shown in Figure 3. In this way, as the polymer is formed it follows the porous surface of the anodized Al substrate, with the Si-O-Al bonds being distributed uniformly into the polymer bulk.

The morphology of the Al surfaces also indicates that the infusion of negative oxygen ions and oxygen based radicals generated in negative corona discharge during the polymerization processes of a PDMS liquid precursor is not limited to

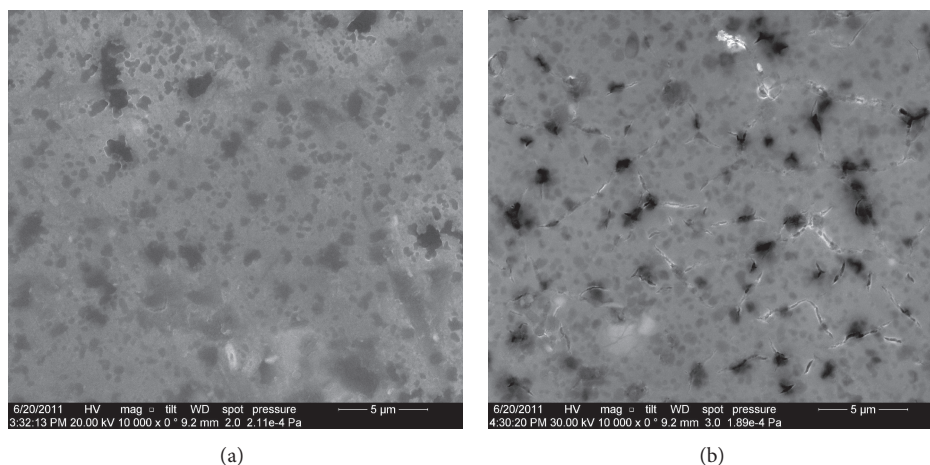


FIGURE 5: SEM images of the anodized Al substrate surface at different corona discharge current intensities: (a) $I = 10 \mu\text{A}$ and (b) $I = 40 \mu\text{A}$.

the polymer surface and polymer bulk, respectively. They can attack directly and indirectly (due to the OH radicals generated into the polymer bulk) the surface of the substrate material by an oxidation process similar to anodization [11, 25].

We did not observe these kinds of structures on the surface of oxidized germanium substrate.

4. Conclusions

The studies performed by reflection-absorption IR spectroscopy coupled with the peak fitting analysis presented in this paper evidenced the type of the silicon oxides structures in the PDMS layer deposited on different supports in corona discharges. At low current intensity of the corona discharge ($10 \mu\text{A}$), the IR spectral analysis of the layers deposited on germanium and aluminium substrates showed that while the $\text{SiO}_{0.5}$, $\text{SiO}_{1.5}$ suboxides and SiO_4 structures are uniformly distributed in the polymer layer, the cage like network of the SiO_4 structures is more present in the very proximity of the polymer surface. The germanium and aluminium oxides were also evidenced.

As the distribution of silicon oxides structures in the PDMS layer deposited on aluminium substrate is strongly dependent on the corona discharge current intensity, we observed that at high currents ($40 \mu\text{A}$) their distribution is influenced by the anodization of the Al substrate.

The SEM images of the Al substrate surface after the complete removal of the polymers indicate the presence of the porous alumina structures which create the possibility of columns formation into the material bulk. These images evidenced the anodization process of the Al substrate confirming the results obtained by reflection-absorption IR spectral analysis of the PDMS layer.

Conflict of Interests

The authors declare that there is no conflict of interests regarding the publication of this paper.

Acknowledgment

This work was supported by the PT-PCCA-2011-3.1-1136 UEFISCDI project.

References

- [1] S. Pinto, P. Alves, C. M. Matos et al., "Poly(dimethyl siloxane) surface modification by low pressure plasma to improve its characteristics towards biomedical applications," *Colloids and Surfaces B: Biointerfaces*, vol. 81, no. 1, pp. 20–26, 2010.
- [2] D. Fuard, T. Tzvetkova-Chevolleau, S. Decossas, P. Tracqui, and P. Schiavone, "Optimization of poly-di-methyl-siloxane (PDMS) substrates for studying cellular adhesion and motility," *Microelectronic Engineering*, vol. 85, no. 5-6, pp. 1289–1293, 2008.
- [3] P. Ferreira, Á. Carvalho, T. R. Correia, B. P. Antunes, I. J. Correia, and P. Alves, "Functionalization of polydimethylsiloxane membranes to be used in the production of voice prostheses," *Science and Technology of Advanced Materials*, vol. 14, no. 5, Article ID 055006, 2013.
- [4] J. C. Selby and M. A. Shannon, "A method to fabricate mesoscopic freestanding polydimethylsiloxane membranes used to probe the rheology of an epithelial sheet," *Journal of Biochemical and Biophysical Methods*, vol. 70, no. 6, pp. 932–944, 2008.
- [5] P. Ingram, M. Im, S. McDermott, M. Wicha, and E. Yoon, "Spheroid cell culture on PDMS hydrophobic surfaces and integration into microfluidic devices," in *Proceedings of the International Conference on Miniaturized Systems for Chemistry and Life Sciences (MicroTAS '11)*, pp. 1539–1541, Seattle, Wash, USA, October 2011.
- [6] K. Mediaswanti, C. Wen, E. P. Ivanova, C. C. Berndt, and J. Wang, "Sputtered hydroxyapatite nanocoatings on novel titanium alloys for biomedical applications," in *Titanium Alloys Advances in Properties Control*, chapter 1, INTECH, 2013.
- [7] S. L. Iconaru, P. Chapon, P. Le Coustumer, and D. Predoi, "Antimicrobial activity of thin solid films of silver doped hydroxyapatite prepared by sol-gel method," *The Scientific World Journal*, vol. 2014, Article ID 165351, 8 pages, 2014.

- [8] A. Groza, A. Surmeian, M. Ganciu, and I. I. Popescu, "Infrared spectral investigation of organosilicon compounds under corona charge injection in air at atmospheric pressure," *Journal of Optoelectronics and Advanced Materials*, vol. 7, no. 5, pp. 2545–2548, 2005.
- [9] A. Groza, A. Surmeian, M. Ganciu, R. Medianu, and I. I. Popescu, "SiO₂ - Like thin films generation in corona discharges in air at atmospheric pressure: IR spectroscopy and atomic force microscopy investigations," *Journal of Optoelectronics and Advanced Materials*, vol. 7, no. 4, pp. 2159–2164, 2005.
- [10] A. Groza, A. Surmeian, C. Diplasu, M. Ganciu, P. Chapon, and I. I. Popescu, "Spectral investigations of the processes observed at polydimethylsiloxane polymer-substrate interface during its polymerization process in negative and positive corona discharges," *Journal of Optoelectronics and Advanced Materials*, vol. 12, no. 11, pp. 2311–2314, 2010.
- [11] A. Groza, A. Surmeian, C. Diplasu et al., "Physico-chemical processes occurring during polymerization of liquid polydimethylsiloxane films on metal substrates under atmospheric pressure air corona discharges," *Surface and Coatings Technology*, vol. 212, pp. 145–151, 2012.
- [12] Z. M. Khoshhesab, "Reflectance IR Spectroscopy," in *Infrared Spectroscopy—Materials Science, Engineering and Technology*, T. Theophanides, Ed., chapter 11, pp. 233–244, InTech, 2012.
- [13] <http://www.vscht.cz/anl/vibspec/FTIR%20Reflection%20Techniques.pdf>.
- [14] B. J. Saikia, G. Parthasarathy, and N. C. Sarmah, "Fourier transform infrared spectroscopic estimation of crystallinity in SiO₂ based rocks," *Bulletin of Materials Science*, vol. 31, no. 5, pp. 775–779, 2008.
- [15] D. Lin-Vien, N. B. Colthup, W. G. Fateley, and J. G. Grasselli, "Organosilicon compounds," in *The Handbook of Infrared and Raman Characteristic Frequency of Organic Molecules*, pp. 251–261, Academic Press, San Diego, Calif, USA, 1991.
- [16] S. W. Hwang, G. R. Lee, J. H. Min et al., "Etch characteristics of silsesquioxane-based low dielectric constant material in fluorocarbon plasma," *Japanese Journal of Applied Physics*, vol. 41, no. 9, pp. 5782–5786, 2002.
- [17] J. Lambers and P. Hess, "Infrared spectra of photochemically grown suboxides at the Si/SiO₂ interface," *Journal of Applied Physics*, vol. 94, no. 5, pp. 2937–2941, 2003.
- [18] A. C. M. Kuo, "Poly(dimethylsiloxane)," in *Polymer Data Handbook*, J. E. Mark, Ed., pp. 411–435, Oxford University Press, 1999.
- [19] S. Wei, L. Wen, and H. Y. Hua, "FTIR analysis of adsorption of polydiallyl-dimethyl-ammonium chloride on kaolinite," *Journal of Central South University of Technology*, vol. 15, pp. 373–377, 2008.
- [20] R. F. S. Lenza and W. L. Vasconcelos, "Preparation of silica by sol-gel method using formamide," *Materials Research*, vol. 4, no. 3, pp. 189–194, 2001.
- [21] X. L. Wu, T. Gao, G. G. Siu, S. Tong, and X. M. Bao, "Defect-related infrared photoluminescence in Ge⁺-implanted SiO₂ films," *Applied Physics Letters*, vol. 74, no. 17, pp. 2420–2422, 1999.
- [22] "MagicPlot 2.5.1 User Guide," Magicplot Systems, LLC, 2013, <http://magicplot.com/downloads.php>.
- [23] M. Goldman and A. Goldman, "Corona discharges," in *Gaseous Electronics*, M. N. Hirsh and H. J. Oskam, Eds., vol. 1, pp. 219–290, Academic Press, New York, NY, USA, 1978.
- [24] B. J. G. de Aragão and Y. Messaddeq, "Peak separation by derivative spectroscopy applied to FTIR analysis of hydrolized silica," *Journal of the Brazilian Chemical Society*, vol. 19, no. 8, pp. 1582–1594, 2008.
- [25] X. Zhao, S.-K. Seo, U.-J. Lee, and K.-H. Lee, "Controlled electrochemical dissolution of anodic aluminum oxide for preparation of open-through pore structures," *Journal of the Electrochemical Society*, vol. 154, no. 10, pp. C553–C557, 2007.
- [26] Y. Y. Ivanova, T. I. Gerganova, M. H. V. Fernandes, and I. M. M. Salvado, "Preparation of nanostructured porous SiO₂-Al₂O₃ oxycarbonitride materials obtained by a new chemical precursor method," *Central European Journal of Chemistry*, vol. 7, no. 1, pp. 42–46, 2009.

Review Article

Multifunctional DNA Nanomaterials for Biomedical Applications

Dick Yan Tam^{1,2} and Pik Kwan Lo^{1,2}

¹Department of Biology and Chemistry, City University of Hong Kong, Tat Chee Avenue, Kowloon, Hong Kong

²Shenzhen Key Laboratory of Biochip Research, City University of Hong Kong, Shenzhen 518057, China

Correspondence should be addressed to Pik Kwan Lo; peggylo@cityu.edu.hk

Received 4 July 2014; Accepted 26 August 2014

Academic Editor: Daniela Predoi

Copyright © 2015 D. Y. Tam and P. K. Lo. This is an open access article distributed under the Creative Commons Attribution License, which permits unrestricted use, distribution, and reproduction in any medium, provided the original work is properly cited.

The rapidly emerging DNA nanotechnology began with pioneer Seeman's hypothesis that DNA not only can carry genetic information but also can be used as molecular organizer to create well-designed and controllable nanomaterials for applications in materials science, nanotechnology, and biology. DNA-based self-assembly represents a versatile system for nanoscale construction due to the well-characterized conformation of DNA and its predictability in the formation of base pairs. The structural features of nucleic acids form the basis of constructing a wide variety of DNA nanoarchitectures with well-defined shapes and sizes, in addition to controllable permeability and flexibility. More importantly, self-assembled DNA nanostructures can be easily functionalized to construct artificial functional systems with nanometer scale precision for multipurposes. Apparently scientists envision artificial DNA-based nanostructures as tool for drug loading and *in vivo* targeted delivery because of their abilities in selective encapsulation and stimuli-triggered release of cargo. Herein, we summarize the strategies of creating multidimensional self-assembled DNA nanoarchitectures and review studies investigating their stability, toxicity, delivery efficiency, loading, and control release of cargos in addition to their site-specific targeting and delivery of drug or cargo molecules to cellular systems.

1. Introduction

Public healthcare is a big issue among the society and has drawn much attention to general public. In general, some organic small-molecules, proteins, and nucleic acids have exhibited their promise as therapeutic agents for biomedical therapy. In the past years, scientists dreamed of improving the delivery efficacy of these target drugs for various biological and biomedical applications. However, problems in terms of solubility, toxicity, cost, and penetration ability need to be solved. They face several transport barriers after they are introduced to human body, before going to their sites of action. For example, first, drug molecules have to be stable in the circulation system, passing through the blood vessel and being recognized by those particular diseased cells. Afterwards, they have to pass through the highly chargeable plasma membrane and/or the nuclear membrane. They also have to withstand the acidic cellular environment. Finally, the multiple drug resistance mechanism also needs to be considered. Thus, it is of great importance developing smart

system which exhibits specific targeting and has high delivery efficacy of active drug molecules.

Scientists envision the rapid development of material sciences offering great advantage for creating smart drug delivery vehicles or carriers. Various drug delivery systems based on different materials have been developed [1]. For example, drugs can be loaded onto the nanoparticles [2] or nanodiamonds [3] for targeted delivery. Active biomolecular drugs can be coordinated to metals inside the carbon nanotube and then released by heating up the nanotubes samples [4]. Another advanced development is to deliver siRNA by PEGylated cyclodextrin molecules [5]. They were released by dissociation of the complexes in lysosome. Particularly, the most commonly used drug delivery system is the polymeric materials [6]. The diblock copolymers tend to form micelle in the presence of drug molecules. Therefore, drug can be easily loaded into the core of micelle [7]. However, being useful drug nanocarriers, it is necessary to consider their toxicity, biocompatibility, and stability in a cellular environment. It is well-known that most of the nanoparticles are toxic; they

may induce cytotoxicity in living systems. Heat triggered-release of drug molecules in a cellular environment is not appreciated because other healthy cells may also be affected. In addition, the efficiency and selectivity of drug loading in polymeric micelles is also highly limited. Therefore, to design new materials as drug carriers, these carriers should have a capability of drug incorporation and controlled release in a highly effective way. They should also be highly stable and biocompatible in a specific cellular environment. It is also necessary for them to target particular areas and carry multifunction in order to enhance the delivery efficiency.

Indeed, developing novel biocompatible and multifunctional nanocarriers remains a key challenge for targeted drug delivery. The rapidly emerging DNA nanotechnology began with pioneer Seeman's hypothesis that DNA not only can carry genetic information but also can be used as molecular organizer to create well-designed and controllable nanomaterials for applications in materials science, nanotechnology, and biology [8, 9]. As DNA has a simple and robust molecular recognition rule of adenine to thymine (A-T) and guanine to cytosine (G-C) pairings, two complementary single-stranded DNA hybridize to form a double helix with predictable and programmable interactions. The structural features of nucleic acids form the basis of constructing a wide variety of well-ordered DNA nanoarchitectures with well-defined shapes and sizes, in addition to controllable permeability and flexibility [10, 11]. This DNA nanotechnology offers new opportunities for the construction of complex DNA structures in different dimensions. More importantly, self-assembled DNA nanostructures can be easily functionalized to construct artificial functional systems for multipurposes. Apparently scientists envision artificial DNA-based nanostructures as tools for drug loading and *in vivo* targeted delivery because of their potential of selective encapsulation and stimuli-triggered release of cargo.

In this review article, we concentrate on a new-comer of drug delivery carriers based on self-assembled DNA nanostructures. We will demonstrate the power and promise of DNA as a scaffold to create DNA nanostructures with precise geometry and versatile functionality. Their structural stability in physiological conditions and internalization will be briefly described. Different cargo loading mechanisms and their control release via external stimuli will be summarized in detail. As a new-comer in drug delivery system, studies of intracellular behaviors/functions of drug loaded DNA nanocarriers and their interactions in specific intracellular compartments *in vitro* or *in vivo* will also be discussed. Some concluding remarks will try to ascertain what the next challenges and outlook of this exciting research area could be.

2. DNA Nanotechnology

To begin with, we first briefly introduce the history and the most updated status of DNA nanotechnology. The innovation of the field of DNA nanotechnology was first demonstrated by Seeman in the early 1980s [12]. Taking advantage of self-recognition property of DNA, his group designed and constructed modified Holliday junctions to convert one-dimensional DNA strands into branched DNA tiles with

sticky ends at the edges (Figure 1(a)). These short single-stranded units provide toeholds for further assembly of 2D-structures [13]. Since then, the structural role of DNA is widely well-recognized and extensively explored. However, these assembly approaches did not offer rigid junctions with well-defined angles and geometry of the final structures. To overcome these drawbacks, researchers started to develop advanced rigid junctions including multicrossover [14–16], cross-shaped tile with arms [17], DNA tensegrity triangle [18], and parallelogram DNA tile (Figure 1(b)) [19]. With such unprecedented talent to construct DNA-based architectures, highly ordered 2D-DNA surfaces with programmable arrangement and a large variety of three-dimensional polyhedral structures were successfully assembled via sticky-end cohesion among those building blocks [20–22]. Nevertheless, these tile-based assemblies have certain limitations. For example, it is difficult to control the size of resulting structures. An exact stoichiometric and a high purity control of individual DNA fragments are still problematic for the assembly of large and complex nanostructures.

Another creation in DNA nanotechnology was made by Rothemund in 2006 [23]. He invented scaffolded DNA origami which successfully offered high complexity and versatility in DNA assembly. In DNA origami, a long piece of single-stranded DNA from the M13 circular bacteriophage genome is folded with itself into a desired pattern with the assistance of short staple strands (Figure 1(c)) [24, 25]. Typical examples consist of nonperiodic 2D-structures, such as a map of the Americas, stars, smiley faces, and other deliberately well-designed patterns [26, 27]. In this approach, the relative stoichiometric ratio on different staple strands to a single DNA scaffold is not highly restricted. More importantly, DNA origami is a versatile and simple one-pot assembly to generate nanostructures with complex shapes of predefined dimensions as compared to the conventional crossover approach [28, 29]. In an advanced development, Kostiaainen's group has recently demonstrated the optical control of the DNA origami formation and release [30]. Although DNA was used as the only component to guide the DNA assembly in tile-based assembly or DNA origami, this resulted in fully double-stranded and DNA-dense structures.

An alternative approach to building DNA nanostructure is to bring together the programmability of DNA with functional and structural diversities offered by supramolecular chemistry [31]. This new emerging area in DNA nanotechnology involves the insertion of synthetic molecules into DNA strand to alter its hybridization and control the assembly outcome (Figure 1(d)). By conjugating synthetic molecules at the insertion points of a DNA strand, typical linear DNA duplexes can be oriented and hybridized relative to one another in a controlled manner. This supramolecular DNA assembly combines the diverse structural features of molecules and their functionalities such as luminescence, redox, magnetic, and catalytic properties to generate discrete well-defined structures.

Taking advantages of synthetic molecules as rigid junctions, this can reduce the amount of DNA strands needed for the structural definition as compared to the previous two methods. For example, Sleiman's group have successfully

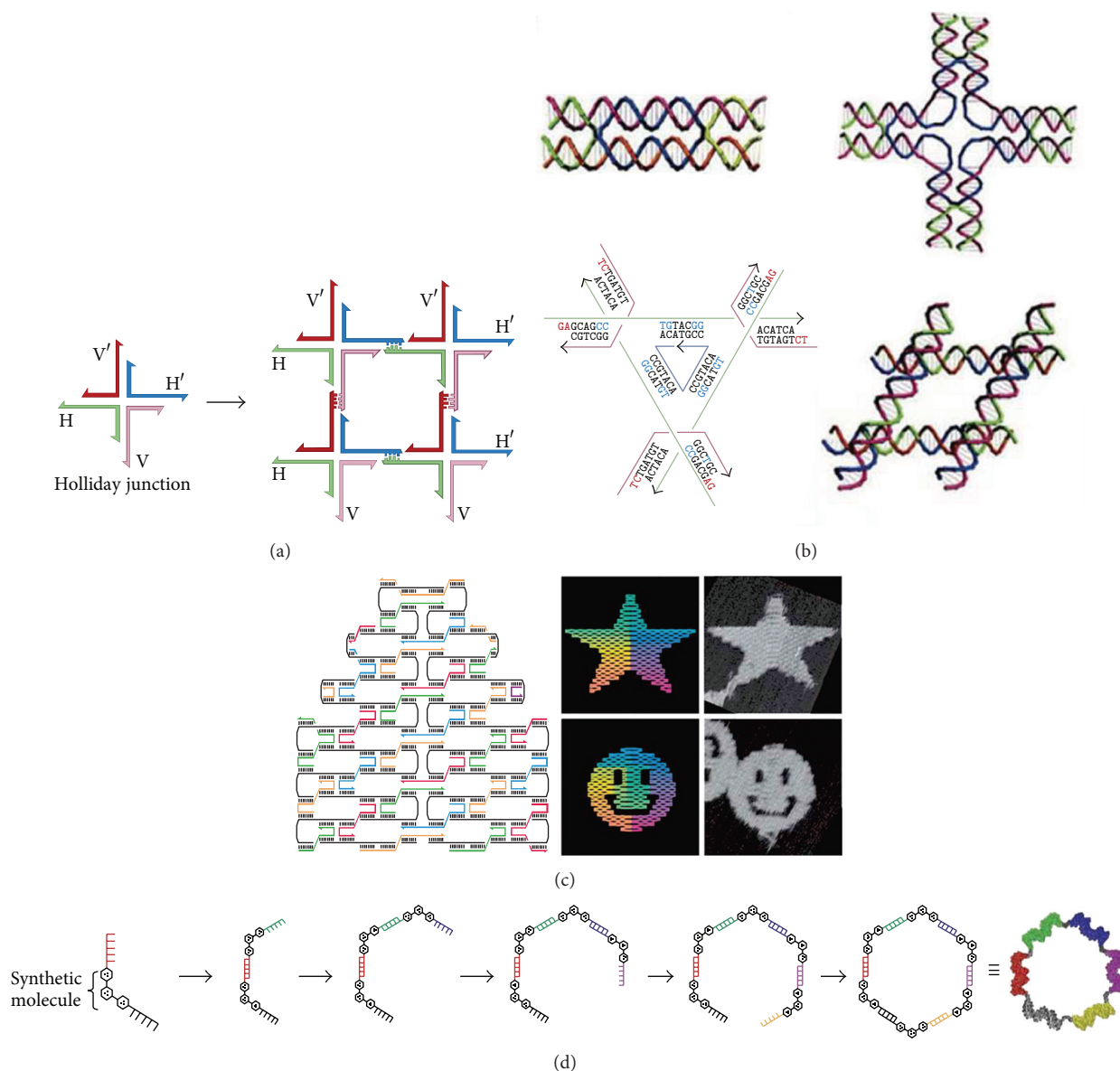


FIGURE 1: Examples of self-assembled DNA nanostructures: (a) A lattice is formed by hybridization of the sticky ends of a Holliday junction; (b) multistranded junction structures and crossover structures including double-crossover structure; cross-shaped tile with four arms; DNA tensegrity triangle and parallelogram DNA tile; (c) the principle of DNA origami and the design of 2D origami formed smiling face and star; (d) sequential self-assembly of hexagonal-shaped DNA nanostructure via supramolecular DNA assembly.

developed DNA-conjugated *m*-terphenyl-based organic vertices for modular construction of cyclic polygons, a library of DNA polyhedral structures and nanotubes with good control over their geometry [32], dimension [33], and flexibility [34]. Besides the organic insertions, other important self-assembly strategies take advantages of transition metal-, ligand-, lipid- and block copolymer-based environments [35–37].

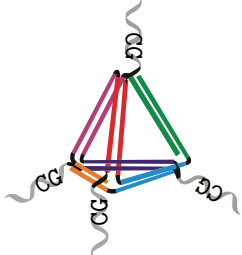
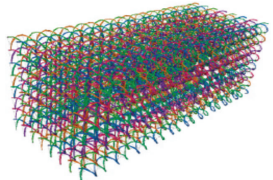
3. Stability of Self-Assembled DNA Nanostructures

Among various DNA assemblies, three-dimensional DNA nanostructures hold promise to be the universal nanocarriers

for smart and targeted drug delivery. In contrast to 1D or 2D DNA structures, the power of self-assembled 3D DNA nanostructures lies in their excellent stability and biocompatibility, high drug loading capability, and passive delivery into live cells. They also possess fine control over geometry, precise and monodisperse dimensions, positioning of guest molecules, stimuli-responsive switching of structure, and triggered-release of cargos. Typical examples of drug delivery systems based on 3D DNA nanostructures [38, 39] include tetrahedron, icosahedron, hexagonal barrel, nanotube, DNA origami box [40], nanorobot, and nanocage.

To be employable as a drug carrier system in mammals, DNA nanostructures must meet several important criteria:

TABLE 1: Stability of different DNA nanostructures.

	Linear dsDNA	CpG-bearing DNA tetrahedral nanostructure	A 3D multilayer rectangular parallelepiped structure
			
Description of the structure	Normal linear DNA strand with DdeI restriction site	It is made up of four 55-mer strands extended with the CpG sequence and a 7-mer oligothymine spacer	A 3D multilayer rectangular parallelepiped structure (8 helix × 8 helix square lattice with dimensions of 16 nm × 16 nm × 30 nm)
Incubation temperature	/	37°C	25°C
Medium	10% FBS	50% non-heat-inactivated fetal bovine serum (FBS)	Cell lysate
Decay time	Decay after 0.8 h	Start decaying after 4 h, but still not completely decayed after 24 h	Still remains stable after 12 h
Citation	[41]	[43]	[44]

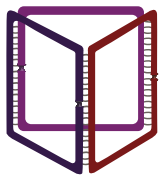
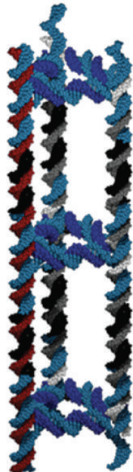
(1) they have to be stable and intact in both extracellular and intracellular environments, particularly stable long enough in the cytoplasm of cells to perform their predefined tasks; (2) they should not have toxic effect in mammals; and (3) the cellular immune system in mammals should tolerate the nanometer-scale DNA nanocarrier systems. Thus far, several research groups have put efforts on the stability studies of DNA constructs. Bermudez's group indicated that oligonucleotide-based tetrahedral made from branch junctions exhibit a strong resistance to enzymatic digestion compared to the linear counterparts in terms of their decay time constants (Table 1) [41]. The reason behind this would highly be due to the steric hindrance effect. Since the endonucleases initially bind to the DNA nonspecifically with a low affinity and then follow by diffusion along the strands. The steric hindrance introduced by three-dimensional tetrahedron would reduce the effective binding of enzymes to DNA and then inhibit DNA cleavage, no matter if the enzyme acts specifically or nonspecifically. Furthermore, shorter sequence or smaller size of DNA complex can enhance the resistance towards various nucleases as they are more difficult to bend and possibly have higher steric hindrance for the action of the enzymes. Walsh and coworkers have demonstrated the first example of 3D DNA nanostructure which can enter live mammalian cells effectively with or without the help of a transfection reagent [42]. They stay intact for up to 48 h in cytoplasm. In a recent study by Li et al., they have modified the tetrahedral with CpG oligonucleotides which have been confirmed to be taken up by macrophage RAW264.7 cells effectively (Table 1) [43].

Regarding scaffold DNA origami, Mei and coworkers demonstrated that different shapes of DNA origami nanostructures are stable and remain intact for 12 h after exposing

to cell lysates of various cell lines and can be easily purified from lysate mixtures, in contrast to single-stranded or duplex DNA (Table 1) [44]. They are not accessible to various DNAses due to negatively charged, large, and rigid origami structures. Their superior structural integrity and versatile functionality are highly preserved in relation to conventional oligonucleotides, validating their use for various biological applications. Subsequently, a further study carried out by Dietz' group tested the enzymatic digestion of DNA origami structures [45]. They are fully exposed to a large variety of endonucleases, including DNase, T7 exonuclease, T7 endonuclease, MseI restriction endonuclease, Lambda exonuclease, and *Escherichia coli* exonuclease. These results indicated that they are highly stable at 37°C towards degradation as compared to duplex plasmid oligonucleotides. More recently, Schüller and his coworkers reported that CpG oligonucleotides-decorated DNA origami tubes amplify a strong immune response, which are completely dependent on TLR9 stimulation in mammalian spleen cell [46].

To further optimize DNA structures in regard to enzymatic digestion resistance, Sleiman's group has modified 3D DNA nanostructures using a number of chemical strategies. They found that simple chemical modification to both ends of DNA oligos with hexanediol and hexaethylene glycol in self-assembled DNA prismatic cage or site-specific hybridization of DNA-block copolymer chains to 3D DNA scaffold would dramatically enhance its nuclease resistance under fetal bovine serum condition (Table 2) [47]. These studies could provide guidelines for decoration of DNA nanostructures with simple chemistry modification and allow imparting momentous stabilization towards nuclease degradation. Meanwhile, the same group also demonstrated that creation of DNA nanotubes with a template generated by rolling circle

TABLE 2: Stability of modified DNA nanostructures generated from supramolecular DNA assembly.

	Triangular prism1	Triangular prism2	Nanotube	RCA-nanotube
				
	Triangular prism (TP)			
Description of the structure	Made up of three 96-mer strands with 20 bp edges	Made up of three 96-mer hexaethylene glycol (HEG) modified strands with 20 bp edges	Triangular prism built up by small unit with short linking DNA strand	Connect small triangular prism units with RCA synthesized DNA strand
Incubation temperature	37°C	37°C	/	/
medium	10% FBS	10% FBS	10% FBS	10% FBS
Decay time	18 h	62 h	1.1 h	3.5 h
Citation	[47]	[47]	[32, 48]	[48]

amplification (RCA) results in increased stability towards nuclease degradation as compared to their previous nanotube design (Table 2) [48]. On the other hand, the high density of DNA and aspect ratio of the RCA-templated DNA nanotubes offer a greater cell penetration ability over normal DNA oligos. Such enhanced cellular stability and nuclease susceptibility are the key requirements for DNA nanostructures to act as delivery carriers or vehicles.

To modulate the stability and uptake profile of self-assembled DNA nanocube, Sleiman's group recently decorated their DNA cubes with hydrophobic (dodecane alkyl, C12) or hydrophilic (hexaethylene glycol, HEG) dendritic DNA chains [49] or block copolymers on the edges [50]. They found that all of the integrating dendritic DNA chains were facing outward, as confirmed by a larger hydrodynamic radius from dynamic light scattering (DLS) study and lower mobility band on gel electrophoresis. In addition, this chemical modification would allow enhancing their cellular stability with a longer half-life as compared to the blunt-ended nanocubes. More importantly, they found that the hydrophobic chains on the cube favor rapid and increased cellular uptake while the hydrophilic chains favor slow and continuous internalization.

4. Cargo Loading and Cellular Delivery

In response to the well-defined and highly programmable properties of DNA-based nanostructures, precise control

of positioning of cargo molecules in DNA nano-objects is highly possible. This valuable property is hardly attainable with inorganic or organic nanomaterials. In general, cargo molecules can be loaded via different strategies such as covalent linkage, nucleic acid base-pairing, biotin-avidin interaction, intercalation, aptamer-target interaction, DNA-protein interaction, and encapsulation.

4.1. Covalent Linkage. To deliver the cargo with the aid of DNA nanostructures, some of the cargos can form covalent bonds with DNA strand in the presence of some molecular linkers. Sleiman's and Mao's groups have shown that self-assembled DNA nanotubes act as carriers to deliver cyanine fluorescent dyes into human cancer cells [48, 51]. In Mao study, Cy3 is covalently conjugated to some of the nucleic acid strands at their 5' ends via a well-established *N*-hydroxysuccinimide (NHS) chemistry. Cy3-functionalized DNA nanotubes were formed by mixing DNA strands with and without Cy3 molecules after a heat-cool cycle. Fluorescent dyes are the most commonly used model cargo for targeted delivery, because they can easily be visualized and traced under various fluorescence microscopes. Taking advantage of automatic solid-phase DNA synthesis, a wide range of fluorescent probes can be readily coupled and labeled on DNA stands. With/without the help of targeting moieties, these structures could be internalized by tumor cells. The fluorescence of the dyes could be localized with fluorescent microscopy, confirming the presence of DNA

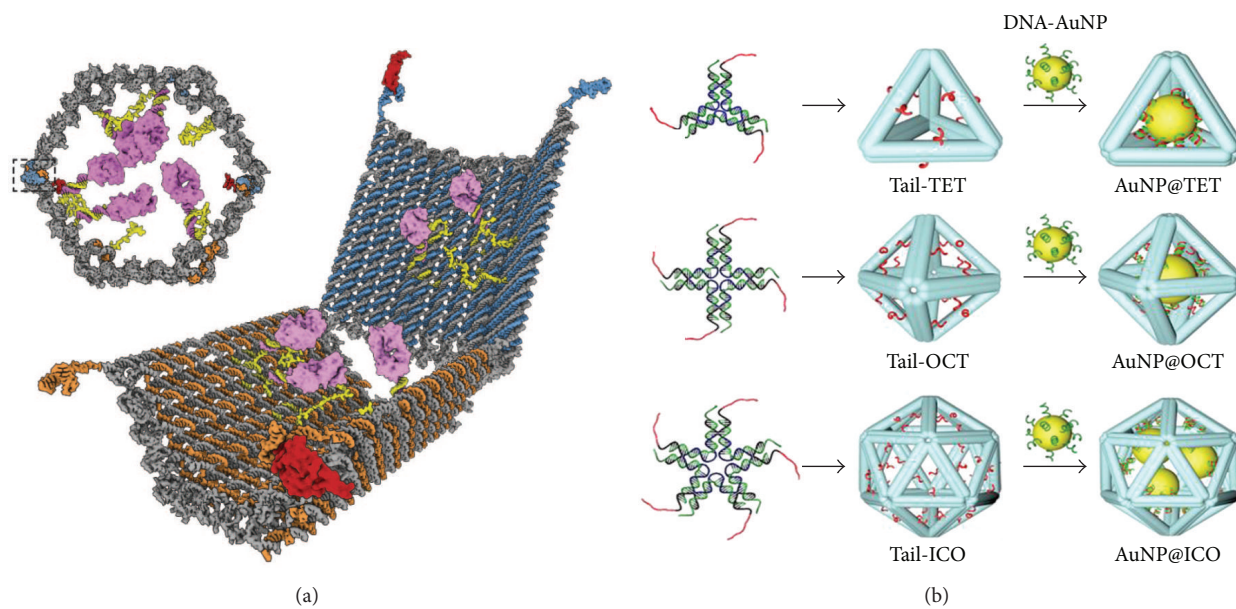


FIGURE 2: (a) Different kinds of antibodies have been tagged on the nanorobot and it can identify different antigens on different cells. (b) The complementary strand is incorporated inside the cavity of the nanocage for encapsulation of gold.

nanoassemblies in cells. Moreover, we are able to precisely control the numbers and positions of these fluorescent cargos such that multiple fluorophores can be labeled on a single DNA nanostructure [42, 52].

4.2. Nucleic Acid Base-Pairing. Hybridization of cargo-consisting of single-stranded nucleic acids offers an alternative strategy for site-specific loading of cargos. The nanorobots produced by Church's group have been chemically modified via covalent attachment of 15-base ssDNA linkers as loading sites to the 5' ends of payloads (Figure 2(a)) [53]. In this structure, twelve loading sites were generated. Subsequently, two types of cargo linkers have been prepared in the following ways: gold nanoparticles covalently conjugated to 5'-thiol-functionalized DNA linkers, and Fab' antibodies were covalently conjugated to 5'-amine-functionalized DNA linkers. Mixing the cargo linkers and the nanorobot in aqueous buffer, the staple strands with 3' extensions localized at the loading sites hybridized with the complementary sequences of cargo linkers. Eventually, two different types of payload molecules are loaded successfully per robot. In their design, different Fab' antibody fragments were bounded covalently to the amine-modified linkers. They found that the antibodies were recognized by certain cell-surface receptors and thus inhibited the growth of the targeted cells. In addition, generality of using these barrel structures as carrier is highly possible because a decrease in T cell activation activity that was observed when Fab fragments targeted to human CD3 and flagellin were loaded on these hexagonal barrel structures.

Mao's group has designed a series of symmetric DNA polyhedral structures consisting of two unpaired, ss DNA tails sticking out on each edge (Figure 2(b)) [54]. When mixing the gold nanoparticles functionalized with DNA

strands (DNA-AuNPs), the DNA-AuNPs are swallowed into the polyhedral structures governed by nucleic acid base pairing between the ssDNA tail on the DNA polyhedral structures and the complementary DNA strands immobilized on AuNPs. The size and number of guest molecules trapped by these DNA polyhedra highly depend on their internal volumes.

An alternative molecular cargo drawing attention is RNA interference (RNAi). It becomes a powerful therapeutic agent to knock down the gene expression, inducing gene silencing. Small interfering RNAs (siRNAs) are chemically synthesized nucleic acids with specific sequences which bind to their complementary mRNA molecules and thus inhibit the corresponding protein synthesis, leading to targeted gene knockdown. By choosing the appropriate siRNA sequence, it is possible to restrain the target gene expression which causes diseases. Anderson and coworkers have successfully developed a new siRNA delivery system by incorporating six double-stranded siRNAs to tetrahedral DNA assemblies. The single-stranded overhangs on DNA strands allow the specific hybridization of complementary siRNA sequences and cancer targeting ligands with better control over their spatial orientation, locations, and density. These nanostructures have been applied in female BALB/c nude mice model bearing Luc-KB tumor. They found that RNA-modified DNA nanostructures are able to knock down the luciferase levels in terms of the protein and mRNA levels, leading to target genes silencing in tumor cells. Importantly, they exhibit a longer blood circulation time than the parent siRNAs do. This work highlights the significance of DNA nanostructures to improve the biostability of tethered RNA strand, thus greatly enhancing the RNAi efficacy in nanomedicine [55].

Recently, Sleiman's group has integrated the firefly Luciferase antisense strands into the DNA triangular prism.

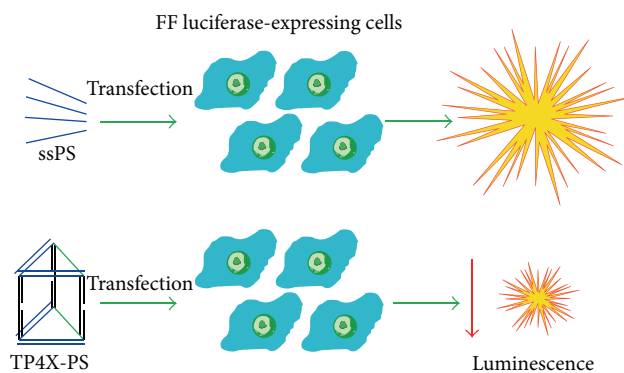


FIGURE 3: A diagram showing the effect on luminescence of bear PS and PS-integrated DNA triangular prism.

They demonstrated that DNA prisms composed of antisense strands can significantly induce gene knockdown in HeLa cells without being influenced by conjugating small fluorescent probes within the structure and by serum conditions. The RNA-modified DNA prisms maintain gene silencing up to 72 h and are still significantly powerful at an initial stage of gene knockdown after they are removed (Figure 3) [56].

In addition, unmethylated cytosino-phosphate-guanine (CpG) oligonucleotides are classified as therapeutic nucleic acids, with a strong immunostimulatory effect [26]. The CpG sequences are commonly present in bacterial and natural viral DNA for immune response, invading pathogens in a host [57, 58]. Interestingly, it is found that CpG oligonucleotides can effectively be recognized by endosomal Toll-like receptor 9 (TLR9) and further induce conformational changes simultaneously [59, 60]. This process ultimately triggers a signaling cascade which leads to the powerful immunostimulatory properties of CpG oligonucleotides. They can be highly used for the immunotherapy of cancer and infectious diseases [61, 62]. However, natural CpG oligonucleotides are easily digested by nucleases in biological systems and difficult to pass through the plasma membrane, entering cell and reaching their target sites. In this regard, it is necessary to develop a nanocarrier with low cytotoxicity and high delivery efficacy for clinical uses of CpG. Given that self-assembled well-defined DNA nanostructures are rigid and insensitive to nuclease digestion, several research groups have appended CpG motifs to multidimensional DNA structures in order to evaluate their uptake efficiency, stability, and immunoregulatory effects.

Nishikawa et al. designed and assembled a Y-shaped DNA unit from three single-stranded DNAs. Interestingly, CpG sequences have been introduced to these strands [63]. They found that Y-shaped DNA units induced a great immune response from RAW264.7 cells compared to ss- or ds-DNAs in terms of producing a higher amount of proinflammatory cytokines such as tumor necrosis factor- α (TNF- α) and interleukin-6 (IL-6). These units also exhibited higher uptake efficiency in macrophage-like cells than natural ds DNAs. Subsequently, the same group further applied this Y-shaped DNA unit to assemble dendrite-like nanostructures. Surprisingly, they demonstrated even a stronger immune

response by inducing a larger amount of proinflammatory cytokines from RAW2674 cells than the monomer Y-shaped DNA units do [64]. Recently, Nishikawa's group developed a series of nanometer-scale polypodna consisting of CpG motifs and examined their structural and immunological properties. Particularly for hexa- and octapodna; they could highly induce the secretion of TNF- α and IL-6 from RAW264.7 cells. Interestingly, large numbers of pod could increase the cellular uptake but also reduce their stability in serum condition. This enhanced stimulatory activity suggests the importance of the stereochemical property of self-assembled DNA nanostructures.

Recently, Li and coworkers have successfully developed a DNA tetrahedron as a CpG nanocarrier [43]. These nanometer-scale 3D structures are structurally rigid, mechanically stable, and nontoxic. They are also highly stable in serum condition and resistance to nuclease digestion in live cultured cells for few hours. As compared to ssDNA, the CpG-functionalized DNA tetrahedral structures can enter RAW264.7 cells efficiently. Importantly, this tetrahedron acts as a carrier to deliver the CpG therapeutic nucleic acids to acquire immune response. The amount of certain cytokines including TNF- α , IL-6 and IL-12 stimulated by them were remarkably increased than those by ss CpG nucleic acid strand. In addition, DNA tetrahedral could load more than one CpG, resulting in even higher stimulatory activity. In such case, the positions of CpG loading can be used to monitor the dose of drug molecule precisely. Additionally, several groups have successfully developed a large variety of origami structures for large amount of CpG loading, leading to a strong immune cell activation in freshly isolated spleen cells or in RAW 264.7 cells by cytokine production in a high level (Figure 4) [46, 65]. In overall, it is highly suggested that various geometries of DNA nanoobjects have shown advantages of cellular delivery and immunostimulatory activity of CpG in macrophage-like cells, making DNA nanostructures promising immunotherapeutic carriers.

4.3. Biotin-Streptavidin Interaction. Biotin, also called vitamin H, is a small molecule and exhibits a strong binding affinity to biotin-binding proteins such as avidin or streptavidin. The high affinity of the biotin-streptavidin interaction not only offers useful bioanalytical advantages [66], but also

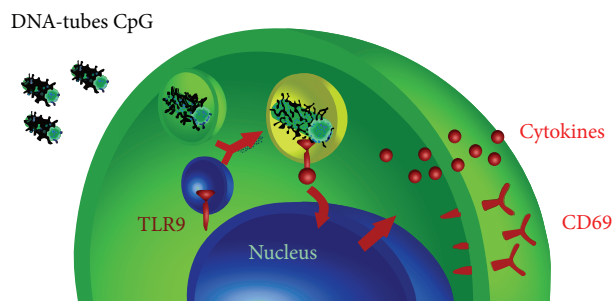


FIGURE 4: A diagram showing how DNA-tubes CpG go into the cell and functionalize.

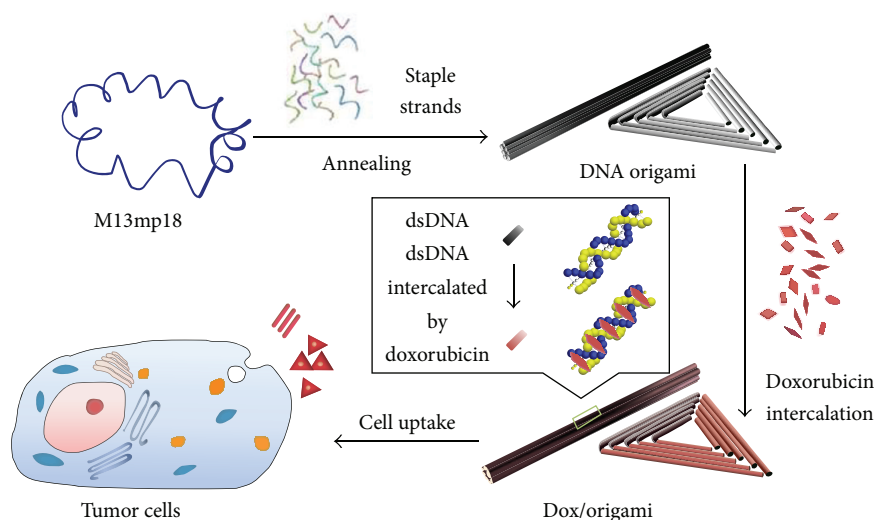


FIGURE 5: A DNA origami designed for doxorubicin transportation.

makes this system to be an attractive model for site-specific loading or positioning of guest molecules in highly ordered DNA assemblies [67, 68]. Recently, Gothelf and coworkers have demonstrated a chemical modification of nucleic acid strands with biotin allowing for streptavidin binding at precise positions in a well-defined self-assembled DNA origami scaffold. In this study, biotin-tethered functional groups including an alkyne, an amine, and an azide reacted with their corresponding reactive groups via either a Huisgen-Sharpley-Medal copper(I) catalyzed click chemistry or N-hydroxysuccinimide chemistry. The results of high yield, selective cleavage, and bond formation in this study offer the potential of applying such interaction for site-selective uptake and triggered release of cargos in a control manner [69].

4.4. Intercalation. In DNA chemistry, intercalation is a reversible insertion of a guest molecule into double helix of DNA strands. The small molecules can interact with nucleobases and disturb the π - π stacking of between double-stranded DNA (dsDNA). Doxorubicin is one of the most common drugs that can be trapped by DNA nanostructures. It can intercalate in G-C base pair of DNA strand. It is small and can be trapped by DNA nanomaterials easily [70–72]. Many newly developed DNA nanocarriers have been tested due to its simplicity [73, 74]. There is another example of

doxorubicin carried by DNA origami which can circumvent drug resistance. It enters and localizes in resistance human breast cancer cell (res-MCF-7) while the free doxorubicin cannot enter. The DNA origami increases pH of lysosome in resistant cancer cells, followed by redistribution of drug. This would allow them to go to their target site (Figure 5) [73]. Zhao and his colleagues have also developed a DNA origami tube for transporting doxorubicin. By optimizing the design of nanostructures, encapsulation efficiency and the release rate of the drug can be adjusted [74].

Shen et al. and Zhu et al. also reported the delivery of DNA-based structures to cells in the presence of intercalated dyes including SYBR Green and carbazole-based biscyanine as fluorescent cargo [75, 76]. These dyes can specifically bind to and intercalate with DNA duplex, giving out strong fluorescence. Subsequently, the intercalated dyes are completely released and a decrease in fluorescence is observed once DNA structures are disrupted by some reasons. Importantly, they realized that the enzymatic degradation of these assemblies lasted for at least few hours in cellular environment, resulting in sustainable release of cargo molecules.

4.5. Aptamer-Target Interaction. Aptamers are either ssDNA or ssRNA molecule that can selectively bind to certain targets such as proteins and peptides, with high affinity and

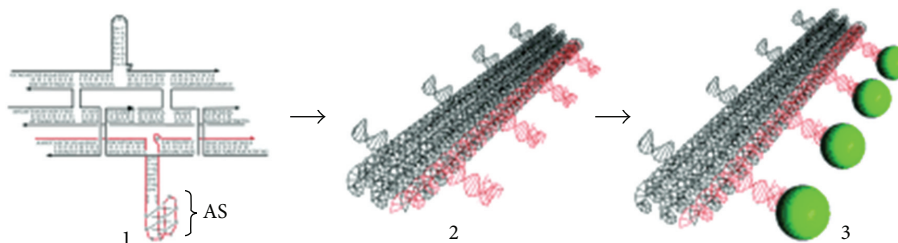


FIGURE 6: Thrombin binding aptamer is introduced into the design of the DNA origami for tagging thrombin.

specificity. These molecules can be presented in a large variety of shapes including helices and single-stranded nucleic acid loops due to their intrinsic propensity and versatility to diverse targets. They can link to various proteins as well as other nucleic acids, small organic compounds, and even entire organisms [77, 78]. Yan's Group has demonstrated the first example of selective DNA aptamer binding as a powerful platform for positioning of proteins in periodic locations of self-assembled DNA arrays (Figure 6) [79]. In these studies, thrombin binding aptamer (TBA) is chosen, which is a well-known 15-base nucleic acid aptamer consisting of specific sequence of d(GGTTGGTGTGGTTGG) [80]. They found that DNA-based array constructed with this TBA can fold into a unimolecular guanine quadruplex and then selectively bind to a protein called thrombin, with nanomolar affinity. This aptamer-target interaction mechanism would provide an alternative choice for cargo uptake with a larger flexibility and simplicity. Only aptamer sequence is required to be implemented in the design of DNA nanocarrier.

In general, aptamers are usually selected from a pool of large random sequences. Because of their high specificity and ease of synthesis, they have been widely used for biosensing and diagnostic applications [81]. More recently, aptamers have become therapeutic candidate as biomedical drugs [82, 83]. Common used human α -thrombin aptamer, which has two binding sites, can be readily loaded on self-assembled DNA structures with appropriate design [84, 85]. Fan's group designed a dynamic DNA tetrahedral nanostructure with an anti-ATP aptamer embedded in one of the edges [60]. This nanostructure could go into cells and monitor the level of ATP via the ATP-induced aptamer conformational change that alters the FRET efficiency of a pair of fluorophores (Cy3 and Cy5) labeled on the structure.

The optical activity of DNA strand used to construct DNA nanomolecules would also affect the structure of nanomaterials. L-DNA and D-DNA has common structure and liability but once the nanostructure is attached to aptamer, mismatching in nanocage made by D-DNA may occur. L-DNA is a better choice for construction because the structure of cage with aptamer is unchanged [86].

4.6. DNA-Protein Interaction. In a cellular environment, there are many different kinds of proteins while some of them can interact with DNA for various cellular reactions. Transcription factor is one of the examples. It has binding site which can interact with DNA sequence. Kapanidis's group

has demonstrated selective trapping of transcription factor (TF) in DNA cage (Figure 7) [87]. Transcription factor is a DNA binding protein which is important in gene regulation. TF catabolite activator protein (CAP) is used as cargo in this experiment. The 22 base pair DNA recognition site is integrated in the DNA tetrahedron. With the presence of cyclic adenosine protein (cAMP), the allosteric effector of protein increases the binding affinity of CAP towards the binding recognition sequence. These results suggested that protein would still be trapped inside the cage even it is already formed, unlike other passive encapsulation methods. The CAP can be released by degradation of cages in presence of DNA nuclease I.

Liu and his coworkers reported a DNA-based delivery system for synthetic vaccines [88]. In their design, biotinylated DNA tetrahedron was used as carrier to deliver antigen streptavidin (STV) into mice with the aid of biotin-STV interaction. Interestingly, the antigen-modified DNA tetrahedron complexes could stimulate strong and continuous antibody responses against the antigen in comparison with antigen itself. On the other hand, unmodified DNA nanostructures did not induce any response. These results indicated the promise of the use of self-assembled DNA nanostructures as a delivery and generic platform for rational design and construction of vaccines.

4.7. Encapsulation. In addition to specific binding interactions between cargos and carriers, payloads can also be directly loaded into container-like DNA nanostructures via passive encapsulation. Recently, Sleiman's group demonstrated the ability of a 3D DNA-based nanoobject to passively encapsulate certain sizes of cargos [89]. DNA nanotubes of longitudinal variation structure have been created in which they can encapsulate gold nanoparticles of specific sizes to form nanoparticle "pea-pod" lines. It is of note that the "sieving" ability is very important, only specific nanoparticle sizes that match the size of the capsules along the nanotubes could be encapsulated, and the process is highly selective. This approach allows controlling of the positioning and loading of a wide range of sizes of guest molecules in a precise way by designing the dimensions of cavities inside the DNA nanoobjects.

Sequentially, Krishnan's group further applied this strategy for the encapsulation of a fluorescent biopolymer, for example, FITC-dextran, in a synthetic icosahedral DNA-based container. Without molecular recognition between

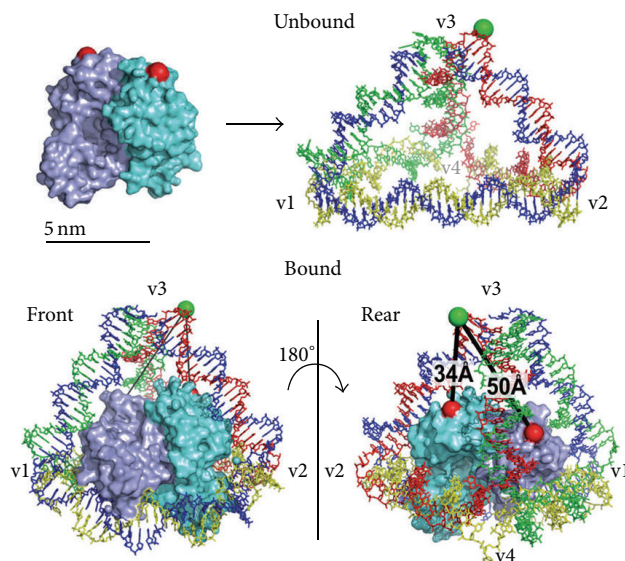


FIGURE 7: The figure is showing that the conformation of bound and unbound CAP integrated in DNA tetrahedron.

the host and guest, cargo molecules are passively loaded to the 3D container during joining the two halves of icosahedron in PBS buffer (Figure 8) [90]. They have reported the delivery of DNA icosahedral encapsulated fluorescent dextran (FD) specifically in *cellulo*. *Drosophila* hemocytes and in *C. elegans* via anionic ligand-binding receptor (ALBR) pathway. The FD cargo is a complex, branched polysaccharide composed of around 10 kDa, 5.2 nm in sizes. It is found that the functionality of the encapsulated FITC-FD in living worms is preserved and the spatially mapping of pH changes during maturation of the endosomes in coelomocytes.

5. Controlled Releases of Cargo Molecules

To act as a nanocarrier for drug delivery, control release of cargo is another significant issue needed to be considered carefully. In the following section, different approaches will be explained and discussed in detail.

5.1. A DNA Strand Displacement. The cargo trapped in DNA nanotube from Sleiman's group is released by strand displacement (Figure 9(a)) [89]. The nanotube is partially hybridized to one strand and gives some tails. Introducing the completely complementary DNA to the tails, the rigidity of the cavity capping gold released. Sleiman has demonstrated selective release of cargo molecules in response to a specific external DNA strand. They have designed and assembled 3D DNA nanotubes with encapsulated gold nanoparticle as well as some modified linking strands consisting of an eight-base overhang protruded from each of their large capsules. After a fully complementary eraser DNA strand is added to these self-assembled nanoobjects, the closing linking strands are erased and hybridized and form a double helix with the complementary eraser DNA strand. The fully doubled-stranded DNA nanotubes become partially single-stranded, so that the encapsulated cargos are released simultaneously.

This release process is highly selective and fast. It is just like unzipping the clothes. As the cavity is more flexible without the rigidified strands, the nanogold can be leaked out easily.

The same group has also applied the same strand displacement technique to release the guest molecules such as the block copolymer micelles loaded on the RCA-nanotubes (Figure 9(b)) [37], and the Nile red or 1.6-diphenyl-1,3,5-hexatriene (DPH) loaded on dendritic alkyl chains-modified DNA cages [91].

Goodman et al. has reported the operation of reconfigurable, braced 3D DNA nanostructure whose structure switches precisely and reversibly in response to specific molecular inputs [92]. Four DNA strands are mixed in solution to form a tetrahedron which consists of a hairpin loop on one edge. This edge can be expanded by adding a fuel DNA strand that is fully complementary to the hairpin region. On the other side, the edge can be contracted by adding the eraser DNA strand which displaces the fuel strand via hybridization of its single-stranded overhang first.

5.2. Addition of Small Molecules. To carefully realize the potential of these 3D DNA nanostructures as nanocarriers, the development of spatiotemporal release of the trapped cargo is of great importance. Recently, Krishnan's group has successfully demonstrated the precise control over the opening of a 3D DNA icosahedron loaded with molecular cargo in response to an external small molecule, called cyclic-di-GMP (cdGMP) (Figure 10(a)) [93]. Generally speaking, cdGMP existed as a second messenger in most bacteria for regulation of various biological processes. In their design, cdGMP aptamers are chosen and have been introduced to the icosahedral design. Upon binding to cdGMP ligands, the aptamer undergoes a conformational change by strand displacement and then dissociate the polyhedral structures into two halves. Simultaneously, the encapsulated fluorescent dextrans are completely released. Therefore, we strongly

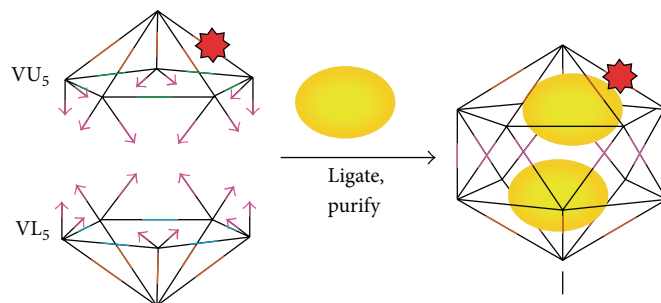


FIGURE 8: Cargo molecules are passively loaded onto 3D DNA-based container after joining the two halves of icosahedron in PBS buffer.

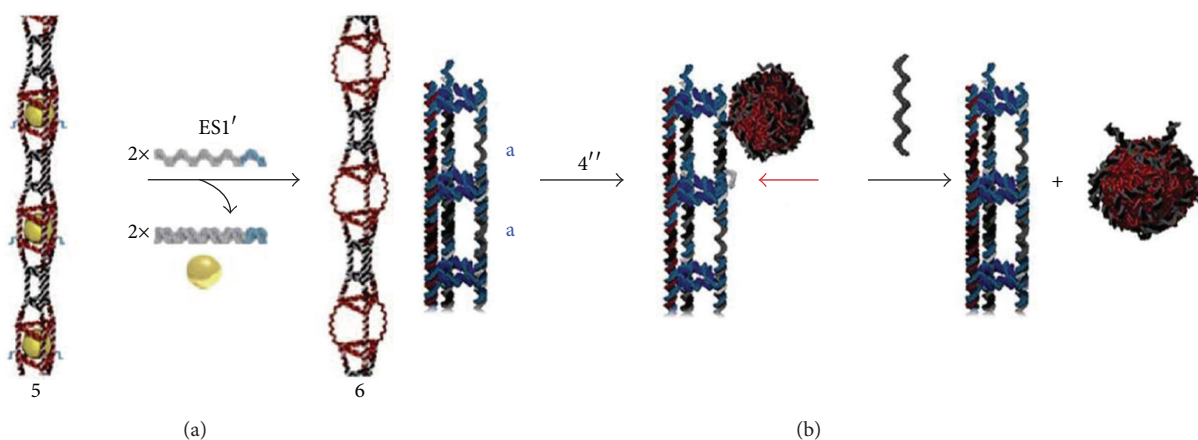


FIGURE 9: A DNA nanotube for gold releasing by strand displacement (a) and demonstration of PEG releasing in RCA-DNA nanotube by strand displacement (b).

envision artificial DNA-based nanostructures as nanotool for drug loading and targeted delivery because of their ability for selective encapsulation and stimuli-triggered release of cargo.

5.3. pH Adjustment. pH adjustment is also a possible stimulant for the structural change of DNA nanostructures. The key element of this structural switching mechanism is i-motif switching. It makes use of the properties of Watson-Crick base-pairing and Hoogsteen hydrogen bonding. In an acidic environment, C is partially protonated as C⁺ which can bind with a G-C nucleobase pairs through Hoogsteen H-bonding in order to generate C+G-C triplets. However, C⁺ loses one electron and turns back to C under neutral environment, discarding the Hoogsteen H-bonding and C+G-C triplets simultaneously. Liu et al. reported the first pH responsive DNA tetrahedron in terms of their reversible assembly and disassembly in response to solution pH changes (Figure 10(b)) [94]. In the current design, three-point-star DNA motif can associate with one another to form a DNA tetrahedron in acidic environment (pH at 5) through DNA triplex formation of cytosine-modified sticky ends. While under neutral pH environment, the tetrahedron dissociates into its building blocks immediately. The design can be improved for drug delivery by adjusting pH value towards the formation of DNA tetrahedral. We strongly believe that

such pH-responsive behavior in self-assembled DNA nanostructures will be important for potential applications such as controlled/targeted drug release in specific cellular environments. The same group also developed a pH biosensor based on DNA nanomachine which is triggered by protons to map temporal and spatial pH changes in a cellular system via similar structural switching mechanism [95].

5.4. Photo Irradiation. Compared with the above input signals, photon is an ideal external source for precise control of photo-manipulation of DNA nanoobject. By using light, DNA nanoobjects can be remotely controlled, offering a novel avenue in nanomedicine and drug delivery. Generally speaking, photo irradiation is a clean switching mechanism. NO waste is generated as only light was used to drive the entire process. It offers capability to precise control light irradiation in both temporal and spatial fashions. More importantly, it would not damage the samples as photo irradiation is noninvasive and noncontact source of stimulus. Recently, azobenzene has been confirmed to be a photo-responsive molecule that can be conjugated to nucleic acid strands for the regulation of hybridization-dehybridization process [96, 97]. It exhibited reversible stereoisomerization property. It switches from the *trans* to *cis* conformation when excited at 330–380 nm wavelength of light. On the other side, it reversibly switches from *cis* to *trans* under excitation of

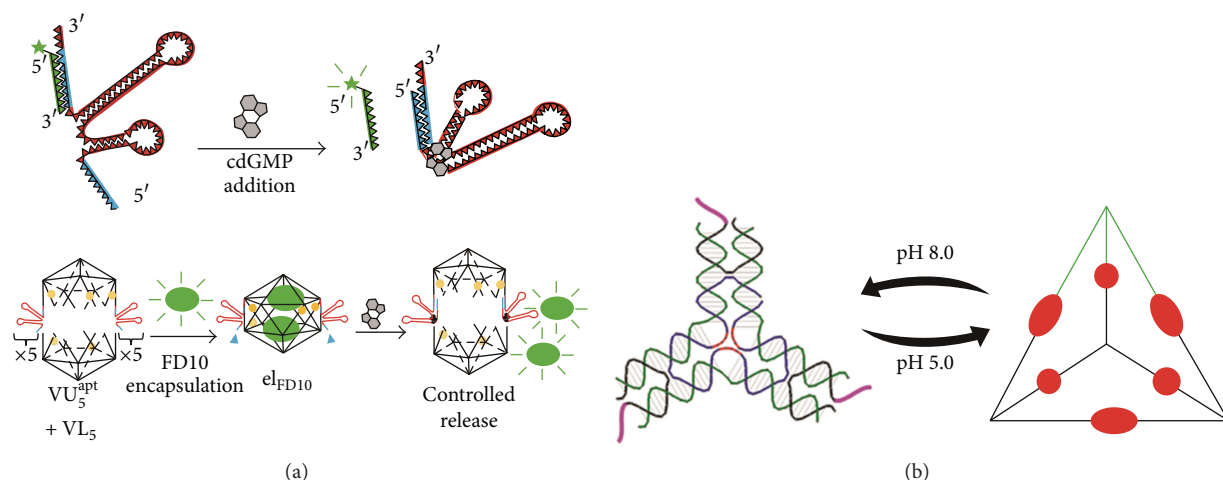


FIGURE 10: (a) By binding the cdGMP to aptamer integrated in DNA icosahedron, nanocage can be opened for molecule releasing. (b) It makes use of the *Watson-Crick base pair* and *Hoogsteen base pair* properties to construct a DNA tetrahedron which can form in low pH and decompose in high pH conditions.

light with wavelength above 400 nm. This intrinsic property of azobenzene allows the photo-manipulation of DNA nanostructures in a precise and control manner. On the basis of this technique, Liang et al. designed photon-fuelled molecular DNA tweezers consisted of photoresponsive azobenzene-modified DNA strand. Photo-induced opening and closing of the tweezers is governed by the irradiation wavelength (Figure 11(a)) [98]. Subsequently, the same group has successfully designed and constructed a supra-photoswitch consisting of alternating natural nucleobase pairs and azobenzene moieties in the form of (AAB)_n, where A and B represent the natural nucleotides and the azobenzene, respectively [99]. They found that the stability of the azobenzene modified DNA duplex is more stable than the neutral one. This property is useful in implementing in different DNA nanocarriers. Kang et al. designed and constructed photoswitchable single-molecular DNA motor with tethered azobenzene moiety [100]. This nanomotor is driven by photo irradiation between UV light and visible light without any additional DNA strand as external fuel.

Recently, highly complex DNA nanostructures incorporated with photo-responsive molecule have been successfully designed and generated. Zou and his coworkers constructed DNA nanoscissors composed of two hairpin structures H1 and H2. In this study, a DNAzyme is used as an example system for DNA cleavage (Figure 11(b)) [101]. Particularly, H2 is a complementary azobenzene-functionalized sequence at the 5-end of DNAzyme. Under visible light irradiation, the two hairpins preserve their hairpin structures as duplexes, blocking the substrate binding and closing down DNA cleavage activity. This is in a closed state of DNA nanoscissors. While under UV light irradiation, H2 is able to be opened due to structural isomerization of azobenzene from its planar to nonplanar conformations, prohibiting duplex formation at H2 and then allowing intermolecular hybridization between DNAzyme and the substrate, thus activating the enzymatic

activity. This is in an open state of DNA nanoscissors. They found that the ON and OFF states of nanoscissors lead to a remarkable change in substrate binding affinity and an obvious difference in the activity of DNA cleavage.

Yang and his colleagues have successfully demonstrated the reversible assembly and disassembly of DNA-based structures by introducing azobenzene-modified DNA strands into hexagonal DNA origami units [102]. A number of nanometer-sized hexagonal DNA origami structures functionalized with photo-responsive oligonucleotides have been generated. They can be assembled into a large variety of 2D regular or irregular nanostructures under visible irradiation. On the other hand, DNA hexagonal origami would obtain the *cis*-conformation under UV light irradiation such that they cannot hybridize together due to steric hindrance effects. By altering the numbers and positions of azobenzene-modified oligonucleotides in the hexagonal shaped DNA origami scaffolds, they can link together in multiorientations in order to achieve different patterns and configurations critically. This photo irradiation switching mechanism shows great potential for the applications in bionanotechnology such as remote and controllable drug release.

Based on the above studies, we strongly believed that photo-triggered release of drug molecules from multidimensional DNA-based nanocarriers would become a promising release mechanism and be highly achievable by careful designs. In an advance study, Han and coworkers have successfully introduced azobenzene moieties into 3D DNA tetrahedron (Figure 11(c)) [103]. Strands with introduced azobenzene groups can hybridize with the single-stranded hairpins, allowing the control of open and closed state of DNA tetrahedron by visible and UV light. The hybridization and dissociation of azobenzene-modified oligonucleotides can be remotely and reversibly controlled by the interconversion of *trans* and *cis* conformations of azobenzene molecules.

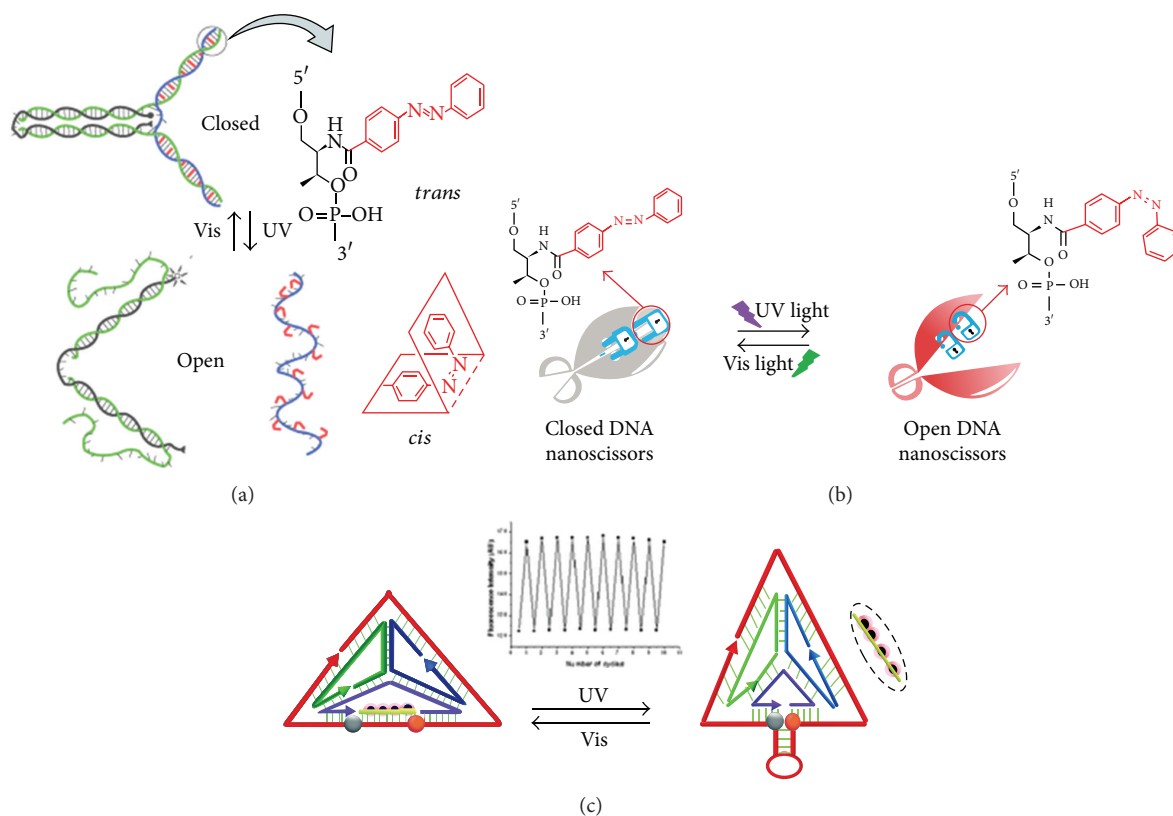


FIGURE 11: (a) A design of photo-sensitive DNA nanodevice that make use of the properties of azobenzene towards different wavelengths of light. (b) Making use of the *cis-trans* properties of azobenzene under different wavelengths to close or disclose the active site of enzyme. (c) The shape of the azobenzene modified DNA tetrahedron can be altered in the presence of different wavelengths.

It is believed that these studies will open doors to implement and facilitate the 3D structural changes for triggered-release of encapsulated cargos in DNA-based nanoobjects.

6. Cellular Internalization and Site-Specific Targeting of DNA Nanostructures

6.1. Passive Delivery. DNA-based molecules usually have great difficulties in delivering to cells as they are highly negatively charged. They are not able to pass through cell membranes directly. Most of them undergo three types of possible mechanisms of getting in cells, Clathrin-mediated endocytosis, Caveolae-mediated endocytosis, and macropinocytosis. In general, Clathrin-mediated endocytosis is a type of endocytosis which requires excitation of receptor. The molecules would then be trapped in early endosome, then in late endosome, and finally in lysosome. The pH in a cellular environment is gradually decreased and then degradation of self-assembled DNA nanostructures is highly possible. Caveolae-mediated endocytosis is another type of endocytosis but it would go to Caveosome and then migrate to Golgi, endoplasmic reticulum, and endosomes. Macropinocytosis is different from the above two endocytic pathways as it is nonspecific. Though the molecules should end up at lysosome but the macropinosome is comparatively leaky which make

them possible to enter the cytosol to escape the destiny of degradation [104–106]. Efforts have been put to improve the cellular uptake of DNA-based nanomaterials in terms of high cell penetration ability and low cytotoxicity [107, 108].

6.2. Targeting of Self-Assembled DNA Nanostructures. To enhance the selective delivery of DNA nanocarriers to cancer cells or particular intracellular organelles for drug delivery purposes, a targeting moiety has to be conjugated to DNA assemblies.

6.2.1. Folate. Folate, water-soluble vitamin B₉, has proven to be an efficient targeting agent for cancer cells as folate receptors are overexpressed on the surfaces of cancer cells. Therefore, DNA nanostructures decorated with folate group via a simple NHS chemistry would provide a higher chance to be taken up by cancer cells over normal cells. Mao's group integrates folate into his DNA nanotubes (Figure 12(a)) [51]. They prove that the folate modified DNA nanotubes enter KB cells through overexpressed folate receptor and be able to internalize in the cells. One hour incubation of these modified nanotubes would be saturated because cells may only be able to take up certain amount of DNA nanotubes. When the folate content in the DNA nanostructures reaches 10%, the uptake capability of DNA nanotubes in cells would reach plateau due to the limited number of folate receptors.

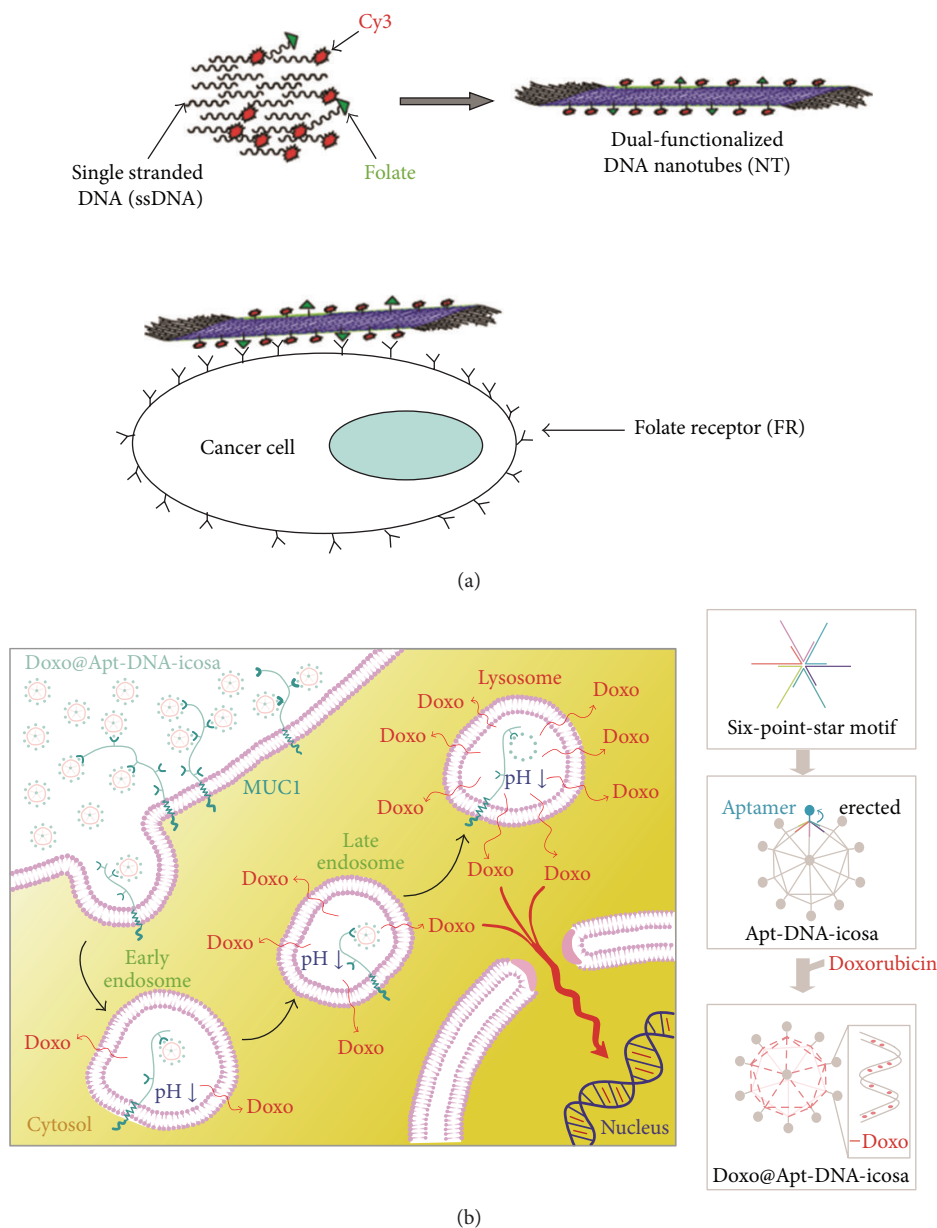


FIGURE 12: (a) Cy3 and folate is covalently conjugated to the ssDNA via NHS chemistry for cell targeting and visualization. (b) The figure is showing the design of the DNA icosahedral nanoparticles and the possible releasing mechanism of doxorubicin.

6.2.2. *Aptamer*. In general, aptamers are short, single-stranded nucleic acid strands with specific sequences derived from systematic evolution of ligands by exponential enrichment (SELEX). They are able to recognize and bind to cellular surface receptors in certain cancer cells and thus allow importing to the cells, leading to target delivery. Huang's group have designed a DNA icosahedra from a six-point-star motif with a sticky end segment of MUC 1 aptamer sequence (Figure 12(b)) [109]. MUC 1 is a major class of tumor surface marker which is abundant on the surface of most epithelial cancer cells [110, 111], serving as entering portals for aptamers [112]. To investigate the targeting selectivity, the

uptakes of DNA polyhedron by MCF-7 cells which are MUC-receptor positive tumor cells, and by CHO-K1 cells which are MUC-receptor negative cells, have been investigated. They found that aptamer-modified DNA polyhedra exhibited higher cellular internalization efficiency than the regular DNA polyhedra do in MCF-7 cells but not in CHO-K1 cells, confirming an aptamer-mediated cellular selectivity of internalization of DNA polyhedra. They have proposed a cellular uptake mechanism for aptamer-modified DNA polyhedra in MCF-7 cells. First, MUC-modified DNA polyhedra recognize MUC 1 which is then rapidly recycled through intracellular compartments. After that, MUC-modified DNA polyhedral

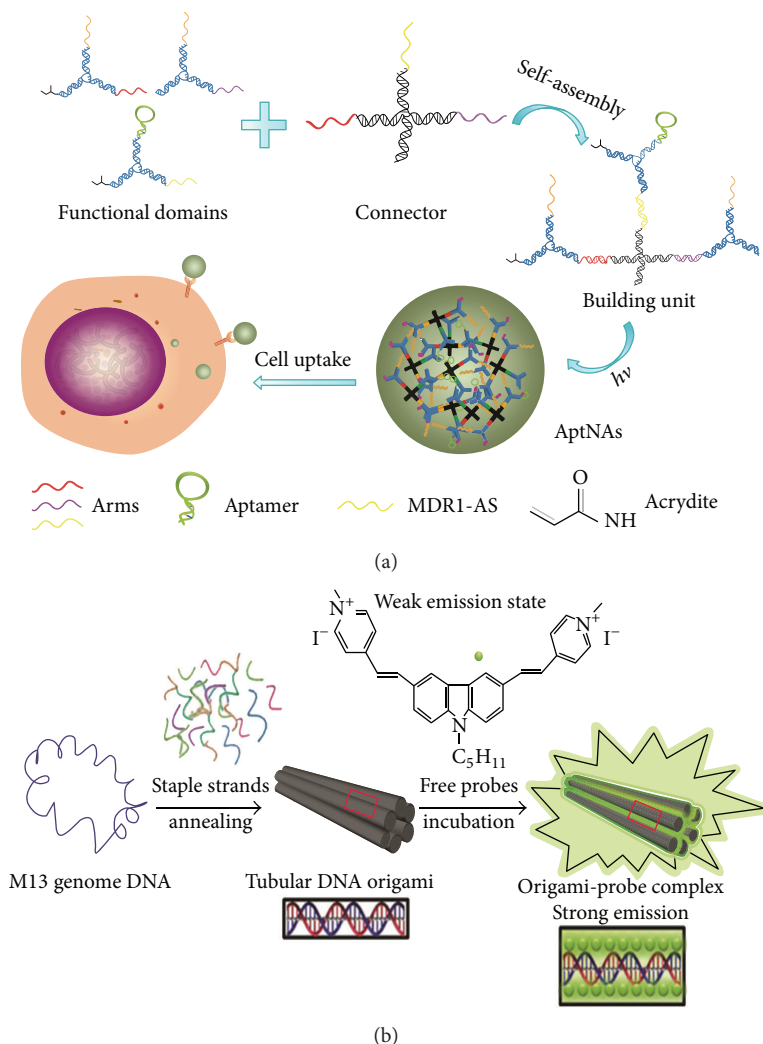


FIGURE 13: (a) DNA strands are modified to bind with different functional domains and photosynthesized to a bigger complex. The nanostructure contains aptamer for differential cell targeting. (b) A design of label-free fluorescent probe incorporated in DNA origami.

structures are smuggled to endosome and later to lysosome by binding to MUC 1.

Tan's group have successfully designed and generated multifunctional DNA nanoassembly by first self-assembling three components, including aptamer, acrydite-modified ssDNA, and antisense oligonucleotides to form Y-shaped DNA domains (Figure 13(a)) [70]. Subsequently, these functional DNA domains were hybridized to an X-shaped DNA connector to form building units. After photo irradiation, all building units were cross-linked to form aptamer-based DNA assemblies. In this study, sgc8 aptamer and KK1B10 aptamer were chosen to demonstrate the generality of selective recognition of target cancer cells by these multifunctional aptamer-based nanoassemblies. Their results indicated that sgc8-functionalized DNA assemblies internalized specifically to CCRF-CEM cancer cells (T cell acute lymphoblastic leukemia cell line) but not to Ramos cells (B cells human Burkitt's lymphoma). While KK1B10 can specifically recognize and internalize into K562/D (Dox-resistant leukemia cell line)

but cannot control Ramos cells. Using this technique, the construction of the nanocarrier is easy to achieve and is highly programmable as the position, number, and size of the aptamer can be adjusted. In addition, this system has been tested *in vitro*, indicating that the nanoassembly is enzymatic resistant and cytotoxic negligible.

Recently, Kim et al. decorated their L-DNA nanocarriers with antiproliferative aptamer, ASI411, allowing them to selectively recognize and take up by cancer cells [86]. This is likely due to the interaction between ASI411 aptamers on L-DNA nanocarriers and the target protein nucleolin expressed on the surface of HeLa cells.

6.2.3. Organelle Localization Signal Peptides. Most of the self-assembled DNA nanostructures are taken up and eventually localized in lysosomes, endosomes, or Golgi networks by means of endocytosis (Figure 13(b)) [75, 95, 113]. It is realized that these locations are highly limited by their biological

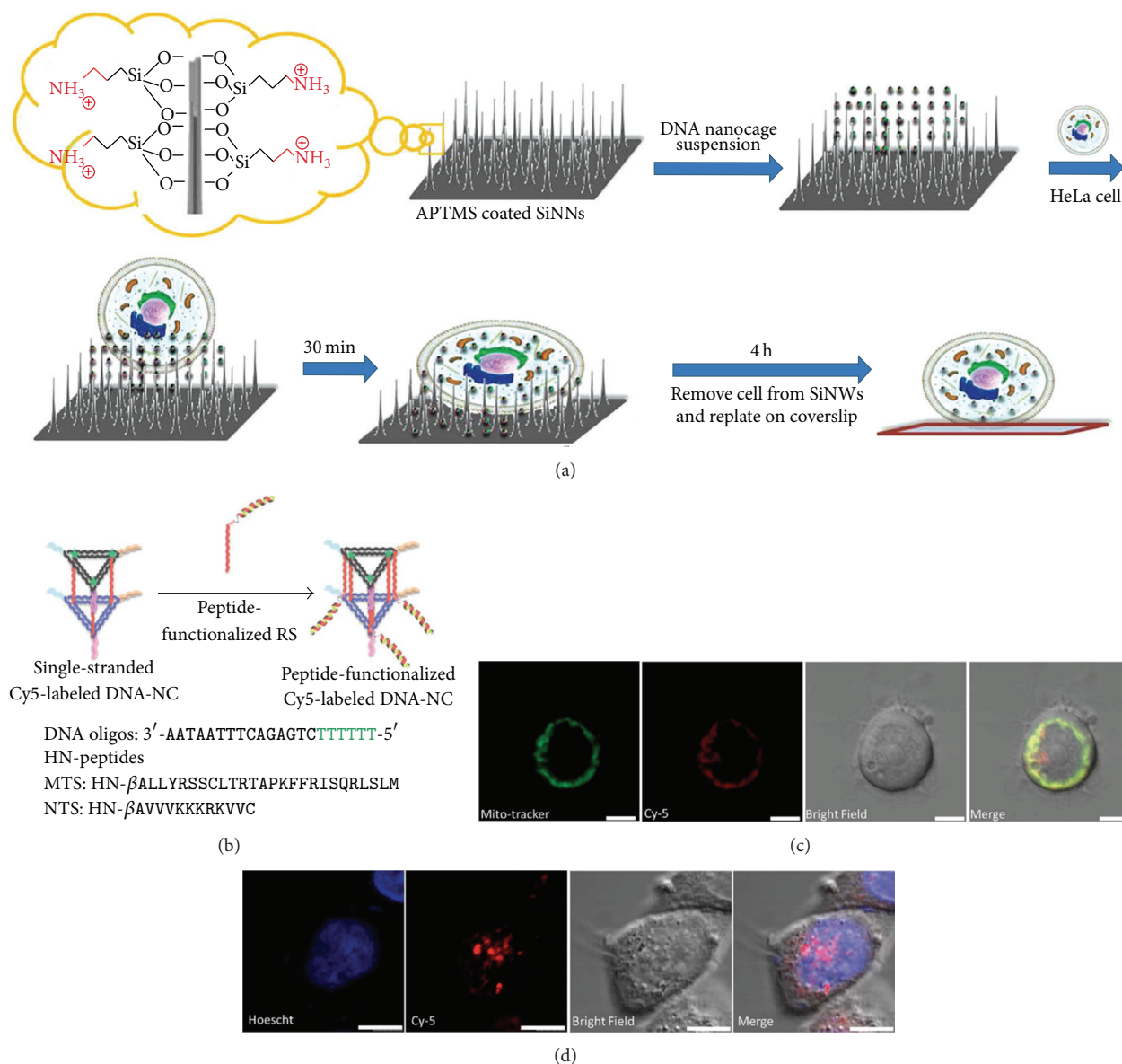


FIGURE 14: (a) Demonstration of how functionalized vertical silicon nanowire arrays help in direct delivery of molecules to cytosol. (b) The triangular prism has been attached to MTS and NTS for specific cell internal targeting to mitochondria and nucleus, respectively. (c) Cy5-labeled MTS DNA-NCs with MitoTracker green and Cy5-labeled. (Scale bar represents 15 μ m).

behaviors and functions in a cellular system among different intracellular compartments.

Our group recently developed a new delivery technology on the basis of functionalized vertical silicon nanowire arrays as a delivery platform to transport intact DNA cages to the cytosol efficiently without endocytosis (Figure 14) [52]. We proved that this delivery strategy exhibits high cellular uptake efficiency together with great stability and low cytotoxicity in a cellular environment. In addition, this delivery approach would preserve the structural integrity of cages and help them escape degradation under endocytosis. More importantly, we demonstrated the first example of site-selective DNA nanocages for targeting mitochondria and nuclei. In this study, specific organelle localization signal peptides such as mitochondrial localization signal (MLS) peptide or nucleus

localization signal (NLS) peptide were incorporated to one of the constituent DNA strands and then further assembled to MLS or NLS peptide-functionalized DNA nanocage. It is found that the modified MLS or NLS-cages are able to localize exclusively in mitochondria or nuclei, respectively, by means of a powerful SiNW delivery platform *in vitro*. This work opens a door for the use of DNA nanocage as smart vehicles, particularly for targeted drug delivery to the specific intracellular organelles.

7. Conclusions and Outlook

DNA nanotechnology becomes a cutting edge research in recent years. The role of DNA in nanotechnology has reached far beyond its intrinsic role in biology. With the well-known

knowledge of self-recognition properties of DNA and its double helix feature on the molecular level, different geometries and sizes of DNA-based nanoarchitectures can be generated very accurately and efficiently in contrast to other self-assembling systems. In this review article, we summarized recent progress of drug delivery system based on multidimensional DNA nanostructures. Thus, self-assembled DNA nanostructures are undoubtedly highly promising scaffold to act as a drug nanocarrier or to display functionalities for therapeutic applications. From the high demand of multifunctional DNA carriers in the context of drug delivery vehicles that have been described in detail here, we can summarize several reasons why self-assembled nucleic acid structures are feasible for targeted drug delivery. First, the DNA nanostructures can be designed and modified with multifunctional groups including drug molecules, targeting motifs, and fluorescence probes and position all of them with high accuracy. Second, in comparison with multistep synthesis of other nanocarrier scaffolds like dendrimers, the desired DNA nanoobjects with great versatility can be easily formed by simple mixing of individual DNA building blocks together in a single step. This strategy can be achieved a large size of DNA nanostructures effortlessly, ranging from only a few nanometers to micrometer scale. Another conspicuous feature suggesting the use of self-assembled DNA-based carrier is that they can pass through the negatively charged plasma membrane and get into the cells efficiently without the need of transfecting agents, except some of the large and flexible DNA origami structures as compared to naked DNA strand itself. In addition, all DNA-based nanomaterials exhibited a very low cytotoxicity, no matter in the presence or absence of the payloads or stimuli. Such feature makes the self-assembled DNA nanoarchitectures a promising delivery system. Another striking advantage of using DNA nanoobjects for the purpose of drug delivery is that a large number of drug loading methods have been utilized for the interaction between drug molecules/cargos and self-assembled DNA nanostructures. We have described the examples briefly in this paper. They included covalent linkage, nucleic acid base-pairing, biotin-streptavidin interaction, intercalation, aptamer-targeted interaction, DNA-protein interaction, and encapsulation. Scientists also demonstrated several possibilities for the control release of drug or cargo molecules. In the presence of the specific and weak hydrogen bonds between A and T, and C and G nucleobases, a strand displacement is a method by adding an eraser DNA or RNA strand, allowing exchange and release of strands consisting of a toehold overhang. This DNA-mediated release strategy highly relies on specific nucleic acid sequences. When those DNA nanostructures are introduced into an environment with different pH values, i-motif switching is a promising mechanism for structural change and control release of cargo simultaneously. Another option for drug release is the use of light. In this case, light acts as a stimulus to facilitate the clean removal process. No accumulation of waste happens. Overall, multifunctional DNA nanostructures have successfully demonstrated their efficient intracellular delivery and specific targeting to cancer cells or particular intracellular organelles including, lysosomes, endosomes, Golgi networks,

mitochondria, and the nuclei. They are also extensively used for the delivery of certain drug or cargo molecules in living cell systems and induced some cellular activities or effects accordingly. To sum up, self-assembled DNA nanostructures offer unprecedented control over their structures and functionalities in a biological or cellular environment, the above examples demonstrate the potential applications, particularly for targeted drug delivery or gene regulation.

However, the use of DNA nanostructures in the biomedical field faces several challenges. As self-assembled DNA nanostructures have been seriously considered for the application in drug delivery, further studies are needed to obtain better information for their practical applications. These consist of the understanding of cellular uptake mechanism such as their intracellular pathway and pharmacokinetics. Can they escape from the fate of being degraded by endocytosis before reaching the target sites and taking biological effects? It is also necessary to investigate the relationship between their intracellular behavior/function and their various chemical/physical properties such as functional group incorporation, surface charges, nucleobase sequences, geometry, and dimensions. Another focus which should be concentrated on is the study of selective targeting of functionalized DNA nanostructures in terms of discrimination of diseased cells from common normal cells *in vitro* and *in vivo*. For instance, how can they be only taken up by cancer cells, but not macrophages? It is also important to look for some chemical modifications to prevent the formation of aggregates in circulating system and overcome the multilayers barriers after the DNA-based nanocarriers enter human body. The last but not the least, an alternative new and safe control release mechanism for drug molecules should be developed such that no waste is accumulated in biological system in addition to no harm being induced to the tissues of human bodies. We strongly believe that these suggested questions and studies are attractive topics to be investigated in the near future.

Conflict of Interests

The authors declare that there is no conflict of interests regarding the publication of this paper.

Acknowledgments

This work was supported by National Science Foundation of China 21324077, CityU Strategic Research Grant 7004026, and CityU Start-up Grant 7200300.

References

- [1] J. A. Hubbell and A. Chilkoti, "Nanomaterials for drug delivery," *Science*, vol. 337, no. 6092, pp. 303–305, 2012.
- [2] M. H. El-Dakdouki, E. Puré, and X. Huang, "Development of drug loaded nanoparticles for tumor targeting. Part 1: synthesis, characterization, and biological evaluation in 2D cell cultures," *Nanoscale*, vol. 5, no. 9, pp. 3895–3903, 2013.
- [3] L. Moore, E. K.-H. Chow, E. Osawa, J. M. Bishop, and D. Ho, "Diamond-lipid hybrids enhance chemotherapeutic tolerance

- and mediate tumor regression," *Advanced Materials*, vol. 25, no. 26, pp. 3532–3541, 2013.
- [4] K. Salazar-Salinas, C. Kubli-Garfias, and J. M. Seminario, "Computational design of a CNT carrier for a high affinity bispecific anti-HER2 antibody based on trastuzumab and pertuzumab Fabs," *Journal of Molecular Modeling*, vol. 19, no. 7, pp. 2797–2810, 2013.
 - [5] M. E. Davis, J. E. Zuckerman, C. H. J. Choi et al., "Evidence of RNAi in humans from systemically administered siRNA via targeted nanoparticles," *Nature*, vol. 464, no. 7291, pp. 1067–1070, 2010.
 - [6] K. Miyata, R. J. Christie, and K. Kataoka, "Polymeric micelles for nano-scale drug delivery," *Reactive and Functional Polymers*, vol. 71, no. 3, pp. 227–234, 2011.
 - [7] Y. L. Colson and M. W. Grinstaff, "Biologically responsive polymeric nanoparticles for drug delivery," *Advanced Materials*, vol. 24, no. 28, pp. 3878–3886, 2012.
 - [8] H. Pei, X. Zuo, D. Zhu, Q. Huang, and C. Fan, "Functional DNA nanostructures for theranostic applications," *Accounts of Chemical Research*, vol. 47, no. 2, pp. 550–559, 2014.
 - [9] C. Song, Z.-G. Wang, and B. Ding, "Smart nanomachines based on DNA self-assembly," *Small*, vol. 9, no. 14, pp. 2382–2392, 2013.
 - [10] L. M. Smith, "Nanostructures: the manifold faces of DNA," *Nature*, vol. 440, no. 7082, pp. 283–284, 2006.
 - [11] J. Fu, M. Liu, Y. Liu, and H. Yan, "Spatially-interactive biomolecular networks organized by nucleic acid nanostructures," *Accounts of Chemical Research*, vol. 45, no. 8, pp. 1215–1226, 2012.
 - [12] N. C. Seeman, "Nucleic acid junctions and lattices," *Journal of Theoretical Biology*, vol. 99, no. 2, pp. 237–247, 1982.
 - [13] N. C. Seeman, "DNA in a material world," *Nature*, vol. 421, no. 6921, pp. 427–431, 2003.
 - [14] N. R. Kallenbach, R. I. Ma, and N. C. Seeman, "An immobile nucleic acid junction constructed from oligonucleotides," *Nature*, vol. 305, no. 5937, pp. 829–831, 1983.
 - [15] R.-I. Ma, N. R. Kallenbach, R. D. Sheardy, M. L. Petrillo, and N. C. Seeman, "Three-arm nucleic acid junctions are flexible," *Nucleic Acids Research*, vol. 14, no. 24, pp. 9745–9753, 1986.
 - [16] E. Winfree, F. Liu, L. A. Wenzler, and N. C. Seeman, "Design and self-assembly of two-dimensional DNA crystals," *Nature*, vol. 394, no. 6693, pp. 539–544, 1998.
 - [17] H. Yan, S. H. Park, G. Finkelstein, J. H. Reif, and T. H. LaBean, "DNA-templated self-assembly of protein arrays and highly conductive nanowires," *Science*, vol. 301, no. 5641, pp. 1882–1884, 2003.
 - [18] D. Liu, M. Wang, Z. Deng, R. Walulu, and C. Mao, "Tensegrity: construction of rigid DNA triangles with flexible four-arm DNA junctions," *Journal of the American Chemical Society*, vol. 126, no. 8, pp. 2324–2325, 2004.
 - [19] C. Mao, W. Sun, and N. C. Seeman, "Designed two-dimensional DNA holliday junction arrays visualized by atomic force microscopy," *Journal of the American Chemical Society*, vol. 121, no. 23, pp. 5437–5443, 1999.
 - [20] C. Zhang, Y. He, M. Su et al., "DNA self-assembly: from 2D to 3D," *Faraday Discussions*, vol. 143, pp. 221–233, 2009.
 - [21] C. Lin, Y. Liu, and H. Yan, "Designer DNA nanoarchitectures," *Biochemistry*, vol. 48, no. 8, pp. 1663–1674, 2009.
 - [22] Z.-G. Wang and B. Ding, "DNA-based self-assembly for functional nanomaterials," *Advanced Materials*, vol. 25, no. 28, pp. 3905–3914, 2013.
 - [23] P. W. K. Rothemund, "Folding DNA to create nanoscale shapes and patterns," *Nature*, vol. 440, no. 7082, pp. 297–302, 2006.
 - [24] H. Yan, T. H. LaBean, L. Feng, and J. H. Reif, "Directed nucleation assembly of DNA tile complexes for barcode-patterned lattices," *Proceedings of the National Academy of Sciences of the United States of America*, vol. 100, no. 14, pp. 8103–8108, 2003.
 - [25] W. M. Shih, J. D. Quispe, and G. F. Joyce, "A 1.7-kilobase single-stranded DNA that folds into a nanoscale octahedron," *Nature*, vol. 427, no. 6975, pp. 618–621, 2004.
 - [26] S. M. Douglas, H. Dietz, T. Liedl, B. Högberg, F. Graf, and W. M. Shih, "Self-assembly of DNA into nanoscale three-dimensional shapes," *Nature*, vol. 459, no. 7245, pp. 414–418, 2009.
 - [27] Z. Li, M. Liu, L. Wang, J. Nangreave, H. Yan, and Y. Liu, "Molecular behavior of DNA origami in higher-order self-assembly," *Journal of the American Chemical Society*, vol. 132, no. 38, pp. 13545–13552, 2010.
 - [28] Z.-G. Wang, C. Song, and B. Ding, "Functional DNA nanostructures for photonic and biomedical applications," *Small*, vol. 9, no. 13, pp. 2210–2222, 2013.
 - [29] V. Linko and H. Dietz, "The enabled state of DNA nanotechnology," *Current Opinion in Biotechnology*, vol. 24, no. 4, pp. 555–561, 2013.
 - [30] A.-P. Eskelinen, H. Rosilo, A. Kuzyk, P. Törmä, and M. A. Kostainen, "Controlling the formation of DNA origami structures with external signals," *Small*, vol. 8, no. 13, pp. 2016–2020, 2012.
 - [31] C. K. McLaughlin, G. D. Hamblin, and H. F. Sleiman, "Supramolecular DNA assembly," *Chemical Society Reviews*, vol. 40, no. 12, pp. 5647–5656, 2011.
 - [32] F. A. Aldaye, P. K. Lo, P. Karam, C. K. McLaughlin, G. Cosa, and H. F. Sleiman, "Modular construction of DNA nanotubes of tunable geometry and single- or double-stranded character," *Nature Nanotechnology*, vol. 4, no. 6, pp. 349–352, 2009.
 - [33] P. K. Lo, F. Altvater, and H. F. Sleiman, "Templated synthesis of DNA nanotubes with controlled, predetermined lengths," *Journal of the American Chemical Society*, vol. 132, no. 30, pp. 10212–10214, 2010.
 - [34] H. Yang, F. Altvater, A. D. de Bruijn, C. K. McLaughlin, P. K. Lo, and H. F. Sleiman, "Chiral metal-DNA four-arm junctions and metalated nanotubular structures," *Angewandte Chemie*, vol. 50, no. 20, pp. 4620–4623, 2011.
 - [35] Y. Wen, C. K. McLaughlin, P. K. Lo, H. Yang, and H. F. Sleiman, "Stable gold nanoparticle conjugation to internal DNA positions: facile generation of discrete gold nanoparticle-DNA assemblies," *Bioconjugate Chemistry*, vol. 21, no. 8, pp. 1413–1416, 2010.
 - [36] H. Yang, K. L. Metera, and H. F. Sleiman, "DNA modified with metal complexes: applications in the construction of higher order metal-DNA nanostructures," *Coordination Chemistry Reviews*, vol. 254, no. 19–20, pp. 2403–2415, 2010.
 - [37] K. M. M. Carneiro, G. D. Hamblin, K. D. Hänni et al., "Stimuli-responsive organization of block copolymers on DNA nanotubes," *Chemical Science*, vol. 3, no. 6, pp. 1980–1986, 2012.
 - [38] P. K. Lo, K. L. Metera, and H. F. Sleiman, "Self-assembly of three-dimensional DNA nanostructures and potential biological applications," *Current Opinion in Chemical Biology*, vol. 14, no. 5, pp. 597–607, 2010.
 - [39] J. Li, C. Fan, H. Pei, J. Shi, and Q. Huang, "Smart drug delivery nanocarriers with self-assembled DNA nanostructures," *Advanced Materials*, vol. 25, no. 32, pp. 4386–4396, 2013.
 - [40] E. S. Andersen, M. Dong, M. M. Nielsen et al., "Self-assembly of a nanoscale DNA box with a controllable lid," *Nature*, vol. 459, no. 7243, pp. 73–76, 2009.

- [41] J.-W. Keum and H. Bermudez, "Enhanced resistance of DNA nanostructures to enzymatic digestion," *Chemical Communications*, no. 45, pp. 7036–7038, 2009.
- [42] A. S. Walsh, H. Yin, C. M. Erben, M. J. A. Wood, and A. J. Turberfield, "DNA cage delivery to mammalian cells," *ACS Nano*, vol. 5, no. 7, pp. 5427–5432, 2011.
- [43] J. Li, H. Pei, B. Zhu et al., "Self-assembled multivalent DNA nanostructures for noninvasive intracellular delivery of immunostimulatory CpG oligonucleotides," *ACS Nano*, vol. 5, no. 11, pp. 8783–8789, 2011.
- [44] Q. Mei, X. Wei, F. Su et al., "Stability of DNA origami nanoarrays in cell lysate," *Nano Letters*, vol. 11, no. 4, pp. 1477–1482, 2011.
- [45] C. E. Castro, F. Kilchherr, D.-N. Kim et al., "A primer to scaffolded DNA origami," *Nature Methods*, vol. 8, no. 3, pp. 221–229, 2011.
- [46] V. J. Schüller, S. Heidegger, N. Sandholzer et al., "Cellular immunostimulation by CpG-sequence-coated DNA origami structures," *ACS Nano*, vol. 5, no. 12, pp. 9696–9702, 2011.
- [47] J. W. Conway, C. K. McLaughlin, K. J. Castor, and H. Sleiman, "DNA nanostructure serum stability: greater than the sum of its parts," *Chemical Communications*, vol. 49, no. 12, pp. 1172–1174, 2013.
- [48] G. D. Hamblin, K. M. M. Carneiro, J. F. Fakhoury, K. E. Bujold, and H. F. Sleiman, "Rolling circle amplification-templated DNA nanotubes show increased stability and cell penetration ability," *Journal of the American Chemical Society*, vol. 134, no. 6, pp. 2888–2891, 2012.
- [49] K. E. Bujold, J. Fakhoury, T. G. W. Edwardson et al., "Sequence-responsive unzipping DNA cubes with tunable cellular uptake profiles," *Chemical Science*, vol. 5, no. 6, pp. 2449–2455, 2014.
- [50] C. K. McLaughlin, G. D. Hamblin, K. D. Hänni et al., "Three-dimensional organization of block copolymers on "DNA-minimal" scaffolds," *Journal of the American Chemical Society*, vol. 134, no. 9, pp. 4280–4286, 2012.
- [51] S. Ko, H. Liu, Y. Chen, and C. Mao, "DNA nanotubes as combinatorial vehicles for cellular delivery," *Biomacromolecules*, vol. 9, no. 11, pp. 3039–3043, 2008.
- [52] M. S. Chan and P. K. Lo, "Nanoneedle-assisted delivery of site-selective peptide-functionalized DNA nanocages for targeting mitochondria and nuclei," *Small*, vol. 10, no. 7, pp. 1255–1260, 2014.
- [53] S. M. Douglas, I. Bachelet, and G. M. Church, "A logic-gated nanorobot for targeted transport of molecular payloads," *Science*, vol. 335, no. 6070, pp. 831–834, 2012.
- [54] C. Zhang, X. Li, C. Tian et al., "DNA nanocages swallow gold nanoparticles (AuNPs) to form AuNP@DNA cage core-shell structures," *ACS Nano*, vol. 8, no. 2, pp. 1130–1135, 2014.
- [55] H. Lee, A. K. R. Lytton-Jean, Y. Chen et al., "Molecularly self-assembled nucleic acid nanoparticles for targeted in vivo siRNA delivery," *Nature Nanotechnology*, vol. 7, no. 6, pp. 389–393, 2012.
- [56] J. J. Fakhoury, C. K. McLaughlin, T. W. Edwardson, J. W. Conway, and H. F. Sleiman, "Development and characterization of gene silencing DNA cages," *Biomacromolecules*, vol. 15, no. 1, pp. 276–282, 2014.
- [57] A. Bianco, J. Hoebeke, S. Godefroy et al., "Cationic carbon nanotubes bind to CpG oligodeoxynucleotides and enhance their immunostimulatory properties," *Journal of the American Chemical Society*, vol. 127, no. 1, pp. 58–59, 2005.
- [58] A. M. Krieg, "Immune effects and mechanisms of action of CpG motifs," *Vaccine*, vol. 19, no. 6, pp. 618–622, 2000.
- [59] H. Hemmi, O. Takeuchi, T. Kawai et al., "A Toll-like receptor recognizes bacterial DNA," *Nature*, vol. 408, no. 6813, pp. 740–745, 2000.
- [60] M. Heikenwalder, M. Polymenidou, T. Junt et al., "Lymphoid follicle destruction and immunosuppression after repeated CpG oligodeoxynucleotide administration," *Nature Medicine*, vol. 10, no. 2, pp. 187–192, 2004.
- [61] M. Schmidt, K. Anton, C. Nordhaus, C. Junghans, B. Wittig, and M. Worm, "Cytokine and Ig-production by CG-containing sequences with phosphodiester backbone and dumbbell-shape," *Allergy*, vol. 61, no. 1, pp. 56–63, 2006.
- [62] M. Wei, N. Chen, J. Li et al., "Polyvalent immunostimulatory nanoagents with self-assembled CpG oligonucleotide-conjugated gold nanoparticles," *Angewandte Chemie*, vol. 51, no. 5, pp. 1202–1206, 2012.
- [63] M. Nishikawa, M. Matono, S. Rattanakit, N. Matsuoka, and Y. Takakura, "Enhanced immunostimulatory activity of oligodeoxynucleotides by Y-shape formation," *Immunology*, vol. 124, no. 2, pp. 247–255, 2008.
- [64] S. Rattanakit, M. Nishikawa, H. Funabashi, D. Luo, and Y. Takakura, "The assembly of a short linear natural cytosine-phosphate-guanine DNA into dendritic structures and its effect on immunostimulatory activity," *Biomaterials*, vol. 30, no. 29, pp. 5701–5706, 2009.
- [65] X. Ouyang, J. Li, H. Liu et al., "Rolling circle amplification-based DNA origami nanostructures for intracellular delivery of immunostimulatory drugs," *Small*, vol. 9, no. 18, pp. 3082–3087, 2013.
- [66] M. Wilchek and E. A. Bayer, "The avidin-biotin complex in bioanalytical applications," *Analytical Biochemistry*, vol. 171, no. 1, pp. 1–32, 1988.
- [67] P. C. Weber, M. W. Pantoliano, and L. D. Thompson, "Crystal structure and ligand-binding studies of a screened peptide complexed with streptavidin," *Biochemistry*, vol. 31, no. 39, pp. 9350–9354, 1992.
- [68] W. A. Hendrickson, A. Pähler, J. L. Smith, Y. Satow, E. A. Merritt, and R. P. Phizackerley, "Crystal structure of core streptavidin determined from multiwavelength anomalous diffraction of synchrotron radiation," *Proceedings of the National Academy of Sciences of the United States of America*, vol. 86, no. 7, pp. 2190–2194, 1989.
- [69] N. V. Voigt, T. Tørring, A. Rotaru et al., "Single-molecule chemical reactions on DNA origami," *Nature Nanotechnology*, vol. 5, no. 3, pp. 200–203, 2010.
- [70] C. Wu, D. Han, T. Chen et al., "Building a multifunctional aptamer-based dna nanoassembly for targeted cancer therapy," *Journal of the American Chemical Society*, vol. 135, no. 49, pp. 18644–18650, 2013.
- [71] M. Huybrechts, M. Symann, and A. Trouet, "Effects of daunorubicin and doxorubicin, free and associated with DNA, on hemopoietic stem cells," *Cancer Research*, vol. 39, no. 9, pp. 3738–3743, 1979.
- [72] A. Bodley, L. F. Liu, M. Israel et al., "DNA topoisomerase II-mediated interaction of doxorubicin and daunorubicin congeners with DNA," *Cancer Research*, vol. 49, no. 21, pp. 5969–5978, 1989.
- [73] Q. Jiang, C. Song, J. Nangreave et al., "DNA origami as a carrier for circumvention of drug resistance," *Journal of the American Chemical Society*, vol. 134, no. 32, pp. 13396–13403, 2012.
- [74] Y.-X. Zhao, A. Shaw, X. Zeng, E. Benson, A. M. Nyström, and B. Högberg, "DNA origami delivery system for cancer therapy

- with tunable release properties,” *ACS Nano*, vol. 6, no. 10, pp. 8684–8691, 2012.
- [75] X. Shen, Q. Jiang, J. Wang et al., “Visualization of the intracellular location and stability of DNA origami with a label-free fluorescent probe,” *Chemical Communications*, vol. 48, no. 92, pp. 11301–11303, 2012.
- [76] G. Zhu, S. Zhang, E. Song et al., “Building fluorescent DNA nanodevices on target living cell surfaces,” *Angewandte Chemie*, vol. 52, no. 21, pp. 5490–5496, 2013.
- [77] E. N. Brody, M. C. Willis, J. D. Smith, S. Jayasena, D. Zichi, and L. Gold, “The use of aptamers in large arrays for molecular diagnostics,” *Molecular Diagnosis*, vol. 4, no. 4, pp. 381–388, 1999.
- [78] J. C. Cox and A. D. Ellington, “Automated selection of anti-protein aptamers,” *Bioorganic and Medicinal Chemistry*, vol. 9, no. 10, pp. 2525–2531, 2001.
- [79] Y. Liu, C. Lin, H. Li, and H. Yan, “Aptamer-directed self-assembly of protein arrays on a DNA nanostructure,” *Angewandte Chemie*, vol. 44, no. 28, pp. 4333–4338, 2005.
- [80] K. Padmanabhan, K. P. Padmanabhan, J. D. Ferrara, J. E. Sadler, and A. Tulinisky, “The structure of α -thrombin inhibited by a 15-mer single-stranded DNA aptamer,” *Journal of Biological Chemistry*, vol. 268, no. 24, pp. 17651–17654, 1993.
- [81] S. Song, L. Wang, J. Li, C. Fan, and J. Zhao, “Aptamer-based biosensors,” *TrAC: Trends in Analytical Chemistry*, vol. 27, no. 2, pp. 108–117, 2008.
- [82] V. Bagalkot, O. C. Farokhzad, R. Langer, and S. Jon, “An aptamer-doxorubicin physical conjugate as a novel targeted drug-delivery platform,” *Angewandte Chemie*, vol. 45, no. 48, pp. 8149–8152, 2006.
- [83] E. Levy-Nissenbaum, A. F. Radovic-Moreno, A. Z. Wang, R. Langer, and O. C. Farokhzad, “Nanotechnology and aptamers: applications in drug delivery,” *Trends in Biotechnology*, vol. 26, no. 8, pp. 442–449, 2008.
- [84] C. Zhou, Z. Yang, and D. Liu, “Reversible regulation of protein binding affinity by a DNA machine,” *Journal of the American Chemical Society*, vol. 134, no. 3, pp. 1416–1418, 2012.
- [85] W. U. Dittmer, A. Reuter, and F. C. Simmel, “A DNA-based machine that can cyclically bind and release thrombin,” *Angewandte Chemie—International Edition*, vol. 43, no. 27, pp. 3550–3553, 2004.
- [86] K.-R. Kim, T. Lee, B.-S. Kim, and D.-R. Ahn, “Utilizing the bioorthogonal base-pairing system of l-DNA to design ideal DNA nanocarriers for enhanced delivery of nucleic acid cargos,” *Chemical Science*, vol. 5, no. 4, pp. 1533–1537, 2014.
- [87] R. Crawford, C. M. Erben, J. Periz et al., “Non-covalent single transcription factor encapsulation inside a DNA cage,” *Angewandte Chemie*, vol. 52, no. 8, pp. 2284–2288, 2013.
- [88] X. Liu, Y. Xu, T. Yu et al., “A DNA nanostructure platform for directed assembly of synthetic vaccines,” *Nano Letters*, vol. 12, no. 8, pp. 4254–4259, 2012.
- [89] P. K. Lo, P. Karam, F. A. Aldaye et al., “Loading and selective release of cargo in DNA nanotubes with longitudinal variation,” *Nature Chemistry*, vol. 2, no. 4, pp. 319–328, 2010.
- [90] D. Bhatia, S. Surana, S. Chakraborty, S. P. Koushika, and Y. Krishnan, “A synthetic icosahedral DNA-based host-cargo complex for functional *in vivo* imaging,” *Nature Communications*, vol. 2, article 339, 2011.
- [91] T. G. W. Edwardson, K. M. M. Carneiro, C. K. McLaughlin, C. J. Serpell, and H. F. Sleiman, “Site-specific positioning of dendritic alkyl chains on DNA cages enables their geometry-dependent self-assembly,” *Nature Chemistry*, vol. 5, no. 10, pp. 868–875, 2013.
- [92] R. P. Goodman, M. Heilemann, S. Doose, C. M. Erben, A. N. Kapanidis, and A. J. Turberfield, “Reconfigurable, braced, three-dimensional DNA nanostructures,” *Nature Nanotechnology*, vol. 3, no. 2, pp. 93–96, 2008.
- [93] A. Banerjee, D. Bhatia, A. Saminathan, S. Chakraborty, S. Kar, and Y. Krishnan, “Controlled release of encapsulated cargo from a DNA icosahedron using a chemical trigger,” *Angewandte Chemie—International Edition*, vol. 52, no. 27, pp. 6854–6857, 2013.
- [94] Z. Liu, Y. Li, C. Tian, and C. Mao, “A smart DNA tetrahedron that isothermally assembles or dissociates in response to the solution pH value changes,” *Biomacromolecules*, vol. 14, no. 6, pp. 1711–1714, 2013.
- [95] S. Modi, M. G. Swetha, D. Goswami, G. D. Gupta, S. Mayor, and Y. Krishnan, “A DNA nanomachine that maps spatial and temporal pH changes inside living cells,” *Nature Nanotechnology*, vol. 4, no. 5, pp. 325–330, 2009.
- [96] M. Zhou, X. Liang, T. Mochizuki, and H. Asanuma, “A light-driven DNA nanomachine for the efficient photoswitching of RNA digestion,” *Angewandte Chemie*, vol. 49, no. 12, pp. 2167–2170, 2010.
- [97] H. Asanuma, X. Liang, H. Nishioka, D. Matsunaga, M. Liu, and M. Komiyama, “Synthesis of azobenzene-tethered DNA for reversible photo-regulation of DNA functions: hybridization and transcription,” *Nature protocols*, vol. 2, no. 1, pp. 203–212, 2007.
- [98] X. Liang, H. Nishioka, N. Takenaka, and H. Asanuma, “A DNA nanomachine powered by light irradiation,” *ChemBioChem*, vol. 9, no. 5, pp. 702–705, 2008.
- [99] X. Liang, T. Mochizuki, and H. Asanuma, “A supra-photoswitch involving sandwiched DNA base Pairs and azobenzenes for light-driven nanostructures and nanodevices,” *Small*, vol. 5, no. 15, pp. 1761–1768, 2009.
- [100] H. Kang, H. Liu, J. A. Phillips et al., “Single-DNA molecule nanomotor regulated by photons,” *Nano Letters*, vol. 9, no. 7, pp. 2690–2696, 2009.
- [101] Y. Zou, J. Chen, Z. Zhu et al., “Single-molecule photon-fueled DNA nanoscissors for DNA cleavage based on the regulation of substrate binding affinity by azobenzene,” *Chemical Communications*, vol. 49, no. 77, pp. 8716–8718, 2013.
- [102] Y. Yang, M. Endo, K. Hidaka, and H. Sugiyama, “Photo-controllable DNA origami nanostructures assembling into pre-designed multiorientational patterns,” *Journal of the American Chemical Society*, vol. 134, no. 51, pp. 20645–20653, 2012.
- [103] D. Han, J. Huang, Z. Zhu et al., “Molecular engineering of photoresponsive three-dimensional DNA nanostructures,” *Chemical Communications*, vol. 47, no. 16, pp. 4670–4672, 2011.
- [104] I. A. Khalil, K. Kogure, H. Akita, and H. Harashima, “Uptake pathways and subsequent intracellular trafficking in nonviral gene delivery,” *Pharmacological Reviews*, vol. 58, no. 1, pp. 32–45, 2006.
- [105] S. Schütze, V. Tchikov, and W. Schneider-Brachert, “Regulation of TNFR1 and CD95 signalling by receptor compartmentalization,” *Nature Reviews Molecular Cell Biology*, vol. 9, no. 8, pp. 655–662, 2008.
- [106] L. W. Zhang and N. A. Monteiro-Riviere, “Mechanisms of quantum dot nanoparticle cellular uptake,” *Toxicological Sciences*, vol. 110, no. 1, pp. 138–155, 2009.

- [107] A. H. Okholm, J. S. Nielsen, M. Vinther, R. S. Sørensen, D. Schaffert, and J. Kjems, “Quantification of cellular uptake of DNA nanostructures by qPCR,” *Methods*, vol. 67, no. 2, pp. 193–197, 2014.
- [108] J. Mikkilä, A.-P. Eskelinen, E. H. Niemelä et al., “Virus-encapsulated DNA origami nanostructures for cellular delivery,” *Nano Letters*, vol. 14, no. 4, pp. 2196–2200, 2014.
- [109] M. Chang, C.-S. Yang, and D.-M. Huang, “Aptamer-conjugated DNA icosahedral nanoparticles as a carrier of doxorubicin for cancer therapy,” *ACS Nano*, vol. 5, no. 8, pp. 6156–6163, 2011.
- [110] M. Brayman, A. Thathiah, and D. D. Carson, “MUC1: a multifunctional cell surface component of reproductive tissue epithelia,” *Reproductive Biology and Endocrinology*, vol. 2, article 4, 2004.
- [111] S. J. Gendler, “MUC1, the renaissance molecule,” *Journal of Mammary Gland Biology and Neoplasia*, vol. 6, no. 3, pp. 339–353, 2001.
- [112] C. S. M. Ferreira, M. C. Cheung, S. Missailidis, S. Bisland, and J. Gariépy, “Phototoxic aptamers selectively enter and kill epithelial cancer cells,” *Nucleic Acids Research*, vol. 37, no. 3, pp. 866–876, 2009.
- [113] S. Modi, C. Nizak, S. Surana, S. Halder, and Y. Krishnan, “Two DNA nanomachines map pH changes along intersecting endocytic pathways inside the same cell,” *Nature Nanotechnology*, vol. 8, no. 6, pp. 459–467, 2013.

Review Article

Advances in Multiferroic Nanomaterials Assembled with Clusters

Shifeng Zhao

School of Physical Science and Technology and Inner Mongolia Key Lab of Nanoscience and Nanotechnology, Inner Mongolia University, Hohhot 010021, China

Correspondence should be addressed to Shifeng Zhao; zhsf@imu.edu.cn

Received 17 June 2014; Accepted 28 October 2014

Academic Editor: Daniela Predoi

Copyright © 2015 Shifeng Zhao. This is an open access article distributed under the Creative Commons Attribution License, which permits unrestricted use, distribution, and reproduction in any medium, provided the original work is properly cited.

As an entirely new perspective of multifunctional materials, multiferroics have attracted a great deal of attention. With the rapidly developing micro- and nano-electro-mechanical system (MEMS&NEMS), the new kinds of micro- and nanodevices and functionalities aroused extensive research activity in the area of multiferroics. As an ideal building block to assemble the nanostructure, cluster exhibits particular physical properties related to the cluster size at nanoscale, which is efficient in controlling the multiferroic properties for nanomaterials. This review focuses on our recent advances in multiferroic nanomaterials assembled with clusters. In particular, the single phase multiferroic films and compound heterostructured multiferroic films assembled with clusters were introduced detailedly. This technique presents a new and efficient method to produce the nanostructured multiferroic materials for their potential application in NEMS devices.

1. Introduction

Multiferroics have attracted increasing attention due to simultaneous coexistence of ferromagnetic, ferroelectric, or ferroelastic ordering [1, 2]. Many researchers focused on the magnetoelectric effect driven by the prospect of controlling polarization by magnetic field and magnetization by electrical field [3], which opens up an entirely new perspective of magnetic/ferroelectric data storage media, spin-based devices (spintronics), magnetocapacitive devices, magnetic sensors, nonvolatile memories, random access memory, and so forth [4–8]. Since its discovery a century ago, ferroelectricity has been linked to the ancient phenomena of magnetism. Attempts to combine the dipole and spin orders into one system started in the 1960s in Cr_2O_3 single crystal [9, 10], and other single phase multiferroics, including boracites ($\text{Ni}_3\text{B}_7\text{O}_{13}\text{I}$, $\text{Cr}_3\text{B}_7\text{O}_{13}\text{Cl}$) [10], fluorides (BaMF_4 , MMn , Fe , Co , Ni) [11, 12], magnetite Fe_3O_4 [13], $(\text{Y}/\text{Yb})\text{MnO}_3$ [14], and BiFeO_3 [15], were identified in the following decades. However, such a combination in these multiferroics has been proven to be unexpectedly tough.

Moreover, by growing composite films combined with piezoelectric and magnetostrictive materials, the strong magnetoelectric coupling effect could be achieved due to product property. Much work has been done to prepare the composite films by combining perovskite ferroelectric oxides (e.g., $\text{Pb}(\text{Zr}_{0.52}\text{Ti}_{0.48})\text{O}_3$ (PZT), BaTiO_3) with ferromagnetic oxides (e.g., CoFe_2O_4 , $\text{La}_{0.67}\text{Sr}_{0.33}\text{MnO}_3$) [16–21]; however, due to the low magnetostriction of these ferromagnetic oxides and Ni metal, the reported magnetoelectric effects in these composite films are generally not strong.

As well known, rare earth iron alloy (R-Fe, R = rare earth element) possesses giant magnetostriction, being an order of magnitude greater than the ferromagnetic oxides [22]. The previous investigations have shown that the magnetoelectric effect in the bulk laminate consisted of R-Fe alloy and ferroelectric oxide (e.g., $\text{Tb}_{0.30}\text{Dy}_{0.70}\text{Fe}_2$ (Terfenol-D)/PZT) with magnetoelectric coupling coefficient α_E of ~ 4680 mV/cm·Oe is much larger than that of the all-oxide laminates (e.g., CoFe_2O_4 /PZT; its α_E is ~ 60 mV/cm·Oe) [23–25]. However, with the applications in the micro-electro-mechanical system (MEMS) devices such as microtransducers, microactuators,

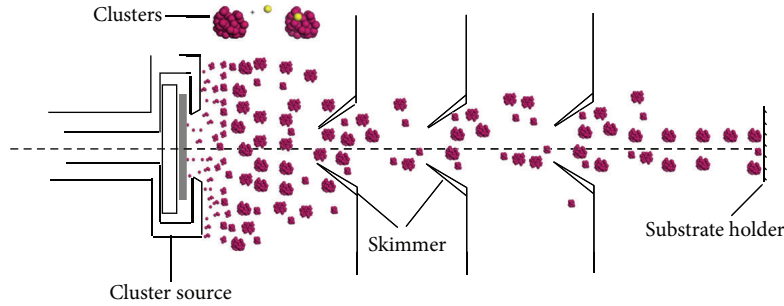


FIGURE 1: The sketched diagram of the growth and deposition process of clusters.

and microsensors [26], the well-defined microstructures together with the tunable properties are necessary for the multiferroics. Therefore, for the laminated composite film (i.e., thin-film heterostructure), it could be expected that magnetoelectric effect would be enhanced significantly if the R-Fe alloy is used in the magnetostriction layer. Though the giant magnetostrictive films have been prepared by song conventional film preparation means [27–30], since the phase-formation temperature of R-Fe alloy is very high (the substrate is generally heated above 500°C), it is unavoidable to bring about serious oxygen diffusion from PZT oxide to Tb-Fe alloy. As a result, both magnetostriction in Tb-Fe alloy and piezoelectricity in PZT are seriously suppressed. Moreover, the serious oxygen diffusion would also generate a new interface layer, which further significantly decreases the magnetoelectric coupling efficiency [31]. Therefore, a progress with low temperature and energy is necessary during deposition. Fortunately, we have developed an effective preparation method, namely, low energy cluster beam deposition (LECBD), to prepare the nanostructured magnetic, giant magnetostrictive, single phase multiferroic, and well-defined microstructured multiferroic heterostructured films [32–38]. This paper aims to review the breakthroughs on the multiferroic nanostructure assembled with clusters.

2. Low Energy Cluster Beam Deposition

As a very important building block of nanomaterials, nanoclusters are aggregates of atoms or molecules of nanometric size, containing a number of constituent particles ranging from 10 to 10^6 [39–41]. All the beam experiments on clusters have a cluster source, in which the clusters are produced. There are a variety of sources available including arc cluster ion source [42], laser vaporization cluster source [43, 44], gas aggregation source [45, 46], seeded supersonic nozzle source [47], ion sputtering source [48, 49], and liquid metal ion source [50, 51]. Based on these we developed low energy cluster beam deposition method. A magnetron-sputtering-gas-aggregation (MSGGA) cluster source produce is used to produce cluster beam to assemble multiferroic films. The growth and deposition process of clusters is shown in Figure 1 using gas aggregation. A direct current (DC) pulse power was used as the sputtering power. As the sputtering gas, one stream of argon gas with 99.9% purity was introduced through a ring

structure close to the surface of the target. Another stream of argon was fed as a buffer gas through a gas inlet near the magnetron discharge head. The cluster condensation and growth region was cooled with liquid nitrogen. A highly oriented cluster beam with a small divergent angle less than one degree was formed by differential pumping controlled by the skimmers. During the process of the deposition, the average velocity perpendicular to the substrate of each cluster is quite low (with less than 50 meV/atom corresponding to kinetic energy), and the velocity parallel to the substrate is about several meV/atom, which are both much lower than the molecular binding energy. The clusters are deposited on the substrate by a soft-landing manner and accumulated randomly but they do not coalesce with each other.

Based on this technique, various cluster-assembled nanostructured films such as metal and oxide have been prepared, which show peculiar properties different from the films prepared by the common methods [52–55]. Since the size, mass, and the assembling manner of the clusters can be precisely tuned by changing the working gas flow, controlling the length of condensation region, changing the buffer gas, and so forth, it is possible to control the microstructures and properties of the cluster-assembled nanostructured films, which makes it an ideal candidate for the fabrication of single phase or heterostructured films.

3. Magnetic Films Assembled with Clusters

3.1. Giant Magnetostrictive R-Fe Films. The cubic Laves phase R-Fe (R = rare earth element such as Tb, Dy, Sm) compounds are well known to be a giant magnetostrictive material at room temperature, which could be widely used as actuators, transducers, dampers, and so forth [56, 57]. With the demand of the rapidly developing nano-electro-mechanical system (NEMS), much work has been done and various methods such as ion plating [27], ion beam sputtering [28], flash evaporation [29] and magnetron sputtering [58], and molecular beam epitaxy [59, 60] have been developed for the preparation of R-Fe films. However, compared with the bulk materials, the saturation magnetostriction of the current R-Fe films is much lower while the magnetic driving field is still higher [58], which limits them to be further used. Fortunately, based on the LECBD technique, a well-defined Tb-Fe nanostructured film has been obtained, which

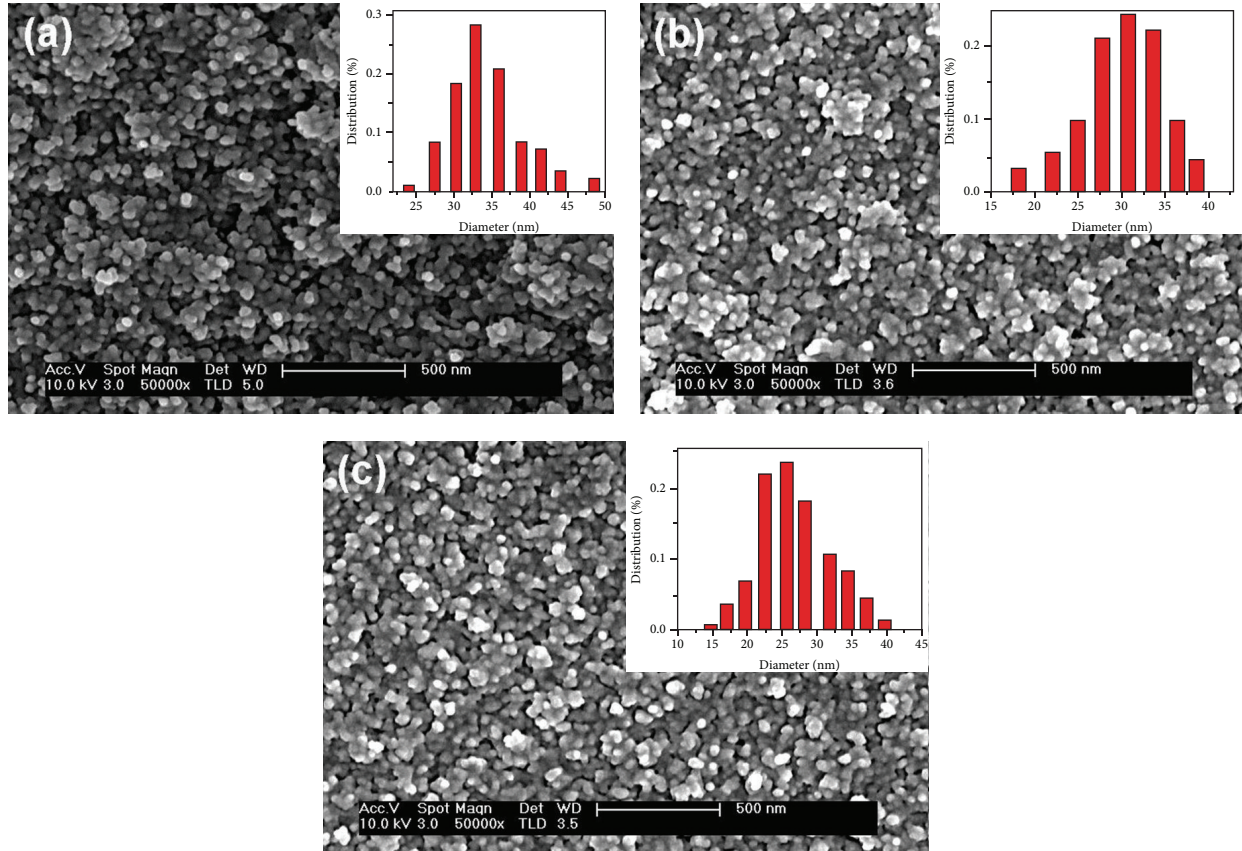


FIGURE 2: SEM images of the typical as-deposited Tb-Fe films and the graph of population versus size distribution of the nanoparticles at different growth region length. (a) 110 mm, (b) 950 mm (c), and 80 mm ([36]).

exhibits excellent magnetostriction, much higher than the common Tb-Fe films [34]. Since the size, mass, and the assembling manner of the R-Fe clusters can be precisely tuned by changing the working gas flow, controlling the length of condensation region, changing the buffer gas, and so forth, it is possible to control the microstructures and magnetic properties of the cluster-assembled R-Fe nanostructured films, which makes it an ideal candidate for the fabrication of the magnetic NEMS devices.

A DC-magnetron-sputtering-gas-aggregation (MSGAG) cluster source was used to produce the Tb-Fe cluster beam, which was finally deposited on the Si(100) substrate at room temperature to form the nanofilm. In order to tune the cluster size, the length of the condensing growth region L was set as 80 mm, 95 mm, and 110 mm, respectively. Figure 2 presents the SEM images and size distributions of the typical Tb-Fe films prepared under different length of the condensing growth region L . One can clearly observe two facts: (i) all films are assembled by the spherical nanoparticles, which are distributed uniformly and monodispersely in the film; (ii) with the increase of the condensing growth region length, the size of the nanoparticle increases, being in the ranges of 31~36 nm for $L = 110$ mm, 28~33 nm for $L = 95$ mm, and 23~28 nm for $L = 80$ mm, respectively. Meanwhile, we note that the particle size distribution was almost lognormal. The formation of such nanoparticle film is attributed to

the unique LECBD preparation process. And the length of the cluster growth region significantly influences the size of the Tb-Fe clusters for the films. In fact, the growth of the clusters as well as their size distribution is mainly determined by the cluster residence time and its distribution [61, 62]. With increasing the length of the condensing growth region, the cluster residence time in the condensing growth region increases, and thus the collision among metal ion, Tb-Fe vapor, carrier gas, and free clusters becomes more sufficient, leading to the bigger size of the clusters.

It has been confirmed that all present nanoparticle-assembled Tb-Fe films exhibit higher magnetostriction comparing to the common nonnanostructured films prepared by other methods [63–65]. And we observe that the magnetostrictive behavior and piezomagnetic coefficient evidently vary with the average size of the nanoparticle. Figure 3 gives the magnetostriction and piezomagnetic coefficient on the magnetic field for the films with various particle sizes. With increasing the particle size, the saturation magnetostriction λ_s and the saturation magnetic field H_m change, for example, $\lambda_s \sim 816 \times 10^{-6}$ and $H_m \sim 6.0$ kOe for $d = 25$ nm, $\lambda_s \sim 1029 \times 10^{-6}$ and $H_m \sim 7.0$ kOe for $d = 30$ nm, and $\lambda_s = 746 \times 10^{-6}$ and $H_m = 5.0$ kOe for $d = 35$ nm. Obviously, the film with $d = 30$ nm has the highest saturation magnetostriction and piezomagnetic coefficient. However, it is not the case at low magnetic field. The film with $d = 35$ nm possesses

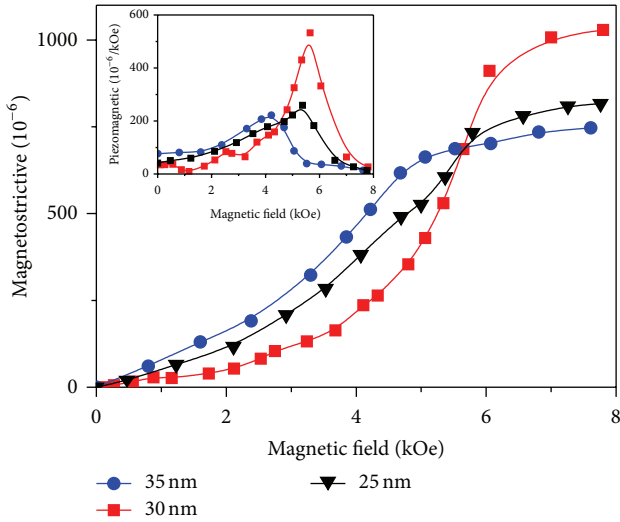


FIGURE 3: The dependence of magnetostriction and piezomagnetic coefficient for the Tb-Fe nanostructured film on various particle sizes.

higher magnetostriction and piezomagnetic coefficient at low magnetic field.

It suggests that the dependence of the magnetostriction and piezomagnetic coefficient on the particle size could be attributed to the difference of the magnetization characteristic for these films. Figure 4 presents the field dependent magnetization at room temperature for the films with the particle sizes of 25 nm, 30 nm, and 35 nm. It is shown that the degree of magnetization anisotropy for the film is significantly affected by the particles size. Both in-plane and out-of-plane saturation magnetization change, as well as the coercivity with variation of the particle size. For the films with particles size of 30 nm, the degree of magnetic anisotropy is the maximum and the difference between in-plane and out-of-plane saturation magnetization is maximum. The easy axis is out-of-plane. Thus particle size dependence of the magnetic anisotropy for the present films should be correlative to the exchange coupling effects between the nanoparticles in the film [66]. Thus the film with $d = 30$ nm may show the highest degree of magnetic anisotropy because the exchange coupling distance is twice of the domain wall width ($R_{Fe} \sim 15$ nm) for magnetic nanoparticles [67]. Therefore, for the film with $d = 30$ nm, it has higher magnetic anisotropy than the other films. It needs far higher magnetic field to rotate the spin into the applied field. Therefore, the magnetostrictive coefficient of this film is lower than the other films at a low magnetic field, but, its saturation magnetostriction is the highest, which could be ascribed to the higher energy of anisotropy exchange interaction [68].

3.2. Enhanced Ferromagnetism of BiFeO₃ Films Assembled with Clusters. BiFeO₃ (BFO) is one of the most outstanding single-phase lead-free multiferroics due to its high ferroelectric Curie ($T_{FE} \sim 1103$ K) [69] and Neel ($T_N \sim 643$ K) temperatures [70]. However, for BFO materials, antiferromagnetism and a superimposed incommensurate cycloid spin structure

with a periodicity of 62 nm along the $[1\ 1\ 0]_h$ axis cancel the macroscopic magnetization at room temperature, which restricts its applications [71]. Some investigations show that weak ferromagnetism is observed in some limited-dimension materials such as nanowires and nanoparticles due to the partial destruction of the spiral periodicity [72–74], which demonstrates a possible way to enhance ferromagnetism in single-phase multiferroics. Thus, as a size controllable building block of nanomaterials, clusters become a candidate to assemble multiferroics. Therefore, using LECBD technique, we have prepared the well-defined BiFeO₃ nanostructured films assembled with 0-characteristic-dimension clusters, and then the films were annealed at 600°C. As we expected, the ferromagnetism of the as-prepared BiFeO₃ films is enhanced [38].

Figure 5 gives the morphologies of cluster-assembled BiFeO₃ nanostructured films before annealing. It can be seen that the films are assembled with clusters, which are nearly spherical and densely packed to form the uniformly continuous films, whereas each individual cluster is still clearly distinguishable. The population versus the size reveals that the average size of the nanoparticles is ~ 22 nm for as-deposited films and ~ 25.5 nm for the annealed films and is attributed to the fact that the size of cluster increases derive from the improvement of crystallizing during the annealing process.

Figure 6 present the XRD patterns of the typical as-deposited and annealed nanostructured films assembled with clusters. They show that both present films are polycrystalline and all of the observed diffraction peaks can be indexed to a perovskite structure. And the as-deposited BFO nanostructured films and other common films belonging to the rhombohedral structure with space group R-3c (161) prepared by other methods annealed BFO films transform to the coexistence of tetragonal and orthorhombic symmetry structure as (104) and (110) diffraction peaks are not obviously split, which is observed by expanding the view of the XRD pattern around $2\theta = 32.6^\circ$ in the inset of Figure 6. At the same time, the lattice constant of cluster-assembled BiFeO₃ films is $a = 5.491$ Å, smaller than those of the films prepared by other methods. It suggests that there exists a crystal distortion for the cluster-assembled BFO films, giving rise to a transition from the rhombohedral structure to tetragonal one [75–77], which means the crystal structure changes from a high symmetry state to a low symmetry state compared to bulk BFO materials. Thus the crystal distortion is due to the size effect of the clusters with the smaller characteristic size, which partially destroys the long-range cycloid spin structure with a periodicity of 62 nm in the rhombohedral structure with space group R-3c (161). It is such crystal distortion of the as-prepared films that brings about the enhancement in magnetization.

Figure 7 shows the magnetic hysteresis loops for the cluster-assembled BFO nanostructured films measured at 5 K and 300 K. As can be seen, obvious ferromagnetism is observed for the cluster-assembled BFO nanostructured films not only at 5 K but also at room temperature. In Particular, the saturation magnetization of the BFO films at room temperature reaches 108 emu/cc, which is comparable

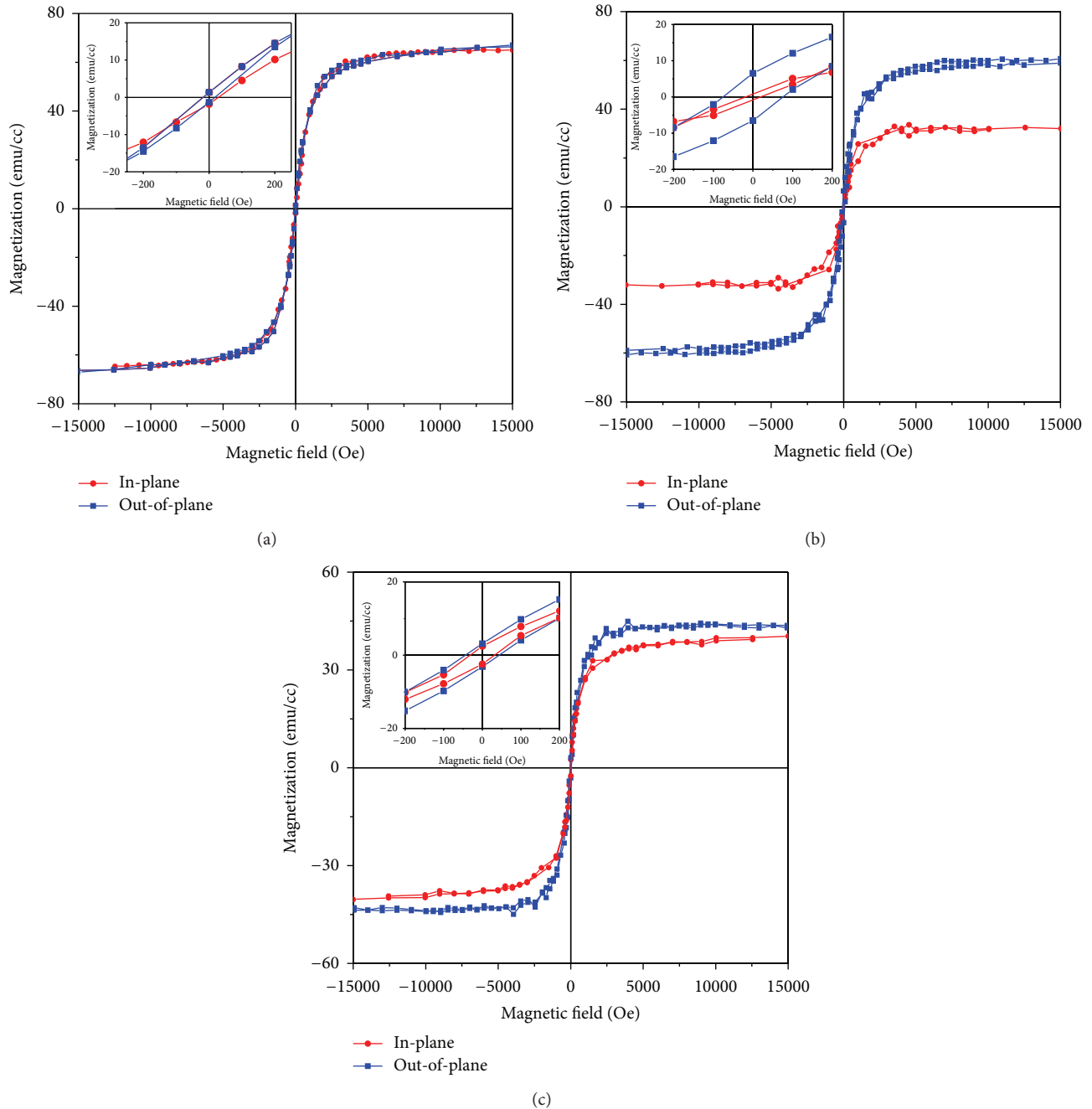


FIGURE 4: Magnetic hysteresis loops for the Tb-Fe nanostructured film assembled by the clusters (a) with 35 nm in diameter, (b) with 30 nm in diameter, and (c) with 25 nm in diameter.

with that of the present films with 125 emu/cc at 5 K. More importantly, the large magnetization of 81 emu/cc is obtained at a magnetic field of 3000 Oe at room temperature, which is a larger response than the common films prepared by other methods [78–80].

Such enhanced room temperature ferromagnetism is attributed to the fact the average size of BFO clusters is much less than the long-range cycloid order of 62 nm along the $[1\ 1\ 0]_h$ axis that the periodicity of the spin cycloid is broken [81]. Antiferromagnetic materials are considered

as the combination of one sublattice with spins along one direction and another with spins along the opposite direction. If no spin canting is considered, the spins of these two sublattices compensate each other so that the net magnetization inside the material would become zero [82]. However, the long-range antiferromagnetic order is frequently interrupted at the cluster surfaces, which forms the uncompensated surface spins. For the cluster-assembled BFO films with the average size of 25.5 nm, the uncompensated surface spins become very significant due to the very large surface to

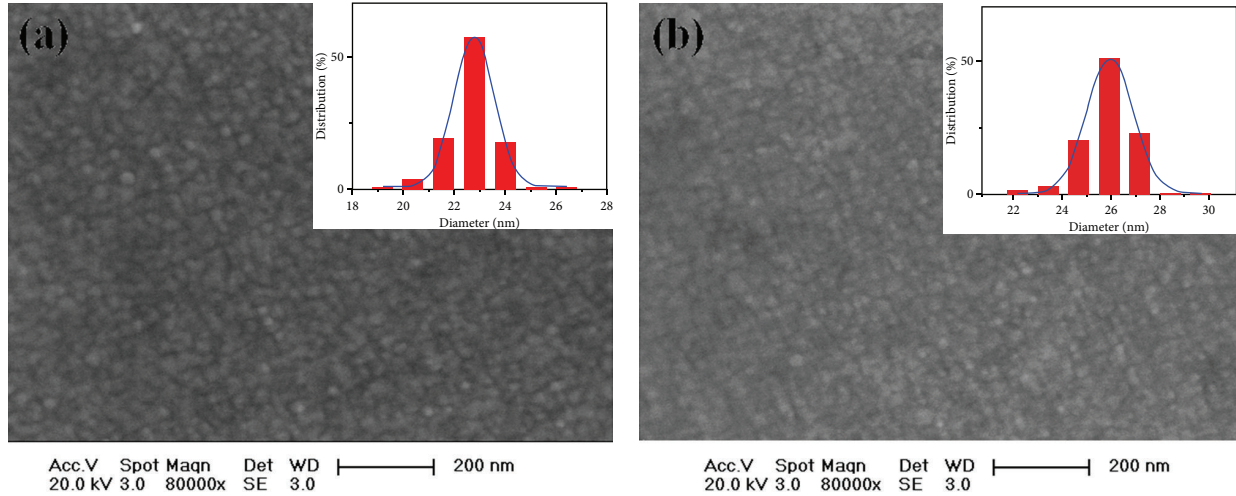


FIGURE 5: (a) Typical SEM image of as-deposited BFO nanostructured films, (b) the films after annealing, and the inset is the graph of population versus size distribution of the clusters.

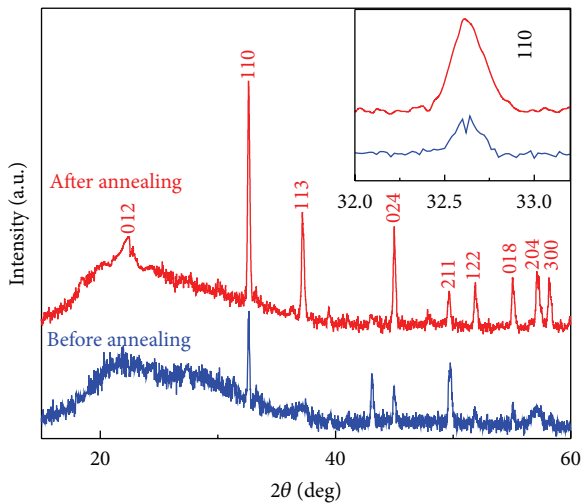


FIGURE 6: The XRD patterns before annealing and after annealing; the inset is the expanded view on the location of diffraction peak around $2\theta = 32.6^\circ$.

volume ratio for the clusters. The uncompensated spins at the surface enhance the contribution to the nanoparticle's overall magnetization. Besides, structural distortion and change of lattice parameter due to the size effect for the cluster-assembled nanostructured films [83] lead to the release of the latent magnetization locked within the cycloid. Then the ferromagnetism of nanostructured films is significantly enhanced.

4. Multiferroic Film Heterostructure Assembled with Clusters

It is well known that composite films combined with piezoelectric and magnetostrictive materials can obtain stronger magnetoelectric effect than single phase materials [84] by

the magnetic-mechanical-electric coupling product interaction via the stress mediation. Some composite films combined by perovskite ferroelectric oxides (e.g., $\text{Pb}(\text{Zr}_{0.52}\text{Ti}_{0.48})\text{O}_3$ (PZT), BaTiO_3) with ferromagnetic oxides (e.g., CoFe_2O_4 , $\text{La}_{0.67}\text{Sr}_{0.33}\text{MnO}_3$) [18, 21, 85, 86] did not acquire strong magnetoelectric effect due to low magnetostriction of the ferromagnetic oxides. Since we had prepared giant magnetostrictive R-Fe films using low energy cluster beam deposition, it is possible to prepare the well-defined microstructured thin-film multiferroic heterostructure consisting of R-Fe alloy and ferroelectric oxide. And the substrate is ferroelectric oxide; the degree of the interfacial reaction or diffusion between Tb-Fe alloy and ferroelectric oxide would be greatly suppressed due to the low temperature and energy during LECBD progress. Thus well-defined microstructure of thin-film heterostructure as well as strong magnetoelectric effect would be obtained.

4.1. Tb-Fe/PZT Thin-Film Heterostructure. Tb-Fe nanocluster beam was deposited onto the surface of the PZT film through the open holes of the mask by LECBD progress. After deposition, not taking off the mask, a Pt electrode layer was deposited on the Tb-Fe dots via pulse laser deposition. Figure 8 presents the surface SEM image of the Tb-Fe layer in the heterostructure. It shows that the Tb-Fe layer is compactly assembled by the regular spherical nanoclusters, which are distributed uniformly and adjacent with each other. The structure of the thin-film heterostructure is sketched in Insert (a) of Figure 8. Insert (b) of Figure 8 shows the cross-sectional SEM image of the thin-film heterostructure. One observes that the interface between Tb-Fe and PZT layers is clear and no transition layer is observed, which is benefit from the LECBD progress. During this process, the phase formation of Tb-Fe nanoclusters (or nanoparticles) is achieved in the condensation chamber with high temperature, while the deposition of Tb-Fe nanocluster beam onto the substrate is achieved in another high vacuum chamber with low energy

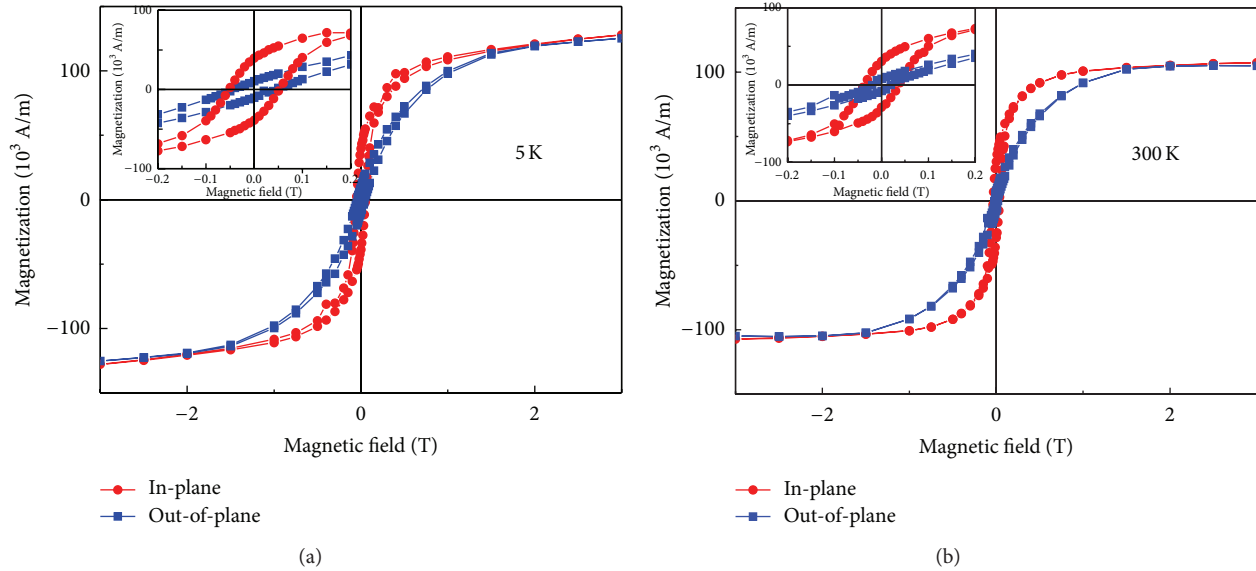


FIGURE 7: The magnetization dependence on the magnetic field of the typical cluster-assembled BFO nanostructured films (a) at low temperature of 5 K, (b) at 300 K. The inset is the expand view of the magnetic hysteresis.

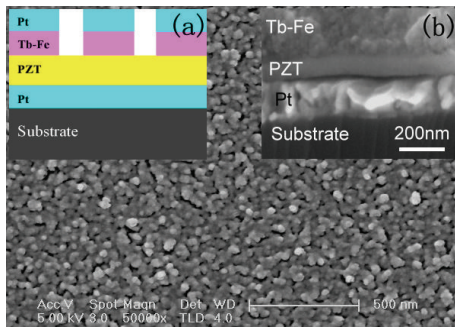


FIGURE 8: The surface SEM image of the Tb-Fe layer in the thin-film heterostructure. Insert (a) is a sketch of the heterostructure, and Insert (b) is the typical cross-sectional SEM image of the heterostructure.

and low temperature (e.g., room temperature). Both processes are independent of each other. It is easy to understand no reaction between Tb-Fe and PZT layers.

No destroying between Tb-Fe and PZT layers gives a feasibility of well ferroelectric and ferromagnetic properties. Figure 9 gives the polarization versus electric field hysteresis loops and magnetic hysteresis loops for the Tb-Fe/PZT thin-film heterostructure. It shows that the well-defined ferroelectric loops are observed. The saturation polarization and remanent polarization for Tb-Fe/PZT thin-film heterostructure have a very slight decrease compared with the pure PZT film. Such slight decrease in ferroelectric properties of the heterostructure should be attributed to the increase of oxygen vacancy concentration in PZT layer, which brings about difficulty for the mobility of domain walls in a certain degree and further leads to the decrease in polarization [87]. Insert of Figure 9(a) shows that the leakage current density in

the heterostructure is quite low, for example, only being $\sim 1.5 \times 10^{-4}$ A/cm² even under the higher electric field of 30 MV/m. In spite of this, we found that the leakage current density in the heterostructure was still higher than that of the pure PZT film, which indicates the increase of free carrier density in PZT layer of the heterostructure [88].

Besides, the heterostructure exhibits the well-defined magnetic hysteresis loops. It shows that both in-plane and out-of-plane coercive field are the same as only $H_c \sim 60$ Oe, much lower than that of the bulk Tb-Fe alloy, while the in-plane and out-of-plane saturation magnetizations are, respectively, ~ 38 emu/cm³ and ~ 47 emu/cm³. We notice that the magnetization character of the heterostructure is almost comparable to the pure nanostructured Tb-Fe film prepared by LECBD process. Since magnetoelectric effect in a two-phase composite mainly originates from the interfacial stress transfer between the magnetostrictive and the ferroelectric phase, the high magnetostriction and ferroelectrics are beneficial to the magnetoelectric coupling. A strong magnetoelectric coupling could be obtained in the thin-film heterostructure.

Figure 10 plots the magnetic bias H_{bias} dependence of the induced voltage increment $|\Delta V_{\text{ME}}|$ at a given ac magnetic field frequency $f = 1.0$ kHz. It shows that thin-film heterostructure exhibits strong magnetoelectric coupling. The calculated maximum increment of the magnetoelectric voltage coefficient is as high as ~ 140 mV/cm·Oe, larger than that of the reported all-oxide ferroelectric-ferromagnetic composite film [16–18]. So strong magnetoelectric effect in Tb-Fe/PZT thin-film heterostructure is evidently beneficial from the unique LECBD process. Based on this process, not only could the interface reaction be avoidably avoided on the maximum degree, but also both ferroelectric and magnetostrictive properties for PZT and Tb-Fe could be maintained well.

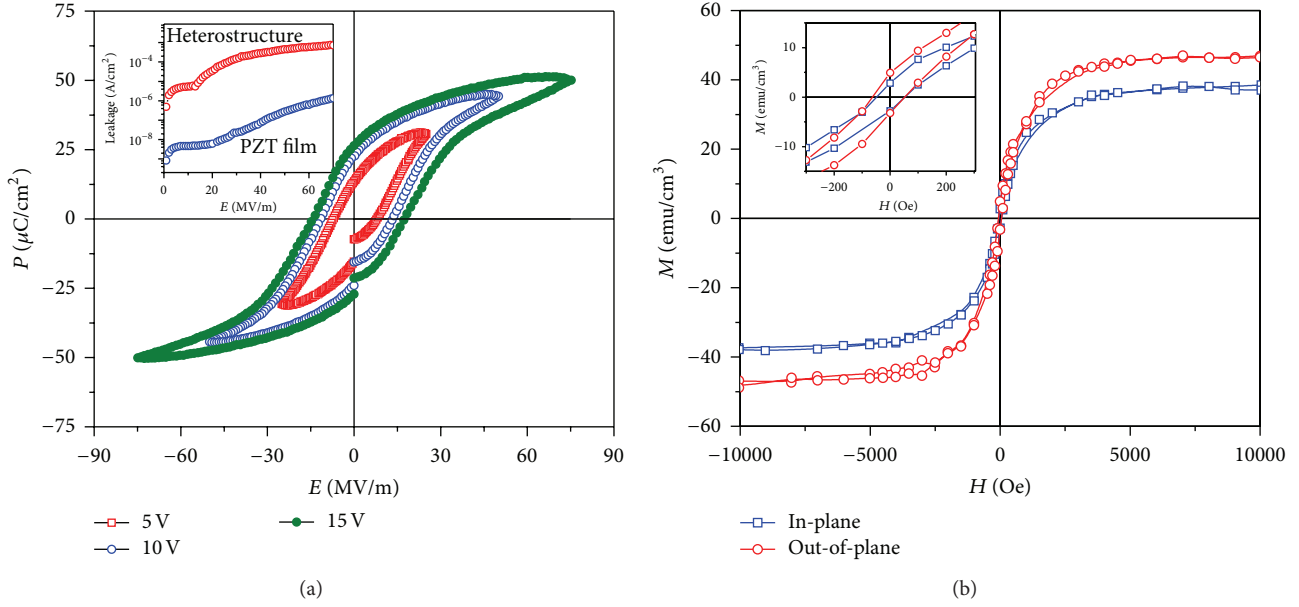


FIGURE 9: (a) Polarization versus electric field hysteresis (P - E) loops for the thin-film heterostructure. Insert is the variation of leakage current density with the applied electric field. (b) The field dependent magnetization (M - H) curves for the thin-film heterostructure.

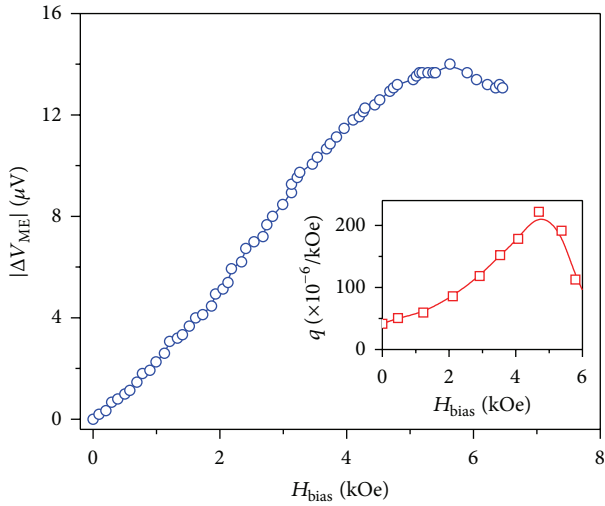


FIGURE 10: The H_{bias} dependence of the induced magnetoelectric voltage increment $|\Delta V_{\text{ME}}|$ at a given dc magnetic frequency $f = 1.0$ kHz for the thin-film heterostructure. Inset is the H_{bias} dependence of piezomagnetic coefficient for the pure Tb-Fe nanostructured film prepared by LECBD process.

Insert of Figure 10 shows the H_{bias} dependence of piezomagnetic coefficient q ($= \delta\lambda/\delta H_{\text{bias}}$) for the pure Tb-Fe nanostructured film prepared by LECBD process. Both $|\Delta V_{\text{ME}}|$ in heterostructure and q in Tb-Fe film have the similar change trend with H_{bias} . This indicates that the magnetoelectric coupling in the heterostructure should be dominated by the magnetic-mechanical-electric transform through the stress-mediated transfer.

4.2. Sm-Fe/PVDF Thin-Film Heterostructure. For Si based magnetolectric composed films, the couple efficiency between ferroelectric and ferromagnetic phases was depressed due to the stress clamping effect of the hard substrate. Therefore a flexible polyvinylidene fluoride (PVDF) film may be used instead of the hard substrate due to its small Young's modulus. Thus the magnetolectric coupling between the ferroelectric and ferromagnetic phases will almost be not influenced. Moreover, piezoelectric voltage constant (g_{31}) of PVDF film is an order higher than that of ordinary PZT film, which allows it to generate a bigger voltage output under a small stress. This indicates that PVDF film is suitable to act as the piezoelectric phase in the magnetolectric thin-film heterostructure.

The flexible PVDF/Sm-Fe heterostructural film was prepared by depositing Sm-Fe nanocluster beam onto the PVDF film at room temperature using LECBD technique. Though it is very easy to destroy the PVDF polymer substrate, it can be avoidable during LECBD progress with quite low energy and low temperature. Figure 11 shows the cross-section SEM image of the Sm-Fe/PVDF film. It can clearly be observed that the interface between the PVDF film and Sm-Fe layer is clear and no evident transition layer appears, indicating that the PVDF film does not get destroyed during the process of LECBD. The well-defined heterostructure makes it possible to generate the strong magnetolectric effect.

The Sm-Fe film exhibits strong negative magnetostrictive effect with a saturation value of $\sim 750 \times 10^{-6}$ at magnetic field of ~ 7.0 kOe as shown in Figure 12. Inset of Figure 12 shows that the Sm-Fe/PVDF film exhibits distinct magnetic anisotropy with an in-plane magnetic easy axis, which obviously makes the magnetolectric coupling in the Sm-Fe/PVDF film be more efficient under an in-plane magnetic field.

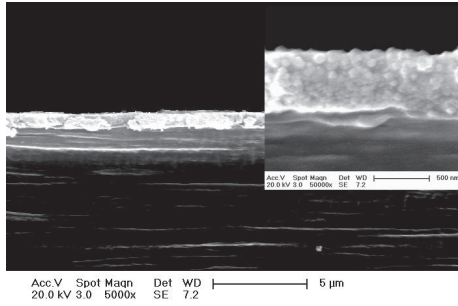


FIGURE 11: The cross-section SEM image of the Sm-Fe/PVDF thin-film heterostructure.

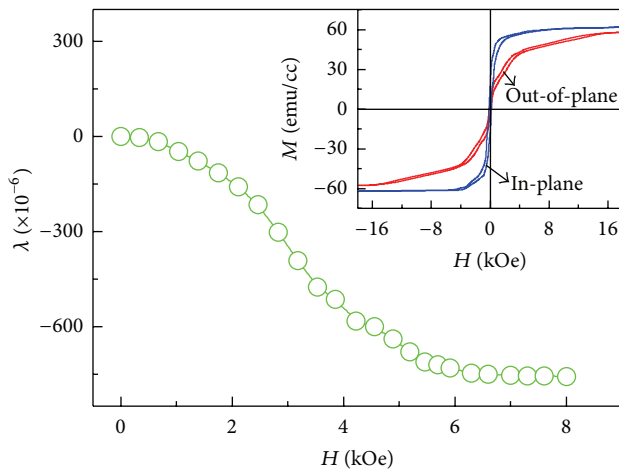


FIGURE 12: Magnetostriction λ dependence of Sm-Fe film on magnetic field H . Inset is the magnetic hysteresis loops for the Sm-Fe/PVDF thin-film heterostructure measured at room temperature.

For thin-film heterostructure, a large magnetoelectric voltage output can be obtained. Figure 13 gives the magnetoelectric voltage output increment $|\Delta V_{ME}|$ value as a function of H_{bias} for the Sm-Fe/PVDF film. It is seen that the film exhibits a large voltage output under the external magnetic bias. The $|\Delta V_{ME}|$ value increases with increasing H_{bias} , reaching the maximum value of $|\Delta V_{ME}| \sim 210 \mu V$ at $H_{bias} = 2.3$ kOe, and then drops. Compared with the previous investigations, the magnetoelectric voltage output in the present Sm-Fe/PVDF film is remarkably large, almost being two orders higher than that of typical all-oxide PZT/CoFe₂O₄/PZT film deposited on the hard wafer [89].

Therefore, by using the flexible PVDF polymer film as the substrate, the substrate clamping effect on the magnetoelectric coupling of the heterostructural film is completely eliminated. The heterostructural film exhibits large magnetoelectric voltage output, which is mainly attributed to the large piezoelectric voltage constant in the piezoelectric PVDF layer and high magnetic anisotropy with in-plane magnetic easy axis as well as the giant negative magnetostriction in the ferromagnetic Sm-Fe layer.

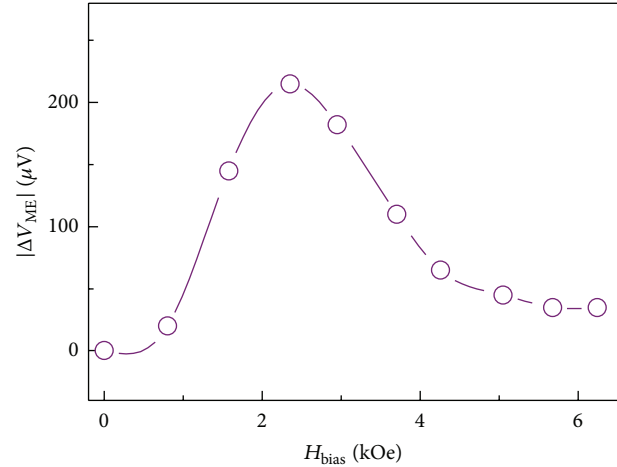


FIGURE 13: Induced voltage increment $|\Delta V_{ME}|$ as a function of magnetic bias H_{bias} .

5. Conclusions

In a conclusion, the single phase multiferroic films and compound heterostructured multiferroic films assembled with clusters were prepared by low energy cluster beam deposition. It shows that the multiferroic properties of the thin-films can be controlled or improved by tuning the size of the clusters. And the structure of the thin-film heterostructure would not be destroyed due to low temperature and energy during LECBD progress. The LECBD technique provides an ideal avenue to prepare multiferroic nanostructure and facilitates their applications on NEMS devices.

Conflict of Interests

The author declares that there is no conflict of interests regarding the publication of this paper.

Acknowledgments

This work was financially supported by National Key Projects for Basic Research of China (973 Projects) (Grant no. 2012CB626815), the National Natural Science Foundation of China (Grant nos. 11264026, 10904065), the Program for Young Talents of Science and Technology in Universities of Inner Mongolia Autonomous Region (Grant no. NJYT-12-B05), and Inner Mongolia Science Foundation for Distinguished Young Scholars (Grant no. 2014JQ01).

References

- [1] J. Wang, J. B. Neaton, H. Zheng et al., "Epitaxial BiFeO₃ multiferroic thin film heterostructures," *Science*, vol. 299, no. 5613, pp. 1719–1722, 2003.
- [2] D. C. Arnold, K. S. Knight, F. D. Morrison, and P. Lightfoot, "Ferroelectric-paraelectric transition in : crystal structure of the orthorhombic phase," *Physical Review Letters*, vol. 102, Article ID 027602, 2009.

- [3] G. Giovannetti, S. Kumar, D. Khomskii, S. Picozzi, and J. van den Brink, "Multiferroicity in rare-earth nickelates $RNiO_3$," *Physical Review Letters*, vol. 103, no. 15, Article ID 156401, 2009.
- [4] C. Ederer and N. A. Spaldin, "Weak ferromagnetism and magnetoelectric coupling in bismuth ferrite," *Physical Review B*, vol. 71, Article ID 060401, 2005.
- [5] W. Eerenstein, F. D. Morrison, J. Dho, M. G. Blamire, J. F. Scott, and N. D. Mathur, "Comment on "epitaxial $BiFeO_3$ multiferroic thin film heterostructures"," *Science*, vol. 307, no. 5713, p. 1203, 2005.
- [6] W. Eerenstein, N. D. Mathur, and J. F. Scott, "Multiferroic and magnetoelectric materials," *Nature*, vol. 442, no. 7104, pp. 759–765, 2006.
- [7] D. Lebeugle, A. Mougin, M. Viret, D. Colson, and L. Ranno, "Electric field switching of the magnetic anisotropy of a ferromagnetic layer exchange coupled to the multiferroic compound $BiFeO_3$," *Physical Review Letters*, vol. 103, no. 25, Article ID 257601, 2009.
- [8] D. Lee, S. M. Yang, T. H. Kim et al., "Multilevel data storage memory using deterministic polarization control," *Advanced Materials*, vol. 24, no. 3, pp. 402–406, 2012.
- [9] G. A. Smolenskii, A. I. Agranovskaya, S. N. Popov, and V. A. Isupov, "Dielectric polarization and losses of some complex compounds," *Soviet Physics Uspekhi*, vol. 3, p. 1981, 1958.
- [10] E. Ascher, H. Rieder, H. Schmid, and H. Stöessel, "Some properties of ferromagnetoelectric nickel-iodine boracite, $Ni_3B_7O_{13}I$," *Journal of Applied Physics*, vol. 37, no. 3, pp. 1404–1405, 1966.
- [11] D. L. Fox, D. R. Tilley, J. F. Scott, and H. J. Guggenheim, "Magnetoelectric phenomena in $BaMnF_4$ and $BaMn_{0.99}Co_{0.01}F_4$," *Physical Review B*, vol. 21, no. 7, pp. 2926–2936, 1980.
- [12] M. DiDomenico Jr., M. Eibschütz, H. J. Guggenheim, and I. Camlibel, "Dielectric behavior of ferroelectric $BaMF_4$ above room temperature," *Solid State Communications*, vol. 7, no. 16, pp. 1119–1122, 1969.
- [13] K. Kato, S. Iida, K. Yanai, and K. Mizushima, "Ferrimagnetic ferroelectricity of Fe_3O_4 ," *Journal of Magnetism and Magnetic Materials*, vol. 31–34, part 2, pp. 783–784, 1983.
- [14] I. G. Ismailza and S. A. Kizhaev, "Determination of the Curie point of ferroelectrics $YMnO_3$ and $YbMnO_3$," *Soviet Physics, Solid State*, vol. 7, p. 236, 1965.
- [15] J. R. Teague, R. Gerson, and W. J. James, "Dielectric hysteresis in single crystal $BiFeO_3$," *Solid State Communications*, vol. 8, no. 13, pp. 1073–1074, 1970.
- [16] H. Ryu, P. Murugavel, J. H. Lee et al., "Magnetoelectric effects of nanoparticulate $Pb(Zr_{0.52}Ti_{0.48})O_3$ - $NiFe_2O_4$ composite films," *Applied Physics Letters*, vol. 89, no. 10, Article ID 102907, 2006.
- [17] Y. G. Ma, W. N. Cheng, M. Ning, and C. K. Ong, "Magnetoelectric effect in epitaxial $Pb(Zr_{0.52}Ti_{0.48})O_3/La_{0.7}Sr_{0.3}MnO_3$ composite thin film," *Applied Physics Letters*, vol. 90, Article ID 152911, 2007.
- [18] J. P. Zhou, H. C. He, Z. Shi, and C. W. Nan, "Magnetoelectric $CoFe_2O_4/Pb(Zr_{0.52}Ti_{0.48})O_3$ double-layer thin film prepared by pulsed-laser deposition," *Applied Physics Letters*, vol. 88, Article ID 013111, 2006.
- [19] K. S. Chang, M. A. Aronova, C. L. Lin et al., "Exploration of artificial multiferroic thin-film heterostructures using composition spreads," *Applied Physics Letters*, vol. 84, no. 16, pp. 3091–3093, 2004.
- [20] H. Zheng, J. Wang, S. E. Lofland et al., "Multiferroic $BaTiO_3$ - $CoFe_2O_4$ Nanostructures," *Science*, vol. 303, no. 5658, pp. 661–663, 2004.
- [21] W. Eerenstein, M. Wiora, J. L. Prieto, J. F. Scott, and N. D. Mathur, "Giant sharp and persistent converse magnetoelectric effects in multiferroic epitaxial heterostructures," *Nature Materials*, vol. 6, no. 5, pp. 348–351, 2007.
- [22] R. C. Ohandley, *Modern Magnetic Materials: Principles and Applications*, John Wiley & Sons, New York, NY, USA, 2000.
- [23] J. Ryu, A. V. Carazo, K. Uchino, and H.-E. Kim, "Magnetoelectric properties in piezoelectric and magnetostrictive laminate composites," *Japanese Journal of Applied Physics*, vol. 40, no. 8, part 1, pp. 4948–4951, 2001.
- [24] C. W. Nan, G. Liu, and Y. H. Lin, "Influence of interfacial bonding on giant magnetoelectric response of multiferroic laminated composites of $Tb_{1-x}Dy_xFe_2$ and $PbZr_xTi_{1-x}O_3$," *Applied Physics Letters*, vol. 83, p. 4366, 2003.
- [25] G. Srinivasan, E. T. Rasmussen, A. A. Bush, K. E. Kametsev, V. F. Meshcheryakov, and Y. K. Fetisov, "Structural and magnetoelectric properties of MFe_2O_4 -PZT ($M = Ni, Co$) and $La_x(Ca, Sr)_{1-x}MnO_3$ -PZT multilayer composites," *Applied Physics A*, vol. 78, no. 5, pp. 721–728, 2004.
- [26] N. A. Spaldin and M. Fiebig, "The renaissance of magnetoelectric multiferroics," *Science*, vol. 309, no. 5733, pp. 391–392, 2005.
- [27] H. H. Uchida, V. Koeninger, M. Wada et al., "Preparation and characterization of $(Tb,Dy)Fe_2$ giant magnetostrictive thin films for surface acoustic wave devices," *Journal of Alloys and Compounds*, vol. 211–212, pp. 455–459, 1994.
- [28] M. Wada, H.-H. Uchida, Y. Matsumura, and H. Kaneko, "Preparation of films of $(Tb,Dy)Fe_2$ giant magnetostrictive alloy by ion beam sputtering process and their characterization," *Thin Solid Films*, vol. 281–282, no. 1–2, pp. 503–506, 1996.
- [29] H. Uchida, M. Wada, K. Koike et al., "Giant magnetostrictive materials: thin film formation and application to magnetic surface acoustic wave devices," *Journal of Alloys and Compounds*, vol. 211–212, pp. 576–580, 1994.
- [30] E. Quandt, B. Gerlach, and K. Seemann, "Preparation and applications of magnetostrictive thin films," *Journal of Applied Physics*, vol. 76, no. 10, pp. 7000–7002, 1994.
- [31] C. W. Nan, G. Liu, Y. H. Lin, and H. Chen, "Magnetic-field-induced electric polarization in multiferroic nanostructures," *Physical Review Letters*, vol. 94, no. 19, Article ID 197203, 4 pages, 2005.
- [32] S. Zhao, J.-G. Wan, M. Yao, J.-M. Liu, F. Song, and G. Wang, "Flexible $Sm-Fe$ /polyvinylidene fluoride heterostructural film with large magnetoelectric voltage output," *Applied Physics Letters*, vol. 97, no. 21, Article ID 212902, 2010.
- [33] S. Zhao, Y. Wu, J.-G. Wan, X. Dong, J.-M. Liu, and G. Wang, "Strong magnetoelectric coupling in $Tb-FePb(Zr_{0.52}Ti_{0.48})O_3$ thin-film heterostructure prepared by low energy cluster beam deposition," *Applied Physics Letters*, vol. 92, no. 1, Article ID 012920, 2008.
- [34] S. Zhao, F. Bi, J.-G. Wan et al., "Cluster-assembled $Tb-Fe$ nanostructured films produced by low energy cluster beam deposition," *Nanotechnology*, vol. 18, no. 26, Article ID 265705, 2007.
- [35] S. Zhao, M. Yao, J.-G. Wan, Y. Mu, J. Zhou, and G. Wang, "The microstructure and magnetic behavior of Co nanostructured film prepared by energetic cluster beam deposition," *European Physical Journal D*, vol. 52, pp. 163–166, 2009.
- [36] S. Zhao, J.-G. Wan, C. Huang et al., "The influence of nanoparticle size on the magnetostrictive properties of cluster-assembled $Tb-Fe$ nanofilms," *Thin Solid Films*, vol. 518, no. 12, pp. 3190–3193, 2010.

- [37] S.-F. Zhao, C.-H. Yao, Q. Lu, F.-Q. Song, J.-G. Wan, and G.-H. Wang, "Cluster-assembled cobalt doped ZnO nanostructured film prepared by low energy cluster beam deposition," *Transactions of Nonferrous Metals Society of China*, vol. 19, no. 6, pp. 1450–1453, 2009.
- [38] S. Zhao, Z. Ma, W. Xing et al., "Enhanced ferromagnetism of cluster-assembled BiFeO₃ nanostructured films," *Thin Solid Films*, 2014.
- [39] A. W. Castleman and K. H. Bowen, "Clusters: structure, energetics, and dynamics of intermediate states of matter," *The Journal of Physical Chemistry*, vol. 100, no. 31, pp. 12911–12944, 1996.
- [40] R. L. Johnston, *Atomic and Molecular Clusters*, Taylor & Francis, London, UK, 2002.
- [41] D. J. Wales, *Energy Landscapes: Applications to Clusters, Biomolecules and Glasses*, Cambridge University Press, Cambridge, UK, 2004.
- [42] R. P. Methling, V. Senz, E. D. Klinkenberg et al., "Magnetic studies on mass-selected iron particles," *The European Physical Journal D*, vol. 16, no. 1, pp. 173–176, 2001.
- [43] V. E. Bondybey and J. H. English, "Laser induced fluorescence of metal clusters produced by laser vaporization: gas phase spectrum of Pb₂," *The Journal of Chemical Physics*, vol. 74, no. 12, pp. 6978–6979, 1981.
- [44] A. N. Andriotis and M. Menon, "Orbital magnetism: pros and cons for enhancing the cluster magnetism," *Physical Review Letters*, vol. 93, no. 2, Article ID 026402, 2004.
- [45] J. Mühlbach, P. Pfau, E. Recknagel, and K. Sattler, "Cluster emission from the surfaces of Bi, Sb and Se," *Surface Science*, vol. 106, pp. 18–26, 1981.
- [46] S. H. Baker, S. C. Thornton, K. W. Edmonds, M. J. Maher, C. Norris, and C. Binns, "The construction of a gas aggregation source for the preparation of size-selected nanoscale transition metal clusters," *Review of Scientific Instruments*, vol. 71, no. 8, pp. 3178–3183, 2000.
- [47] W. A. de Heer, K. Selby, V. Kresin et al., "Collective dipole oscillations in small sodium clusters," *Physical Review Letters*, vol. 59, no. 16, pp. 1805–1808, 1987.
- [48] T. Bergmann and T. P. Martin, "High-resolution time-of-flight mass spectrometers: part I. Effects of field distortions in the vicinity of wire meshes," *Review of Scientific Instruments*, vol. 60, no. 3, p. 347, 1989.
- [49] T. Bergmann, T. P. Martin, and H. Schaber, "High-resolution time-of-flight mass spectrometer," *Review of Scientific Instruments*, vol. 60, no. 4, p. 792, 1989.
- [50] N. D. Bhaskar, R. P. Frueholz, C. M. Klimcak, and R. A. Cook, "Evidence of electronic shell structure in Rb_N⁺ (N = 1–100) produced in a liquid-metal ion source," *Physical Review B*, vol. 36, p. 4418, 1987.
- [51] Y. Saito, K. Minami, T. Ishida, and T. Noda, "Abundance of Na cluster ions ejected from a liquid metal ion source," *Zeitschrift für Physik D Atoms, Molecules and Clusters*, vol. 11, no. 1, pp. 87–91, 1989.
- [52] F. Q. Song, M. Han, M. D. Liu, B. Chen, J. G. Wan, and G. H. Wang, "Experimental observation of nanojets formed by heating PbO-coated Pb clusters," *Physical Review Letters*, vol. 94, no. 9, Article ID 093401, 4 pages, 2005.
- [53] M. Han, J. F. Zhou, F. Q. Song et al., "Silicon-riched-oxide cluster assembled nanostructures formed by low energy cluster beam deposition," *The European Physical Journal D*, vol. 24, no. 1–3, pp. 269–272, 2003.
- [54] J. G. Wan, M. Han, J. F. Zhou, and G. H. Wang, "Nanofilms of Si clusters confined in SiO nanoparticles prepared by low energy cluster beam deposition," *Physics Letters A*, vol. 280, no. 5–6, pp. 357–360, 2001.
- [55] J. Antony, X. B. Chen, J. Morrison, L. Bergman, and Y. Qiang, "ZnO nanoclusters: synthesis and photoluminescence," *Applied Physics Letters*, vol. 87, Article ID 241917, 2005.
- [56] T. Honda, K. I. Arai, and M. Yamaguchi, "Fabrication of magnetostrictive actuators using rare-earth (Tb,Sm)-Fe thin films (invited)," *Journal of Applied Physics*, vol. 76, no. 10, pp. 6994–6999, 1994.
- [57] E. Quandt and F. Claeysen, "Magnetostrictive materials and actuators," in *Proceedings of the ACTUATORS*, Messe Bremen GmbH, Bremen, Germany, June 2000.
- [58] Y. Hayashi, T. Honda, K. I. Arai, K. Ishiyama, and M. Yamaguchi, "Dependence of magnetostriction of sputtered Tb-Fe films on preparation conditions," *IEEE Transactions on Magnetics*, vol. 29, no. 6, pp. 3129–3131, 1993.
- [59] V. Odero, C. Dufour, K. Dumesnil, P. Mangin, and G. Marchal, "Epitaxial growth of (110) DyFe₂, TbFe₂ and Dy_{0.7}Tb_{0.3}Fe₂ thin films by molecular beam epitaxy," *Journal of Crystal Growth*, vol. 165, no. 1–2, pp. 175–178, 1996.
- [60] A. Mougin, C. Dufour, K. Dumesnil, and P. Mangin, "Strain-induced magnetic anisotropy in single-crystal RFe₂ (110) thin films (R = Dy, Er, Tb, Dy_{0.7}Tb_{0.3}, Sm, Y)," *Physical Review B: Condensed Matter and Materials Physics*, vol. 62, no. 14, pp. 9517–9531, 2000.
- [61] J. Söderlund, L. B. Kiss, G. A. Niklasson, and C. G. Granqvist, "Lognormal size distributions in particle growth processes without coagulation," *Physical Review Letters*, vol. 80, no. 11, pp. 2386–2388, 1998.
- [62] L. B. Kiss, J. Söderlund, G. A. Niklasson, and C. G. Granqvist, "Real origin of lognormal size distributions of nanoparticles in vapor growth processes," *Nanostructured Materials*, vol. 12, no. 1, pp. 327–332, 1999.
- [63] A. G. Jenner, J. P. Hayes, L. A. Stone, H. V. Snelling, and R. D. Greenough, "Pulsed laser deposition—an alternative route to the growth of magnetic thin films," *Applied Surface Science*, vol. 138–139, no. 1–4, pp. 408–412, 1999.
- [64] S. M. Na, S. J. Suh, and S. H. Lim, "Fabrication condition effects on the magnetic and magnetostrictive properties of sputtered Tb-Fe thin films," *Journal of Applied Physics*, vol. 93, no. 10, pp. 8507–8509, 2003.
- [65] T. Yamaki, M. Sekine, T. Haraki, H. Uchida, and Y. Matsumura, "Giant magnetostrictive thin film formation by plasma process," *Surface and Coatings Technology*, vol. 169–170, pp. 613–615, 2003.
- [66] G. Herzer, "Grain size dependence of coercivity and permeability in nanocrystalline ferromagnets," *IEEE Transactions on Magnetics*, vol. 26, no. 5, pp. 1397–1402, 1990.
- [67] L. H. Lewis, A. R. Moodenbaugh, and D. O. Welch, "Stress, strain and technical magnetic properties in 'exchange-spring' Nd₂Fe₁₄B+α-Fe nanocomposite magnets," *Journal of Physics D: Applied Physics*, vol. 34, no. 5, pp. 744–751, 2001.
- [68] J. Huang, C. Prados, J. E. Evetts, and A. Hernando, "Giant magnetostriction of amorphous Tb_xFe_{1-x} (0.10 < x < 0.45) thin films and its correlation with perpendicular anisotropy," *Physical Review B*, vol. 51, no. 1, pp. 297–304, 1995.
- [69] D. C. Arnold, K. S. Knight, F. D. Morrison, and P. Lightfoot, "Ferroelectric-paraelectric transition in BiFeO₃: crystal structure of the orthorhombic β phase," *Physical Review Letters*, vol. 102, no. 2, Article ID 027602, 4 pages, 2009.

- [70] D. Lebeugle, A. Mougin, M. Viret, D. Colson, and L. Ranno, "Electric field switching of the magnetic anisotropy of a ferromagnetic layer exchange coupled to the multiferroic compound BiFeO₃," *Physical Review Letters*, vol. 103, no. 25, Article ID 257601, 2009.
- [71] D. Sando, A. Agbelele, D. Rahmedov et al., "Crafting the magnonic and spintronic response of BiFeO₃ films by epitaxial strain," *Nature Materials*, vol. 12, no. 7, pp. 641–646, 2013.
- [72] S. Zhao and Q. Yun, "Enhanced ferromagnetism of Ho, Mn co-doped BiFeO₃ nanoparticles," *Integrated Ferroelectrics*, vol. 141, no. 1, pp. 18–23, 2013.
- [73] S. Roy and S. B. Majumder, "Recent advances in multiferroic thin films and composites," *Journal of Alloys and Compounds*, vol. 538, pp. 153–159, 2012.
- [74] T.-J. Park, G. C. Papaefthymiou, A. J. Viescas, A. R. Moodenbaugh, and S. S. Wong, "Size-dependent magnetic properties of single-crystalline multiferroic BiFeO₃ nanoparticles," *Nano Letters*, vol. 7, no. 3, pp. 766–772, 2007.
- [75] Z. L. Hou, H. F. Zhou, L. B. Kong, H. B. Jin, X. Qi, and M. S. Cao, "Enhanced ferromagnetism and microwave absorption properties of BiFeO₃ nanocrystals with Ho substitution," *Materials Letters*, vol. 84, pp. 110–113, 2012.
- [76] Q. Zhang, X. Zhu, Y. Xu et al., "Effect of La³⁺ substitution on the phase transitions, microstructure and electrical properties of Bi_{1-x}La_xFeO₃ ceramics," *Journal of Alloys and Compounds*, vol. 546, pp. 57–62, 2013.
- [77] N. Panwar, I. Coondoo, A. Tomar, A. L. Kholkin, V. S. Puli, and R. S. Katiyar, "Nanoscale piezoresponse and magnetic studies of multiferroic Co and Pr co-substituted BFO thin films," *Materials Research Bulletin*, vol. 47, no. 12, pp. 4240–4245, 2012.
- [78] J. G. Wu, D. Q. Xiao, and J. G. Zhu, "Effect of (Bi, La)(Fe, Zn)O₃ thickness on the microstructure and multiferroic properties of BiFeO₃ thin films," *Journal of Applied Physics*, vol. 112, Article ID 094109, 2012.
- [79] X. W. Tang, J. M. Dai, X. B. Zhu, and Y. P. Sun, "In situ magnetic annealing effects on multiferroic Mn-doped BiFeO₃ thin films," *Journal of Alloys and Compounds*, vol. 552, pp. 186–189, 2013.
- [80] Y. Wang, Q. H. Jiang, H. C. He, and C. W. Nan, "Multiferroic BiFeO₃ thin films prepared via a simple sol-gel method," *Applied Physics Letters*, vol. 88, Article ID 142503, 2006.
- [81] I. Sosnowska, T. P. Neumaier, and E. Steichele, "Spiral magnetic ordering in bismuth ferrite," *Journal of Physics C: Solid State Physics*, vol. 15, no. 23, article 020, pp. 4835–4846, 1982.
- [82] G. S. Arya and N. S. Negi, "Effect of In and Mn co-doping on structural, magnetic and dielectric properties of BiFeO₃ nanoparticles," *Journal of Physics D: Applied Physics*, vol. 46, no. 9, Article ID 095004, 2013.
- [83] K. Chakrabarti, K. Das, B. Sarkar, S. Ghosh, and S. K. De, "Enhanced magnetic and dielectric properties of Eu and Co co-doped BiFeO₃ nanoparticles," *Applied Physics Letters*, vol. 101, no. 4, Article ID 042401, 2012.
- [84] J. Ryu, S. Priya, K. Uchino, and H.-E. Kim, "Magnetoelectric effect in composites of magnetostrictive and piezoelectric materials," *Journal of Electroceramics*, vol. 8, no. 2, pp. 107–119, 2002.
- [85] Y. G. Ma, W. N. Cheng, M. Ning, and C. K. Ong, "Magnetoelectric effect in epitaxial Pb(Zr_{0.52}Ti_{0.48})O₃/La_{0.7}Sr_{0.3}MnO₃ composite thin film," *Applied Physics Letters*, vol. 90, Article ID 152911, 2007.
- [86] H. Zheng, J. Wang, L. Mohaddes-Ardabili et al., "Three-dimensional heteroepitaxy in self-assembled BaTiO₃-CoFe₂O₄ nanostructures," *Applied Physics Letters*, vol. 85, no. 11, pp. 2035–2037, 2004.
- [87] J. F. Scott and M. Dawber, "Oxygen-vacancy ordering as a fatigue mechanism in perovskite ferroelectrics," *Applied Physics Letters*, vol. 76, no. 25, pp. 3801–3803, 2000.
- [88] C. Wang, M. Takahashi, H. Fujino et al., "Leakage current of multiferroic (Bi_{0.6}Tb_{0.3}La_{0.1})FeO₃ thin films grown at various oxygen pressures by pulsed laser deposition and annealing effect," *Journal of Applied Physics*, vol. 99, no. 5, Article ID 054104, 2006.
- [89] Y. J. Wu, J. G. Wan, J. M. Liu, and G. H. Wang, "Significant enhancement of magnetoelectric output in multiferroic heterostructural films modulated by electric polarization cycles," *Applied Physics Letters*, vol. 96, Article ID 152902, 2010.

Research Article

Hydrothermal Synthesis of Bi_2MoO_6 Visible-Light-Driven Photocatalyst

Anukorn Phuruangrat,¹ Sunisa Putdum,¹ Phattranit Dumrongrojthanath,² Somchai Thongtem,^{3,4} and Titipun Thongtem^{2,4}

¹ Department of Materials Science and Technology, Faculty of Science, Prince of Songkla University, Hat Yai, Songkhla 90112, Thailand

² Department of Chemistry, Faculty of Science, Chiang Mai University, Chiang Mai 50200, Thailand

³ Department of Physics and Materials Science, Faculty of Science, Chiang Mai University, Chiang Mai 50200, Thailand

⁴ Materials Science Research Center, Faculty of Science, Chiang Mai University, Chiang Mai 50200, Thailand

Correspondence should be addressed to Anukorn Phuruangrat; phuruangrat@hotmail.com and Titipun Thongtem; tptthongtem@yahoo.com

Received 13 May 2014; Accepted 12 October 2014

Academic Editor: Philippe Le Coustumer

Copyright © 2015 Anukorn Phuruangrat et al. This is an open access article distributed under the Creative Commons Attribution License, which permits unrestricted use, distribution, and reproduction in any medium, provided the original work is properly cited.

Bismuth molybdate (Bi_2MoO_6) nanoplates were synthesized by the hydrothermal reaction of bismuth nitrate and sodium molybdate as starting materials at 120–180°C for 5–20 h. X-ray diffraction (XRD), Fourier transform infrared (FTIR) spectroscopy, Raman spectroscopy, and scanning electron microscopy (SEM) were used to investigate the effect of reaction temperature and length of reaction time on phase and morphologies of the as-synthesized Bi_2MoO_6 samples. In this research, orthorhombic well-crystallized Bi_2MoO_6 nanoplates with the presence of stretching and bending vibrations of MoO_6 and BiO_6 octahedrons were detected, and the Bi_2MoO_6 nanoplates synthesized at 180°C for 5 h exhibit the highest photocatalytic efficiency over 96% within 100 min visible-light irradiation.

1. Introduction

Photocatalysis of semiconductors under sun light energy has attracted worldwide researchers because they can apply it for the splitting of water and the degradation of organic pollutants [1, 2]. Visible-light-driven photocatalysis has accounted for approximately 43% of solar energy, while that of UV radiation has taken up only 5% [1, 3]. Thus it is very urgent to develop new photocatalytic materials responding in the visible light.

Bi_2MoO_6 with 2.9 eV narrow energy gap is typical Aurivillius-phase perovskite with its structure containing perovskite layers ($\text{A}_{m-1}\text{B}_m\text{O}_{3m+1}$) between Bi_2O_2 layers of bismuth oxide family with corner-shared octahedral structure [1, 2, 4]. It was found that Bi_2MoO_6 is very interesting due to its unique physical properties for using as dielectric material, gas sensors, ionic conductors, luminescent material, and photocatalyst for water splitting under visible-light irradiation [1, 4, 5]. There are a number of researchers

studying photocatalytic activities of Bi_2MoO_6 under visible-light irradiation [1, 2, 4–10]. Among them, Bi et al. [6] reported that Bi_2MoO_6 samples were successfully synthesized by a solvothermal process in different types of solvent including water, isopropanol, and ethylene glycol. The visible-light-driven photocatalytic activities for decomposition of rhodamine B (RhB) under visible-light irradiation ($\lambda > 420$ nm) were also investigated. They found that the sample synthesized using glycol as a solvent showed the best performance in the photodegradation of RhB under visible-light irradiation due to the large surface area, unique morphology, and small particle size. Yin et al. [7] reported that cage-like Bi_2MoO_6 hollow spheres were synthesized by a hard-template method and found that Bi_2MoO_6 could degrade phenol under visible-light irradiation. Jung et al. [8] found that the calcination temperature has the influence on the catalytic performance of Bi_2MoO_6 toward the oxidative dehydrogenation of n-butene to 1,3-butadiene under visible-light irradiation.

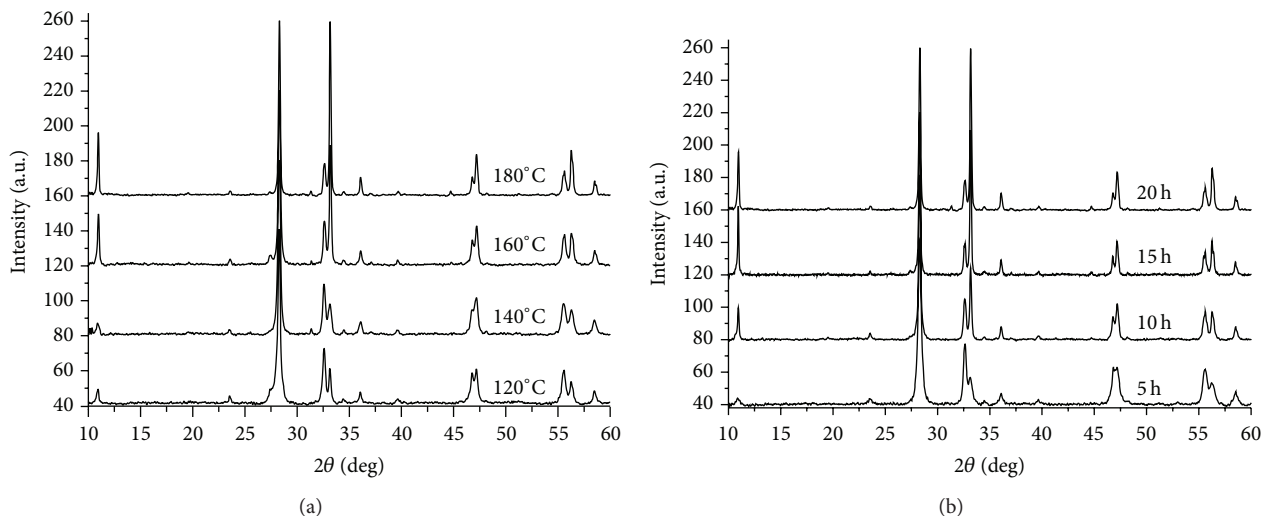


FIGURE 1: XRD patterns of Bi_2MoO_6 synthesized by the hydrothermal method at (a) 120–180°C for 20 h and (b) 180°C for 5–20 h.

In this paper, Bi_2MoO_6 crystallites were successfully synthesized by the hydrothermal process. Reaction time and temperature can play the role in the Bi_2MoO_6 crystallites via the hydrothermal process. Phase, morphologies, and photocatalytic activities were characterized by X-ray powder diffraction (XRD), Raman spectrophotometry, Fourier transform infrared (FTIR) spectrometry, scanning electron microscopy (SEM), and UV-visible spectrophotometry. The photocatalytic properties of Bi_2MoO_6 crystallites have also been investigated.

2. Experimental Procedures

In a typical procedure, each 0.01 mmol $\text{Bi}(\text{NO}_3)_3$ and each 0.005 mmol Na_2MoO_4 was dissolved into 60 mL deionized water. Subsequently, these two above solutions were mixed together under vigorous stirring, including the pH of the mixture which was adjusted to six. The mixture was stirred for another 30 min and transferred into Teflon-lined stainless steel autoclaves of 150 mL capacity. The hydrothermal process was carried out at 120–180°C for 5–20 h and the autoclaves were left to cool down to room temperature. Finally the products were synthesized, centrifuged for collection, washed with deionized water and ethanol for several times, and dried in air at 60°C for 12 h.

X-ray powder diffraction (XRD) patterns were obtained on a Philips PANalytical X'Pert PRO MPD diffractometer using $\text{Cu-K}\alpha$ radiation source ($\lambda = 1.54056 \text{ \AA}$) at a scan rate of $5 \text{ deg}\cdot\text{min}^{-1}$. Raman spectrum was recorded on a HORIBA Jobin Yvon T64000 Raman spectrometer at 50 mW and 514.5 nm wavelength Ar green laser, and FTIR spectrum was recorded on a BRUKER TENSOR 27 Fourier transform infrared (FTIR) spectrometer with KBr as a diluting agent and operated in the range of $400\text{--}4.000 \text{ cm}^{-1}$. Scanning electron microscopic (SEM) images were taken by a JSM-6335F field emission SEM (FESEM, JEOL). UV-visible spectra of

the solutions were obtained using a UV/VIS spectrophotometer (Lambda 25, PerkinElmer).

The photodegradation reaction of rhodamine B (RhB) was carried out in a photochemical reactor under visible light at room temperature. The photochemical reaction system was composed of 150 mg Bi_2MoO_6 catalyst in 10^{-5} M of 150 mL RhB solution. Prior to the UV light irradiation, the RhB solutions containing the photocatalyst were kept in the dark room for 30 min to obtain an adsorption/desorption equilibrium. The photochemical reaction system was irradiated by visible light from Xe-lamp. The sampling analysis was conducted at 20 min interval. The solutions were analyzed by a Lambda 25 spectrometer using a 450 W of Xe-lamp with the wavelength of 554 nm. The decolorization efficiency was calculated by the following formula:

$$\text{Decolorization efficiency (\%)} = \frac{C_0 - C_t}{C_0} \times 100, \quad (1)$$

where C_0 is the initial absorbency of RhB at adsorption equilibrium and C_t is the absorbency of RhB after the sampling analysis within the length of time (t).

3. Results and Discussion

Formation of Bi_2MoO_6 for different temperatures and lengths of reaction time was investigated by XRD. The XRD patterns of the samples synthesized by hydrothermal reaction at 120–180°C for 20 h are shown in Figure 1(a). XRD patterns of the samples can be readily indexed as pure orthorhombic well-crystallized Bi_2MoO_6 structure with cell parameters of $a = 5.51 \text{ \AA}$, $b = 16.21 \text{ \AA}$, and $c = 5.49 \text{ \AA}$, in good agreement with those of the JCPDS file number 21-0102 [11]. Figure 1(b) shows the XRD patterns of the samples synthesized by hydrothermal method at 180°C for 5–20 h. All the diffraction peaks can be readily indexed as a pure orthorhombic well-crystallized Bi_2MoO_6 structure of the JCPDS file number 21-0102 [11]. When the length of reaction time or temperature

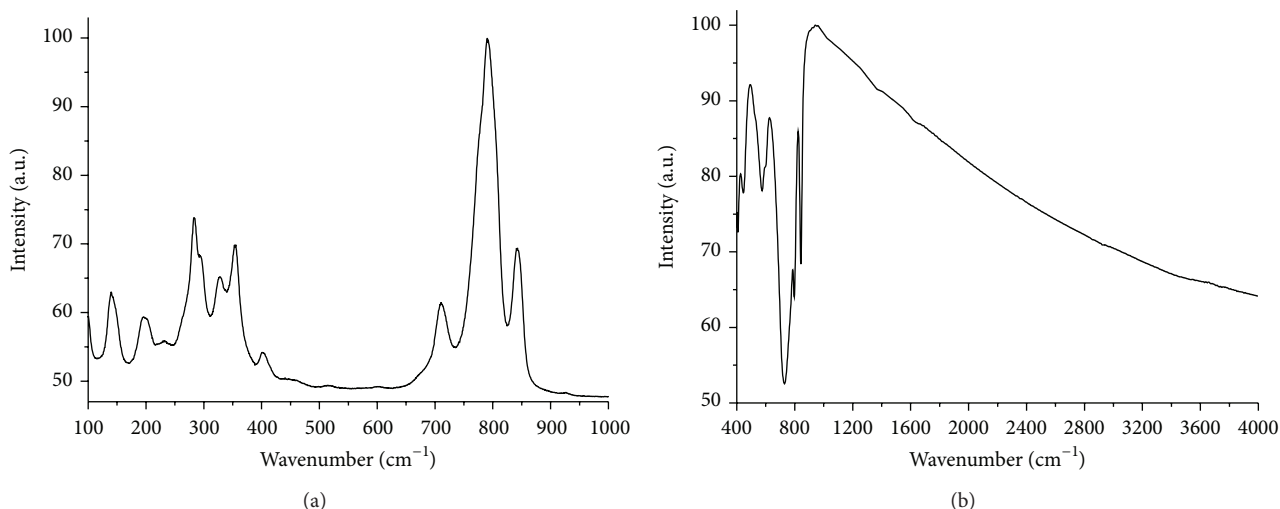


FIGURE 2: (a) Raman and (b) FTIR spectra of Bi_2MoO_6 synthesized by the hydrothermal method at 180°C for 20 h.

was increased, all the diffraction peaks of orthorhombic Bi_2MoO_6 phase were accordingly increased. They implied that the crystalline degree of orthorhombic Bi_2MoO_6 phase was increased. The XRD results indicate that nanostructured Bi_2MoO_6 could be selectively synthesized by adjusting the hydrothermal temperature and length of reaction time.

Raman spectrum of Bi_2MoO_6 sample synthesized by hydrothermal method at 180°C for 20 h is shown in Figure 2(a). The mode below 180 cm^{-1} could be the translation of molybdenum and bismuth atoms. That at 144 cm^{-1} was mainly specified as the lattice mode of Bi^{3+} atoms in the direction normal to the layers. The intense Raman modes near 290 and 280 cm^{-1} are likely to be the E_g bending vibration. Those at 323 , 345 , and 398 cm^{-1} were specified as the E_u symmetric bending. The mode at 712 cm^{-1} was specified as the asymmetric stretching vibration (E_u mode) of the MoO_6 octahedrons relating to the motion of equatorial oxygen atoms joining the MoO_6 octahedrons within the layers. The Raman vibrations at 793 cm^{-1} (A_{1g} mode) and 840 cm^{-1} (A_{2u} mode) were, respectively, specified as the symmetric and asymmetric stretching vibrations of MoO_6 octahedrons relating to the motion of apical oxygen atoms, in the direction normal to the $(\text{Bi}_2\text{O}_2)^{2+}$ layers [12–14].

Figure 2(b) shows the FTIR spectrum of Bi_2MoO_6 sample. The bands at 843 and 797 cm^{-1} were assigned to the asymmetric and symmetric stretching modes of MoO_6 relating to the vibration of apical oxygen atoms. The 734 cm^{-1} mode was attributed to the asymmetric stretching mode of MoO_6 relating to the vibration of the equatorial oxygen atoms. Those at 603 and 570 cm^{-1} corresponded to the bending vibration of MoO_6 . Furthermore, a small band at 454 cm^{-1} was attributed to the stretching and bending vibrations of BiO_6 octahedrons [12, 15].

SEM images of Bi_2MoO_6 synthesized by different hydrothermal temperatures and lengths of reaction time are shown in Figure 3. The hydrothermal temperature and

reaction time have significant influence on the size and morphology of the products. Figure 3(a) clearly illustrates that Bi_2MoO_6 hydrothermally synthesized at 120°C for 20 h is composed of relatively uniform nanoplates with edge length of 200 nm without detection of other morphologies. The products synthesized at 140 and 160°C for 20 h also show similar morphologies. Figure 3(b) is the SEM image of Bi_2MoO_6 synthesized by hydrothermal method at 180°C for 5 h. The grains are very small in size. Clearly, the formation of nanoplates was almost uniform size distribution. Figure 3(c) shows the SEM image of Bi_2MoO_6 synthesized at 180°C for 15 h, suggesting that the morphology of Bi_2MoO_6 remains as nanoplates with edge length of $0.5\text{ }\mu\text{m}$. Figure 3(d) shows that the product hydrothermally synthesized at 180°C for 20 h is composed of well-defined lamellar structure with dimension in the range of $1 \times 1.2\text{ }\mu\text{m}$. In summary, size of the products was increased when the reaction time and temperature were increased due to Ostwald ripening mechanism.

In this research, RhB was chosen as a representative dye to evaluate the photocatalytic performance of the as-synthesized Bi_2MoO_6 . The UV-visible spectra of RhB aqueous solutions containing Bi_2MoO_6 as a function of visible-light irradiation time are illustrated in Figure 4. The changes can be seen from the UV-visible absorbance. The strong absorption peak of RhB solution at 554 nm steadily decreased and showed the blue-shift to 498 nm of rhodamine during increasing in the length of irradiation time [2, 14]. It is assumed that the RhB was photodegraded to deethylated intermediates under the visible-light irradiation [2, 14, 16]. Further, Bi_2MoO_6 excellently exhibited photocatalytic activity to degrade RhB under visible-light irradiation.

The photodegradation efficiency of Bi_2MoO_6 photocatalyst under visible-light irradiation is shown in Figure 5(a). Under visible-light irradiation, the catalyst shows obvious photocatalytic activities for degradation of RhB. The Bi_2MoO_6 sample synthesized at 180°C for 5 h exhibits the highest activity. The RhB photodegradation efficiency of

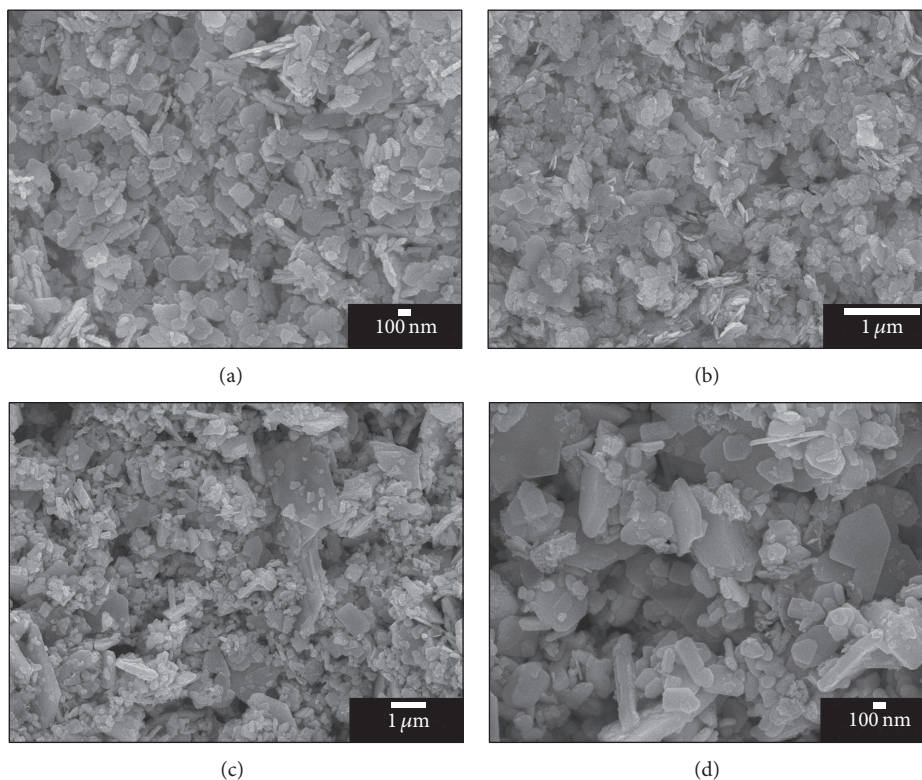


FIGURE 3: SEM images of Bi_2MoO_6 synthesized by the hydrothermal method at (a) 120°C for 20 h, (b) 180°C for 5 h, (c) 180°C for 15 h, and (d) 180°C for 20 h.

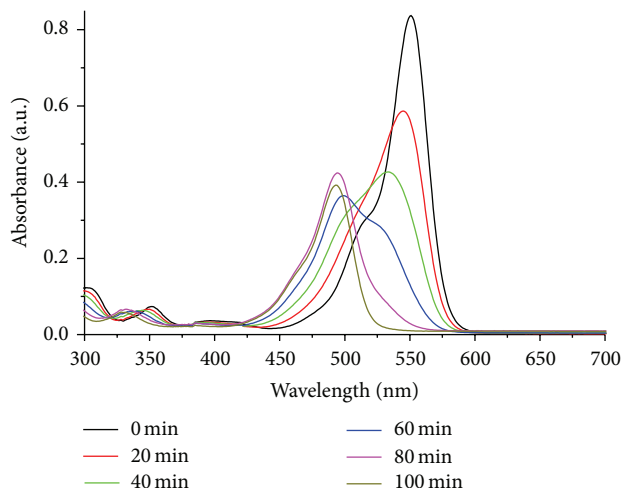


FIGURE 4: UV-visible absorption of RhB in the solutions containing Bi_2MoO_6 nanoplates synthesized at 180°C for 5 h.

Bi_2MoO_6 sample at 180°C for 5 h is over 96% within 100 min of visible-light irradiation. But, for the Bi_2MoO_6 sample synthesized at 120°C and 180°C for 20 h, their activities were over 65% and 74%, respectively. The degradation of RhB is in accordance with the pseudo-first-order kinetics by linear transforming of $\ln(C_0/C_t) = kt$, where C_0 is the initial concentration of RhB, C_t is the concentration of RhB within the length of time t , and k is the kinetics constant [1, 16]. The kinetics plots and the corresponding kinetics constants

were given in Figure 5(b). The kinetics constant for Bi_2MoO_6 synthesized at 180°C for 5 h is the highest at 0.0365 min^{-1} .

4. Conclusions

The effect of reaction temperature and time of photocatalytic nanoplates on phase, morphology, and photocatalytic properties was studied. The XRD patterns were specified as pure orthorhombic well-crystallized Bi_2MoO_6 phase. SEM

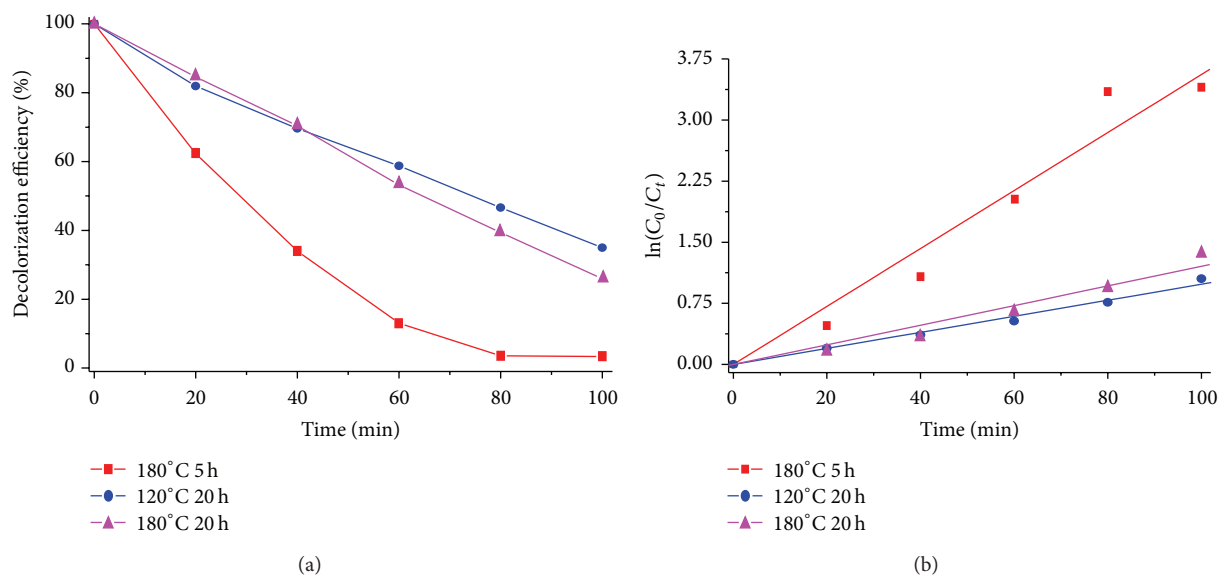


FIGURE 5: Decolorization efficiencies of RhB in the solutions containing Bi_2MoO_6 nanoplates under Xe light irradiation.

analysis showed that the products were nanoplates. The photocatalytic properties of the samples were determined by decomposing the RhB organic dye. In this research, photocatalytic activity of Bi_2MoO_6 nanoplates synthesized at 180°C for 5 h shows 96% degradation of rhodamine B under the Xe light irradiation.

Conflict of Interests

The authors declare that there is no conflict of interests regarding the publication of this paper.

Acknowledgment

The authors are extremely grateful to the Prince of Songkla University, Hat Yai, Songkhla, Thailand, for providing financial support through Contract no. SCI560002S.

References

- [1] X. Wang, F. Gu, L. Li, and G. Fang, "A facile mixed-solvothermal route to $\gamma\text{-Bi}_2\text{MoO}_6$ nanoflakes and their visible-light-responsive photocatalytic activity," *Materials Research Bulletin*, vol. 48, no. 10, pp. 3761–3765, 2013.
- [2] Y. Miao, G. Pan, Y. Huo, and H. Li, "Aerosol-spraying preparation of Bi_2MoO_6 : a visible photocatalyst in hollow microspheres with a porous outer shell and enhanced activity," *Dyes and Pigments*, vol. 99, no. 2, pp. 382–389, 2013.
- [3] Z. Zhang, W. Wang, W. Yin, M. Shang, L. Wang, and S. Sun, "Inducing photocatalysis by visible light beyond the absorption edge: effect of upconversion agent on the photocatalytic activity of Bi_2WO_6 ," *Applied Catalysis B: Environmental*, vol. 101, no. 1-2, pp. 68–73, 2010.
- [4] T. Zhang, J. Huang, S. Zhou, H. Ouyang, L. Cao, and A. Li, "Microwave hydrothermal synthesis and optical properties of flower-like Bi_2MoO_6 crystallites," *Ceramics International*, vol. 39, no. 7, pp. 7391–7394, 2013.
- [5] J. Ren, W. Wang, M. Shang, S. Sun, and E. Gao, "Heterostructured bismuth molybdate composite: preparation and improved photocatalytic activity under visible-light irradiation," *ACS Applied Materials and Interfaces*, vol. 3, no. 7, pp. 2529–2533, 2011.
- [6] J. Bi, J. Che, L. Wu, and M. Liu, "Effects of the solvent on the structure, morphology and photocatalytic properties of Bi_2MoO_6 in the solvothermal process," *Materials Research Bulletin*, vol. 48, no. 6, pp. 2071–2075, 2013.
- [7] W. Yin, W. Wang, and S. Sun, "Photocatalytic degradation of phenol over cage-like Bi_2MoO_6 hollow spheres under visible-light irradiation," *Catalysis Communications*, vol. 11, no. 7, pp. 647–650, 2010.
- [8] J. C. Jung, H. Lee, D. R. Park, J. G. Seo, and I. K. Song, "Effect of calcination temperature on the catalytic performance of $\gamma\text{-Bi}_2\text{MoO}_6$ in the oxidative dehydrogenation of *n*-butene to 1,3-butadiene," *Catalysis Letters*, vol. 131, no. 3-4, pp. 401–405, 2009.
- [9] E. L. Cuéllar, A. Cruz, K. H. L. Rodríguez, and U. O. Méndez, "Preparation of $\gamma\text{-Bi}_2\text{MoO}_6$ thin films by thermal evaporation deposition and characterization for photocatalytic applications," *Catalysis Today*, vol. 166, no. 1, pp. 140–145, 2011.
- [10] A. Martínez-de la Cruz and S. Obregón Alfaro, "Synthesis and characterization of $\gamma\text{-Bi}_2\text{MoO}_6$ prepared by co-precipitation: photoassisted degradation of organic dyes under vis-irradiation," *Journal of Molecular Catalysis A: Chemical*, vol. 320, no. 1-2, pp. 85–91, 2010.
- [11] Powder Diffract. File, JCPDS Internat. Centre Diffract. Data, Newtown Square, Pa, USA, 2001.
- [12] L. Zhang, T. Xu, X. Zhao, and Y. Zhu, "Controllable synthesis of Bi_2MoO_6 and effect of morphology and variation in local structure on photocatalytic activities," *Applied Catalysis B: Environmental*, vol. 98, no. 3-4, pp. 138–146, 2010.
- [13] M. MacZka, P. T. C. Freire, C. Luz-Lima, W. Paraguassu, J. Hanuza, and J. Mendes Filho, "Pressure-induced phase transitions in ferroelectric Bi_2MoO_6 —a Raman scattering study," *Journal of Physics Condensed Matter*, vol. 22, no. 1, Article ID 015901, 2010.

- [14] H. Li, C. Liu, K. Li, and H. Wang, "Preparation, characterization and photocatalytic properties of nanoplate Bi_2MoO_6 catalysts," *Journal of Materials Science*, vol. 43, no. 22, pp. 7026–7034, 2008.
- [15] A. Phuruangrat, P. Jitrou, P. Dumrongrojthanath et al., "Hydrothermal synthesis and characterization of Bi_2MoO_6 nanoplates and their photocatalytic activities," *Journal of Nanomaterials*, vol. 2013, Article ID 789705, 8 pages, 2013.
- [16] P. Dumrongrojthanath, T. Thongtem, A. Phuruangrat, and S. Thongtem, "Synthesis of Bi_2MoO_6 nanoplates with the assistance of PEG by hydrothermal method and their photocatalytic activities," *Digest Journal of Nanomaterials and Biostructures*, vol. 9, no. 2, pp. 593–598, 2014.

Review Article

Rare Earth Doped Apatite Nanomaterials for Biological Application

Thalagalage Shalika Harshani Perera,^{1,2} Yingchao Han,¹ Xiaofei Lu,¹ Xinyu Wang,¹ Honglian Dai,¹ and Shipu Li^{1,3}

¹ Biomedical Materials and Engineering Center, Wuhan University of Technology, Wuhan 430070, China

² Faculty of Applied Sciences, Sabaragamuwa University of Sri Lanka, 70140 Belihuloya, Sri Lanka

³ State Key Laboratory of Advanced Technology for Materials Synthesis and Processing, 122 Luoshi Road, Wuhan 430070, China

Correspondence should be addressed to Yingchao Han; hanyingchao@whut.edu.cn

Received 3 July 2014; Accepted 2 October 2014

Academic Editor: Daniela Predoi

Copyright © 2015 Thalagalage Shalika Harshani Perera et al. This is an open access article distributed under the Creative Commons Attribution License, which permits unrestricted use, distribution, and reproduction in any medium, provided the original work is properly cited.

In most biological analyses, a sensitive detection technique is primarily dependent on the fluorescence labeling agent. New generation of fluorophores called rare earth doped apatite nanoparticle (REAnp) has the ability to emit near infrared radiations which are of low absorptivity by tissue chromophores and especially suitable for biological system imaging. Moreover, bioapatite is demonstrated to be an excellent candidate for biomedical applications because of its biocompatibility, biodegradability, and bioactivity. During recent years a lot of efforts have been made for achievement of REAnp for medical diagnostics and targeted therapeutics applications. In this review, we discuss the significance of REAnps in biological systems, different routes of synthesis, and biological applications. Also we discuss the future studies for the effective biological applications of REAnps.

1. Introduction

The apatite group is a group of similar isomorphous hexagonal minerals and can be commonly found in nature as both geological materials and biominerals in calcified tissues. Apatite generally has the formula $M_{10}(TO_4)_6X_2$, with a hexagonal symmetry (space group $P6_3/m$), where M is a large divalent cation (Ca^{2+} , Sr^{2+} , Pb^{2+} , etc.), TO_4 is a trivalent anionic group (PO_4^{3-} , SiO_4^{3-} , VO_4^{3-} , etc.), and X is usually a monovalent anion (F^- , OH^- , etc.) [1]. As a mineral, apatite is mainly used as a phosphorus source for the manufacture of fertilizers, for fluoridating water, and a protective coat on metals to prevent rust and used to remove radioactive as well as metallic contaminants from waste water and polluted soil [2, 3]. The last decade has in particular witnessed the birth or evaluation of numerous biomaterials based on apatite. With the progress of nanotechnology, the decrease of particle size of apatite host can result in important modification of their properties which are significantly different from those of microsized hosts because of quantum confinement effect

and surface effect of nanometer materials. Apatite nanoparticles (Anps) demonstrate favorable biodegradability and biocompatibility, affinity to biopolymers, and high osteogenic and low toxicity [4]. Therefore this bioapatite has been extensively used in biomedical field for hard tissue repair and replacement, drug/gene delivery, and tumor treatments [5–9]. Nanodimension allows the prolonged circulation in the blood stream escaping the capture from macrophages and the accumulation at the tumor site by “passive targeting” through the enhanced permeability and retention effect as nanocarrier [10]. Moreover it shows high stability in normal cellular pH environment but degradable at acidic environment specially in tumor region which allows drug release [6, 7]. Another very important characteristic of nanosized bioapatite is its structural capacity to accept many ionic substitutions such as lanthanide ions as luminescent centers for offering an environment to sensitize the fluorescence of the dopant ions [11, 12].

The labeling or staining, especially the fluorescent labeling, has been demonstrated as an indispensable tool in the

study of complex biological interaction. Traditional fluorescence cell labeling procedures in cell biology were mainly based on organic dyes, fluorescent proteins, and lanthanide chelates, which were prone to problems such as short lifetime, broad spectrum profiles, poor photochemical stability and photobleaching thresholds, potential toxicity to the cells, and simultaneous detection of multiple signals [13]. Therefore last few decades a lot of investigations have been conducted to find novel biological luminescent labeling methods for medical diagnostics and targeted therapeutics applications. In this context, use of quantum dots for cell labeling achieves much more attentions [14]. However, the photoblinking and high cytotoxicity limited their application for cell labelling and they require surface modification for improving biocompatibility [15]. Rare earth doped apatite nanoparticles (REAnps) show several advantageous properties such as long fluorescence lifetime, high quantum yield, sharp emission peaks, color tuning depending on the ions doped, and good resistance to photobleaching from environmental and other factors [16]. Therefore REAnps are hopeful to become excellent cell labels.

In view of the growing interest in the lanthanide ions doped Anps for biomedical application, this review article will discuss apatite environment for holding RE ions, different procedures of preparation of Anp with rare earth ions, and biological application of luminescent Anps. Currently identified challenges for use REAnps in biological environment and perspectives of these nanoparticles are also discussed at the end of this review.

2. The Characteristics of the Lanthanide Doped Apatite Nanoparticles

The physical, chemical, and biological properties of apatite are controlled by its crystal structure and composition. One of the main characteristics of apatite is capable to be substituted by other metal ions for calcium ions, which can endue the new properties for apatite [17]. The elements in the lanthanide series have gained huge attention due to their unique optical characteristics, especially as a fluorophore in a variety of biological applications [18, 19]. Their unique optical properties arise from electronic transitions within the 4f shell or from 4f to 5d shell [20]. These fluorophores can absorb light of a specific wavelength and reemit a quantum of light with an energy corresponding to the energy difference between the excited state and the ground state [21]. The extreme stability of lanthanides is attributed to the electronic transitions occurring in the ions, as compared to the involvement of chemical bonds in organic fluorophores and fluorescent proteins. As a host material, apatite provides a crystal lattice, which can fit the dopant ions so that the ions are held tightly in the crystal. Recent progress in nanoscience has enabled scientist to develop new fluorescent rare earth doped inorganic nanomaterials as cell labels with the detectable and stable fluorescent signal for understanding the complex and dynamic biological interaction at the molecular level [22].

The presence of multiple metastable states in lanthanide ions makes them good candidates for upconversion. Due to

their unique characteristic of absorbing Near Infrared (NIR) light and emitting in the visible region paved way for their exploration in biological applications [23]. Upconversion is very well suited for biological application because NIR light does not excite any tissue components and hence there is almost zero background autofluorescence, which is especially advantageous in microscopic techniques. The use of NIR light for exciting the nanoparticles also offers high tissue penetration depth compared to Ultra Violet and visible light, enabling high resolution in vivo imaging. The phototoxicity from NIR is negligible [24]. REAnps show excellent photostability, chemical stability, and the thermal stability. Good photostability ensures long term tracking of these nanoparticles, which is not possible in conventional organic fluorescent labels with very quick photobleach. They also do not exhibit the phenomenon of “on-off” photoblinking, which is prevalent in quantum dots and causes the loss of information about the process under study when it is in an “off” state [25]. These particles can also be turned to emit various colors depending on the type of lanthanide dopant ions. The commonly used lanthanide ions for doping are Ce^{3+} , Pr^{3+} , Nd^{3+} , Sm^{3+} , Eu^{3+} , Tb^{3+} , Dy^{3+} , Er^{3+} , Tm^{3+} , and Yb^{3+} [26]. Additionally, the codoping of rare earth elements such as Eu^{3+} and Gd^{3+} can enhance the NIR emission and the luminescence intensity can be adjusted by changing the doping element ratio. The NIR emission is of low absorptivity by tissue chromophores and especially suitable for biological system [27].

Other than these luminescent properties, rare earth elements also lead to some changes about physical-chemical properties of apatite nanoparticles. For example, the doping of rare earth elements such as Eu^{3+} normally caused the size decrease in cross-section direction of needle-like hydroxyapatite crystals and inhibited the crystallinity of apatite [1]. These changes also influence the solubility as well as the biological properties of apatite to some extent. However, these are not the main content in this paper. So we do not discuss them here in detail.

3. Synthesis of REAnps

The biological properties of various Anps used in in vitro and in vivo applications are strongly depended on their structural characteristics [28]. Therefore, it is important to select suitable method to synthesize Anps for application at cellular level. There are two main approaches for the synthesis of nanoparticles called top-down and bottom-up. Top-down approach refers to break down of bulk materials to get a nanosized particles. Nanosized materials build up from the basic chemical reaction called as bottom-up approach [29]. Most of published researches normally use bottom-up approach to synthesize Anps for the biomedical application due to their potential ability to load various agents, that is, therapeutic, bioimaging, and so forth [30, 31]. According to the literature, there are several methods reported to prepare RE doped apatite particles for biomedical application such as solid state synthesis method, chemical precipitation method, and sol gel method.

3.1. Solid State Reaction. As a simple procedure, solid state reaction can be employed in the mass production of apatite particles. Generally the first procedure is to mix and mill the raw materials in solid state and then calcine the mixture at a very high temperature of more than 1000°C. This high calcination temperature leads to the formation of RE doped apatite with well crystallized structure [32,33]. However, solid state method is not suited for preparing REAnps because apatite particles generated from solid state method are usually large in size and irregular in shape. The relatively large particles are not easily internalized by living cells and cannot be used in biological application [29].

3.2. Coprecipitation Method. Nowadays, the precise preparation of nanoscale particles with controllable sizes and well defined morphologies remains a significantly challenging issue [34]. As a typical solution based approach, chemical precipitation method is identified as an effective and convenient way to prepare various apatite biomaterials with tunable architectures and morphologies, attributed to its mild reaction conditions, ease of operation, and large scale production capabilities [35]. Moreover, reaction can be performed at a number of synthesis ways involving diverse chemicals, apparatus, and using auxiliary additives. Various researches had discussed the effects of synthesis parameters such as temperature, time, reaction concentration, calcination procedures, and use of different reagents on the morphological properties of these nanoparticles.

The luminescent Eu^{3+} ion doped calcium hydroxyl apatite was prepared using a precipitation reaction followed by high calcined temperature (950°C) [36]. Although samples showed good luminescence, due to use of high temperature, the particle size of the crystals was large and not at nanoscale level, which was unfavorable for biological application. Subsequently, researchers focused on the effect of temperature on the particle size and luminescence property. Mondejar et al. obtained lanthanide doped nanoparticles by precipitation method. They used two different reaction temperatures of 37°C and 80°C and a calcined temperature of 1100°C. As a result of heat treatment, the thermal diffusion of the fluorescent ions to the crystallographic site of Ca^{2+} occurred and consequently a strong emission was achieved. According to the fluorescence emission, the sample calcined at 1100°C would be the most suitable one to be used as fluorescent labels due to its strong luminescence; however, the particle size of this sample is larger than 1 μm , which is not suitable for cellular uptake. In contrast, the particle size of the samples obtained at 37°C lies between 20 and 50 nm, but their fluorescence is weak. Therefore the nanocrystalline samples obtained at 80°C without additional heat treatment represent a good compromise between fluorescence and biologically necessary particle size [37].

Consequently, coprecipitation method without high temperature calcination attracted more attentions for preparing REAnps. Doat et al. synthesized europium doped Anps at 37°C by coprecipitation in water-ethanol medium. This apatite showed hydrogen phosphate ions rich, calcium

deficient, and poorly crystallized nanosized crystals which were similar to the mineral component of calcified tissues of living organisms and thus a biomimetic material [38]. Some researchers synthesized luminescent europium doped hydroxyapatite nanocrystals by coprecipitation method followed by a heating at temperature around 100°C [1, 11, 39]. They obtained biomimic apatitic particles with the best economical way.

In addition, the properties such as morphology and luminescence of REAnps can be controlled by coprecipitation method. Ciobanu et al. prepared europium doped hydroxyapatite nanocrystals using simple coprecipitation method at low temperature with different atomic ratios of Eu^{3+} and Ca^{2+} ions. According to their results Eu^{3+} has been successfully doped into hydroxy-Anps and doping Eu^{3+} ions little influence the ellipsoidal morphology [39]. However, other studies showed that as the Eu^{3+} concentration was increased to 20% the emission spectrum became broaden, suggesting that the doping inhibits the apatite crystal growth and/or causes lattice perturbations (microstrain) [1]. At low concentration of Eu^{3+} , the sample showed less intense Eu^{3+} related red emissions at 590 nm and 616 nm, whereas, with increased doping, the emission intensity was increased significantly with better spectral resolution. They emphasized that more efficient intensity was found at 700 nm in 2% and 3% of Eu^{3+} concentration [26]. Ternane et al. reported that Ce^{3+} luminescence in well characterized calcium borohydroxyapatite for different boron content and due to introduction of borate groups causes an increase in structural disorder and a shift of the emission bands to longer wavelengths resulting in sharp luminescence intensity [40].

3.3. Sol Gel Method. Sol gel offers advantages of molecular level mixing of reactants, improving the chemical homogeneity of the resulting powder, small crystal size ranging from 50 nm to 1 μm (depending on synthesis parameters), and excellent bioresorbability [41]. However only a few studies directly focused on the sol gel synthesis method because it is required to calcine the dried gel to remove the harmful component and form apatite crystals at high temperature [18, 42].

3.4. In-Situ and Ex-Situ Doping of RE. According to reported documents there are many strategies that have been employed to load rare earth element ions to nanosized apatite lattice. Generally, these strategies can be broadly summarized into two groups: doping RE ions during the synthesis of apatite nanoparticles called as in-situ doping and doping RE ions after synthesis of apatite nanoparticles called as ex-situ doping [43]. In-situ doping of RE ions in apatite is well documented in the literature and most of research works report synthesis method of lanthanide doped Anps is mainly using chemical precipitation method [32, 33, 37, 38, 44].

A careful survey of literature shows that only a few researchers have used ex-situ doping for synthesis RE labeled Anps [45–47]. They especially used ex-situ doping for apatite particles to make radiolabeled particles. However, the ex-situ

loading technique has generally a lower loading efficiency as compared to the in-situ techniques.

4. Biological Applications

Optical materials have much attention due to their importance in the fields of biology, chemistry, medical science, material science, and biotechnology. The performances of REAnps mainly depend on their morphologies, structure, and chemical compositions [48]. RE doped nanoparticles have been investigated in a wide range of biological applications such as imaging, immunocytochemistry, DNA detection. Fluorescence microscopy involves the visualization of cells or cellular components with subcellular resolution by labeling them with fluorescent probes [49].

Imaging of live cells and their various cellular components and tracking specific biomolecules are essential parts of cell and molecular biology. The REAnps show stable luminescence and possess NIR radiation. They provide a high signal to noise ratio, strong penetration ability, and less photo damage to the cell and tissue which has great advantages in cell and tissue imaging [50].

Han et al. demonstrated Eu^{3+} doped HAP nanoparticles for labeling of Bel-7402 human liver cancer cells. After internalization by cells they could observe strong green fluorescence and red fluorescence with excitation of blue light and green light, respectively, in the visible region. They also found that after 6.5 h incubation time the fluorescence intensity showed a trend to decline slowly due to activity of lysosome inside the cell, indicating that the intracellular degradation of apatite nanoparticles might be tracked by the change of fluorescence [43]. Therefore, they showed that Eu-HAP nanoparticles have the potential as valuable biocompatible fluorescent labeling material in biological studies.

Doat et al. showed europium doped apatitic tricalcium phosphate in human epithelial cells detected by confocal microscopy with the aid of its stable luminescence. Therefore these nanoparticles show interesting luminescent probe for observing the traffic and grafted biomolecules in cells [18]. Niu et al. and colleagues monitored strontium fluorapatite doped with Tb^{3+} or Eu^{3+} samples gives characteristics emissions even after the loading of organic drug molecules and they suggested its feasible possibility to be monitored or tracked during the drug release and disease therapy process [51]. RE doped Anps can be used as a tracking device for the particle and give an observable indication of agent delivery, while the nanoparticle can serve to protect the agent in vivo until it has reached the destination.

Anps have been explored in research as feasible delivery platforms for therapeutic applications. Hydroxyapatite (HAP) is of particular interest due to its appealing attributes such as interconnecting porosity of bulk material, good biocompatibility, resistance to mechanical force, and sustained release capacity. Thus, HAP nanoparticles are actively being investigated for drug delivery [27, 52], gene and siRNA delivery [53], and immunoadjuvant therapy. And also HAP nanoparticles can deliver therapeutic drugs, antigens, and

proteins without degradation and can release them in proper place at a slow rate [54]. And also it can be functionalized with special characteristics for qualitative or quantitative detection of tumor cells [55]. Chen et al. and group developed Eu^{3+} and Gd^{3+} dual doped calcium phosphate in the presence of amphiphilic block copolymer and demonstrated imaging and drug release capacity. They showed their hybrid material can be used as the drug nanocarriers and have a high drug loading capacity and ultralong sustained drug release using ibuprofen as a model drug, and the drug release from the drug delivery system can sustain for a very long period of time more than 80 days [27]. REAnps have been applied as nonviral carriers for drug delivery and gene therapy. After loading with genes or drugs, REAnps provide a protective environment that shields them from degradation while providing a convenient pathway for cell membrane penetration and controlled release of the genes and drugs. The experimental results proved that Anp possessed a higher penetration rate into cell membrane and their transfection efficiency could be 25-fold higher than that of the micron-sized particles [4].

5. Conclusion and Perspectives

To optimize and achieve better performances, controlling the structure and size of nanostructured apatite materials has become a hot field. This account summarizes some recent progress on the synthesis, properties, and application of lanthanide doped Anps. Up to now, many synthesis methods have been reported and in-situ precipitation method is identified as effective method. Frequently to obtain well diffused RE ion in apatite structure, precipitation method followed by high temperature around 1000°C is required. But this much of high temperature causes production of large particle size of apatite particles and it may not interline with biological applications. Because research on lanthanide doped apatite particles is still in its infancy, many of the efficient synthesis procedures are yet to be discovered. Currently some of investigators try to use macromolecular such as PEI (polyethyleneimine), DNA, PEG (polyethylene glycol), and PAA (polyacrylic acid) to eliminate use of high temperature step and obtain well diffused RE ions in apatite structure. But further experiments are required to select the most appropriate stabilizer for this.

Also there is growing interest in the trace method of luminescent Anps within biological system. Luminescent property of the lanthanide ions can be used to trace Anps within the biological system. There are more experiments conducted to check cytotoxicity of Anp at the cellular level and fortunately they still could obtain positive results. But further investigation should find out biodistribution and final destination of these particles. Additionally, due to their excellent favorable osteoconductive and bioactive properties, Anps are preferred as the inorganic component of composite biomaterials [56, 57], which are valuable for bone grafting and drug delivery. So, REAnp in the composite biomaterials might be used as contrast agent to monitor the bone regeneration in vivo. On the other hand there are a number of

challenges ahead in the practical applications of REAnps such as the luminescent efficiency, biological compatibility, and stability within biological systems.

Conflict of Interests

The authors declare that there is no conflict of interests regarding the publication of this paper.

Acknowledgments

This work was supported by the National Natural Science Foundation of China (51002109, 81190133, and 51172171), the Fundamental Research Funds for the Central Universities (WUT: 2014-IV-121, 2014-VII-028), and the project supported by State Key Laboratory of Advanced Technology for Materials Synthesis and Processing (Wuhan University of Technology).

References

- [1] C. S. Ciobanu, F. Massuyeau, E. Andronescu, M. S. Stan, A. Dinischiotu, and D. Predoi, "Biocompatibility study of europium doped crystalline hydroxyapatite bioceramics," *Digest Journal of Nanomaterials and Biostructures*, vol. 6, no. 4, pp. 1639–1647, 2011.
- [2] C. S. Ciobanu, C. L. Popa, and D. Predoi, "Sm:HAp nanopowders present antibacterial activity against *Enterococcus faecalis*," *Journal of Nanomaterials*, vol. 2014, Article ID 780686, 9 pages, 2014.
- [3] Z. Li, M.-M. Zhou, and W. Lin, "The research of nanoparticle and microparticle hydroxyapatite amendment in multiple heavy metals contaminated soil remediation," *Journal of Nanomaterials*, vol. 2014, Article ID 168418, 8 pages, 2014.
- [4] S. V. Dorozhkin, "Nanodimensional and nanocrystalline calcium orthophosphates," *American Journal of Biomedical Engineering*, vol. 2, no. 3, pp. 48–97, 2012.
- [5] R. Z. LeGeros and J. P. LeGeros, "Calcium phosphate bioceramics: past, present and future," *Key Engineering Materials*, vol. 240–242, pp. 3–10, 2003.
- [6] S. Tada, E. H. Chowdhury, C.-S. Cho, and T. Akaike, "pH-sensitive carbonate apatite as an intracellular protein transporter," *Biomaterials*, vol. 31, no. 6, pp. 1453–1459, 2010.
- [7] E. V. Giger, J. Puigmartí-Luis, R. Schlatter, B. Castagner, P. S. Dittrich, and J.-C. Leroux, "Gene delivery with bisphosphonate-stabilized calcium phosphate nanoparticles," *Journal of Controlled Release*, vol. 150, no. 1, pp. 87–93, 2011.
- [8] M.-Z. Yin, Y.-C. Han, I. W. Bauer, P. Chen, and S.-P. Li, "Effect of hydroxyapatite nanoparticles on the ultrastructure and function of hepatocellular carcinoma cells *in vitro*," *Biomedical Materials*, vol. 1, no. 1, pp. 38–41, 2006.
- [9] M. Yin, Y. Yin, Y. Han, H. Dai, and S. Li, "Effects of uptake of hydroxyapatite nanoparticles into hepatoma cells on cell adhesion and proliferation," *Journal of Nanomaterials*, vol. 2014, Article ID 731897, 7 pages, 2014.
- [10] Y. Chen and H. Liang, "Applications of quantum dots with upconverting luminescence in bioimaging," *Journal of Photochemistry and Photobiology B: Biology*, vol. 135, pp. 23–32, 2014.
- [11] I. Mayer, J. D. Layani, A. Givan, M. Gaft, and P. Blanc, "La ions in precipitated hydroxyapatites," *Journal of Inorganic Biochemistry*, vol. 73, no. 4, pp. 221–226, 1999.
- [12] P. Martin, G. Carlot, A. Chevarier, C. Den-Auwer, and G. Panczer, "Mechanisms involved in thermal diffusion of rare earth elements in apatite," *Journal of Nuclear Materials*, vol. 275, no. 3, pp. 268–276, 1999.
- [13] F. Wang, W. B. Tan, Y. Zhang, X. Fan, and M. Wang, "Luminescent nanomaterials for biological labelling," *Nanotechnology*, vol. 17, no. 1, pp. R1–R13, 2006.
- [14] O. Akinfiyeva, I. Nabiev, and A. Sukhanova, "New directions in quantum dot-based cytometry detection of cancer serum markers and tumor cells," *Critical Reviews in Oncology/Hematology*, vol. 86, no. 1, pp. 1–14, 2013.
- [15] S. Ranjbarvaziri, S. Kiani, A. Akhlaghi, A. Vosough, H. Baharvand, and N. Aghdami, "Quantum dot labeling using positive charged peptides in human hematopoietic and mesenchymal stem cells," *Biomaterials*, vol. 32, no. 22, pp. 5195–5205, 2011.
- [16] M. Manoharan, "Research on the frontiers of materials science: the impact of nanotechnology on new material development," *Technology in Society*, vol. 30, no. 3–4, pp. 401–404, 2008.
- [17] J. Rakovan and R. J. Reeder, "Intracrystalline rare earth element distributions in apatite: surface structural influences on incorporation during growth," *Geochimica et Cosmochimica Acta*, vol. 60, no. 22, pp. 4435–4445, 1996.
- [18] A. Doat, M. Fanjul, F. Pellé, E. Hollande, and A. Lebugle, "Europium-doped bioapatite: a new photostable biological probe, internalizable by human cells," *Biomaterials*, vol. 24, no. 19, pp. 3365–3371, 2003.
- [19] B. Basar, A. Tezcaner, D. Keskin, and Z. Evis, "Improvements in microstructural, mechanical, and biocompatibility properties of nano-sized hydroxyapatites doped with yttrium and fluoride," *Ceramics International*, vol. 36, no. 5, pp. 1633–1643, 2010.
- [20] H. Bazin, M. Préaudat, E. Trinquet, and G. Mathis, "Homogeneous time resolved fluorescence resonance energy transfer using rare earth cryptates as a tool for probing molecular interactions in biology," *Spectrochimica Acta A: Molecular and Biomolecular Spectroscopy*, vol. 57, no. 11, pp. 2197–2211, 2001.
- [21] J. G. Bünzli, S. Comby, A.-S. Chauvin, and C. D. B. Vandevyver, "New opportunities for lanthanide luminescence," *Journal of Rare Earths*, vol. 25, no. 3, pp. 257–274, 2007.
- [22] Y. Lü, Y. Li, D. Zhao, L. Zhang, and S. Zhong, "Uniform YF₃ nanorods: synthesis, luminescent properties and cytotoxicity study," *Journal of Rare Earths*, vol. 29, no. 11, pp. 1036–1039, 2011.
- [23] F. Wang and X. Liu, "Recent advances in the chemistry of lanthanide-doped upconversion nanocrystals," *Chemical Society Reviews*, vol. 38, no. 4, pp. 976–989, 2009.
- [24] J. H. Rao, A. Dragulescu-Andrasi, and H. Q. Yao, "Fluorescence imaging *in vivo*: recent advances," *Current Opinion in Biotechnology*, vol. 18, no. 1, pp. 17–25, 2007.
- [25] E. Chang, N. Thekkekk, W. W. Yu, V. L. Colvin, and R. Drezek, "Evaluation of quantum dot cytotoxicity based on intracellular uptake," *Small*, vol. 2, no. 12, pp. 1412–1417, 2006.
- [26] R. Reisfeld, M. Gaft, G. Boulon, C. Panczer, and C. K. Jørgensen, "Laser-induced luminescence of rare-earth elements in natural fluor-apatites," *Journal of Luminescence*, vol. 69, no. 5–6, pp. 343–353, 1996.
- [27] F. Chen, P. Huang, Y. J. Zhu, J. Wu, and D. X. Cui, "Multi-functional Eu³⁺/Gd³⁺ dual doped calcium phosphate vesicle like nanospheres for sustained drug release and imaging," *Biomaterials*, vol. 33, pp. 6447–6455, 2012.
- [28] D. Gopi, S. Ramya, D. Rajeswari, P. Karthikeyan, and L. Kavitha, "Strontium, cerium co-substituted hydroxyapatite nanoparticles: synthesis, characterization, antibacterial activity towards

- prokaryotic strains and in vitro studies," *Colloids and Surfaces A: Physicochemical and Engineering Aspects*, vol. 451, no. 1, pp. 172–180, 2014.
- [29] S. C. J. Loo, T. Moore, B. Banik, and F. Alexis, "Biomedical applications of hydroxyapatite nanoparticles," *Current Pharmaceutical Biotechnology*, vol. 11, no. 4, pp. 333–342, 2010.
- [30] J. Gómez-Morales, M. Iafisco, J. M. Delgado-López, S. Sarda, and C. Drouet, "Progress on the preparation of nanocrystalline apatites and surface characterization: overview of fundamental and applied aspects," *Progress in Crystal Growth and Characterization of Materials*, vol. 59, no. 1, pp. 1–46, 2013.
- [31] S. V. Dorozhkin, "Nanosized and nanocrystalline calcium orthophosphates," *Acta Biomaterialia*, vol. 6, no. 3, pp. 715–734, 2010.
- [32] R. El Ouenzerfi, N. Kbir-Ariguib, M. Trabelsi-Ayedi, and B. Piriou, "Spectroscopic study of Eu^{3+} in strontium hydroxyapatite $\text{Sr}_{10}(\text{PO}_4)_6(\text{OH})_2$," *Journal of Luminescence*, vol. 85, no. 1–3, pp. 71–77, 1999.
- [33] Y. Han, X. Wang, H. Dai, and S. Li, "Synthesis and luminescence of Eu^{3+} doped hydroxyapatite nanocrystallines: effects of calcinations and Eu^{3+} content," *Journal of Luminescence*, vol. 135, pp. 281–287, 2013.
- [34] G. Wang, Q. Peng, and Y. Li, "Lanthanide-doped nanocrystals: synthesis, optical-magnetic properties, and applications," *Accounts of Chemical Research*, vol. 44, no. 5, pp. 322–332, 2011.
- [35] M. Sadat-Shojai, M. T. Khorasani, E. Dinpanah-Khoshdargi, and A. Jamshidi, "Synthesis methods for nanosized hydroxyapatite with diverse structures," *Acta Biomaterialia*, vol. 9, no. 8, pp. 7591–7621, 2013.
- [36] R. Ternane, M. Trabelsi-Ayedi, N. Kbir-Ariguib, and B. Piriou, "Luminescent properties of Eu^{3+} in calcium hydroxyapatite," *Journal of Luminescence*, vol. 81, no. 3, pp. 165–170, 1999.
- [37] S. P. Mondéjar, A. Kovtun, and M. Epple, "Lanthanide-doped calcium phosphate nanoparticles with high internal crystallinity and with a shell of DNA as fluorescent probes in cell experiments," *Journal of Materials Chemistry*, vol. 17, no. 39, pp. 4153–4159, 2007.
- [38] A. Doat, F. Pellé, N. Gardant, and A. Lebugle, "Synthesis of luminescent bioapatite nanoparticles for utilization as a biological probe," *Journal of Solid State Chemistry*, vol. 177, no. 4–5, pp. 1179–1187, 2004.
- [39] C. S. Ciobanu, S. L. Iconaru, F. Massuyeau, L. V. Constantin, A. Costescu, and D. Predoi, "Synthesis, structure, and luminescent properties of europium-doped hydroxyapatite nanocrystalline powders," *Journal of Nanomaterials*, vol. 2012, Article ID 942801, 9 pages, 2012.
- [40] R. Ternane, M. T. Cohen-Adad, G. Panczer et al., "Structural and luminescent properties of new Ce^{3+} doped calcium borophosphate with apatite structure," *Solid State Sciences*, vol. 4, no. 1, pp. 53–59, 2002.
- [41] M. H. Fathi and A. Hanifi, "Evaluation and characterization of nanostructure hydroxyapatite powder prepared by simple sol-gel method," *Materials Letters*, vol. 61, no. 18, pp. 3978–3983, 2007.
- [42] Y. Han, X. Wang, S. Li, and X. Ma, "Synthesis of terbium doped calcium phosphate nanocrystalline powders by citric acid sol-gel combustion method," *Journal of Sol-Gel Science and Technology*, vol. 49, no. 1, pp. 125–129, 2009.
- [43] Y. Han, X. Wang, and S. Li, "Biocompatible europium doped hydroxyapatite nanoparticles as a biological fluorescent probe," *Current Nanoscience*, vol. 6, no. 2, pp. 178–183, 2010.
- [44] A. Ashokan, D. Menon, S. Nair, and M. Koyakutty, "A molecular receptor targeted, hydroxyapatite nanocrystal based multimodal contrast agent," *Biomaterials*, vol. 31, no. 9, pp. 2606–2616, 2010.
- [45] S. Chakraborty, T. Das, H. D. Sarma, M. Venkatesh, and S. Banerjee, "Preparation and preliminary studies on ^{177}Lu -labeled hydroxyapatite particles for possible use in the therapy of liver cancer," *Nuclear Medicine and Biology*, vol. 35, no. 5, pp. 589–597, 2008.
- [46] U. Pandey, K. Bapat, H. D. Sarma et al., "Bioevaluation of ^{90}Y -labeled particles in animal model of arthritis," *Annals of Nuclear Medicine*, vol. 23, no. 4, pp. 333–339, 2009.
- [47] T. Das, S. Chakraborty, H. D. Sarma, M. Venkatesh, and S. Banerjee, " ^{166}Ho -labeled hydroxyapatite particles: A possible agent for liver cancer therapy," *Cancer Biotherapy and Radiopharmaceuticals*, vol. 24, no. 1, pp. 7–14, 2009.
- [48] F. Chen, Y. Zhu, J. Wu, P. Huang, and D. Cui, "Nanostructured calcium phosphates: preparation and their application in biomedicine," *Nano Biomedicine and Engineering*, vol. 4, no. 1, pp. 41–49, 2012.
- [49] M. Tourbin, A. Al-Kattan, and C. Drouet, "Study on the stability of suspensions based on biomimetic apatites aimed at biomedical applications," *Powder Technology*, vol. 255, pp. 17–22, 2014.
- [50] I. R. Corrêa, "Live-cell reporters for fluorescence imaging," *Current Opinion in Chemical Biology*, vol. 20, pp. 36–45, 2014.
- [51] N. Niu, D. Wang, S. Huang et al., "Controlled synthesis of luminescent F-substituted strontium hydroxyapatite with hierarchical structures for drug delivery," *CrystEngComm*, vol. 14, no. 5, pp. 1744–1752, 2012.
- [52] H. T. Ong, J. S. C. Loo, F. Y. C. Boey, S. J. Russell, J. Ma, and K.-W. Peng, "Exploiting the high-affinity phosphonate-hydroxyapatite nanoparticle interaction for delivery of radiation and drugs," *Journal of Nanoparticle Research*, vol. 10, no. 1, pp. 141–150, 2008.
- [53] Y. Kakizawa, S. Furukawa, and K. Kataoka, "Block copolymer-coated calcium phosphate nanoparticles sensing intracellular environment for oligodeoxynucleotide and siRNA delivery," *Journal of Controlled Release*, vol. 97, no. 2, pp. 345–356, 2004.
- [54] Y. T. Li, M. J. Chua, A. P. Kunnath, and E. H. Chowdhury, "Reversing multidrug resistance in breast cancer cells by silencing ABC transporter genes with nanoparticle-facilitated delivery of target siRNAs," *International Journal of Nanomedicine*, vol. 7, pp. 2473–2481, 2012.
- [55] A. Al-Kattan, S. Girod-Fullana, C. Charvillat et al., "Biomimetic nanocrystalline apatites: emerging perspectives in cancer diagnosis and treatment," *International Journal of Pharmaceutics*, vol. 423, no. 1, pp. 26–36, 2012.
- [56] M. Fikai, E. Andronescu, D. Fikai, G. Voicu, and A. Fikai, "Synthesis and characterization of COLL-PVA/HA hybrid materials with stratified morphology," *Colloids and Surfaces B: Biointerfaces*, vol. 81, no. 2, pp. 614–619, 2010.
- [57] A. Fikai, E. Andronescu, G. Voicu, C. Ghitulica, and D. Fikai, "The influence of collagen support and ionic species on the morphology of collagen/hydroxyapatite composite materials," *Materials Characterization*, vol. 61, no. 4, pp. 402–407, 2010.

Research Article

Generation of Porous Alumina Layers in a Polydimethylsiloxane/Hydrogen Peroxide Medium on Aluminum Substrate in Corona Discharges

A. Groza,¹ A. Surmeian,¹ C. Diplasu,¹ C. Luculescu,¹ C. Negrila,² and M. Ganciu¹

¹ National Institute of Lasers, Plasma and Radiation Physics, Magurele, 077125 Bucharest, Romania

² National Institute for Materials Physics, Magurele, 077125 Bucharest, Romania

Correspondence should be addressed to A. Groza; andreea@infim.ro

Received 2 July 2014; Accepted 1 August 2014; Published 3 September 2014

Academic Editor: Daniela Predoi

Copyright © 2014 A. Groza et al. This is an open access article distributed under the Creative Commons Attribution License, which permits unrestricted use, distribution, and reproduction in any medium, provided the original work is properly cited.

The porous alumina (Al_2O_3) layer obtained at the interface between polydimethylsiloxane/hydrogen peroxide medium and aluminum substrate under charged and neutral species injection produced in negative corona discharges in air at atmospheric pressure is analyzed by different methods in this paper. The scanning electron microscopy investigations showed the uniform distribution of the pores formed in the alumina layer and their columnar structures. Both energy dispersive X-ray spectroscopy (EDS) and X-ray photoelectron spectroscopy (XPS) measurements indicate that during the anodization process of the aluminum in the polydimethylsiloxane/hydrogen peroxide medium in corona discharge the incorporation of silicon in the structure of the alumina layer is possible.

1. Introduction

The porous alumina (Al_2O_3) layers are aluminum oxide films consisting of cylindrical pores arranged parallel to each other.

By conventional methods, these layers are prepared by an anodization process, namely, the electrochemical oxidation of aluminum films in acid reactive medium under direct current conditions. Although the chemical and physical aspects of this process are not completely understood, it is generally accepted that the porous form of the alumina layer is produced in two steps: (a) growth of an aluminum oxide at the alumina/Al interface due to the counter migration of Al^{3+} , OH^- , and O^{2-} ions and (b) dissolution of aluminum oxide at alumina film/solution interface [1].

Recent research studies in the field of anodization methods of aluminum were directed toward alternative methods for the generation of alumina layers, namely, corona discharge treatments [2]. Running of these kinds of discharges in air at atmospheric pressure has the unique advantage of simultaneous production of charged (negative or positive

ions) and neutral (e.g., O_3) species of oxygen known for their reactive character in the interaction with materials.

Over the time, alumina layers have been intensely studied due to their widespread application in corrosion protection for aerospace, automotive, architectural, or packaging [2]. Their nontoxic and biocompatible properties make them also attractive for biotechnological applications [3]. Alumina nanoparticles can be trapped and studied in electromagnetic fields [4, 5] and are of great interest for their antimicrobial activity and their possible clinical applications [6].

As substrates, porous anodic Al oxide layers can improve the adherence of different types of thin layers [7–9]. On the other hand, a PDMS layer deposited on an anodized porous Al oxide layer [10] could act as an effective barrier preventing the contact of water based corrosive media with the underlying metallic surfaces [11, 12].

In our previous papers, we showed that, during the polymerization of a polydimethylsiloxane (PDMS) liquid film lying on the surface of an aluminum substrate in corona discharge, an Al oxide layer is generated at polymer/substrate

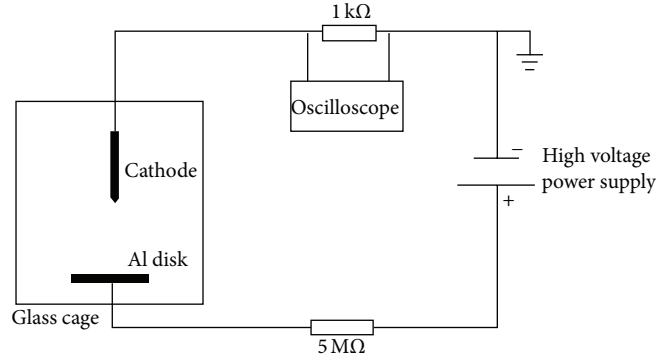


FIGURE 1: Experimental setup.

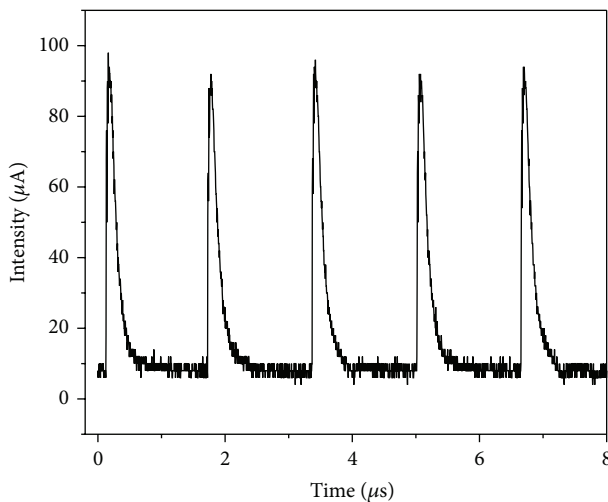


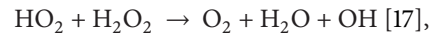
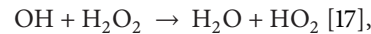
FIGURE 2: Waveform of the discharge current in the Trichel pulse regime.

interface [10]. The OH and Si-OH groups present at polymer/substrate interface determine the formation of Si-O-Al bonds announcing the possibility of counter migration of Si and Al atoms. The aluminum oxide layer has porous structure, the pores having a nonuniform distribution on the alumina layer [13]. The dependence of the pores structure on the corona discharge current values [14, 15] and the formation of the Si-O-Al bonds evidenced the existence of an anodization process at polymer/Al substrate interface.

Responsible for oxidation of the Al surface in negative corona discharge are the negative ions of oxygen (O_2^- , O_3^- , O_4^- , CO_2^- , and CO_3^-), the water, and consequently the OH radicals present either in liquid or in solid film further formed on the substrate due to the PDMS polymerization process [10]. Even these species are able to generate an anodization process of the Al in a similar way with the classical one; the nonuniform distribution of the pores structure in the alumina layer suggests that the experimental conditions need further improvements.

In this paper, we report for the first time a uniform distribution of the pores in the alumina layer generated

in corona discharge operating conditions by mixing the hydroxyl terminated PDMS liquid precursor with hydrogen peroxide (H_2O_2). In this way, the water molecules and the density of OH radicals at Al substrate interface are enhanced, knowing that hydrogen peroxide can be involved in the following reactions:



The morphology, the elemental composition, and the processes which determine the porous alumina layer formation in negative corona discharge in the presence of a PDMS/ H_2O_2 chemical medium are investigated by scanning electron microscopy (SEM), electron dispersion spectroscopy (EDS), and X-ray photoelectron spectroscopy (XPS).

2. Materials and Methods

2.1. Description of the Experimental Conditions Used for the Generation of the Porous Alumina Layers. The experimental setup used for the operating of the negative corona discharge in a Trichel pulse regime is presented in Figure 1. It consists in a point to plane corona discharge electrode configuration, the distance between electrodes being 10 mm. The cathode is a 20 mm tungsten wire placed perpendicular to the centre of the anode (plane electrode) in a glass cage in air at atmospheric pressure. As anode, we used an Al disk electrode with a diameter of 10 mm. A high voltage of 11 kV was applied between electrodes, through a resistor of 5 MΩ, the mean value of the discharge current being 40 μA.

The negative ions of oxygen O_2^- , O_3^- , O_4^- , CO_2^- , and CO_3^- produced in the Trichel regime of the negative corona discharge in the vicinity of the cathode [18] travel to the anode in regular packages. The transport of these particles through the interelectrode gap have a pulsating nature due to the periodical character of positive/negative ions production respectively destruction processes occurring at the cathode. Thus, the corona discharge current, Figure 2, is formed by regular pulses with a period of about 1.5 μs.

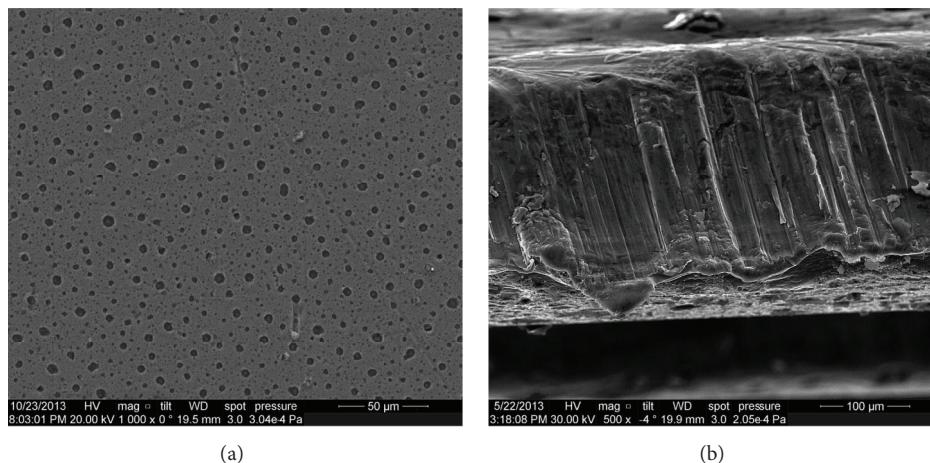


FIGURE 3: SEM images of (a) porous anodic Al oxide layer and (b) transversal section of the alumina layer.

Due to the uniformity of the current density distribution on the anode surface and to the O_2^- , O_3^- , O_4^- , CO_2^- , and CO_3^- negative ions production, the Trichel pulse regime of the corona discharge is proper to be used for thin film generation [10]. It was shown [19] that, in a Trichel pulse regime, the distribution of the current density on the plane electrode is uniform on a circular surface with a radius given by the relation $r = \sqrt{3d}$, where d is the interelectrode gap. In our experimental conditions $r = 17.2$ mm.

Previously [10], we showed that a drop of $0.1 \mu\text{L}$ hydroxyl terminated polydimethylsiloxane (PDMS) liquid precursor stretched on an Al substrate in negative corona discharge is transformed into a solid polymer layer after 2 hours. As a result of the polymerization process, water molecules are generated in the PDMS layer. They can be decomposed under the influence of corona electric fields and associated charges injection generating OH radicals in the polymer. The Si-OH groups present also in the PDMS layer have proved their utility in the generation of Si-O-Al bonds at polymer/Al substrate interface. In the same time, at polymer/Al substrate interface an anodization process occurs. The negative ions of oxygen produced in corona discharge, the water molecules and the OH groups resulting as byproducts of the polymerization process [10] are mainly responsible for the alumina layer formation.

In experimental conditions described above, we placed a $10 \mu\text{L}$ of liquid precursor on an optical polished Al substrate (anode). This liquid precursor contains a proportion of 33% PDMS with hydroxyl end groups and 67% hydrogen peroxide (H_2O_2). The addition of H_2O_2 to the PDMS liquid precursor does not change the electrical regime of the corona discharge and its optical characteristics. Under negative corona charge injection, the stretch of the PDMS liquid assures the uniform covering of the substrate with the H_2O_2 . The further decomposition of H_2O_2 in negative corona discharge produced in air gives an enhanced infusion of water molecules and OH radicals at the surface of the Al substrate.

The solid layer formed after 5 hours of irradiation in negative corona discharge of the PDMS/ H_2O_2 has been

chemically removed. Thus, the anodization processes of the Al substrate were revealed through the morphology and elemental composition analysis of porous anodic Al oxide layer.

2.2. SEM Measurements. The morphology of the alumina layers has been investigated using a FEI Inspect S scanning electron microscope in both high- and low-vacuum modes.

2.3. EDS Measurements. Elemental composition analysis was performed by energy dispersive X-ray spectroscopy using an EDAX Inc. SiLi detector attached inside the scanning electron microscope. The measurements were performed at a voltage of 10 kV.

2.4. XPS Measurements. The X-ray photoelectron spectroscopy (XPS) measurements were performed using a VG ESCA 3 MK II XPS installation ($E_{K\alpha} = 1486.7$ eV). The vacuum analysis chamber pressure was $p = 3 \times 10^{-8}$ torr. The XPS recorded spectrum involved an energy window $w = 20$ eV with the resolution $R = 50$ eV with 256 recording channels. The XPS spectra were processed using Spectral Data Processor v 2.3 (SDP) software. The measured binding energy (BE) scale was referenced to a C 1s peak at the BE value of 284.8 eV [20]. The accuracy for BE assignments is ± 0.2 eV.

3. Results and Discussions

3.1. SEM Investigations. In our previous papers [10, 14, 15] we showed that the pores formed into the alumina layer during the polymerization process of the PDMS liquid precursor on Al substrate in negative corona discharge do not present uniform and regular structures.

In the present paper, by matching the current intensity ($40 \mu\text{A}$) with the liquid precursor's composition (33% PDMS with hydroxyl end groups and 67% H_2O_2) and with the operating time of the negative corona discharge (5 hours), we succeed to generate a uniform distribution of the pores

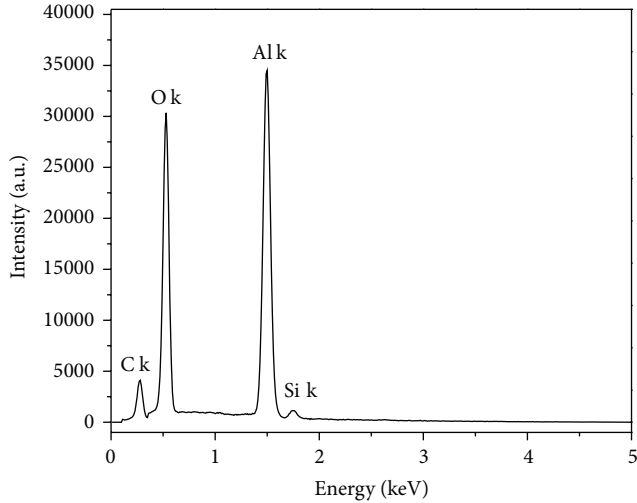


FIGURE 4: EDS spectrum of porous anodic Al oxide layer.

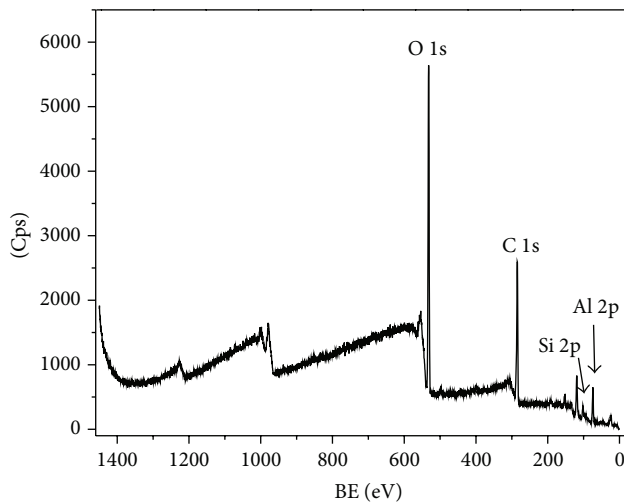


FIGURE 5: XPS wide scan energy spectrum of the alumina layer.

in the anodic Al oxide layer, Figure 3(a). The columnar structure of these pores is revealed in Figure 3(b). Thus, under the experimental conditions presented above, the uniform injection of the negative oxygen ions into a liquid/layer rich in water molecules and OH groups is proper for the generation in a controllable manner of an advanced anodization process (columnar structure formation [20]) of the Al substrate.

3.2. EDS Investigations. The establishment of the elements contained in the porous alumina layer is important in order to determine the mechanisms responsible for the anodization of the Al substrate.

In Figure 4, the EDS spectrum of the porous anodic Al oxide layer displayed in Figure 3 is presented. It can be observed that, besides the peaks of Al and O, a peak char-

acteristic to Si atoms appears in this spectrum. As in the SEM image from Figure 3(a), there are no residual pieces of polymer on the surface of porous Al oxide layer; it means that during the anodization process of the substrate the Si atoms are incorporated into the anodic Al oxide layer

3.3. XPS Investigations. The chemical processes induced by the PDMS/H₂O₂ into the Al substrate were investigated by X-ray photoelectron spectroscopy (XPS) measurements.

The XPS spectrum of the porous anodic Al oxide layer is displayed in Figure 5.

In order to better reveal the processes that take place during the anodization of Al substrate in corona discharge in the presence of PDMS/H₂O₂, we applied a peak fitting analysis for the experimental bands specific to the Al 2p, Si 2p, and O 1s XPS peaks. For each peak, we used as fitted curve a Gaussian type profile curve.

The experimental XPS bands characteristic to Al 2p, Si 2p, and O 1s together with the fitted curves are presented in Figure 6. The intensity of the deconvoluted XPS band from 73.6 eV belonging to Al₂O₃ [21] is almost the same with that one located at 74.9 eV and assigned to aluminosilicates (Al₂SiO₅), Figure 6(a) [22].

The deconvolution of the Si 2p XPS peak reveals the nature of the Si incorporated into the anodic Al oxide porous layer. The presence of the 99.8 eV (Si), 101.3 eV (SiO) [23], 102.8 eV (Al₂SiO₅) [24], and 104.2 eV (SiO₂) [25] XPS bands in the Si 2p spectrum from Figure 6(b) indicates how Si atoms are linked in the porous anodic Al oxide layer.

Two fitted peaks located at 530.7 eV and 532.1 eV were observed in the high resolution XPS spectrum of O 1s shown in Figure 6(c). This certified the formation of Al-O-Si bonds [26], respectively, of the Al₂O₃ [27].

The XPS and EDS measurements presented above are in good agreement with one another showing that Si atoms (coming from PDMS/H₂O₂ medium) can be incorporated into the porous alumina layer. This result can be understood if we consider that in a classical electrochemical anodization process there are two stages in the pores formation due to the competing oxidation and dissolution processes: (a) the growth of aluminum oxide due to the counter migration of Al³⁺, OH⁻, and O²⁻ ions and (b) the dissolution of aluminum oxide at the interface between the alumina film and solution [1, 20].

4. Conclusions

In this paper, we report for the first time the formation of a porous anodic Al oxide layer in negative corona discharge in the presence of the PDMS/H₂O₂ lying on the surface of the Al substrate. This process is favored by the enhanced infusion of H₂O and OH radicals, respectively, by the negative ions of oxygen and neutral species (O₃) produced in negative corona discharge in air at atmospheric pressure. The OH radicals are produced at PDMS/H₂O₂/substrate interface as a result of the H₂O₂ and H₂O decomposition.

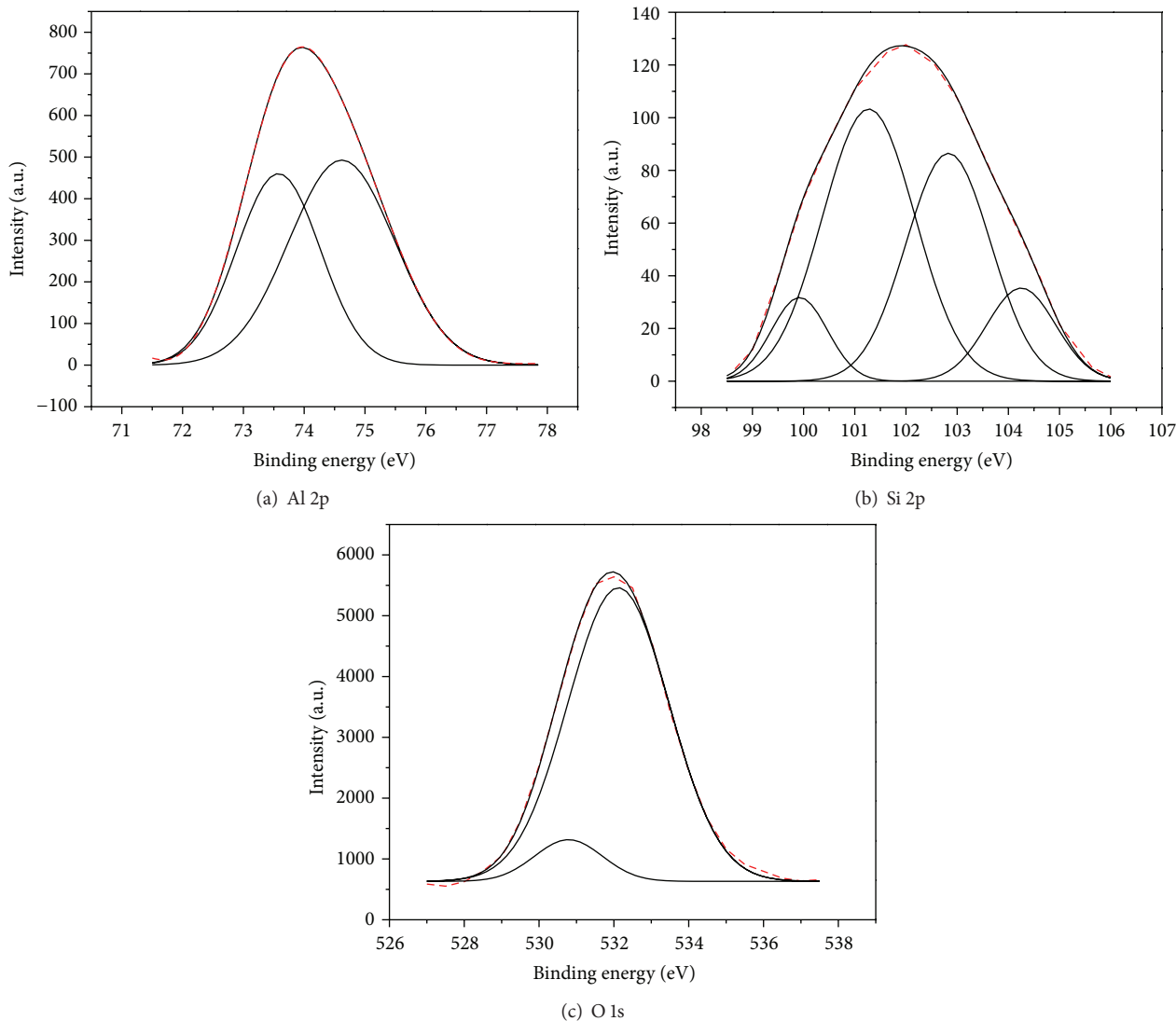


FIGURE 6: High resolution XPS spectra for (a) Al 2p, (b) Si 2p, and (c) O 1s peaks. The experimental curve is plotted in black and the theoretical fitted curve is in red dot line.

The pores present a uniform distributed structure on the surface and in the bulk of the alumina layer as the SEM analysis shows.

The XPS and EDS measurements indicate that during the pores formation mechanism the Si atoms coming from the PDMS are incorporated into the porous anodic Al oxide layer in an Al_2SiO_5 structure.

Conflict of Interests

The authors declare that there is no conflict of interests regarding the publication of this paper.

Acknowledgment

This work was supported by the PN-II-ID-PCE-2011-3-0958 and PT-PCCA-2011-3.1-1136 UEFISCDI projects.

References

- [1] Z. Wu, C. Richter, and L. Menon, "A study of anodization process during pore formation in nanoporous alumina templates," *Journal of the Electrochemical Society*, vol. 154, no. 1, pp. E8–E12, 2007.
- [2] D. Minzari, P. Møller, P. Kingshott, L. H. Christensen, and R. Ambat, "Surface oxide formation during corona discharge treatment of AA 1050 aluminium surfaces," *Corrosion Science*, vol. 50, no. 5, pp. 1321–1330, 2008.
- [3] C. J. Ingham, J. ter Maat, and W. M. de Vos, "Where bio meets nano: the many uses for nanoporous aluminum oxide in biotechnology," *Biotechnology Advances*, vol. 30, no. 5, pp. 1089–1099, 2012.
- [4] B. M. Mihalcea, "Nonlinear harmonic boson oscillator," *Physica Scripta*, vol. 140, Article ID 014056, 2010.
- [5] B. M. Mihalcea, "Quantum parametric oscillator in a radiofrequency trap," *Physica Scripta*, vol. 135, Article ID 014006, 2009.

- [6] I. M. Sadiq, B. Chowdhury, N. Chandrasekaran, and A. Mukherjee, "Antimicrobial sensitivity of *Escherichia coli* to alumina nanoparticles," *Nanomedicine: Nanotechnology, Biology, and Medicine*, vol. 5, no. 3, pp. 282–286, 2009.
- [7] S. L. Iconaru, P. Chapon, P. Le Coustumer, and D. Predoi, "Antimicrobial activity of thin solid films of silver doped hydroxyapatite prepared by sol-gel method," *The Scientific World Journal*, vol. 2014, Article ID 165351, 8 pages, 2014.
- [8] C. S. Ciobanu, C. L. Popa, and D. Predoi, "Sm:HAp nanoparticles present antibacterial activity against *Enterococcus faecalis*," *Journal of Nanomaterials*, vol. 2014, Article ID 780686, 9 pages, 2014.
- [9] C. S. Ciobanu, S. L. Iconaru, P. Chapon, and D. Predoi, "Antimicrobial activity of silver doped hydroxyapatite thin films," *FEBS Journal*, vol. 280, supplement 1, pp. 358–360, 2013.
- [10] A. Groza, A. Surmeian, C. Diplasu et al., "Physico-chemical processes occurring during polymerization of liquid polydimethylsiloxane films on metal substrates under atmospheric pressure air corona discharges," *Surface and Coatings Technology*, vol. 212, pp. 145–151, 2012.
- [11] W. E. G. Hansal, T. S. Hansal, M. Pözlner, A. Kornherr, G. Zifferer, and G. E. Nauer, "Investigation of polysiloxane coatings as corrosion inhibitors of zinc surfaces," *Surface & Coatings Technology*, vol. 200, no. 9, pp. 3056–3060, 2006.
- [12] K. H. Wu, C. M. Chao, T. F. Yeh, and T. C. Chang, "Thermal stability and corrosion resistance of polysiloxane coatings on 2024-T3 and 6061-T6 aluminum alloy," *Surface and Coatings Technology*, vol. 201, no. 12, pp. 5782–5788, 2007.
- [13] A. Groza, "Review of the processes identified during the polymerization of organic and organosilicon liquid films in atmospheric pressure air corona discharges," *Romanian Reports in Physics*, vol. 64, no. 4, pp. 1227–1242, 2012.
- [14] A. Groza, A. Surmeian, C. Diplasu, C. Luculescu, A. Tempez, and M. Ganciu, "Evidence of aluminum oxides formation at polymer/Al substrate interface in atmospheric pressure discharges," in *Proceeding of the Europhysics Conference on Atomic and Molecular Physics of Ionized Gases*, 2012.
- [15] A. Groza, A. Surmeian, C. Diplasu, C. Luculescu, and M. Ganciu, "Electrochemical anodization of aluminium surfaces in atmospheric pressure air corona discharge," in *Proceeding of the International Conference of Plasma and Ionized Gases*, 2013.
- [16] Ø. Hasvold and K. H. Johansen, "The alkaline aluminium hydrogen peroxide semi-fuel cell for the hugin 3000 autonomous underwater vehicle," in *Proceedings of the Workshop on Autonomous Underwater Vehicles (AUV '02)*, pp. 89–94, IEEE, June 2002.
- [17] Z. Kozáková, *Electric discharges in water solutions habilitation [Ph.D. thesis]*, Brno University of Technology, Faculty of Chemistry, 2011.
- [18] M. Goldman and A. Goldman, *Gaseous Electronics*, vol. 1, Academic Press, 1978.
- [19] R. S. Sigmond, "Simple approximate treatment of unipolar space-charge-dominated coronas: the Warburg law and the saturation current," *Journal of Applied Physics*, vol. 53, no. 2, pp. 891–898, 1982.
- [20] R. Ghita, C. Logofatu, C. C. Negrila et al., *Study of SiO₂/Si Interface by Surface Techniques, Crystalline Silicon Properties and Uses*, InTech, 2011, edited by S. Basu.
- [21] G. Gusmano, G. Montesperelli, E. Traversa et al., "Magnesium aluminium spinel thin film as a humidity sensor," *Sensors and Actuators B*, vol. 7, no. 1–3, pp. 460–463, 1992.
- [22] A. E. Hughes, M. M. Hedges, and B. A. Sexton, "Reactions at the Al/SiO₂/SiC layered interface," *Journal of Materials Science*, vol. 25, no. 11, pp. 4856–4865, 1990.
- [23] X. Zhao, S. Seo, U. Lee, and K. Lee, "Controlled electrochemical dissolution of anodic aluminum oxide for preparation of open-through pore structures," *Journal of the Electrochemical Society*, vol. 154, no. 10, pp. C553–C557, 2007.
- [24] P. R. Anderson and W. E. Swartz Jr., "X-ray photoelectron spectroscopy of some aluminosilicates," *Inorganic Chemistry*, vol. 13, no. 9, pp. 2293–2294, 1974.
- [25] I. F. Husein, C. Chan, S. Qin, and P. K. Chu, "The effect of high-dose nitrogen plasma immersion ion implantation on silicone surfaces," *Journal of Physics D: Applied Physics*, vol. 33, no. 22, pp. 2869–2874, 2000.
- [26] T. L. Barr, "The nature of the relative bonding chemistry in zeolites: an XPS study," *Zeolites*, vol. 10, no. 8, pp. 760–765, 1990.
- [27] C. Hinnen, D. Imbert, J. M. Siffre, and P. Marcus, "An in situ XPS study of sputter-deposited aluminium thin films on graphite," *Applied Surface Science*, vol. 78, no. 3, pp. 219–231, 1994.

Research Article

Tetraethyl Orthosilicate Coated Hydroxyapatite Powders for Lead Ions Removal from Aqueous Solutions

Rodica V. Ghita,¹ Simona Liliana Iconaru,^{1,2} Cristina Liana Popa,^{1,3} Adrian Costescu,⁴ Philippe Le Coustumer,⁵ Mikael Motelica-Heino,² and Carmen Steluta Ciobanu¹

¹ National Institute of Materials Physics, P.O. Box MG 07, 077125 Magurele, Romania

² ISTO, UMR 7327 CNRS-Université d'Orléans, 1A rue de la Férollerie, 45071 Orléans Cedex 2, France

³ Faculty of Physics, University of Bucharest, 405 Atomistilor, P.O. Box MG-1, 077125 Magurele, Romania

⁴ Hyperion University of Bucharest, 169 Calea Călărășilor, 030615 Bucharest, Romania

⁵ Université Bordeaux, EA 4592 Géorressources & Environnement, ENSEGID, 1 allée F. Daguin, 33607 Pessac Cedex, France

Correspondence should be addressed to Carmen Steluta Ciobanu; ciobanucs@gmail.com

Received 21 June 2014; Accepted 8 July 2014; Published 21 July 2014

Academic Editor: Daniela Predoi

Copyright © 2014 Rodica V. Ghita et al. This is an open access article distributed under the Creative Commons Attribution License, which permits unrestricted use, distribution, and reproduction in any medium, provided the original work is properly cited.

The goal of this study was to synthesize and characterize a porous material based on tetraethyl orthosilicate (TEOS) coated hydroxyapatite (HApTh) after removal experiments of Pb^{2+} ions from aqueous solutions. In order to study the morphology and composition, the samples obtained after removal experiments of Pb^{2+} ions from aqueous solution with the initial Pb^{2+} ion concentrations of the aqueous solutions were $0.1\text{ g}\cdot\text{L}^{-1}$ (HApTh-50) and $0.9\text{ g}\cdot\text{L}^{-1}$ (HApTh-450) have been investigated by scanning electron microscopy (SEM) equipped with an energy dispersive X-ray spectrometer (EDS), Fourier transform infrared spectroscopy (FTIR), and transmission electron microscopy (TEM). Removal experiments of Pb^{2+} ions were carried out in aqueous solutions with controlled concentration of Pb^{2+} . After the removal experiment of Pb^{2+} ions from solutions, porous hydroxyapatite nanoparticles were transformed into HApTh-50 and HApTh-450 due to the adsorption of Pb^{2+} ions followed by a cation exchange reaction. The obtained results show that the porous HApTh nanopowders could be used for Pb^{2+} ions removal from aqueous solutions.

1. Introduction

One of the major problems encountered in the public health area worldwide is the poisoning with various heavy metals. Researchers around the world have turned their attention to finding new effective and cost-efficient methods for depollution, considering the fact that heavy metals are nonbiodegradable, having the tendency to accumulate in living bodies, leading to disorders of different functions and to serious diseases [1, 2]. Lead (Pb) is a very toxic heavy metal, found in the earth's crust with an average concentration of 16 mg/kg in soils [3, 4]. On the other hand, lead has been extensively used in various industries, being a constituent in building materials, pipes, lead-acid batteries, bullets, and paints. In a report released by the Agency for Toxic Substances and Disease Registry (ATSDR), in 2007, the harmful effect of lead on the human nervous and reproductive systems was emphasized. Contamination of wastewaters represents a major concern

because this is one way of lead bioaccumulation in the food chain [3]. Recent studies have revealed that children are more susceptible to lead poisoning, their bodies being able to absorb around 50% of inhaled or ingested lead and the effects being more pronounced and long-lasting, compared to adults [5]. Moreover, the effects of chronic lead exposure to various functions of the human body have already been reported [3, 6]. In this context, many researchers have focused their attention to developing different methods for dangerous heavy metals removal from wastewaters. Among the methods already used, chemical precipitation, membrane filtration, ion-exchange, and adsorption could be mentioned [7–9]. Of all these methods, the most preferred one is the adsorption of heavy metals ions from aqueous solution using cost-efficient materials [7–9]. Previous studies have revealed that apatites are able to successfully remove lead from aqueous solutions [4, 10]. The best known member of the apatite family is hydroxyapatite (HAp). Synthetic hydroxyapatite,

$\text{Ca}_{10}(\text{PO}_4)_6(\text{OH})_2$, has been used in the last decades in many biomedical applications as coating for orthopedic or dental implants or as filling material for various injuries or defects, being similar to the natural mineral component of the human bones and teeth [11]. Furthermore, two of the most appealing properties for environmental applications that HAp possesses are its ability to adsorb complex organic materials and the capacity of heavy metals ion-exchanging [11–14]. Previous studies have shown that Pb^{2+} ions exchange rapidly with Ca, this process inducing morphological changes in the surface region [15–17]. In order to increase the adsorption ability of hydroxyapatite, an increase in its porosity must be obtained. Therefore, doping hydroxyapatite with silicon ions may be the key to increase the porosity, thus creating a better material for lead removal from aqueous solutions. Recent studies have shown that the addition of tetraethoxysilane (TEOS) can induce the formation of large textural pores [18]. Consequently, in order to increase the lead adsorption capacity of hydroxyapatite, it must be doped with a silicon based compound, such as TEOS.

The goal of this study was to synthesize and characterize new porous material based on tetraethyl orthosilicate (TEOS) and hydroxyapatite (HApTh) after removal experiment of Pb^{2+} ions from aqueous solution. The obtained powders after removal experiment of Pb^{2+} ions from aqueous solution when the initial Pb^{2+} ion concentrations of the aqueous solutions were $0.1 \text{ g}\cdot\text{L}^{-1}$ (HApTh-50) and $0.9 \text{ g}\cdot\text{L}^{-1}$ (HApTh-450) have been investigated by scanning electron microscopy (SEM), transmission electron microscopy (TEM), and Fourier transform infrared spectroscopy (FTIR). Another objective was to investigate the removal of Pb^{2+} ions from aqueous solutions with different pH values using HApTh nanopowders.

2. Experimental Section

2.1. Materials. All the reagents including ammonium dihydrogen phosphate $[(\text{NH}_4)_2\text{HPO}_4]$ (Alpha Aesar), calcium nitrate tetrahydrate $[\text{Ca}(\text{NO}_3)_2\cdot 4\text{H}_2\text{O}]$ (Alpha Aesar), ethanol, and tetraethyl orthosilicate (TEOS) with 99.999% purity were purchased from Sigma-Aldrich and lead nitrate $[\text{Pb}(\text{NO}_3)_2]$ with 99.5% purity was purchased from Merck and used without further purification.

2.2. Synthesis of Hydroxyapatite/TEOS Nanocomposites. Hydroxyapatite/TEOS nanocomposites (HApTh) were prepared using tetraethyl orthosilicate and hydroxyapatite. The hydroxyapatite $(\text{Ca}_{10}(\text{PO}_4)_6(\text{OH})_2)$ nanoparticles were prepared by setting the atomic ratio of Ca/P at 1.67 in accord with [19, 20]. The hydroxyapatite (HAp) was immobilized into a tetraethyl orthosilicate foam using the technique reported in the literature [20]. HApTh was obtained when tetraethyl orthosilicate solution (1g HAp/10 mL) was dropped on the HAp powder. The mixtures were then stirred vigorously for 30 min until homogeneity was achieved. After forming stable structures, HApTh composites were allowed to dry at 80°C for 24 h in a vacuum oven for the excess solvent to evaporate. Finally, HApTh composite samples were then ground in order to obtain powders.

2.3. Samples Characterization. In order to investigate the composition and morphology of the samples an equipment FESEM HITACHI 4700 coupled with an energy dispersive X-ray attachment (EDAX/2001 device) was used. TEM studies were carried out using a FEI Tecnai 12 (FEI Company, Hillsboro, OR, USA) equipped with a low-dose digital camera from Gatan Inc. (Pleasanton, CA, USA). Small quantities of HApTh powder were dispersed in deionised water and deposited on a copper grid coated with carbon film. This technique allows a good definition of crystal morphology.

The FTIR spectra were acquired using a Spectrum BX spectrometer. Pellets of 10 mm diameter for FTIR measurements were prepared (1% of the powder was mixed and ground with 99% KBr) by pressing the powder mixture at a load of 5 tons for 2 min. The spectra were registered in the range from 400 to 4000 cm^{-1} with a resolution of 4 and 128 times scanning.

The Raman spectra were registered with a Renishaw InVia dispersive Raman spectrometer (2012), equipped with a Leica DM microscope and one laser source at 514 nm (gas-type), Spectra Physics Ar ion laser (20 mW). The samples were analyzed using the 514 nm laser with a power at 0.2 mW and 1800 L/mm gratings. The spectral range covered for all spectra is 100 – 2000 cm^{-1} with a resolution below 2 cm^{-1} . Prior to each reference measurement, the instrument was calibrated on the internal Si-reference standard ($520.6 \pm 0.1 \text{ cm}^{-1}$).

The removal performance of Pb^{2+} ions by the HApTh powders was investigated by batch experiments, monitoring the change of Pb^{2+} ion concentration in the aqueous solutions. For these experiments, 5 g of HApTh nanocomposites were added to 500 mL aqueous solution with various initial Pb^{2+} ion concentrations and pH values in accord with Jang et al. [21]. The initial Pb^{2+} ion concentrations of the aqueous solutions were controlled and the values were set in the range 0.1 – $1.5 \text{ g}\cdot\text{L}^{-1}$ by dissolving lead nitrate $[\text{Pb}(\text{NO}_3)_2]$ in deionized water. The pH values of aqueous solutions with controlled initial Pb^{2+} ion concentrations were adjusted from 3 to 6 by adding small amounts of 0.1 M HCl standard solution. For all experiments the solution was stirred constantly for 24 h by a mechanical stirrer at room temperature.

3. Results and Discussions

Scanning electron microscopy (SEM) was used to characterize the morphology and elemental composition of synthesized powders after lead removal experiments. SEM images presented in Figure 1 showed that lead incorporation into HApTh samples affects the particle shape. The crystal clusters with needle or rod-like shapes were observed in SEM micrographs for the HApTh-50 and HApTh-450 samples. The clusters with needle or rod-like shapes were distinguished when the Pb^{2+} ion concentration from the aqueous solutions was $0.9 \text{ g}\cdot\text{L}^{-1}$ (HApTh-450 samples).

The EDX analysis indicates that calcium, phosphorus, silicon, and oxygen are the major constituents of the samples. The presence of Pb is also observed.

Figure 2 shows the TEM image of HApTh powders after the sorption experiment. These nanoparticles exhibit

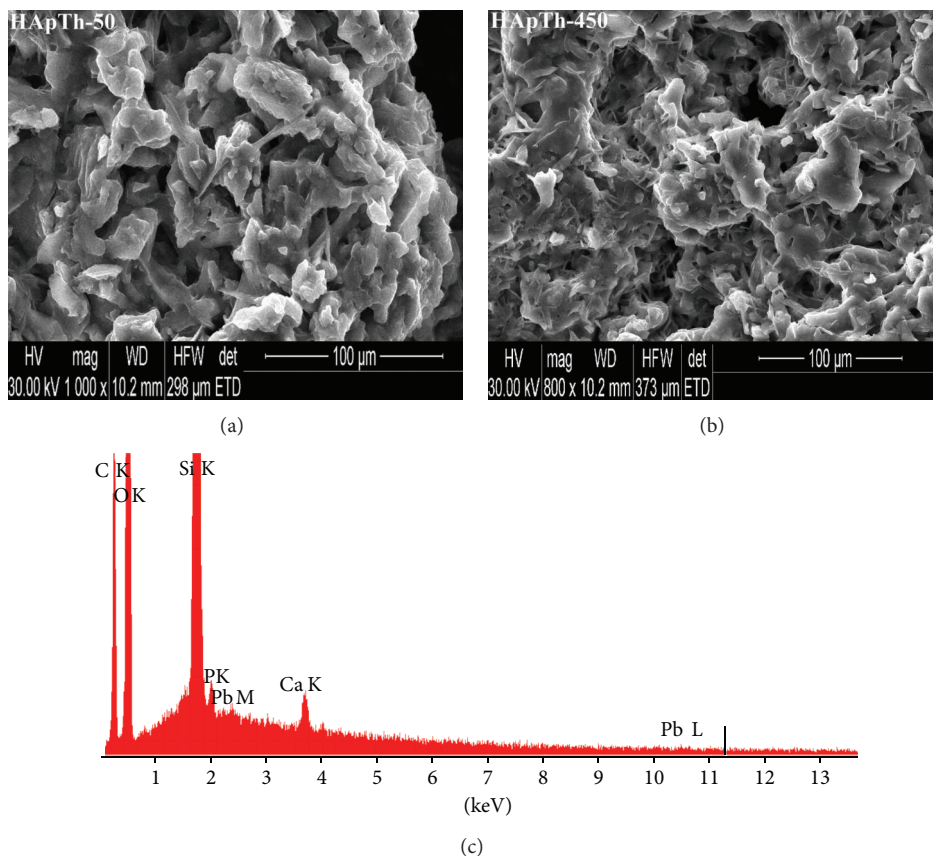


FIGURE 1: SEM micrographs with EDX spectra for the (a) HApTh-50 and (b) HApTh-450 samples.

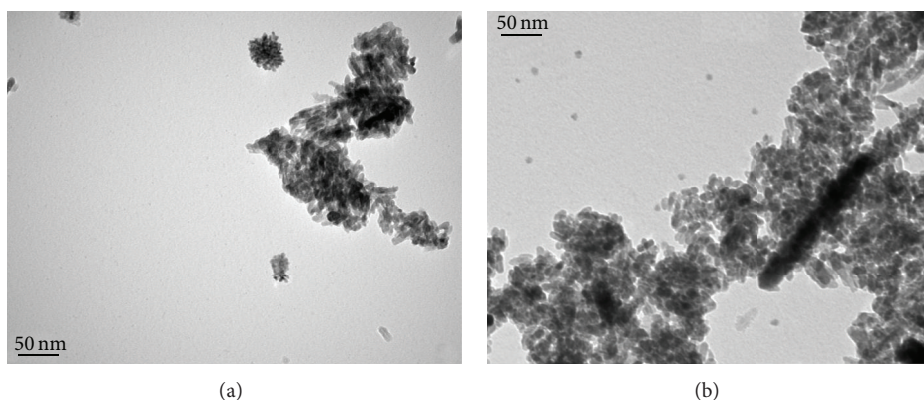


FIGURE 2: TEM micrograph of HAp after Pb^{2+} removal experiments for: (a) HApTh-50 and (b) HApTh-450 samples.

a needle-like morphology usually observed on HAp powders obtained by coprecipitation method [22]. Moreover, in TEM images it is easy to observe the formation of a new phase (pyromorphite) with a plate-like morphology (especially in the case of HApTh-450 samples). This behavior suggests that the incorporation of lead in the HApTh matrix stimulates local calcium enrichment.

These images also confirm the hypothesis that the main mechanism of lead immobilization is first of all based on the dissolution of HApTh followed by the precipitation of phases with higher lead content [23].

The Fourier transform infrared spectroscopy provides valuable information about the short-range ordering of materials. In Figure 3 are presented the FTIR spectra of the obtained powders after Pb^{2+} removal experiments. The interaction between lead (II) and HApTh structure led to some modifications of infrared vibrations of the functional groups. This behavior can be explained by the reaction mechanism which involves the HApTh dissolution in acid environment and HApTh Pb crystallisation [24].

In all the spectra the presence at around 640 cm^{-1} of OH vibration peak could be noticed. The broad peaks in the

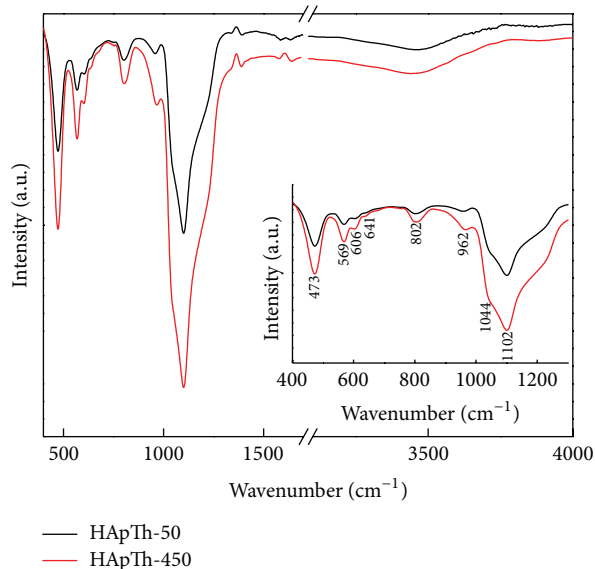


FIGURE 3: FT-IR spectra of HApTh-50 and HApTh-450 samples.

regions $1600\text{--}1700\text{ cm}^{-1}$ and $3200\text{--}3400\text{ cm}^{-1}$ are attributed to the hydroxyl groups [25–27].

The specific bands of (PO_4^{3-}) phosphate groups characteristic to hydroxyapatite structure were observed at 568 cm^{-1} , 637 cm^{-1} , 605 cm^{-1} , 964 cm^{-1} , and $1000\text{--}1100\text{ cm}^{-1}$ [28, 29]. The 964 cm^{-1} band can be associated to the ν_1 nondegenerated symmetric stretching mode of P–O. The vibrational bands at 605 cm^{-1} and 568 cm^{-1} are attributed to the triply degenerated ν_4 vibration of O–P–O bond, and the band at 472 cm^{-1} may be attributed to the ν_2 bending of O–P–O bond. Moreover, the weak band observed around 1500 cm^{-1} could be assigned to the A-type carbonate ion substitutions, whereas the bands at $1422\text{--}1456\text{ cm}^{-1}$ (ν_3) can be attributed to B-type CO_3^{2-} substitutions [30–32].

Moreover, it is well known that the vibrations bands (stretching and bending) assigned to the Si–O–Si bonds appear in the $1100\text{--}900\text{ cm}^{-1}$ and $550\text{--}400\text{ cm}^{-1}$ spectral regions. In the FTIR spectra (Figure 3) it is obvious that the stretching and bending bands of SiO_4 groups are overlapping with the band of the PO_4 group [30, 31, 33–37].

According to Ping et al. [38] the vibration band at 806 cm^{-1} (HApTh-450 sample) could be attributed to Si–O stretching of dimer silicate chains, indicating the start of silicate polymerization.

The Raman spectra of the HApTh-50 and HApTh-450 powders are reported in Figure 4. The Raman vibrations bands at 959 and 924 cm^{-1} are attributed to the ν_1 PO_4 vibration modes. In HApTh-50 samples, only the 959 cm^{-1} band appears, whereas the HApTh-450 samples exhibit two bands, one strong at 959 cm^{-1} and the other band at 924 cm^{-1} . This behavior is caused by the $A_g\text{-}E_{2g}$ splitting in the hexagonal C_{6h} symmetry [38, 39].

For the all samples, the vibrational spectra exhibit a strong molecular character associated with the internal modes of the tetrahedral PO_4^{3-} . The ν_2 bands (426 cm^{-1} and 450 cm^{-1})

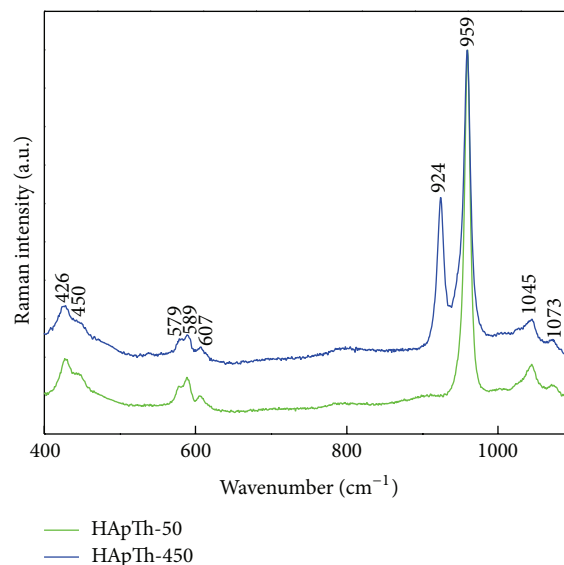


FIGURE 4: Raman spectra for the HApTh-50 and HApTh-450 samples.

are attributed to the O–P–O bending modes; ν_3 vibration bands (1073 cm^{-1} and 1045 cm^{-1}) correspond to asymmetric P–O stretching and the ν_4 bands (579 cm^{-1} , 589 cm^{-1} and 607 cm^{-1}) are attributed mainly to O–P–O bending.

In order to evaluate the impact of the lead concentration in the aqueous solution, absorption experiments were performed. HApTh solutions with concentration varying from 0.1 to $1.5\text{ g}\cdot\text{L}^{-1}$ at pH 5 were used. The measurements were performed on 500 mL solution (pH 5) with an initial Pb^{2+} ion concentration of $63\text{ mg}\cdot\text{L}^{-1}$. In Figure 5 the adsorption efficiency of Pb^{2+} ions as a function of the Pb^{2+} concentration in the solution is presented. It was observed that the removal efficiency is dependent on the initial Pb^{2+} concentration. For a lead concentration of $0.2\text{ g}\cdot\text{L}^{-1}$, the removal efficiency reached 98.6% , showing that the adsorbent material (HApTh) has a strong affinity to Pb^{2+} ions. For Pb^{2+} concentration ranging from $0.4\text{ g}\cdot\text{L}^{-1}$ to $1.5\text{ g}\cdot\text{L}^{-1}$, the removal efficiency was around 100% . This behavior could be explained by the fact that the Pb^{2+} ions were completely removed from the solution.

Figure 5 shows the measured lead concentration in the solution after the reaction with HApTh has taken place. For the studies on the effect of the solution pH, a solution containing $0.9\text{ g}\cdot\text{L}^{-1}$ of lead was selected (Figure 6). A solution containing $563\text{ mg}\cdot\text{L}^{-1}$ of Pb^{2+} ions was obtained from 0.9 g of $\text{Pb}(\text{NO}_3)_2$ in 1 L of distilled water.

A removal efficiency of 100% was achieved for pH 6. On the other hand, the removal efficiency of Pb^{2+} ions was 98.5% at pH 3. The removal efficiency of Pb^{2+} ions was 99% for pH 4. When the pH value was set to 5 the removal efficiency of Pb^{2+} ions was 99.5% . The present studies have shown that the removal of Pb^{2+} ions from aqueous solution by hydroxyapatite/TEOS nanocomposites was greater than 98.6% at all pH values of the aqueous solution used for the removal of Pb^{2+} ions.

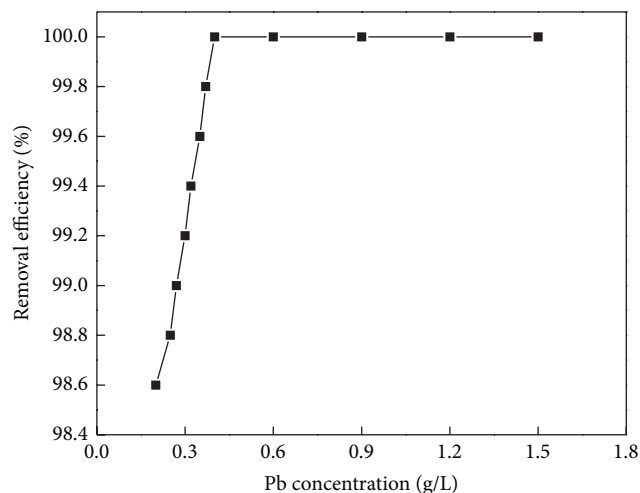


FIGURE 5: Effect of the Pb^{2+} concentration on the removal of the Pb^{2+} ions by HApTh.

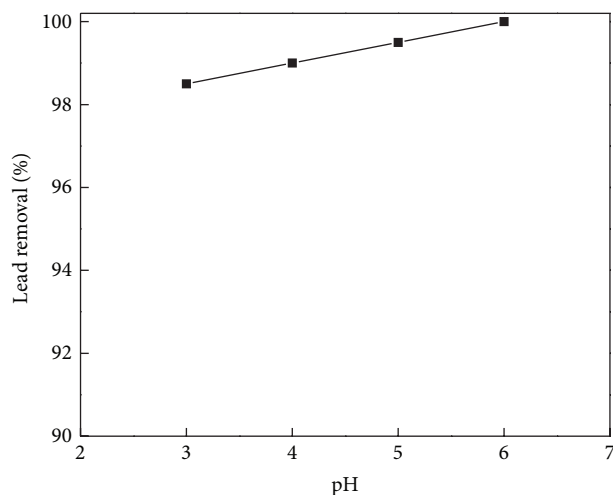


FIGURE 6: Effect of the solution pH on the removal of Pb^{2+} ions by HApTh.

According to these results, it can be highlighted the fact that the HApTh can really remove Pb^{2+} ions from aqueous solutions.

One of the most important parameters which must be considered in the absorption experiments is the pH of the solutions due to the fact that the pH of groundwater and surface waters varies between 5 and 7 [40]. The results of our studies have shown that the solid reaction products of aqueous Pb^{2+} with the HApTh are mainly pH-dependent, this being in good agreement with other results reported in literature [40].

For the assimilation of different metals from aqueous solutions by hydroxyapatite [17, 41–43] different processes have been proposed, such as metal complexation on the HAp surface, apatite dissolution followed by a new metal phase precipitation, and cation exchange. In previous studies [44], it has been shown that the formation of a stable lead apatite

such as $\text{Ca}_{(10-x)}\text{Pb}_x(\text{PO}_4)_6(\text{OH})_2$ by ion exchange mechanism where Pb^{2+} present in the solution replaces Ca^{2+} ions from the hydroxyapatite lattice is possible. Furthermore, the $\text{Pb}_{(10-x)}\text{Ca}_x(\text{PO}_4)_6(\text{OH})_2$ crystals with higher content of calcium are unstable [45]. Therefore, the HAp should be subject of a permanent process of dissolution and precipitation in order to obtain more stable materials with a higher lead percentage.

4. Conclusions

The main goal of this study was to synthesize a new porous nanocomposite material based on tetraethyl orthosilicate (TEOS) coated hydroxyapatite. In this study we investigated the ability of these new materials to remove Pb^{2+} ions from aqueous solutions with different concentration and pH values. After HApTh reacted with the solution containing Pb^{2+} ions, the lead ions were completely removed from the solution and the dissolution of $\text{Ca}_{10}(\text{PO}_4)_6(\text{OH})_2$ occurred. The HApTh powders exhibited the higher removal efficiency of Pb^{2+} ions at pH 6. The TEM studies confirm the hypothesis that the main mechanism of lead immobilization is first of all based on the dissolution of HAp followed by the precipitation of phases with higher lead content. This study showed that the HApTh nanopowders are promising materials for lead ions removal from aqueous solutions with different pH values, being able to be used in the future for depollution of wastewaters.

Conflict of Interests

The authors declare that there is no conflict of interests regarding the publication of this paper.

Acknowledgment

The financial and encouragement support was provided by the Ministry of Educations of Romania under the project IFA-CEA C2-06.

References

- [1] D. Liao Dexiang, W. Zheng, X. Li et al., "Removal of lead(II) from aqueous solutions using carbonate hydroxyapatite extracted from eggshell waste," *Journal of Hazardous Materials*, vol. 177, no. 1-3, pp. 126–130, 2010.
- [2] S. H. Jang, B. G. Min, Y. G. Jeong, W. S. Lyoo, and S. C. Lee, "Removal of lead ions in aqueous solution by hydroxyapatite/polyurethane composite foams," *Journal of Hazardous Materials*, vol. 152, no. 3, pp. 1285–1292, 2008.
- [3] H. Xu, L. Yang, P. Wang, Y. Liu, and M. Peng, "Kinetic research on the sorption of aqueous lead by synthetic carbonate hydroxyapatite," *Journal of Environmental Management*, vol. 86, no. 1, pp. 319–328, 2008.
- [4] Q. Y. Ma, T. J. Logan, S. J. Traina, and J. A. Ryan, "Effects of NO_3^- , Cl^- , F^- , SO_4^{2-} , and CO_3^{2-} on Pb^{2+} immobilization by hydroxyapatite," *Environmental Science and Technology*, vol. 28, no. 3, pp. 408–418, 1994.

- [5] A. L. Morrison, "An assessment of the effectiveness of lead pollution reduction strategies in North Lake Macquarie, NSW, Australia," *The Science of the Total Environment*, vol. 303, no. 1-2, pp. 125-138, 2003.
- [6] G. B. Freeman, J. A. Dill, J. D. Johnson, P. J. Kurtz, F. Parham, and H. B. Matthews, "Comparative absorption of lead from contaminated soil and lead salts by weanling Fischer 344 rats," *Fundamental and Applied Toxicology*, vol. 33, no. 1, pp. 109-119, 1996.
- [7] A. Günay, E. Arslankaya, and I. Tosun, "Lead removal from aqueous solution by natural and pretreated clinoptilolite: adsorption equilibrium and kinetics," *Journal of Hazardous Materials*, vol. 146, no. 1-2, pp. 362-371, 2007.
- [8] A. Groza, "Review of the processes identified during the polymerization of organic and organosilicon liquid films in atmospheric pressure air corona discharges," *Romanian Reports in Physics*, vol. 64, no. 4, pp. 1227-1242, 2012.
- [9] S. E. Bailey, T. J. Olin, R. M. Bricka, and D. D. Adrian, "A review of potentially low-cost sorbents for heavy metals," *Water Research*, vol. 33, no. 11, pp. 2469-2479, 1999.
- [10] P. Zhang, J. A. Ryan, and J. Yang, "In vitro soil Pb solubility in the presence of hydroxyapatite," *Environmental Science and Technology*, vol. 32, no. 18, pp. 2763-2768, 1998.
- [11] E. S. Bogya, R. Barabás, A. Csavdári, V. Dejeu, and I. Bâldea, "Hydroxyapatite modified with silica used for sorption of copper(II)," *Chemical Papers*, vol. 63, no. 5, pp. 568-573, 2009.
- [12] A. Corami, S. Mignardi, and V. Ferrini, "Cadmium removal from single- and multi-metal (Cd + Pb + Zn + Cu) solutions by sorption on hydroxyapatite," *Journal of Colloid and Interface Science*, vol. 317, no. 2, pp. 402-408, 2008.
- [13] R. Barabás, A. Pop, E. S. Bogya, and V. Dejeu, "Synthesis and properties of intelligent biomaterials. In 4th Edition of the National Symposium of Biomaterials," *Biomaterials and Medical-Surgery Applications*, vol. 18-20, pp. 1-12, 2007.
- [14] M. Czerniczyniec, S. Fariás, J. Magallanes, and D. Cicerone, "Arsenic(V) adsorption onto biogenic hydroxyapatite: solution composition effects," *Water, Air, and Soil Pollution*, vol. 180, no. 1-4, pp. 75-82, 2007.
- [15] D. E. Ellis, J. Terra, O. Warschkow et al., "A theoretical and experimental study of lead substitution in calcium hydroxyapatite," *Physical Chemistry Chemical Physics*, vol. 8, no. 8, pp. 967-976, 2006.
- [16] Y. Xu and F. W. Schwartz, "Lead immobilization by hydroxyapatite in aqueous solutions," *Journal of Contaminant Hydrology*, vol. 15, no. 3, pp. 187-206, 1994.
- [17] Q. Y. Ma, S. J. Traina, T. J. Logan, and J. A. Ryan, "In situ lead immobilization by apatite," *Environmental Science and Technology*, vol. 27, no. 9, pp. 1803-1810, 1993.
- [18] J. Liu, Q. Yang, X. S. Zhao, and L. Zhang, "Pore size control of mesoporous silicas from mixtures of sodium silicate and TEOS," *Microporous and Mesoporous Materials*, vol. 106, no. 1-3, pp. 62-67, 2007.
- [19] C. S. Ciobanu, E. Andronescu, A. Stoicu et al., "Influence of annealing treatment of nano-hydroxyapatite bioceramics on the vibrational properties," *Digest Journal of Nanomaterials and Biostructures*, vol. 6, no. 2, pp. 609-624, 2011.
- [20] D. Dieterich, E. Grigat, W. Hahn, H. Hesse, and H. G. Schmelzer, "Principles of polyurethane chemistry and special applications," in *Polyurethane Handbook: Chemistry, Raw Materials, Processing, Application, Properties*, G. Oertel, Ed., pp. 11-31, Hanser, Munich, Germany, 2nd edition, 1994.
- [21] S. H. Jang, Y. G. Jeong, B. G. Min, W. S. Lyoo, and S. C. Lee, "Preparation and lead ion removal property of hydroxyapatite/polyacrylamide composite hydrogels," *Journal of Hazardous Materials*, vol. 159, no. 2-3, pp. 294-299, 2008.
- [22] E. Mavropoulos, A. M. Rossi, N. C. C. da Rocha, G. A. Soares, J. C. Moreira, and G. T. Moure, "Dissolution of calcium-deficient hydroxyapatite synthesized at different conditions," *Materials Characterization*, vol. 50, no. 2-3, pp. 203-207, 2003.
- [23] E. Mavropoulos, N. C. C. Rocha, J. C. Moreira, A. M. Rossi, and G. A. Soares, "Characterization of phase evolution during lead immobilization by synthetic hydroxyapatite," *Materials Characterization*, vol. 53, no. 1, pp. 71-78, 2004.
- [24] A. Melinescu, C. Țârdei, C. M. Simionescu, V. Marinescu, and A. Miclea, "Removal of Pb²⁺ toxic ions from aqueous solutions on porous hydroxyapatite granules," *Romanian Journal of Materials*, vol. 43, no. 2, pp. 223-226, 2013.
- [25] D. Predoi, R. V. Ghita, F. Ungureanu, C. C. Negrila, R. A. Vatasescu-Balcan, and M. Costache, "Characteristics of hydroxyapatite thin films," *Journal of Optoelectronics and Advanced Materials*, vol. 9, no. 12, pp. 3827-3831, 2007.
- [26] D. Predoi, M. Barsan, E. Andronescu, R. A. Vatasescu-Balcan, and M. Costache, "Hydroxyapatite-iron oxide bioceramic prepared using nano-size powders," *Journal of Optoelectronics and Advanced Materials*, vol. 9, no. 11, pp. 3609-3613, 2007.
- [27] A. Costescu, I. Pasuk, F. Ungureanu et al., "Physico-chemical properties of nano-sized hexagonal hydroxyapatite powder synthesized by sol-gel," *Digest Journal of Nanomaterials and Biostructures*, vol. 5, no. 4, pp. 989-1000, 2010.
- [28] J. Jeanjean, U. Vincent, and M. Fedoroff, "Structural modification of calcium hydroxyapatite induced by sorption of cadmium ions," *Journal of Solid State Chemistry*, vol. 108, no. 1, pp. 68-72, 1994.
- [29] I. Smičiklas, A. Onjia, S. Raičević, D. Janačković, and M. Mitrić, "Factors influencing the removal of divalent cations by hydroxyapatite," *Journal of Hazardous Materials*, vol. 152, no. 2, pp. 876-884, 2008.
- [30] I. Rehman and W. Bonfield, "Characterization of hydroxyapatite and carbonated apatite by photo acoustic FTIR spectroscopy," *Journal of Materials Science: Materials in Medicine*, vol. 8, no. 1, pp. 1-4, 1997.
- [31] N. Y. Mostafa, H. M. Hassan, and O. H. Abd Elkader, "Preparation and characterization of Na⁺, SiO₄⁴⁻, and CO₃²⁻ Co-substituted hydroxyapatite," *Journal of the American Ceramic Society*, vol. 94, no. 5, pp. 1584-1590, 2011.
- [32] M. Palard, E. Champion, and S. Foucaud, "Synthesis of silicated hydroxyapatite Ca₁₀(PO₄)_{6-x}(SiO₄)_x(OH)_{2-x}," *Journal of Solid State Chemistry*, vol. 181, no. 8, pp. 1950-1960, 2008.
- [33] A. Bianco, I. Cacciotti, M. Lombardi, and L. Montanaro, "Si-substituted hydroxyapatite nanoparticles: synthesis, thermal stability and sinterability," *Materials Research Bulletin*, vol. 44, no. 2, pp. 345-354, 2009.
- [34] G. Socrates, *Infrared and Raman Characteristic Group Frequencies: Tables and Charts*, John Wiley & Sons, New York, NY, USA, 2001.
- [35] L. Borum and O. C. Wilson Jr., "Surface modification of hydroxyapatite. Part II. Silica," *Biomaterials*, vol. 24, no. 21, pp. 3681-3688, 2003.
- [36] A. Groza, A. Surmeian, M. Ganciu, R. Medianu, and I. I. Popescu, "SiO₂ - Like thin films generation in corona discharges in air at atmospheric pressure: IR spectroscopy and atomic force microscopy investigations," *Journal of Optoelectronics and Advanced Materials*, vol. 7, no. 4, pp. 2159-2164, 2005.

- [37] A. Groza, A. Surmeian, M. Ganciu, R. Medianu, and I. I. Popescu, "Infrared spectral investigation of organosilicon compounds under corona charge injection in air at atmospheric pressure," *Journal of Optoelectronics and Advanced Materials*, vol. 7, no. 5, pp. 2545–2548, 2005.
- [38] Y. Ping, R. J. Kirkpatrick, P. Brent, P. F. McMillan, and X. Cong, "Structure of calcium silicate hydrate (C-S-H): near-, mid-, and far-infrared spectroscopy," *Journal of the American Ceramic Society*, vol. 82, no. 3, pp. 742–748, 1999.
- [39] G. Bartholomäi and W. E. Klee, "The vibrational spectra of pyromorphite, vanadinite and mimetite," *Spectrochimica Acta A: Molecular Spectroscopy*, vol. 34, no. 7-8, pp. 831–843, 1978.
- [40] A. Hadrich, A. Lautié, and T. Mhiri, "Vibrational study and fluorescence bands in the FT-Raman spectra of $\text{Ca}_{10-x}\text{Pb}_x(\text{PO}_4)_6(\text{OH})_2$ compounds," *Spectrochimica Acta A*, vol. 57, no. 8, pp. 1673–1681, 2001.
- [41] A. G. Leyva, J. Marrero, P. Smichowski, and D. Cicerone, "Sorption of antimony onto hydroxyapatite," *Environmental Science and Technology*, vol. 35, no. 18, pp. 3669–3675, 2001.
- [42] T. Suzuki, T. Hatsushika, and Y. Hayakawa, "Synthetic hydroxyapatites employed as inorganic cation-exchangers," *Journal of the Chemical Society, Faraday Transactions*, vol. 77, no. 5, pp. 1059–1062, 1981.
- [43] Y. Suzuki and Y. Takeuchi, "Uptake of a few divalent heavy metal ionic species by a fixed bed of hydroxyapatite particles," *Journal of Chemical Engineering of Japan*, vol. 27, no. 5, pp. 571–576, 1994.
- [44] T. Suzuki, K. Ishigaki, and M. Miyake, "Hydroxyapatites as inorganic cation exchangers. Part 3: exchange characteristics of lead ions (Pb^{2+}), Journal of the Chemical Society," *Journal of the Chemical Society, Faraday Transactions*, vol. 80, pp. 3157–3165, 1984.
- [45] G. Lusvardi, G. Malavasi, L. Menabue, and M. Saladini, "Removal of cadmium ion by means of synthetic hydroxyapatite," *Waste Management*, vol. 22, no. 8, pp. 853–857, 2002.

Research Article

Preparation of Mesoporous SBA-16 Silica-Supported Biscinchona Alkaloid Ligand for the Asymmetric Dihydroxylation of Olefins

Shaheen M. Sarkar,¹ Md. Equb Ali,² Md. Lutfur Rahman,¹ and Mashitah Mohd Yusoff¹

¹ Faculty of Industrial Sciences and Technology, University Malaysia Pahang, 26300 Gambang, Kuantan, Malaysia

² Nanotechnology and Catalysis Research Centre (NanoCat), University of Malaya, Level 3, Block A, IPS Building, 50603 Kuala Lumpur, Malaysia

Correspondence should be addressed to Md. Equb Ali; eaqubali@gmail.com

Received 21 March 2014; Revised 20 May 2014; Accepted 21 May 2014; Published 15 June 2014

Academic Editor: Daniela Predoi

Copyright © 2014 Shaheen M. Sarkar et al. This is an open access article distributed under the Creative Commons Attribution License, which permits unrestricted use, distribution, and reproduction in any medium, provided the original work is properly cited.

Optically active cinchona alkaloid was anchored onto mesoporous SBA-16 silica and the as-prepared complex was used as a heterogeneous chiral ligand of osmium tetroxide for the asymmetric dihydroxylation of olefins. The prepared catalytic system provided 90–93% yield of vicinal diol with 92–99% enantioselectivity. The ordered mesoporous SBA-16 silica was found to be a valuable support for the cinchona alkaloid liganded osmium catalyst system which is frequently used in chemical industries and research laboratories for olefin functionalization.

1. Introduction

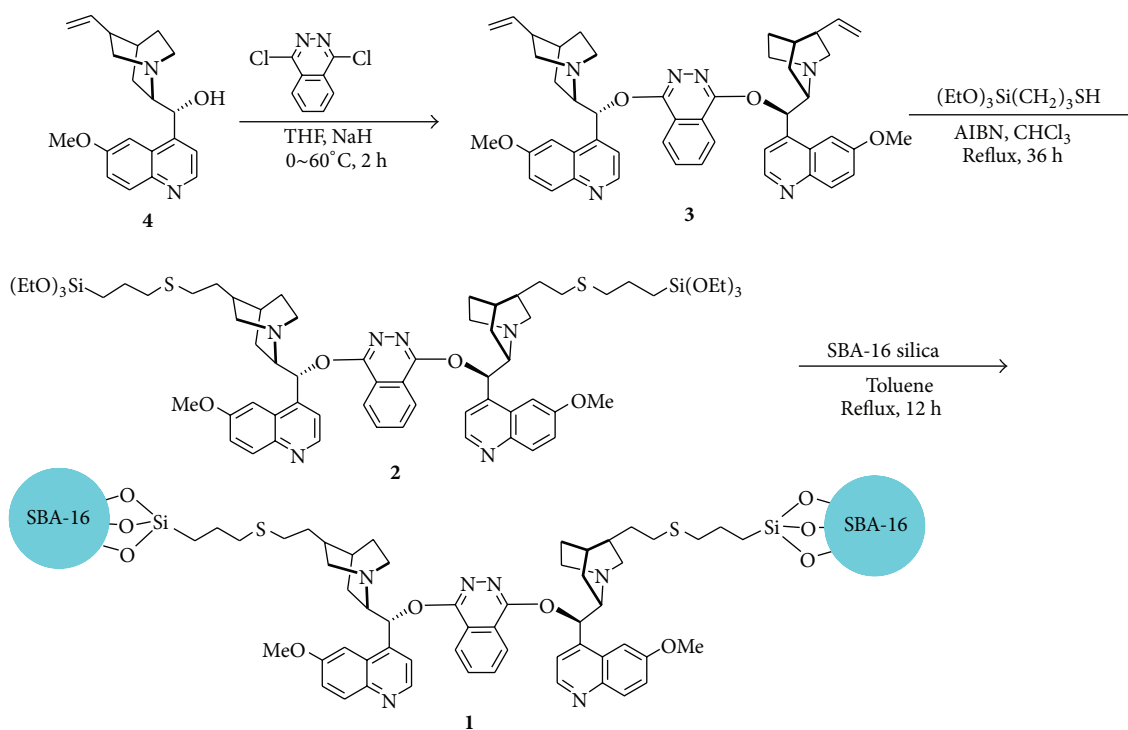
The discovery of highly ordered mesoporous materials has opened up new fields of research in advanced chemistry, modern electronics, and nanotechnology [1–3]. Ordered mesoporous SBA-16 is a nanostructured porous material with a 3D cubic arrangement of mesopores that corresponds to the *Im3m* space group [4–9]. The surface properties of such materials could be significantly modified by adding organic groups and various functionalities onto them [10]. Our interest in the field led us to prepare SBA-16 silica-supported biscinchona alkaloid for osmium-catalyzed asymmetric dihydroxylation (AD) of olefins. Osmium-catalyzed asymmetric dihydroxylation of olefins is an attractive method for the synthesis of optically active diols [11–14]. Cinchona alkaloid-based osmium complexes are harmless and known to be the most effective chiral catalysts for AD reactions in terms of both reactivity and enantioselectivity [15–18].

However, the high cost and toxicity of osmium are a serious concern and many efforts have been devoted to overcome the issue including the development of heterogeneous catalyst ligand to trap the osmium [19, 20]. Immobilization

of homogeneous catalysts onto various supports has emerged as a major route to prepare heterogeneous catalysts [21, 22]. Such a heterogeneous catalyst system offers practical advantages in catalyst separation and potential recycling over its homogeneous counterpart [23, 24]. Silica gel such as mesoporous silica MCM-41 and SBA-15 has been successfully used as inorganic supports for the immobilization of homogeneous catalysts [25–27]. However, despite having highly ordered mesopores, SBA-16 silica has been scarcely explored in this area. Herein, we described the synthesis of SBA-16 supported cinchona alkaloid ligand and tested it for the osmium catalyzed AD reaction of olefins to diols, a key reaction in organic synthesis.

2. Experimental Details

2.1. Preparation of the SBA-16 Silica. SBA-16 silica was synthesized at room temperature under acidic condition using Pluronic F127 ($\text{EO}_{106}\text{PO}_{70}\text{EO}_{106}$, $M_w = 12.6$ K) as a structure-directing agent (SDA) [28]. The acidic solution was made by adding 1.5 g of deionized (DI) water to 120 g of



SCHEME 1: Preparation of SBA-16-supported biscinchona alkaloid **1**.

2 M HCl solution at room temperature. Subsequently, 8.5 g of tetraethoxysilane (TEOS) was added onto the solution and stirring continued for 20 h. The reaction mixture was kept at 100°C for 48 h. During this time the solid SBA-16 was produced under static conditions in a Teflon-lined vessel. The solid product was recovered and washed with DI water. Calcination was carried out slowly by increasing temperature from room temperature to 500°C in 8 h and heating at 500°C for another 6 h.

2.2. Preparation of the 1,4-Bis(9-O-quininyl)phthalazine 3. NaH (2.24 mmol) at 0°C was slowly added to a stirred solution of 1,4-dichlorophthalazine (0.5 mmol) and quinine **4** (1.15 mmol) in THF (8 mL). The solution was stirred at 60°C for 2 h and then it was quenched at 0°C by careful addition of water. The mixture was extracted in ethyl acetate (EtOAc) and the solvent was removed under reduced pressure. The residue was purified by short column chromatography to separate 1,4-bis(9-O-quininyl)phthalazine **3** and 82% yield was obtained.

2.3. Preparation of the Triethoxysilane 1,4-Bis(9-O-quininyl)phthalazine 2. 1,4-Bis(9-O-quininyl)phthalazine **3** (0.5 mmol) was added to a solution of (3-mercaptopropyl) triethoxysilane (1.25 mmol) and α,α' -azoisobutyronitrile (AIBN) (0.10 mmol) in degassed chloroform (10 mL) under N₂ atmosphere. The reaction mixture was refluxed for 30 h and concentrated under reduced pressure. The residue was purified by flash short column on silica gel to give compound **2** with 80% yield.

2.4. Immobilization of Biscinchona Alkaloid 2 onto SBA-16 Silica 1. SBA-16 silica (1.0 g) was suspended in toluene and refluxed with compound **2** (145 mg, 0.124 mmol). After 12 h, the powder was collected by filtration and washed with methanol and methylene chloride. After drying under vacuum at 70°C, SBA-16-supported alkaloid **1** (1.077 g) was obtained. Elemental analysis and weight gain showed that 0.073 mmol of 1,4-bis(9-O-quininyl)phthalazine was anchored on 1.0 g of SBA-16-supported chiral Ligand **1**.

2.5. Characterization of SBA-16-Supported Chiral Ligand 1. Powder X-ray diffractometry (Philips PW 1729) was used for the determination of crystalline structure using Cu K_α radiation over $0.5^\circ \leq 2\theta \leq 3^\circ$. The XRD sample of SBA-16 was analyzed at 30°C. The diffractograms showed 3 peaks at $2\theta \approx 0.74^\circ, 1.1^\circ, \text{ and } 1.4^\circ$ that corresponded to (110), (200), and (211) planes, respectively, in the cubic *Im3m* structure. The transmission electron microscopy (TEM) was performed with a FEI Tecnai G² microscope operated at 200 kV. The TEM sample was prepared by placing a few drops of SBA-16 powder dispersed in acetone on a carbon grid and allowing it to dry for 5 min before TEM analysis. Large particles were crushed by submerging them in liquid nitrogen followed by mechanical grinding in a mortar prior to acetone dispersion. The nitrogen adsorption-desorption measurements were performed at -196°C on a Micromeritics ASAP 2020 surface area and porosity analyzer. Approximately 0.5 g of SBA-16 was degassed at 300°C for 9 h before taking the measurement. The surface area determination was performed by the Brunauer-Emmett-Teller (BET) method [29] over the relative pressure

(P/P_0) range of 0.05–0.2. The pore-size distribution was determined using the Broekhoff-de Boer (BdB) method [30] applied to the adsorption branch. Finally, the total pore volume was calculated from the amount of adsorbed N_2 at $P/P_0 = 0.99$, and the microporous volume was determined using the t -plot method.

2.6. Asymmetric Dihydroxylation of Olefin Using SBA-16-Supported Chiral Ligand 1. A mixture of SBA-16-supported biscinchona alkaloid **1** (1 mol%), potassium ferricyanide (1.5 mmol), potassium carbonate (1.5 mmol), and OsO_4 (1 mol%, 0.5 M in water) in *tert*-butyl alcohol-water (6 mL, 1:1, v/v) was stirred at room temperature for 30 min. Olefin (0.5 mmol) was added at once and stirred for 7–15 h. The reaction mixture was diluted with water and CH_2Cl_2 and the immobilized Ligand **1** was separated by filtration. The crude product was purified by flash column chromatography, and the enantiomeric excess of the diol was determined by chiral gas chromatography (GC) analysis (Agilent HP Chiral-20B 30MX0.25MMX0.25UM GC Column).

3. Results and Discussion

To synthesize a SBA-16-supported biscinchona alkaloid **1**, we started with quinine and 1,4-dichlorophthalazine following a route shown in Scheme 1.

Treatment of optically active quinine **4** with 1,4-dichlorophthalazine in the presence of excess NaH synthesized 4-bis(9-*O*-quininyl)phthalazine **3** with high yield (82%). Radical reaction of dimeric quinine **3** with (3-mercaptopropyl)triethoxysilane in the presence of AIBN radical initiator provided compound **2** having a pendant triethoxysilane functional group. The desired immobilized biscinchona alkaloid SBA-16 **1** (loading ratio: 0.073 mmol/g) was readily obtained by condensation of **2** with surface silanols of SBA-16 support in refluxing toluene. The degree of functionalization was determined by elemental analysis and weight gain. As shown in Table 1, the surface area and pore diameter were decreased following the modification. The high resolution transmission electron microscopy (HRTEM) image of SBA-16-supported Ligand **1** is shown in Figure 1. The 3D cubic structure and the pore arrays were conserved after the immobilization of 1,4-bis(9-*O*-quininyl)phthalazine onto SBA-16 silica and it was also confirmed by XRD (Figure 2).

The AD reaction of stilbene was performed in the presence of immobilized cinchona alkaloid **1** (1 mol%) and OsO_4 (1 mol%) at room temperature. Potassium carbonate and potassium ferricyanide were used as a secondary oxidant in *tert*-butyl alcohol-water mixture (1:1). The results are summarized in Table 2. Surprisingly, catalytic AD reactions of stilbene provided excellent enantioselectivities and high yields (entries 1 and 2). Osmium catalyst loading of 0.5 mol% was sufficient to obtain outstanding enantioselectivity as well as high reactivity. Moreover, the SBA-16-supported alkaloid- OsO_4 complex could be reused for the AD reaction of stilbene without a significant loss of reactivity and enantioselectivity (entry 3). The catalyst was also highly effective to

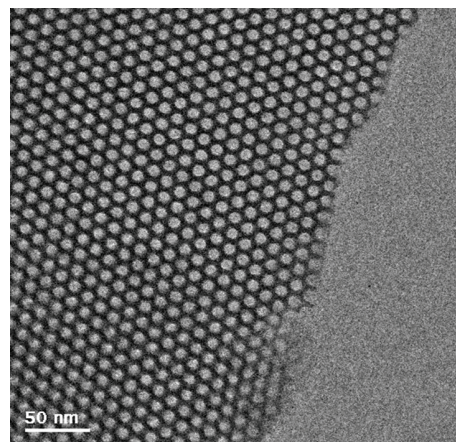


FIGURE 1: HRTEM image of SBA-16-supported Ligand **1**.

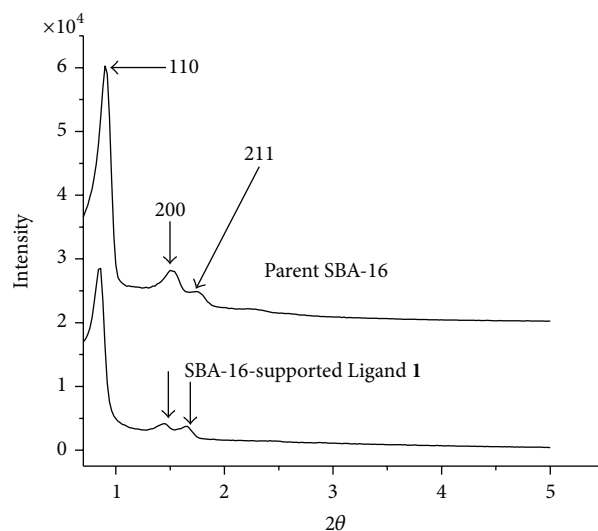


FIGURE 2: XRD pattern of SBA-16-supported Ligand **1**.

AD of methylcinnamate, 1-phenyl-1-cyclohexene, and styrene (entries 4–6).

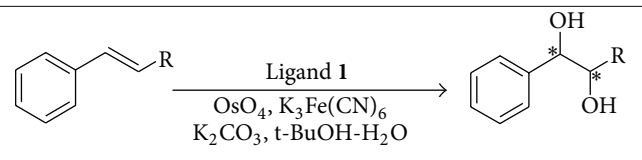
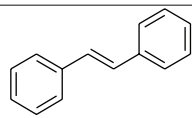
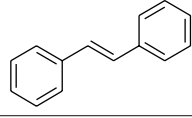
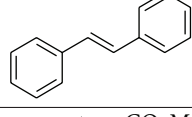
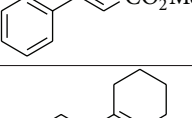
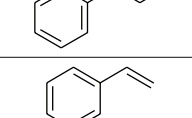
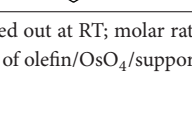
The SBA-16-supported Ligand **1** reported here showed somewhat higher reactivity and better asymmetric induction over amorphous silica-supported biscinchona alkaloid [25]. The improved outcome of the reaction seems to be attributed to the ordered array of chiral catalytic site on the nanopore surface of SBA-16 support. The ordered array leads to elegant site isolation which may result in enhanced enantioselectivity.

Romero et al. [31] reported the asymmetric dihydroxylation reaction of olefin using ionic liquid, which involves high cost and toxicity. The yield and enantioselectivity of the styrene were also very poor (87% yield, 62% ee) [32]. On the other hand, Junttila and Hormi [33] used methanesulfonamide as an accelerator of the asymmetric dihydroxylation reaction using potassium osmate (vi) and obtained 97% ee with low yield (70%) of the diol product. It is noteworthy here that the alkaloid ligand complexes synthesized in this report produced excellent results in terms of both yield (93%) and enantioselectivity (92–99%).

TABLE 1: Structural characteristics of SBA-16-supported Ligand 1.

Sample	Surface area	Pore diameter	Pore volume	Functional group
SBA-16	820 m ² /g	5.13 nm	0.73 cm ³ /g	—
1	490 m ² /g	3.68 nm	0.45 cm ³ /g	0.073 mmol/g

TABLE 2: Heterogeneous AD of olefins using SBA-16-supported Ligand 1^a.

Entry	Olefin	Time (h)	Yield (%)	(%) Ee ^b	Config. ^b
					
1		7	93	>99	S, S
2 ^c		7	91	98	S, S
3 ^d		8	90	97	S, S
4		9	91	96	2R, 3S
5		10	92	94	2S, 3S
6		15	92	92	S

^aThe reactions were carried out at RT; molar ratio of olefin/OsO₄/supported ligand = 1/0.01/0.01. ^bEe and absolute configuration were determined by chiral GC analysis. ^cMolar ratio of olefin/OsO₄/supported ligand = 1/0.005/0.005. ^dReaction was carried out with regenerated 1 without further addition of OsO₄.

4. Conclusion

We successfully synthesized air and moisture stable SBA-16-supported bisquinona alkaloid chiral ligand. Osmium tetroxide readily formed a chiral complex with the SBA-16-supported bisquinona alkaloid at room temperature. The synthesized SBA-16 supported Os-complex efficiently promoted the asymmetric dihydroxylation of olefin to corresponding diols with 92–99% enantioselectivity and 93% yield, demonstrating SBA-16 silica as an excellent support material for the heterogeneous chiral ligand.

Conflict of Interests

The authors declare that they have no conflict of interests regarding the publication of this paper.

Acknowledgment

This work was supported by University of Malaya fund no. RP005A-13AET to M. E. Ali.

References

- [1] A. Corma, "From microporous to mesoporous molecular sieve materials and their use in catalysis," *Chemical Reviews*, vol. 97, no. 6, pp. 2373–2420, 1997.
- [2] U. Ciesla and F. Schüth, "Ordered mesoporous materials," *Microporous and Mesoporous Materials*, vol. 27, no. 2-3, pp. 131–149, 1999.
- [3] A. Taguchi and F. Schüth, "Ordered mesoporous materials in catalysis," *Microporous and Mesoporous Materials*, vol. 77, no. 1, pp. 1–45, 2005.

- [4] Y. K. Hwang, J.-S. Chang, Y.-U. Kwon, and S.-E. Park, "Microwave synthesis of cubic mesoporous silica SBA-16," *Microporous and Mesoporous Materials*, vol. 68, no. 1–3, pp. 21–27, 2004.
- [5] R. A. Fernandes and A. K. Chowdhury, "Stereoselective total synthesis of (+)-nephrosteranic acid and (+)-roccellaric acid through asymmetric dihydroxylation and Johnson–Claisen rearrangement," *European Journal of Organic Chemistry*, vol. 2011, no. 6, pp. 1106–1112, 2011.
- [6] D. Yamashita, Y. Murata, N. Hikage, K.-I. Takao, A. Nakazaki, and S. Kobayashi, "Total synthesis of (-)-norzoanthamine," *Angewandte Chemie—International Edition*, vol. 48, no. 8, pp. 1404–1406, 2009.
- [7] P. Gao, Z. Tong, H. Hu et al., "Synthesis of (+)-9a-epi-stemoamide via DBU-catalyzed michael addition of nitroalkane," *Synlett*, no. 13, pp. 2188–2190, 2009.
- [8] C. Yu, B. Tian, J. Fan, G. D. Stucky, and D. Zhao, "Nonionic block copolymer synthesis of large-pore cubic mesoporous single crystals by use of inorganic salts," *Journal of the American Chemical Society*, vol. 124, no. 17, pp. 4556–4557, 2002.
- [9] Y. Sakamoto, M. Kaneda, O. Terasaki et al., "Direct imaging of the pores and cages of three-dimensional mesoporous materials," *Nature*, vol. 408, no. 6811, pp. 449–453, 2000.
- [10] N. Md. Alam, S. M. Sarkar, and R. Md. Miah, "Heterogeneous Heck reaction catalysed by silica gel-supported 1,2-diaminocyclohexane-Pd complex," *Reaction Kinetics and Catalysis Letters*, vol. 98, no. 2, pp. 383–389, 2009.
- [11] E. N. Jacobsen, A. Pfaltz, and H. Yamamoto, in *Comprehensive Asymmetric Catalysis II*, Springer, Berlin, Germany, 1999.
- [12] D. J. Smaltz and A. G. Myers, "Scalable synthesis of enantiomerically pure *syn*-2,3-dihydroxybutyrate by sharpless asymmetric dihydroxylation of *p*-phenylbenzyl crotonate," *The Journal of Organic Chemistry*, vol. 76, no. 20, pp. 8554–8559, 2011.
- [13] J. Peed, I. R. Davies, L. R. Peacock, J. E. Taylor, G. K. Köhn, and S. D. Bull, "Dihydroxylation-based approach for the asymmetric syntheses of hydroxy- γ -butyrolactones," *The Journal of Organic Chemistry*, vol. 77, no. 1, pp. 543–555, 2012.
- [14] M. X. Zhao, H. L. Bi, H. Zhou, H. Yang, and M. Shi, "Cinchona alkaloid squaramide catalyzed enantioselective hydrazination/cyclization cascade reaction of α -isocyanoacetates and azodicarboxylates: synthesis of optically active 1,2,4-triazolines," *The Journal of Organic Chemistry*, vol. 78, p. 9377, 2013.
- [15] H. C. Kolb, M. S. VanNieuwenhze, and K. B. Sharpless, "Catalytic asymmetric dihydroxylation," *Chemical Reviews*, vol. 94, no. 8, pp. 2483–2547, 1994.
- [16] H. Salim and O. Piva, "A short access to 3-hydroxy-4-hydroxymethyltetrahydrofurans: application to the total synthesis of amphiasterin B4," *The Journal of Organic Chemistry*, vol. 74, no. 5, pp. 2257–2260, 2009.
- [17] G.-B. Ren and Y. Wu, "Enantioselective total synthesis and correction of the absolute configuration of megislactone," *Tetrahedron*, vol. 64, no. 19, pp. 4408–4415, 2008.
- [18] X. Huo, X. Ren, Y. Xu, X. Li, X. She, and X. Pan, "Enantioselective total synthesis of hydramicromelin B," *Tetrahedron Asymmetry*, vol. 19, no. 3, pp. 343–347, 2008.
- [19] L. L. Lazarusa and R. L. Brutchey, "Heterogeneous fullerene-supported osmium tetroxide catalyst for the *cis*-dihydroxylation of olefins," *Dalton Transactions*, vol. 39, pp. 7888–7890, 2010.
- [20] R. Cano, J. M. Pérez, and D. J. Ramón, "Osmium impregnated on magnetite as a heterogeneous catalyst for the *syn*-dihydroxylation of alkenes," *Applied Catalysis A: General*, vol. 470, pp. 177–182, 2004.
- [21] S. M. Sarkar, N. Md. Alam, and R. Md. Miah, "Highly efficient silica gel-supported 1,2-diaminocyclohexane-Pd catalyst for Suzuki–Miyaura and Sonogashira coupling reactions," *Reaction Kinetics and Catalysis Letters*, vol. 96, no. 1, pp. 175–183, 2009.
- [22] N. Md. Alam and S. M. Sarkar, "Mesoporous MCM-41 supported N-heterocyclic carbene-Pd(II) complex for Suzuki coupling reaction," *Reaction Kinetics, Mechanisms, and Catalysis*, vol. 103, no. 2, pp. 493–500, 2011.
- [23] M. S. Sarkar, H. Qiu, and M.-J. Jin, "Encapsulation of Pd complex in ionic liquid on highly ordered mesoporous silica MCM-41," *Journal of Nanoscience and Nanotechnology*, vol. 7, no. 11, pp. 3880–3883, 2007.
- [24] H. Qiu, S. M. Sarkar, H. Do. Lee, and M. J. Jin, "Highly effective silica gel-supported N-heterocyclic carbene-Pd catalyst for Suzuki–Miyaura coupling reaction," *Green Chemistry*, vol. 10, pp. 37–40, 2008.
- [25] C. E. Song, J. W. Yang, and H.-J. Ha, "Silica gel supported bis-cinchona alkaloid: a highly efficient chiral ligand for heterogeneous asymmetric dihydroxylation of olefins," *Tetrahedron Asymmetry*, vol. 8, no. 6, pp. 841–844, 1997.
- [26] S. H. Kim and M. J. Jin, "Asymmetric dihydroxylation catalyzed by MCM-41 silica-supported bis-cinchona alkaloid," *Studies in Surface Science and Catalysis*, vol. 146, pp. 677–680, 2003.
- [27] H. M. Lee, S.-W. Kim, T. Hyeon, and B. M. Kim, "Asymmetric dihydroxylation using heterogenized cinchona alkaloid ligands on mesoporous silica," *Tetrahedron Asymmetry*, vol. 12, no. 11, pp. 1537–1541, 2001.
- [28] D. Zhao, Q. Huo, J. Feng, B. F. Chmelka, and G. D. Stucky, "Nonionic triblock and star diblock copolymer and oligomeric surfactant syntheses of highly ordered, hydrothermally stable, mesoporous silica structures," *Journal of the American Chemical Society*, vol. 120, no. 24, pp. 6024–6036, 1998.
- [29] S. Brunauer, P. H. Emmett, and E. Teller, "Adsorption of gases in multimolecular layers," *Journal of the American Chemical Society*, vol. 60, no. 2, pp. 309–319, 1938.
- [30] W. W. Lukens Jr., P. Schmidt-Winkel, D. Zhao, J. Feng, and G. D. Stucky, "Evaluating pore sizes in mesoporous materials: a simplified standard adsorption method and a simplified Broekhoff-de Boer method," *Langmuir*, vol. 15, no. 16, pp. 5403–5409, 1999.
- [31] A. Romero, A. Santos, J. Tojo, and A. Rodríguez, "Toxicity and biodegradability of imidazolium ionic liquids," *Journal of Hazardous Materials*, vol. 151, no. 1, pp. 268–273, 2008.
- [32] L. C. Branco and C. A. M. Afonso, "Ionic liquids as a convenient new medium for the catalytic asymmetric dihydroxylation of olefins using a recoverable and reusable osmium/ligand," *The Journal of Organic Chemistry*, vol. 69, no. 13, pp. 4381–4389, 2004.
- [33] M. H. Junttila and O. O. E. Hormi, "Methanesulfonamide: a cosolvent and a general acid catalyst in sharpless asymmetric dihydroxylation," *Journal of Organic Chemistry*, vol. 74, no. 8, pp. 3038–3047, 2009.

Research Article

Improved Ferroelectric and Leakage Properties of Ce Doped in BiFeO₃ Thin Films

Alima Bai, Shifeng Zhao, and Jieyu Chen

School of Physical Science and Technology and Inner Mongolia Key Lab of Nanoscience and Nanotechnology, Inner Mongolia University, Hohhot 010021, China

Correspondence should be addressed to Shifeng Zhao; zhsf@imu.edu.cn

Received 10 May 2014; Accepted 20 May 2014; Published 8 June 2014

Academic Editor: Daniela Predoi

Copyright © 2014 Alima Bai et al. This is an open access article distributed under the Creative Commons Attribution License, which permits unrestricted use, distribution, and reproduction in any medium, provided the original work is properly cited.

Ce doped BiFeO₃ thin films with a perovskite structure were prepared using solution-gelation method. It shows that the ferroelectric properties have been enhanced after doping Ce. The enhanced ferroelectric properties are attributed to the structural transformation and the reduced leakage current after doping rare metal of Ce. It has been found that the phase structures of the films transfer from rhombohedral symmetry structure to the coexistence of the tetragonal and orthorhombic symmetry structure. And Fe²⁺ ions have been reduced, which leads to the decreased leakage for Ce doped BiFeO₃ thin films. The present work can provide an available way to improve the ferroelectric and leakage properties for multiferroic BiFeO₃ based thin films.

1. Introduction

Multiferroic materials exhibit ferroelectric, ferromagnetic, and ferroelasticity properties simultaneously in a certain temperature range. The single phase BiFeO₃ (BFO) materials with perovskite structure have aroused wide concerns due to its high Curie temperature (T_N) of 1103 K and Neel temperature (T_C) of 643 K [1], which make it a most promising candidate in ferroelectric memory storage and magnetoelectric devices [2–5]. However, for BiFeO₃ materials with a rhombohedrally distorted perovskite structure belonging to the space group R3c, it is difficult to gain a large saturation and remnant polarization due to the higher leakage current arising from defects such as impurity phases and oxygen vacancies [6, 7]. Several investigations have been carried out to prove that it is an effective approach for rare earth iron doping at Bi site to overcome the technical barrier and improve the ferroelectric and leakage properties of BiFeO₃ materials [8–10]. Evidently, donor and acceptor dopants have contrary effects on modulating the charged defects. Thus, it becomes necessary to further understand how they affect the respective polarity and polarization stability of BiFeO₃ thin films. However, most of these studies were focused on ceramics and bulk materials [11, 12], which are not fit for the rapidly developing micro- and nanoelectromechanical system (MEMS&NEMS).

Therefore, in this work, Ce doped BiFeO₃ thin films were prepared using solution-gelation method as this technique can well control the stoichiometric ratio. Ce will replace Bi of A sites in perovskite structure of ABO₃. The choice of the dopant ion was based on the fact that Ce³⁺ has a more stable electronic configuration than Bi³⁺, which minimizes the leakage current and further improves ferroelectric properties in BiFeO₃ thin films. The origins of the improved ferroelectric and leakage properties are discussed in detail in this paper. The present work can provide an available way to improve the ferroelectric properties for single phase multiferroic BiFeO₃ based thin films.

2. Experiment

The pure and Ce doped BiFeO₃ thin films were prepared using the solution-gelation method. All the reactions were carried out at room temperature under ambient conditions. High-purity bismuth nitrate [Bi(NO₃)₃·5H₂O], ferric nitrate [Fe(NO₃)₃·9H₂O], and cerium nitrate [Ce(NO₃)₃·6H₂O] were obtained from commercial sources (Alfa Aesar); they were dissolved in solvent ethylene glycol monomethyl ether in proper proportions of 0.99:1:0.1 and stirred until the solutions turn into transparent for about three to four hours.

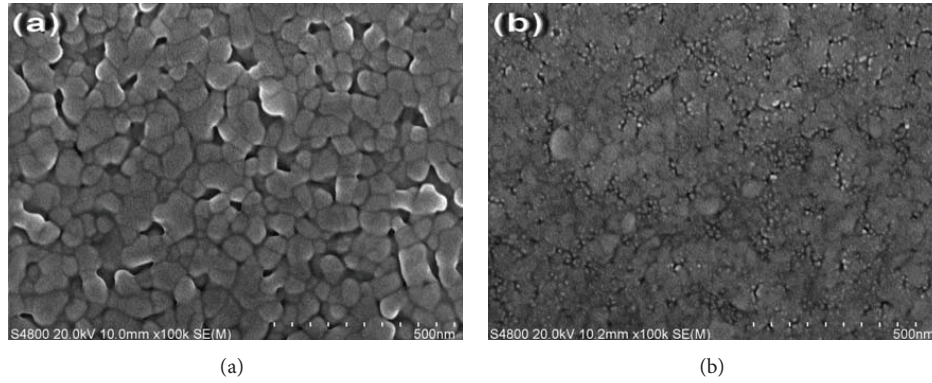


FIGURE 1: The typical SEM images of the thin films, (a) pure BiFeO_3 thin films, (b) Ce doped BiFeO_3 thin films.

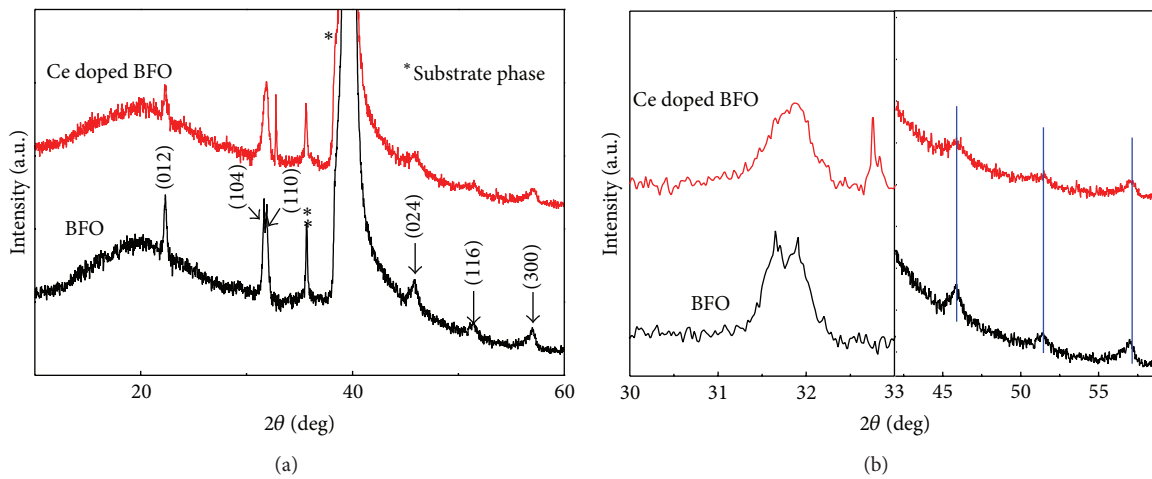


FIGURE 2: (a) XRD patterns of pure and Ce doped BiFeO_3 thin films, (b) magnified XRD patterns.

$[\text{Bi}(\text{NO}_3)_3 \cdot 5\text{H}_2\text{O}]$ should be added by excessive 10% for volatilizing Bi in process of dissolving and annealing. The process of preparing pure BiFeO_3 solution is similar to the above one, but $[\text{Bi}(\text{NO}_3)_3 \cdot 5\text{H}_2\text{O}]$ and $[\text{Fe}(\text{NO}_3)_3 \cdot 9\text{H}_2\text{O}]$ had the proportion of 1.1:1. Further, the prepared solutions were aged for several days. Then, the thin films were coated by spin coater. Here are conditions of rotation speed; low velocity is 400 r/min and high velocity is 3500 r/min. Next thin films were baked on the heating stage for five minutes at 280°C and annealed with rapid thermal processor system for five minutes at 550°C . This process was repeated twelve times and final annealing was for twenty minutes to obtain the BiFeO_3 thin films with the thickness of 300 nm. The orientation, crystal structure, and phase purity of the thin films were analyzed by X-ray diffraction (XRD, Panalytical-Empyrean) with $\text{Cu-K}\alpha$ radiation ($\lambda = 0.15406 \text{ nm}$). The surface morphologies of the thin films were investigated by a scanning electron microscope (SEM, Hitachi S-4800). Raman spectroscopy measurements were performed at room temperature using a confocal Raman spectroscope (NT-MDT NTEGRA Spectra) with a 633 nm excitation laser with an initial power of 10 mW. For the fabrication of BiFeO_3 based multiferroic thin film capacitors, Au top electrodes with

a diameter of 0.2 mm were deposited on the surface of the thin films using an ion sputtering method. The ferroelectric and leakage properties of the thin films capacitors were measured using a multiferroic tester system (MultiFerroic100V, Radient Technology, USA) at room temperature. The binding energies of atoms and orbits for the samples were characterized by X-ray photoelectron spectroscopy (XPS, KRATOS-AMICUS). The cleaning treatments of thin films were carried out using Ar ion bombardment. And all binding energies were calibrated with respect to C 1s spectral line at 284.8 eV.

3. Results and Discussion

The typical SEM images of the pure and Ce doped BiFeO_3 thin films were shown in Figure 1. One can clearly observe that both thin films are assembled with uniformly distributed grains. Some small voids can be observed from the surface of the pure BiFeO_3 thin films in Figure 1(a), while for Ce doped BiFeO_3 thin films, it exhibits more dense morphology and less small holes than the pure BiFeO_3 thin films as shown in Figure 1(b). That is, the microstructure of thin films becomes more compact, which leads to the reduced voids for thin films. Thus result is attributed to the fact that Ce is more

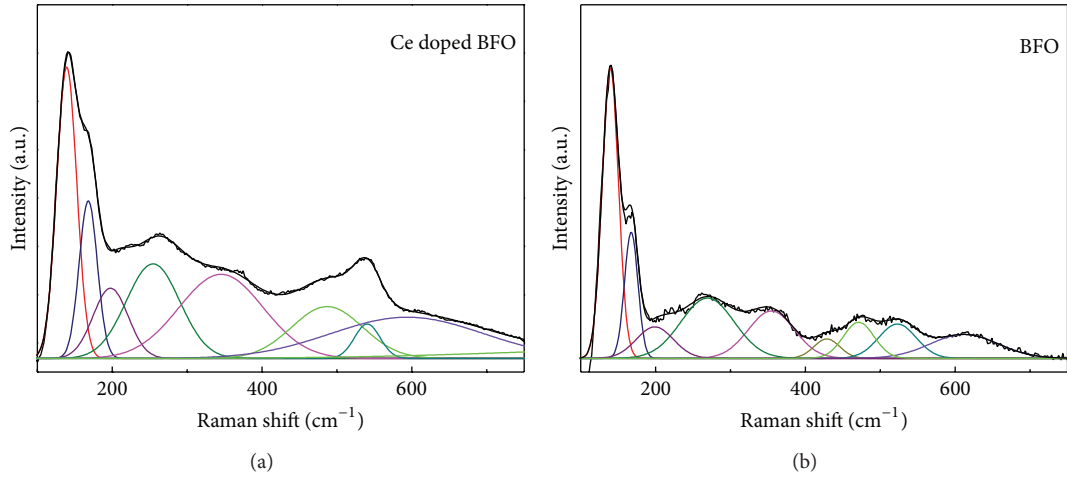


FIGURE 3: Raman scattering spectra of (a) Ce doped BiFeO_3 and (b) pure BiFeO_3 thin films.

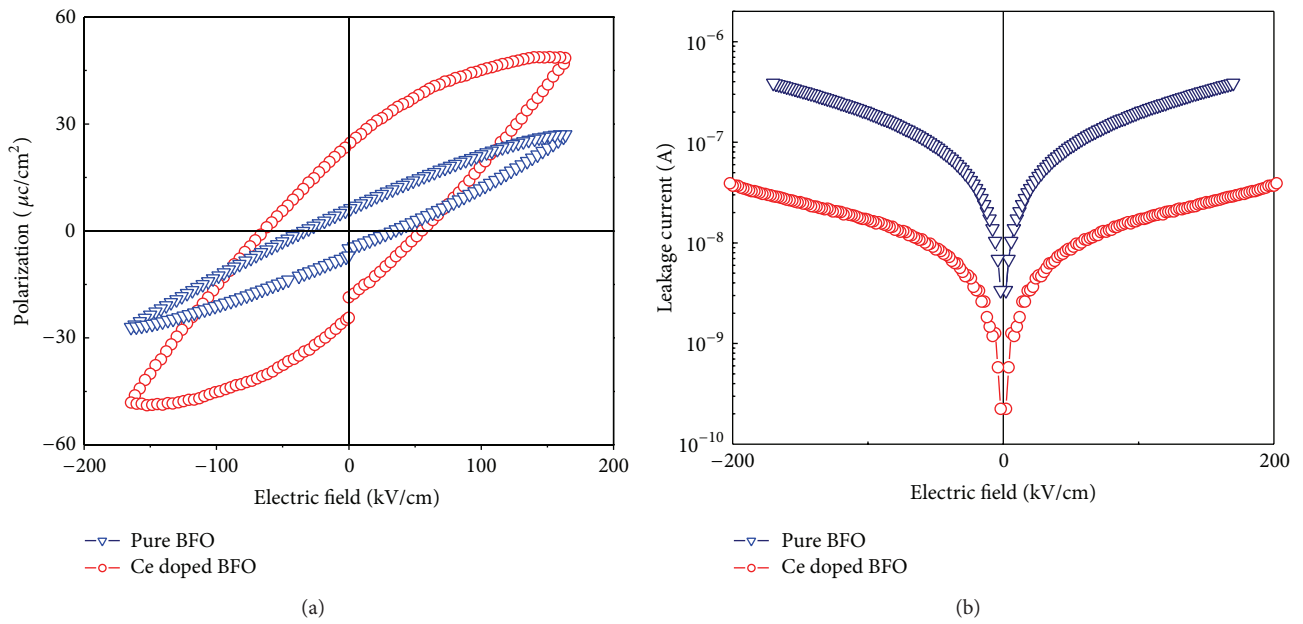


FIGURE 4: (a) Ferroelectric hysteresis of the pure and Ce doped BiFeO_3 thin films, (b) leakage current curves of the pure and Ce doped BiFeO_3 thin films.

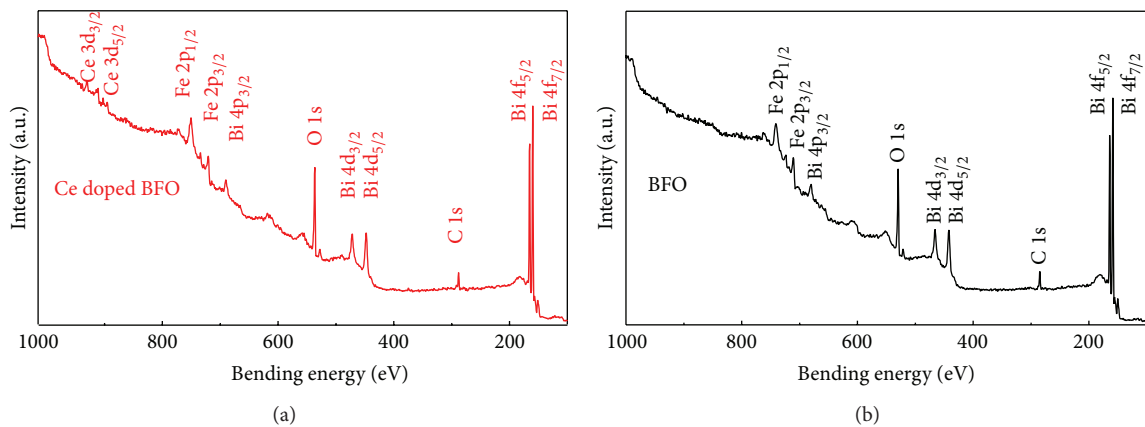


FIGURE 5: XPS survey spectra of pure and Ce doped BiFeO_3 thin films.

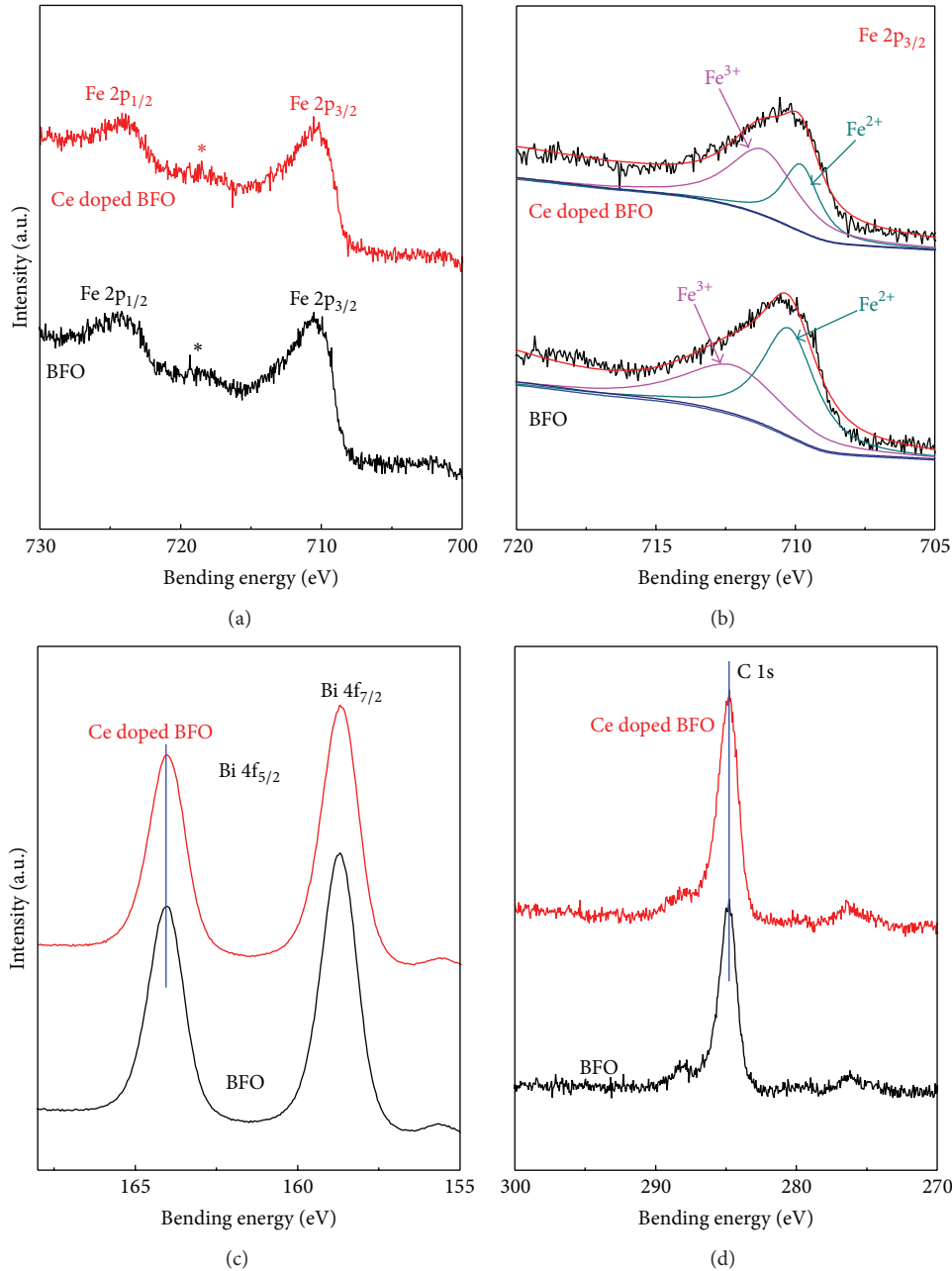


FIGURE 6: XPS patterns of the typical pure BiFeO_3 and Ce doped BiFeO_3 thin films. (a) High-resolution Fe 2p spectra, (b) fitting spectra of the $\text{Fe}2p_{3/2}$ peaks, (c) high-resolution Bi 4f spectra, and (d) high-resolution C 1s spectra.

stable than Bi element, which reduces oxygen vacancy and increases the combining of elements. This compact surface morphology is available to improve the properties such as ferroelectricity and the leakage current of thin films.

Figure 2 presents the XRD patterns of the pure and Ce doped BiFeO_3 thin films. It can be seen that the thin films are polycrystalline perovskite structure without any prominent impurity peaks (e.g., $\text{Bi}_2\text{Fe}_4\text{O}_9$, $\text{Bi}_{25}\text{FeO}_{40}$, etc.) observed. The absence of the diffraction peaks of Ce and its oxides implies that Ce is incorporated with the BiFeO_3 by the means of substitution for Bi. Figure 1(b) further gives an expanded view on the location of diffraction peaks in the

range of 30–33 and 47–57 degree (2θ). It shows clearly that the pure BiFeO_3 thin film has a perovskite rhombohedral structure belonging to the space group R3c as the (104) and (110) diffraction peaks are almost completely separated, while the two diffraction peaks were greatly overlapped to form one peak with the Ce substitution doping at Bi site, which indicates that the rhombohedral distortion is reduced toward the coexistence of tetragonal and orthorhombic symmetry structure after doping Ce. This structural transformation is consistent with the other reports on rare earth doped BiFeO_3 ceramics [13, 14]. Besides, it can be seen that the position of all the diffraction peaks does not

TABLE 1: Raman scattering modes of the pure and Ce doped BiFeO₃ thin films.

Raman modes	BiFeO ₃ thin films	Ce doped BiFeO ₃ thin films
A ₁ -1 (cm ⁻¹)	141.10	139.06
A ₁ -2 (cm ⁻¹)	167.88	167.35
A ₁ -3 (cm ⁻¹)	198.66	197.66
E-2 (cm ⁻¹)	268.60	254.68
E-5 (cm ⁻¹)	355.53	346.64
A ₁ -4 (cm ⁻¹)	428.25	—
E-7 (cm ⁻¹)	471.04	487.72
E-8 (cm ⁻¹)	523.04	541.48
E-9 (cm ⁻¹)	612.05	595.63

obviously shift. That is attributed to the almost equal ionic radius of Ce³⁺ (1.02 Å) compared with that of Bi³⁺ (1.03 Å).

Figure 3 shows the Raman scattering spectra of the pure and Ce doped BiFeO₃ thin films. Table 1 reveals the Raman scattering modes of pure BiFeO₃ and Ce doped BiFeO₃ thin films including A₁-1, A₁-2, A₁-3, A₁-4, E-2, E-5, E-7, E-8, and E-9 modes, respectively. The observed scattering modes were in close agreement with the irreducible representation: $\Gamma = 4A_1 + 9E$ [15, 16]. Combining Table 1 and Figure 3, we found that A₁-1, A₁-2, E-2, and A₁-3 modes have got red shift and the scattering peak at 428.25 cm⁻¹ has disappeared after doping Ce. The reason for this phenomenon can be stated as the following two aspects: one is that the change of the interaction between atoms due to the heavier atom of Bi replaced by the lighter atom of Ce causes the change of the phonon frequencies after doping Ce; another reason is structural phase transformation from rhombohedral symmetry structure to the coexistence of tetragonal and orthorhombic symmetry structure after doping Ce, which leads to the change in Bi-O covalent bonds as the bond controls the E-1, A₁-1, A₁-2, A₁-3, and E-2 modes.

Figure 4(a) illustrates ferroelectric hysteresis and leakage current of the pure and Ce doped BiFeO₃ thin films, respectively. As shown in Figure 4(a), the ferroelectric properties change after doping Ce. For the pure BiFeO₃ thin films, the ferroelectric properties are poor and unsaturated ferroelectric hysteresis is observed, while the polarization has been enhanced for the film of Ce doped BiFeO₃ thin films, especially under large electric field. After doping Ce, the remanent and saturation polarization have been increased from 6.22 μC/cm² to 25.10 μC/cm² and from 27.07 μC/cm² to 49.22 μC/cm², respectively. It is caused by the structural transformation from the R3c space group of rhombohedral structure of the pure BiFeO₃ thin films to the Pna2₁ space group of orthorhombic structure of Ce doped BiFeO₃ thin films. Moreover, the improvement of ferroelectricity is also closely related to the leakage current behavior as discussed below.

Figure 4(b) further shows the leakage current versus electric field (*E*) characteristics plots recorded with a voltage step width of 0.1 V of the thin films capacitors. It shows that the leakage currents of Ce doped BiFeO₃ thin films are decreased by one to two orders of magnitude in comparison

with the pure BiFeO₃ thin films. For the pure BiFeO₃ thin films, a substantial number of oxygen vacancies and Fe²⁺ ion are created to compensate the positive charge deficiency caused by the vaporization of Bi [17]. They serve as donor-like trapping centers for electrons, which can be activated to be free for current conduction at the applied electric field, further leading to the higher leakage current in the pure BiFeO₃ thin films [18], while the leakage current of BiFeO₃ thin films was decreased after doping Ce, which is attributed to two factors. On one hand, the reduction of leakage current results from the structural transformation as discussed above. The leakage current of the pure BiFeO₃ thin films is larger than that of Ce doped BiFeO₃ thin films, which indicates the rhombohedral structure is closely related to the higher leakage current density. The coexistence structure of tetragonal and orthorhombic symmetry structure in BiFeO₃ thin films is an important reason to decrease the leakage current. On the other hand, the creation of oxygen vacancies and the presence of Fe²⁺ ion were suppressed as it is effective for Ce substitution doping to control the volatility of Bi atoms. Thus XPS investigations further confirm those points.

In order to intensify the oxidation of Fe, oxygen vacancies, and the elements for the pure and Ce doped BiFeO₃ thin films, XPS survey spectra are presented in Figure 5. It reveals the presence of Bi, Fe, O, and Ce without any other trace impurities except for a small amount of carbon for Ce doped BiFeO₃ thin films. This confirms the chemical compositions of the pure and Ce doped BiFeO₃ thin films.

In order to further intensify the oxidation of Fe, Figure 6(a) presents the representative Fe 2p XPS spectra of the pure and Ce doped BiFeO₃ thin films. Two main XPS peaks for Fe 2p_{1/2} and Fe 2p_{3/2} were observed in both the pure and the Ce doped BiFeO₃ thin films. Moreover, a satellite peak was also identified, which was considered to be characteristic of the oxidation state of Fe. Due to different d orbital electron configuration, during the relaxation of metal cations, Fe²⁺ and Fe³⁺ cations always show the satellite peaks with the gap of 6 eV and 8 eV above the Fe 2p_{3/2} peaks, respectively [19].

We further analyze the peak of the Fe_{2p_{3/2}} by Lorentzian-Gaussian fitting, as shown in Figure 6(b). It suggests that Fe³⁺ and Fe²⁺ cations are coexistence in both the thin films and the binding energy changes after doping Ce. The Fe_{2p_{3/2}} peak position for the pure BiFeO₃ thin films is confirmed at 710.30 eV for Fe²⁺ cations and 712.49 eV for Fe³⁺ ions, respectively, while the Fe_{2p_{3/2}} peak position for Ce doped BiFeO₃ films is confirmed at 709.79 eV for Fe²⁺ ions and 711.28 eV for Fe³⁺ cations, respectively. It is easy to conclude that the binding energy between Fe and O decreases after doping rare earth metal of Ce. The change in Bi-O covalent bonds is attributed to the structural phase transformation from rhombohedral symmetry structure to the coexistence of tetragonal and orthorhombic symmetry structure, which is accordant with the results of the Raman shift spectra discussed above. At the same time, the binding energy between Bi and O does not change after doping Ce, as shown in Figure 6(c). The peak position is confirmed at 164.02 eV for Bi 4f_{5/2} and 158.68 eV for Bi 4f_{7/2}. Figure 6(d) further presents the XPS peak of C for the pure and Ce doped BiFeO₃ thin

films, which suggests that the peak shifts above would come from the change of binding energy rather than the measure errors.

As we know, electron hops between Fe^{3+} cations and Fe^{2+} ions are accordant with charged compensated oxygen vacancies. More Fe^{2+} ions imply more oxygen vacancies, which would cause large leakage current and further decrease ferroelectric properties. Fortunately, the ratio of Fe^{2+} to Fe^{3+} cations changes from about 1 : 1 to 1 : 2 by calculating the area of peak. It obviously means that the concentration of the Fe^{2+} is decreased after doping Ce. Therefore, the Ce doping was helpful to reduce the Fe^{2+} ions concentration in BiFeO_3 based thin films, which decrease their leakage currents and further improve ferroelectric properties.

4. Conclusions

In summary, the pure and Ce doped BiFeO_3 thin films were prepared by solution-gelation process and their phase structures, ferroelectric properties, and leakage were systematically investigated. The enhanced ferroelectric properties have been obtained after doping Ce. Thus enhancement is attributed to the structural transformation from rhombohedral symmetry structure to coexistence of orthorhombic symmetry structure revealed by XRD measurements. At the same time, the leakage current decreases obviously, which originates from the change of the binding energy between Fe–O increases and the decrease of the concentration of the Fe^{2+} after doping Ce. The present work provides an available way on enhancing ferroelectric properties and possible multifunctional applications for BiFeO_3 based thin films.

Conflict of Interests

The authors declare that there is no conflict of interests regarding the publication of this paper.

Acknowledgments

This work was financially supported by National Key Projects for Basic Research of China (973 Projects) (Grant no. 2012CB626815), the National Natural Science Foundation of China (Grant nos. 11264026 and 10904065), the Program for Young Talents of Science and Technology in Universities of Inner Mongolia Autonomous Region (Grant no. NJYT-12-B05), and Program of Higher-Level Talents of Inner Mongolia University (Grant no. 115109).

References

- [1] D. Lebeugle, A. Mougin, M. Viret, D. Colson, and L. Ranno, "Electric field switching of the magnetic anisotropy of a ferromagnetic layer exchange coupled to the multiferroic compound BiFeO_3 ," *Physical Review Letters*, vol. 103, no. 25, Article ID 257601, 2009.
- [2] S. Mathews, R. Ramesh, T. Venkatesan, and J. Benedetto, "Ferroelectric field effect transistor based on epitaxial perovskite heterostructures," *Science*, vol. 276, no. 5310, pp. 238–240, 1997.
- [3] C. Ederer and N. A. Spaldin, "Weak ferromagnetism and magnetoelectric coupling in bismuth ferrite," *Physical Review B*, vol. 71, no. 6, Article ID 060401, 2005.
- [4] W. Eerenstein, N. D. Mathur, and J. F. Scott, "Multiferroic and magnetoelectric materials," *Nature*, vol. 442, no. 7104, pp. 759–765, 2006.
- [5] D. Lee, S. M. Yang, T. H. Kim et al., "Multilevel data storage memory using deterministic polarization control," *Advanced Materials*, vol. 24, no. 3, pp. 402–406, 2012.
- [6] M. S. Bernardo, T. Jardiel, M. Peiteado et al., "Intrinsic compositional inhomogeneities in bulk Ti-doped BiFeO_3 : microstructure development and multiferroic properties," *Chemistry of Materials*, vol. 25, no. 9, pp. 1533–1541, 2013.
- [7] H. Ke, W. Wang, Y. B. Wang et al., "Factors controlling pure-phase multiferroic BiFeO_3 powders synthesized by chemical coprecipitation," *Journal of Alloys and Compounds*, vol. 509, no. 5, pp. 2192–2197, 2011.
- [8] A. P. Chen, H. H. Zhou, Z. X. Bi et al., "A new class of room-temperature multiferroic thin films with bismuth-based supercell structure," *Advanced Materials*, vol. 25, no. 7, pp. 1028–1032, 2013.
- [9] D. P. Dutta, B. P. Mandal, R. Naik, G. Lawes, and A. K. Tyagi, "Magnetic, ferroelectric, and magnetocapacitive properties of sonochemically synthesized Sc-doped BiFeO_3 nanoparticles," *The Journal of Physical Chemistry C*, vol. 117, no. 5, pp. 2382–2389, 2013.
- [10] N. Jeon, D. Rout, W. Kim, and S. J. L. Kang, "Enhanced multiferroic properties of single-phase BiFeO_3 bulk ceramics by Ho doping," *Applied Physics Letters*, vol. 98, no. 7, Article ID 072901, 2011.
- [11] J.-B. Li, G. H. Rao, Y. Xiao et al., "Structural evolution and physical properties of $\text{Bi}_{1-x}\text{Gd}_x\text{FeO}_3$ ceramics," *Acta Materialia*, vol. 58, no. 10, pp. 3701–3708, 2010.
- [12] G. L. Yuan, S. W. Or, J. M. Liu, and Z. G. Liu, "Structural transformation and ferroelectromagnetic behavior Structural transformation and ferroelectromagnetic behavior in single-phase $\text{Bi}_{1-x}\text{Nd}_x\text{FeO}_3$ multiferroic ceramics," *Applied Physics Letters*, vol. 89, no. 5, Article ID 052905, 2006.
- [13] X. Q. Zhang, Y. Sui, X. J. Wang, Y. Wang, and Z. Wang, "Effect of Eu substitution on the crystal structure and multiferroic properties of BiFeO_3 ," *Journal of Alloys and Compounds*, vol. 507, no. 1, pp. 157–161, 2010.
- [14] L. R. Luo, W. Wei, X. Y. Yuan, K. Shen, M. X. Xu, and Q. Y. Xu, "Multiferroic properties of Y-doped BiFeO_3 ," *Journal of Alloys and Compounds*, vol. 540, pp. 36–38, 2012.
- [15] M. K. Singh, H. M. Jang, S. Ryu, and M. H. Jo, "Polarized Raman scattering of multiferroic BiFeO_3 epitaxial films with rhombohedral $R3c$ symmetry," *Applied Physics Letters*, vol. 88, no. 4, Article ID 042907, 2006.
- [16] V. A. Khomchenko, I. O. Troyanchuk, M. I. Kovetskaya, and J. A. Paixao, "Mn substitution-driven structural and magnetic phase evolution in $\text{Bi}_{1-x}\text{Sm}_x\text{FeO}_3$ multiferroics," *Journal of Applied Physics*, vol. 111, no. 1, Article ID 014110, 2012.
- [17] S. H. Jo, S. G. Lee, and S. H. Lee, "Structural and pyroelectric properties of sol-gel derived multiferroic BFO thin films," *Materials Research Bulletin*, vol. 47, no. 2, pp. 409–412, 2012.
- [18] G. D. Hu, S. H. Fan, C. H. Yang, and W. B. Wu, "Low leakage current and enhanced ferroelectric properties of Ti and Zn

codoped BiFeO₃ thin film,” *Applied Physics Letters*, vol. 92, no. 19, Article ID 192905, 2008.

- [19] L. Bi, A. R. Taussig, H.-S. Kim et al., “Structural, magnetic, and optical properties of BiFeO₃ and Bi₂ FeMnO₆ epitaxial thin films: an experimental and first-principles study,” *Physical Review B*, vol. 78, no. 10, Article ID 104106, 2008.